

1      **The Sensitivity to Oscillation Parameters**  
2      **from a Simultaneous Beam and**  
3      **Atmospheric Neutrino Analysis that**  
4      **combines the T2K and SK Experiments**



6      Daniel Robert Clement Barrow  
7      Magdalen College  
8      University of Oxford

9      A thesis submitted for the degree of  
10     *Doctor of Philosophy*  
11     Michaelmas 2022

# Abstract

12

13 Lorem ipsum dolor sit amet, consectetur adipiscing elit. Pellentesque sit amet  
14 nibh volutpat, scelerisque nibh a, vehicula neque. Integer placerat nulla massa,  
15 et vestibulum velit dignissim id. Ut eget nisi elementum, consectetur nibh in,  
16 condimentum velit. Quisque sodales dui ut tempus mattis. Duis malesuada arcu  
17 at ligula egestas egestas. Phasellus interdum odio at sapien fringilla scelerisque.  
18 Mauris sagittis eleifend sapien, sit amet laoreet felis mollis quis. Pellentesque  
19 dui ante, finibus eget blandit sit amet, tincidunt eu neque. Vivamus rutrum  
20 dapibus ligula, ut imperdiet lectus tincidunt ac. Pellentesque ac lorem sed  
21 diam egestas lobortis.

22 Suspendisse leo purus, efficitur mattis urna a, maximus molestie nisl. Aenean  
23 porta semper tortor a vestibulum. Suspendisse viverra facilisis lorem, non  
24 pretium erat lacinia a. Vestibulum tempus, quam vitae placerat porta, magna  
25 risus euismod purus, in viverra lorem dui at metus. Sed ac sollicitudin nunc.  
26 In maximus ipsum nunc, placerat maximus tortor gravida varius. Suspendisse  
27 pretium, lorem at porttitor rhoncus, nulla urna condimentum tortor, sed suscipit  
28 nisi metus ac risus.

29 Aenean sit amet enim quis lorem tristique commodo vitae ut lorem. Duis  
30 vel tincidunt lacus. Sed massa velit, lacinia sed posuere vitae, malesuada vel  
31 ante. Praesent a rhoncus leo. Etiam sed rutrum enim. Pellentesque lobortis  
32 elementum augue, at suscipit justo malesuada at. Lorem ipsum dolor sit amet,  
33 consectetur adipiscing elit. Praesent rhoncus convallis ex. Etiam commodo nunc  
34 ex, non consequat diam consectetur ut. Pellentesque vitae est nec enim interdum  
35 dapibus. Donec dapibus purus ipsum, eget tincidunt ex gravida eget. Donec  
36 luctus nisi eu fringilla mollis. Donec eget lobortis diam.

37 Suspendisse finibus placerat dolor. Etiam ornare elementum ex ut vehicula.  
38 Donec accumsan mattis erat. Quisque cursus fringilla diam, eget placerat neque  
39 bibendum eu. Ut faucibus dui vitae dolor porta, at elementum ipsum semper.  
40 Sed ultrices dui non arcu pellentesque placerat. Etiam posuere malesuada turpis,  
41 nec malesuada tellus malesuada.

# Acknowledgements

## <sup>43</sup> Personal

<sup>44</sup> This is where you thank your advisor, colleagues, and family and friends.

<sup>45</sup> Lorem ipsum dolor sit amet, consectetur adipiscing elit. Vestibulum feugiat  
<sup>46</sup> et est at accumsan. Praesent sed elit mattis, congue mi sed, porta ipsum. In  
<sup>47</sup> non ullamcorper lacus. Quisque volutpat tempus ligula ac ultricies. Nam sed  
<sup>48</sup> erat feugiat, elementum dolor sed, elementum neque. Aliquam eu iaculis est,  
<sup>49</sup> a sollicitudin augue. Cras id lorem vel purus posuere tempor. Proin tincidunt,  
<sup>50</sup> sapien non dictum aliquam, ex odio ornare mauris, ultrices viverra nisi magna  
<sup>51</sup> in lacus. Fusce aliquet molestie massa, ut fringilla purus rutrum consectetur.  
<sup>52</sup> Nam non nunc tincidunt, rutrum dui sit amet, ornare nunc. Donec cursus  
<sup>53</sup> tortor vel odio molestie dignissim. Vivamus id mi erat. Duis porttitor diam  
<sup>54</sup> tempor rutrum porttitor. Lorem ipsum dolor sit amet, consectetur adipiscing  
<sup>55</sup> elit. Sed condimentum venenatis consectetur. Lorem ipsum dolor sit amet,  
<sup>56</sup> consectetur adipiscing elit.

<sup>57</sup> Aenean sit amet lectus nec tellus viverra ultrices vitae commodo nunc. Mauris  
<sup>58</sup> at maximus arcu. Aliquam varius congue orci et ultrices. In non ipsum vel  
<sup>59</sup> est scelerisque efficitur in at augue. Nullam rhoncus orci velit. Duis ultricies  
<sup>60</sup> accumsan feugiat. Etiam consectetur ornare velit et eleifend.

<sup>61</sup> Suspendisse sed enim lacinia, pharetra neque ac, ultricies urna. Phasellus sit  
<sup>62</sup> amet cursus purus. Quisque non odio libero. Etiam iaculis odio a ex volutpat, eget  
<sup>63</sup> pulvinar augue mollis. Mauris nibh lorem, mollis quis semper quis, consequat  
<sup>64</sup> nec metus. Etiam dolor mi, cursus a ipsum aliquam, eleifend venenatis ipsum.  
<sup>65</sup> Maecenas tempus, nibh eget scelerisque feugiat, leo nibh lobortis diam, id laoreet  
<sup>66</sup> purus dolor eu mauris. Pellentesque habitant morbi tristique senectus et netus  
<sup>67</sup> et malesuada fames ac turpis egestas. Nulla eget tortor eu arcu sagittis euismod  
<sup>68</sup> fermentum id neque. In sit amet justo ligula. Donec rutrum ex a aliquet egestas.

## <sup>69</sup> Institutional

<sup>70</sup> If you want to separate out your thanks for funding and institutional support,  
<sup>71</sup> I don't think there's any rule against it. Of course, you could also just remove  
<sup>72</sup> the subsections and do one big traditional acknowledgement section.

<sup>73</sup>        Lorem ipsum dolor sit amet, consectetur adipiscing elit. Ut luctus tempor ex at  
<sup>74</sup>        pretium. Sed varius, mauris at dapibus lobortis, elit purus tempor neque, facilisis  
<sup>75</sup>        sollicitudin felis nunc a urna. Morbi mattis ante non augue blandit pulvinar.  
<sup>76</sup>        Quisque nec euismod mauris. Nulla et tellus eu nibh auctor malesuada quis  
<sup>77</sup>        imperdiet quam. Sed eget tincidunt velit. Cras molestie sem ipsum, at faucibus  
<sup>78</sup>        quam mattis vel. Quisque vel placerat orci, id tempor urna. Vivamus mollis,  
<sup>79</sup>        neque in aliquam consequat, dui sem volutpat lorem, sit amet tempor ipsum felis  
<sup>80</sup>        eget ante. Integer lacinia nulla vitae felis vulputate, at tincidunt ligula maximus.  
<sup>81</sup>        Aenean venenatis dolor ante, euismod ultrices nibh mollis ac. Ut malesuada  
<sup>82</sup>        aliquam urna, ac interdum magna malesuada posuere.

# Contents

83

84	<b>1 Introduction</b>	1
85	<b>2 Neutrino Oscillation Physics</b>	2
86	2.1 Discovery of Neutrinos . . . . .	3
87	2.2 Theory of Neutrino Oscillation . . . . .	4
88	2.3 Neutrino Oscillation Measurements . . . . .	8
89	2.4 Summary Of Oscillation Parameter Measurements . . . . .	18
90	2.5 Overview of Oscillation Effects . . . . .	19
91	<b>3 T2K and SK Experiment Overview</b>	27
92	3.1 The Super-Kamiokande Experiment . . . . .	27
93	3.2 The Tokai to Kamioka Experiment . . . . .	38
94	<b>4 Bayesian Statistics and Markov Chain Monte Carlo Techniques</b>	53
95	4.1 Bayesian Statistics . . . . .	54
96	4.2 Monte Carlo Simulation . . . . .	56
97	4.3 Understanding the MCMC Results . . . . .	64
98	<b>5 Simulation, Reconstruction, and Event Reduction</b>	69
99	5.1 Simulation . . . . .	69
100	5.2 Event Reconstruction at SK . . . . .	75
101	5.3 Event Reduction at SK . . . . .	86
102	<b>6 Sample Selections and Systematics</b>	91
103	6.1 Atmospheric Samples . . . . .	93
104	6.2 Near Detector Beam Samples . . . . .	99
105	6.3 Far Detector Beam Samples . . . . .	101
106	6.4 Systematic Uncertainties . . . . .	107
107	6.5 Likelihood Calculation . . . . .	127
108	<b>7 Oscillation Probability Calculation</b>	131
109	7.1 Treatment of Fast Oscillations . . . . .	132
110	7.2 Calculation Engine . . . . .	139
111	7.3 Matter Density Profile . . . . .	143
112	7.4 Production Height Averaging . . . . .	148

113	<b>8 Oscillation Analysis</b>	<b>151</b>
114	8.1 Monte Carlo Prediction . . . . .	152
115	8.2 Sensitivities . . . . .	165
116	<b>9 Conclusions and Outlook</b>	<b>214</b>
117	<b>Appendices</b>	
118	<b>A Atmospheric Sample Spectra</b>	<b>216</b>
119	A.1 Binning . . . . .	216
120	A.2 Fully Contained Sub-GeV Samples . . . . .	216
121	A.3 Fully Contained Multi-GeV Samples . . . . .	220
122	A.4 Fully Contained Multi-Ring Samples . . . . .	221
123	A.5 Partially Contained Samples . . . . .	222
124	A.6 Upward-Going Muon Samples . . . . .	223

# 1

125

126

## Introduction

# 2

127

128

## Neutrino Oscillation Physics

129 When first proposed, neutrinos were expected to be approximately massless  
130 fermions that only interact through weak and gravitational forces. This meant  
131 they were very difficult to detect as they can pass through significant amounts  
132 of matter without interacting. Despite this, experimental neutrino physics has  
133 developed many different detection techniques and observed neutrinos from  
134 both natural and artificial sources. In direct tension with Standard Model physics,  
135 neutrinos have been determined to oscillate between different lepton flavours,  
136 requiring them to have mass.

137 The observation techniques which led to the discovery of the neutrino are doc-  
138 umented in section 2.1. The theory underpinning neutrino oscillation is described  
139 in section 2.2 and includes the approximations which can be made to simplify  
140 the understanding of neutrino oscillation in the two-flavour approximation. Past,  
141 current, and future neutrino experiments are detailed in section 2.3, including the  
142 reactor, atmospheric, and long-baseline accelerator neutrino sources that have  
143 been used to successfully constrain oscillation parameters. Finally, the current  
144 state of oscillation parameter measurements are summarised in section 2.4.

## 2.1 Discovery of Neutrinos

At the start of the 20<sup>th</sup> century, the electrons emitted from the  $\beta$ -decay of the nucleus were found to have a continuous energy spectrum [1, 2]. This observation seemingly broke the energy conservation invoked within that period's nuclear models. In 1930, Pauli provided a solution to this problem in the form of a new particle, the neutrino (originally termed "neutron"). It was theorized to be an electrically neutral spin-1/2 fermion with a mass smaller than that of the electron [3]. This neutrino was emitted with the electron in  $\beta$ -decay to alleviate the apparent breaking of energy conservation. As a predecessor of today's weak interaction model, Fermi's theory of  $\beta$ -decay developed the understanding by coupling the four constituent particles: electron, proton, neutron, and neutrino, into a quantitative model [4].

Whilst Pauli was not convinced of the ability to detect neutrinos, the first observations of the particle were made in the mid-1950s when neutrinos from a reactor were observed via the inverse  $\beta$ -decay (IBD) process,  $\bar{\nu}_e + p \rightarrow n + e^+$  [5, 6]. The detector consisted of two parts: a neutrino interaction medium and a liquid scintillator. The interaction medium was built from two water tanks, loaded with cadmium chloride to allow for increased efficiency in the detection of neutron capture. The positron emitted from IBD annihilates,  $e^+ + e^- \rightarrow 2\gamma$ , generating a prompt signal and the neutron is captured on the cadmium via  $n + ^{108}Cd \rightarrow ^{109*}Cd \rightarrow ^{109}Cd + \gamma$ , producing a delayed signal. An increase in the coincidence rate was observed when the reactor was operating which was interpreted as interactions from neutrinos generated in the reactor.

After the discovery of the  $\nu_e$ , the question of how many flavours of neutrino exist was asked. In 1962, a measurement of the  $\nu_\mu$  was conducted at the Brookhaven National Laboratory [7]. A proton beam was directed at a beryllium target, generating pions which then decayed via  $\pi^\pm \rightarrow \mu^\pm + (\nu_\mu, \bar{\nu}_\mu)$ , and the subsequent interactions of the  $\nu_\mu$  were observed. As the subsequent interaction of the neutrino generated muons rather than electrons, it was determined that

<sup>174</sup> the  $\nu_\mu$  was fundamentally different from  $\nu_e$ . The final observation to be made  
<sup>175</sup> was that of the  $\nu_\tau$  from the DONUT experiment [8]. Three neutrinos seem the  
<sup>176</sup> obvious solution as it mirrors the known number of charged leptons (as they form  
<sup>177</sup> weak isospin doublets) but there could be evidence of more. Several neutrino  
<sup>178</sup> experiments have found anomalous results [9, 10] which could be attributed  
<sup>179</sup> to “sterile” neutrinos. These hypothesised particles are not affected by gauge  
<sup>180</sup> interactions in the Standard Model so their presence can only be inferred through  
<sup>181</sup> the observation of non-standard oscillation modes. However, cosmological  
<sup>182</sup> observations indicate the number of neutrino species  $N_{eff} = 2.99 \pm 0.17$  [11], as  
<sup>183</sup> measured from the cosmic microwave background power spectrum. LEP also  
<sup>184</sup> measured the number of active neutrino flavours to be  $N_\nu = 2.9840 \pm 0.0082$  [12]  
<sup>185</sup> from measurements of the Z-decay width, but this does not strongly constrain  
<sup>186</sup> the number of sterile neutrinos.

## <sup>187</sup> 2.2 Theory of Neutrino Oscillation

<sup>188</sup> A neutrino generated with lepton flavour  $\alpha$  can change into a different lepton  
<sup>189</sup> flavour  $\beta$  after propagating some distance. This phenomenon is called neutrino  
<sup>190</sup> oscillation and requires that neutrinos must have a non-zero mass. This behaviour  
<sup>191</sup> has been characterised by the Pontecorvo-Maki-Nakagawa-Sakata (PMNS) [13–  
<sup>192</sup> 15] mixing matrix which describes how the flavour and mass of neutrinos are  
<sup>193</sup> associated. This is analogous to the Cabibbo-Kobayashi-Maskawa (CKM) [16]  
<sup>194</sup> matrix measured in quark physics.

### <sup>195</sup> 2.2.1 Three Flavour Oscillations

<sup>196</sup> The PMNS parameterisation defines three flavour eigenstates,  $\nu_e$ ,  $\nu_\mu$  and  $\nu_\tau$   
<sup>197</sup> (indexed  $\nu_\alpha$ ), which are eigenstates of the weak interaction and three mass  
<sup>198</sup> eigenstates,  $\nu_1$ ,  $\nu_2$  and  $\nu_3$  (indexed  $\nu_i$ ). Each mass eigenstate is the superposition

<sup>199</sup> of all three flavour states,

$$|\nu_i\rangle = \sum_{\alpha} U_{\alpha i} |\nu_{\alpha}\rangle. \quad (2.1)$$

<sup>200</sup> Where  $U$  is the  $3 \times 3$  PMNS matrix which is unitary and connects the mass  
<sup>201</sup> and flavour eigenstates.

<sup>202</sup> The weak interaction, when interacting via a  $W^{\pm}$  boson, couples to flavour  
<sup>203</sup> eigenstates so neutrinos interact with leptons of the same flavour. The prop-  
<sup>204</sup> agation of a neutrino flavour eigenstate, in a vacuum, can be re-written as a  
<sup>205</sup> plane-wave solution to the time-dependent Schrödinger equation,

$$|\nu_{\alpha}(t)\rangle = \sum_i U_{\alpha i}^{*} |\nu_i\rangle e^{-i\phi_i}. \quad (2.2)$$

<sup>206</sup> The  $\phi_i$  term can be expressed in terms of the energy,  $E_i$ , and magnitude of the  
<sup>207</sup> three momenta,  $p_i$ , of the neutrino,  $\phi_i = E_i t - p_i x$  ( $t$  and  $x$  being time and position  
<sup>208</sup> coordinates). The probability of observing a neutrino of flavour eigenstate  $\beta$  from  
<sup>209</sup> one which originated as flavour  $\alpha$  can be calculated as,

$$P(\nu_{\alpha} \rightarrow \nu_{\beta}) = |\langle \nu_{\beta} | \nu_{\alpha}(t) \rangle|^2 = \sum_{i,j} U_{\alpha i}^{*} U_{\beta i} U_{\alpha j} U_{\beta j}^{*} e^{-i(\phi_j - \phi_i)}. \quad (2.3)$$

<sup>210</sup> The term within the exponential can be represented as,

$$\phi_j - \phi_i = E_j t - E_i t - p_j x + p_i x. \quad (2.4)$$

<sup>211</sup> For a relativistic particle,  $E_i \gg m_i$ , a Taylor series expansion means,

$$p_i = \sqrt{E_i^2 - m_i^2} \approx E_i - \frac{m_i^2}{2E_i}. \quad (2.5)$$

<sup>212</sup> Making the approximations that neutrinos are relativistic, the mass eigenstates  
<sup>213</sup> were created with the same energy and that  $x = L$ , where  $L$  is the distance  
<sup>214</sup> travelled by the neutrino, Equation 2.4 then becomes

$$\phi_j - \phi_i = \frac{\Delta m_{ij}^2 L}{2E}, \quad (2.6)$$

where  $\Delta m_{ij}^2 = m_i^2 - m_j^2$ . This, combined with further use of unitarity relations results in Equation 2.3 becoming

$$\begin{aligned} P(\nu_\alpha \rightarrow \nu_\beta) &= \delta_{\alpha\beta} - 4 \sum_{i>j} \Re \left( U_{\alpha i}^* U_{\beta i} U_{\alpha j} U_{\beta j}^* \right) \sin^2 \left( \frac{\Delta m_{ij}^2 L}{4E} \right) \\ &\quad + (-) 2 \sum_{i>j} \Im \left( U_{\alpha i}^* U_{\beta i} U_{\alpha j} U_{\beta j}^* \right) \sin \left( \frac{\Delta m_{ij}^2 L}{2E} \right). \end{aligned} \quad (2.7)$$

Where  $\delta_{\alpha\beta}$  is the Kronecker delta function and the negative sign on the last term is included for the oscillation probability of antineutrinos. As an important point to note, the observation of oscillation probability requires a non-zero value of  $\Delta m_{ij}^2$ , which in turn requires that neutrinos have differing masses.

Typically, the PMNS matrix is parameterised into three mixing angles, a charge parity (CP) violating phase  $\delta_{CP}$ , and two Majorana phases  $\alpha_{1,2}$ ,

$$U = \underbrace{\begin{pmatrix} 1 & 0 & 0 \\ 0 & c_{23} & s_{23} \\ 0 & -s_{23} & c_{23} \end{pmatrix}}_{\text{Atmospheric, Accelerator}} \underbrace{\begin{pmatrix} c_{13} & 0 & s_{13} e^{-i\delta_{CP}} \\ 0 & 1 & 0 \\ -s_{13} e^{-i\delta_{CP}} & 0 & c_{13} \end{pmatrix}}_{\text{Reactor, Accelerator}} \times \underbrace{\begin{pmatrix} c_{12} & s_{12} & 0 \\ -s_{12} & c_{12} & 0 \\ 0 & 0 & 1 \end{pmatrix}}_{\text{Reactor, Solar}} \underbrace{\begin{pmatrix} e^{i\alpha_1/2} & 0 & 0 \\ 0 & e^{i\alpha_2/2} & 0 \\ 0 & 0 & 1 \end{pmatrix}}_{\text{Majorana}}. \quad (2.8)$$

Where  $s_{ij} = \sin(\theta_{ij})$  and  $c_{ij} = \cos(\theta_{ij})$ . The oscillation parameters are often grouped: (1,2) as “solar”, (2,3) as “atmospheric” and (1,3) as “reactor”. Many neutrino experiments aim to measure the PMNS parameters from a wide array of origins, as is the purpose of this thesis.

The Majorana phase,  $\alpha_{1,2}$ , included within the fourth matrix in Equation 2.8 is only included for completeness. For an oscillation analysis experiment, any terms containing this phase disappear due to taking the expectation value of the PMNS matrix. Measurements of these phases can be performed by experiments searching for neutrino-less double  $\beta$ -decay [17].

232 A two-flavour approximation can be obtained when one assumes the third  
233 mass eigenstate is degenerate with another. This results in the two-flavour  
234 approximation being reasonable for understanding the features of the oscillation.  
235 In this two-flavour case, the mixing matrix becomes,

$$U_{2\text{ Flav.}} = \begin{pmatrix} \cos(\theta) & \sin(\theta) \\ -\sin(\theta) & \cos(\theta) \end{pmatrix}. \quad (2.9)$$

236 This culminates in the oscillation probability,

$$\begin{aligned} P(\nu_\alpha \rightarrow \nu_\alpha) &= 1 - \sin^2(2\theta) \sin^2\left(\frac{\Delta m^2 L}{4E}\right), \\ P(\nu_\alpha \rightarrow \nu_\beta) &= \sin^2(2\theta) \sin^2\left(\frac{\Delta m^2 L}{4E}\right). \end{aligned} \quad (2.10)$$

237 Where  $\alpha \neq \beta$ . For a fixed neutrino energy, the oscillation probability is  
238 a sinusoidal function depending upon the distance over which the neutrino  
239 propagates. The frequency and amplitude of oscillation are dependent upon  
240  $\Delta m^2/4E$  and  $\sin^2 2\theta$ , respectively. The oscillation probabilities presented thus far  
241 assume  $c = 1$ , where  $c$  is the speed of light in a vacuum. In more familiar units, the  
242 maximum oscillation probability for a fixed value of  $\theta$  is given at  $L[\text{km}] / E[\text{GeV}] \sim$   
243  $1.27/\Delta m^2$ . It is this calculation that determines the best  $L/E$  value for a given  
244 experiment to be designed around for measurements of a specific value of  $\Delta m^2$ .

### 245 2.2.2 The MSW Effect

246 The theory of neutrino oscillation in a vacuum has been described in subsec-  
247 tion 2.2.1. However, the beam neutrinos and atmospheric neutrinos originating  
248 from below the horizon propagate through the matter in the Earth. The coherent  
249 scattering of neutrinos from a material target modifies the Hamiltonian of the  
250 system which results in a change in the oscillation probability. This modification  
251 is termed the Mikheyev-Smirnov-Wolfenstein (MSW) effect [18–20]. This occurs  
252 because charged current scattering ( $\nu_e + e^- \rightarrow \nu_e + e^-$ , propagated by a W boson)  
253 only affects electron neutrinos whereas the neutral current scattering ( $\nu_l + l^- \rightarrow$

<sup>254</sup>  $\nu_l + l^-$ , propagated by a  $Z^0$  boson) interacts through all neutrino flavours equally.  
<sup>255</sup> In the two-flavour approximation, the effective mixing parameter becomes

$$\sin^2(2\theta) \rightarrow \sin^2(2\theta_m) = \frac{\sin^2(2\theta)}{(A/\Delta m^2 - \cos(2\theta))^2 + \sin^2(2\theta)}, \quad (2.11)$$

<sup>256</sup> where  $A = 2\sqrt{2}G_F N_e E$ ,  $N_e$  is the electron density of the medium and  $G_F$   
<sup>257</sup> is Fermi's constant. It is clear that there exists a value of  $A = \Delta m^2 \cos(2\theta)$  for  
<sup>258</sup>  $\Delta m^2 > 0$ , which results in a divergent mixing parameter, colloquially called the  
<sup>259</sup> matter resonance. This resonance regenerates the electron neutrino component of  
<sup>260</sup> the neutrino flux [18–20]. The density at which the resonance occurs is given by

$$N_e = \frac{\Delta m^2 \cos(2\theta)}{2\sqrt{2}G_F E}. \quad (2.12)$$

<sup>261</sup> At densities lower than this critical value, the oscillation probability will  
<sup>262</sup> be much closer to that of vacuum oscillation. For antineutrinos,  $N_e \rightarrow -N_e$   
<sup>263</sup> [21]. The resonance occurring from the MSW effect depends on the sign of  $\Delta m^2$ .  
<sup>264</sup> Therefore, any neutrino oscillation experiment which observes neutrinos and  
<sup>265</sup> antineutrinos which have propagated through matter can have some sensitivity  
<sup>266</sup> to the ordering of the neutrino mass eigenstates.

## <sup>267</sup> 2.3 Neutrino Oscillation Measurements

<sup>268</sup> As evidence of beyond Standard Model physics, the 2015 Nobel Prize in Physics  
<sup>269</sup> was awarded to the Super-Kamiokande (SK) [22] and Sudbury Neutrino Ob-  
<sup>270</sup> servatory (SNO) [23] collaborations for the first definitive observation of solar  
<sup>271</sup> and atmospheric neutrino oscillation [24]. Since then, the field has seen a wide  
<sup>272</sup> array of oscillation measurements from a variety of neutrino sources. As seen  
<sup>273</sup> in subsection 2.2.1, the neutrino oscillation probability is dependent on the ratio  
<sup>274</sup> of the propagation baseline,  $L$ , to the neutrino energy,  $E$ . It is this ratio that  
<sup>275</sup> determines the type of neutrino oscillation a particular experiment is sensitive to.

<sup>276</sup> As illustrated in Figure 2.1, there are many neutrino sources that span a  
<sup>277</sup> wide range of energies. The least energetic neutrinos are from reactor and

<sup>278</sup> terrestrial sources at  $O(1)$ MeV whereas the most energetic neutrinos originate  
<sup>279</sup> from atmospheric and galactic neutrinos of  $> O(1)$ TeV.

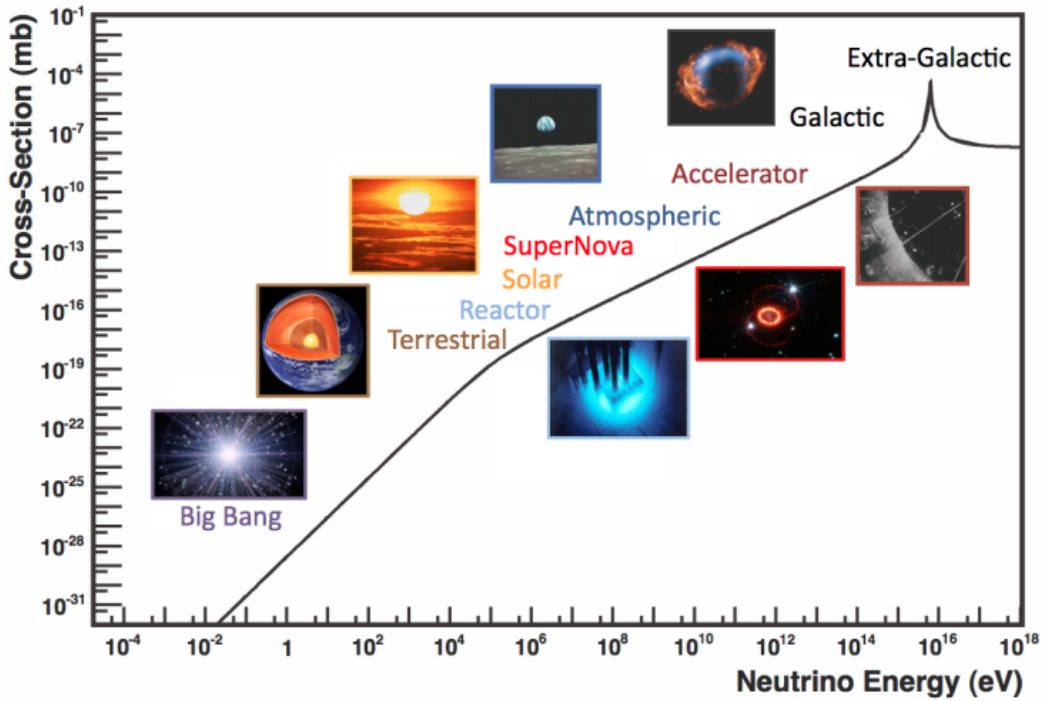


**Figure 2.1:** The electro-weak cross-section for  $\bar{\nu}_e + e^- \rightarrow \bar{\nu}_e + e^-$  scattering on free electrons from various natural and man-made neutrino sources, as a function of neutrino energy. Taken from [25]

### <sup>280</sup> 2.3.1 Solar Neutrinos

<sup>281</sup> Solar neutrinos are emitted from fusion reaction chains at the centre of the Sun.  
<sup>282</sup> The solar neutrino flux, given as a function of neutrino energy for different  
<sup>283</sup> fusion and decay chains, is illustrated in Figure 2.2. Whilst proton-proton fusion  
<sup>284</sup> generates the largest flux of neutrinos, the neutrinos are low energy and are  
<sup>285</sup> difficult to reconstruct due to the IBD interaction threshold of 1.8MeV [26].  
<sup>286</sup> Consequently, most experiments focus on the neutrinos from the decay of  $^8B$   
<sup>287</sup> (via  $^8B \rightarrow ^8Be^* + e^+ + \nu_e$ ), which are higher energy.

<sup>288</sup> The first measurements of solar neutrinos observed a significant reduction in  
<sup>289</sup> the event rate compared to predictions from the Standard Solar Model [28, 29]. A  
<sup>290</sup> proposed solution to this “solar neutrino problem” was  $\nu_e \leftrightarrow \nu_\mu$  oscillations in a



**Figure 2.2:** The solar neutrino flux as a function of neutrino energy for various fusion reactions and decay chains as predicted by the Standard Solar Model. Taken from [27].

291 precursory version of the PMNS model [30]. The Kamiokande [31], Gallex [32]  
 292 and Sage [33] experiments confirmed the  $\sim 0.5$  factor deficit of solar neutrinos.

293 The conclusive solution to this problem was determined by the SNO col-  
 294 laboration [34]. Using a deuterium water target to observe  ${}^8B$  neutrinos, the  
 295 event rate of charged current (CC), neutral current (NC), and elastic scattering  
 296 (ES) interactions (Given in Equation 2.13) was simultaneously measured. CC  
 297 events can only occur for electron neutrinos, whereas the NC channel is agnostic  
 298 to neutrino flavour, and the ES reaction has a small excess sensitivity for the  
 299 detection of electron neutrino interactions. This meant that there were direct  
 300 measurements of the  $\nu_e$  and  $\nu_x$  neutrino flux. It was concluded that the CC and  
 301 ES interaction rates were consistent with the deficit previously observed. Most  
 302 importantly, the NC reaction rate was only consistent with the others under the

303 hypothesis of flavour transformation.

$$\begin{aligned} \nu_e + d &\rightarrow p + p + e^- & (CC) \\ \nu_x + d &\rightarrow p + n + \nu_x & (NC) \\ \nu_x + e^- &\rightarrow \nu_x + e^- & (ES) \end{aligned} \quad (2.13)$$

304 Since the SNO measurement, many experiments have since measured the  
 305 neutrino flux of different interaction chains within the sun [35–37]. The most  
 306 recent measurement was that of CNO-cycle neutrinos which were recently  
 307 observed with  $5\sigma$  significance by the Borexino collaboration [35].

### 308 2.3.2 Accelerator Neutrinos

309 The concept of using an artificial “neutrino beam” was first realised in 1962 [38].  
 310 Since then, many experiments have adopted the same fundamental concepts.  
 311 Typically, a proton beam is aimed at a target producing charged mesons that  
 312 decay to neutrinos. The mesons can be sign-selected by the use of magnetic  
 313 focusing horns to generate a neutrino or antineutrino beam. Pions are the primary  
 314 mesons that decay and depending on the orientation of the magnetic field, a  
 315 muon (anti-)neutrino beam is generated via  $\pi^+ \rightarrow \mu^+ + \nu_\mu$  or  $\pi^- \rightarrow \mu^- + \bar{\nu}_\mu$ .  
 316 The decay of muons and kaons results in an irreducible intrinsic electron neutrino  
 317 background. In T2K, this background contamination is  $O(< 1\%)$  [39]. There is  
 318 also an approximately  $\sim 5\%$  “wrong-sign” neutrino background of  $\bar{\nu}_\mu$  generated  
 319 via the same decays. As the beam is generated by proton interactions (rather  
 320 than anti-proton interactions), the wrong-sign component in the antineutrino  
 321 beam is larger when operating in neutrino mode.

322 Tuning the proton energy in the beam and using beam focusing techniques  
 323 allows the neutrino energy to be set to a value that maximises the disappear-  
 324 ance oscillation probability in the  $L/E$  term in Equation 2.10. This means that  
 325 accelerator experiments are typically more sensitive to the mixing parameters as  
 326 compared to a natural neutrino source. However, the disadvantage compared  
 327 to atmospheric neutrino experiments is the cost of building a facility to provide

328 high-energy neutrinos, with a high flux, which is required for longer baselines.  
 329 Consequently, there is typically less sensitivity to matter effects and the ordering  
 330 of the neutrino mass eigenstates.

331 A neutrino experiment measures

$$R(\vec{x}) = \Phi(E_\nu) \times \sigma(E_\nu) \times \epsilon(\vec{x}) \times P(\nu_\alpha \rightarrow \nu_\beta), \quad (2.14)$$

332 where  $R(\vec{x})$  is the event rate of neutrinos at position  $\vec{x}$ ,  $\Phi(E_\nu)$  is the flux of  
 333 neutrinos with energy  $E_\nu$ ,  $\sigma(E_\nu)$  is the cross-section of the neutrino interaction and  
 334  $\epsilon(\vec{x})$  is the efficiency and resolution of the detector. In order to leverage the most  
 335 out of an accelerator neutrino experiment, the flux and cross-section systematics  
 336 need to be constrained. This is typically done via the use of a “near detector”,  
 337 situated at a baseline of  $O(1)$ km. This detector observes the unoscillated neutrino  
 338 flux and constrains the parameters used within the flux and cross-section model.

339 The first accelerator experiments to precisely measure oscillation parameters  
 340 were MINOS [40] and K2K [41]. These experiments confirmed the  $\nu_\mu$  disappear-  
 341 ance seen in atmospheric neutrino experiments by finding consistent parameter  
 342 values for  $\sin^2(\theta_{23})$  and  $\Delta m_{32}^2$ . The current generation of accelerator neutrino  
 343 experiments, T2K and NO $\nu$ A extended this field by observing  $\bar{\nu}_\mu \rightarrow \bar{\nu}_e$  and lead  
 344 the sensitivity to atmospheric mixing parameters as seen in Figure 2.6 [42]. The  
 345 two experiments differ in their peak neutrino energy, baseline, and detection tech-  
 346 nique. The NO $\nu$ A experiment is situated at a baseline of 810km from the NuMI  
 347 beamline which delivers 2GeV neutrinos. The T2K neutrino beam is peaked  
 348 around 0.6GeV and propagates 295km [43]. Additionally, the NO $\nu$ A experiment  
 349 uses functionally identical detectors (near and far) whereas T2K uses a plastic  
 350 scintillator technique at the near detector and a water Cherenkov far detector.  
 351 The future generation experiments DUNE [44] and Hyper-Kamiokande [45]  
 352 will succeed these experiments as the high-precision era of neutrino oscillation  
 353 parameter measurements develops.

354 Several anomalous results have been observed in the LSND [9] and Mini-  
 355 BooNE [10] detectors which were designed with purposefully short baselines.

356 Parts of the neutrino community attributed these results to oscillations induced  
357 by a fourth “sterile” neutrino [46] but several searches in other experiments,  
358 MicroBooNE [47] and KARMEN [48], found no hints of additional neutrino  
359 species. The solution to the anomalous results is still being determined.

### 360 2.3.3 Atmospheric Neutrinos

361 The interactions of primary cosmic ray protons in the Earth’s upper atmosphere  
362 generate showers of energetic hadrons. These are mostly pions and kaons that  
363 decay to produce a natural source of neutrinos spanning energies of MeV to  
364 TeV [49]. The main decay is via,

$$\begin{aligned} \pi^\pm &\rightarrow \mu^\pm + (\nu_\mu, \bar{\nu}_\mu), \\ \mu^\pm &\rightarrow e^\pm + (\nu_e, \bar{\nu}_e) + (\nu_\mu, \bar{\nu}_\mu), \end{aligned} \tag{2.15}$$

365 such that for a single pion decay, three neutrinos can be produced. The  
366 atmospheric neutrino flux energy spectra as predicted by the Bartol [50], Honda  
367 [51–53], and FLUKA [54] models are illustrated in Figure 2.3. The flux distribution  
368 peaks at an energy of  $O(10)$ GeV. The uncertainties associated with these models  
369 are dominated by the hadronic production of kaon and pions as well as the  
370 primary cosmic flux.

371 Unlike long-baseline experiments which have a fixed baseline, the distance  
372 atmospheric neutrinos propagate is dependent upon the zenith angle at which  
373 they interact. This is illustrated in Figure 2.4. Neutrinos that are generated  
374 directly above the detector ( $\cos(\theta) = 1.0$ ) have a baseline equivalent to the  
375 height of the atmosphere, whereas neutrinos that interact directly below the  
376 detector ( $\cos(\theta) = -1.0$ ) have to travel a length equal to the diameter of the Earth.  
377 This means atmospheric neutrinos have a baseline that varies from  $O(20)$ km to  
378  $O(6 \times 10^3)$ km. Any neutrino generated at or below the horizon will be subject  
379 to MSW matter resonance as they propagate through the Earth.

380 Figure 2.5 highlights the neutrino flux as a function of the zenith angle for  
381 different slices of neutrino energy. For medium to high-energy neutrinos (and to



**Figure 2.3:** Left panel: The atmospheric neutrino flux for different neutrino flavours as a function of neutrino energy as predicted by the 2007 Honda model (“This work”) [51], the 2004 Honda model (“HKKM04”)[52], the Bartol model [50] and the FLUKA model [54]. Right panel: The ratio of the muon to electron neutrino flux as predicted by all the quoted models. Both figures taken from [51].



**Figure 2.4:** A diagram illustrating the definition of zenith angle as used in the Super Kamiokande experiment [55].

382 a lesser degree for low-energy neutrinos), the flux is approximately symmetric  
 383 around  $\cos(\theta) = 0$ . To the accuracy of this approximation, the systematic  
 384 uncertainties associated with atmospheric flux for comparing upward-going  
 385 and down-going neutrino cancels. This allows the down-going events, which are

- 386 mostly insensitive to oscillation probabilities, to act as an unoscillated prediction  
 387 (similar to a near detector in an accelerator neutrino experiment).



**Figure 2.5:** Prediction of  $\nu_e$ ,  $\bar{\nu}_e$ ,  $\nu_\mu$ ,  $\bar{\nu}_\mu$  fluxes as a function of zenith angle as calculated by the HKKM model [53]. The left, middle and right panels represent three values of neutrino energy, 0.32GeV, 1.0GeV and 3.2GeV respectively. Predictions for other models including Bartol [50], Honda [51] and FLUKA [54] are given in [55].

388 Precursory hints of atmospheric neutrinos were observed in the mid-1960s  
 389 searching for  $\nu_\mu + X \rightarrow X^* + \mu^\pm$  [56]. This was succeeded by the IMB-3 [57]  
 390 and Kamiokande [58] experiments which measured the double ratio of muon  
 391 to electron neutrinos in data to Monte Carlo,  $R(\nu_\mu/\nu_e) = (\mu/e)_{Data}/(\mu/e)_{MC}$ .  
 392 Both experiments were found to have a consistent deficit of muon neutrinos,  
 393 with  $R(\nu_\mu/\nu_e) = 0.67 \pm 0.17$  and  $R(\nu_\mu/\nu_e) = 0.658 \pm 0.016 \pm 0.035$ , respectively.  
 394 Super-Kamiokande (SK) [55] extended this analysis by fitting oscillation pa-  
 395 rameters in  $P(\nu_\mu \rightarrow \nu_\tau)$  which found best fit parameters  $\sin^2(2\theta) > 0.92$  and  
 396  $1.5 \times 10^{-3} < \Delta m^2 < 3.4 \times 10^{-3}\text{eV}^2$ .

397 Since then, atmospheric neutrino experiments have been making precision  
 398 measurements of the  $\sin^2(\theta_{23})$  and  $\Delta m^2_{32}$  oscillation parameters. Atmospheric  
 399 neutrino oscillation is dominated by  $P(\nu_\mu \rightarrow \nu_\tau)$ , where SK observed a  $4.6\sigma$   
 400 discovery of  $\nu_\tau$  appearance [59]. Figure 2.6 illustrates the current estimates on  
 401 the atmospheric mixing parameters, from a wide range of atmospheric and  
 402 accelerator neutrino observatories.



**Figure 2.6:** Constraints on the atmospheric oscillation parameters,  $\sin^2(\theta_{23})$  and  $\Delta m_{32}^2$ , from atmospheric and long-baseline experiments: SK [60], T2K [61], NOvA [62], IceCube [63] and MINOS [64]. Figure taken from [65].

### 2.3.4 Reactor Neutrinos

As illustrated in the first discovery of neutrinos (section 2.1), nuclear reactors are a very useful artificial source of electron antineutrinos. For reactors that use low-enriched uranium  $^{235}\text{U}$  as fuel, the antineutrino flux is dominated by the  $\beta$ -decay fission of  $^{235}\text{U}$ ,  $^{238}\text{U}$ ,  $^{239}\text{Pu}$  and  $^{241}\text{Pu}$  [66] as illustrated in Figure 2.7.

Due to their low energy, reactor electron antineutrinos predominantly interact via the inverse  $\beta$ -decay (IBD) interaction. The typical signature contains two signals delayed by  $O(200)\mu\text{s}$ ; firstly the prompt photons from positron annihilation, and secondly the photon emitted ( $E_{tot}^\gamma = 2.2\text{MeV}$ ) from de-excitation after neutron capture on hydrogen. Searching for both signals improves the detector's ability to distinguish between background and signal events [68].

There are many short baseline experiments ( $L \sim O(1)\text{km}$ ) that have measured the  $\sin^2(\theta_{13})$  and  $\Delta m_{32}^2$  oscillation parameters. Daya Bay [69], RENO [70] and Double Chooz [71] have all provided precise measurements, with the first discovery of a non-zero  $\theta_{13}$  made by Daya Bay and RENO (and complemented by T2K [71]). The constraints on  $\sin^2(\theta_{13})$  by the reactor experiments lead the field. They



**Figure 2.7:** Reactor electron antineutrino fluxes for  $^{235}\text{U}$  (Black),  $^{238}\text{U}$  (Green),  $^{239}\text{Pu}$  (Purple), and  $^{241}\text{Pu}$  (Orange) isotopes. The inverse  $\beta$ -decay cross-section (Blue) and corresponding measurable neutrino spectrum (Red) are also given. Top panel: Schematic of Inverse  $\beta$ -decay interaction including the eventual capture of the emitted neutron. This capture emits a  $\gamma$ -ray which provides a second signal of the event. Taken from [67].

are often used as external inputs to accelerator neutrino experiments to improve their sensitivity to  $\delta_{CP}$  and mass hierarchy determination. JUNO-TAO [72], a small collaboration within the larger JUNO experiment, is a next-generation reactor experiment that aims to precisely measure the isotopic antineutrino yields from the different fission chains.

Kamland [73] is the only experiment to have observed reactor neutrinos using a long baseline (flux weighted averaged baseline of  $L \sim 180\text{km}$ ) which allows it to have sensitivity to  $\Delta m_{21}^2$ . Combined with the SK solar neutrino experiment, the combined analysis puts the most stringent constraint on  $\Delta m_{21}^2$  [74].

## 2.4 Summary Of Oscillation Parameter Measurements

Since the first evidence of neutrino oscillations, numerous measurements of the mixing parameters have been made. Many experiments use neutrinos as a tool for the discovery of new physics (diffuse supernova background, neutrinoless double beta decay and others) so the PMNS parameters are summarised in the Particle Data Group (PDG) review tables. The analysis presented in this thesis focuses on the 2020 T2K oscillation analysis presented in [75] which the 2020 PDG constraints [76] were used. These constraints are outlined in Table 2.1.

Parameter	2020 Constraint
$\sin^2(\theta_{12})$	$0.307 \pm 0.013$
$\Delta m_{21}^2$	$(7.53 \pm 0.18) \times 10^{-5} \text{ eV}^2$
$\sin^2(\theta_{13})$	$(2.18 \pm 0.07) \times 10^{-2}$
$\sin^2(\theta_{23})$ (I.H.)	$0.547 \pm 0.021$
$\sin^2(\theta_{23})$ (N.H.)	$0.545 \pm 0.021$
$\Delta m_{32}^2$ (I.H.)	$(-2.546^{+0.034}_{-0.040}) \times 10^{-3} \text{ eV}^2$
$\Delta m_{32}^2$ (N.H.)	$(2.453 \pm 0.034) \times 10^{-3} \text{ eV}^2$

**Table 2.1:** The 2020 Particle Data Group constraints of the oscillation parameters taken from [76]. The value of  $\Delta m_{32}^2$  is given for both normal hierarchy (N.H.) and inverted hierarchy (I.H.) and  $\sin^2(\theta_{23})$  is broken down by whether its value is below (Q1) or above (Q2) 0.5.

The  $\sin^2(\theta_{13})$  measurement stems from the electron antineutrino disappearance,  $P(\bar{\nu}_e \rightarrow \bar{\nu}_e)$ , and is taken as the average best-fit from the combination of Daya Bay, Reno and Double Chooz. It is often used as a prior uncertainty within other neutrino oscillation experiments, typically termed the reactor constraint. The  $\sin^2(\theta_{12})$  parameter is predominantly measured through electron neutrino disappearance,  $P(\nu_e \rightarrow \nu_{\mu,\tau})$ , in solar neutrino experiments. The long-baseline reactor neutrino experiment Kamland also has a sensitivity to this parameter and is used in a joint fit to solar data from SNO and SK, using the reactor constraint. Measurements of  $\sin^2(\theta_{23})$  are made by long-baseline and atmospheric neutrino experiments. The PDG value is a joint fit of T2K, NO $\nu$ A, MINOS and IceCube DeepCore experiments. The latest T2K-only measurement, provided at Neutrino2020 and is the basis of this thesis, is given as  $\sin^2(\theta_{23}) = 0.546^{+0.024}_{-0.046}$  [75].

The PDG constraint on  $\Delta m_{21}^2$  is provided by the KamLAND experiment using solar and geoneutrino data. This measurement utilised a  $\sin^2(\theta_{13})$  constraint from accelerator (T2K, MINOS) and reactor neutrino (Daya Bay, RENO, Double Chooz) experiments. Accelerator measurements make some of the most stringent constraints on  $\Delta m_{32}^2$  although atmospheric experiments have more sensitivity to the mass hierarchy determination. The PDG performs a joint fit of accelerator and atmospheric data, in both normal and inverted hierarchies separately. The latest T2K-only result is  $\Delta m_{32}^2 = 2.49^{+0.058}_{-0.082} \times 10^{-3} \text{ eV}^2$  favouring normal hierarchy [75]. The value of  $\delta_{CP}$  is largely undetermined. CP-conserving values of 0 and  $\pi$  were rejected with  $\sim 2\sigma$  intervals, as published in Nature, although more recent analyses have reduced the credible intervals to 90%. Since the 2020 PDG publication, there has been a new measurement of  $\sin^2(\theta_{13}) = (2.20 \pm 0.07) \times 10^{-2}$  [77], alongside updated  $\Delta m_{32}^2$  and  $\sin^2(\theta_{23})$  measurements.

Throughout this thesis, several sample spectra predictions and contours are presented, which require oscillation parameters to be assumed. Table 2.2 defines two sets of oscillation parameters, with “Asimov A” set being close to the preferred values from a previous T2K-only fit [78] and “Asimov B” being CP-conserving and further from maximal  $\theta_{23}$  mixing.

Parameter	Asimov A	Asimov B
$\Delta m_{12}^2$	$7.53 \times 10^{-5} \text{ eV}^2$	
$\Delta m_{32}^2$	$2.509 \times 10^{-3} \text{ eV}^2$	
$\sin^2(\theta_{12})$	0.304	
$\sin^2(\theta_{13})$	0.0219	
$\sin^2(\theta_{23})$	0.528	0.45
$\delta_{CP}$	-1.601	0.0

**Table 2.2:** Reference values of the neutrino oscillation parameters for two different oscillation parameter sets.

## 2.5 Overview of Oscillation Effects

The analysis presented within this thesis focuses on the determination of oscillation parameters from atmospheric and beam neutrinos. Whilst subject to the

<sup>469</sup> same oscillation formalism, the way in which the two samples have sensitivity  
<sup>470</sup> to the different oscillation parameters differs significantly.

<sup>471</sup> Atmospheric neutrinos have a varying baseline, or “path length”  $L$ , such that  
<sup>472</sup> the distance each neutrino travels before interacting is dependent upon the zenith  
<sup>473</sup> angle,  $\theta_Z$ . As primary cosmic rays can interact anywhere between the Earth’s  
<sup>474</sup> surface and  $\sim 50\text{km}$  above that, the height,  $h$ , in the atmosphere at which the  
<sup>475</sup> neutrino was generated also affects the path length,

$$L = \sqrt{(R_E + h)^2 - R_E^2 (1 - \cos^2(\theta_Z))} - R_E \cos(\theta_Z). \quad (2.16)$$

<sup>476</sup> DB: Ask Giles what he means about the horizontal issue and Layering in  
<sup>477</sup> the ProdH section

<sup>478</sup> Where  $R_E = 6,371\text{km}$  is the Earth’s radius. Consequently, the oscillation  
<sup>479</sup> probability is dependent upon two parameters,  $\cos(\theta_Z)$  and  $E_\nu$ .

<sup>480</sup> The oscillation probability used within this analysis is based on [21]. The  
<sup>481</sup> neutrino wavefunction in the vacuum Hamiltonian evolves in each layer of  
<sup>482</sup> constant matter density via

$$i \frac{d\psi_j(t)}{dt} = \frac{m_j^2}{2E_\nu} \psi_j(t) - \sum_k \sqrt{2} G_F N_e U_{ej} U_{ke}^\dagger \psi_k(t), \quad (2.17)$$

<sup>483</sup> where  $m_j^2$  is the square of the  $j^{\text{th}}$  vacuum eigenstate mass,  $E_\nu$  is the neutrino  
<sup>484</sup> energy,  $G_F$  is Fermi’s constant,  $N_e$  is the electron number density and  $U$  is the  
<sup>485</sup> PMNS matrix. The transformation  $N_e \rightarrow -N_e$  and  $\delta_{CP} \rightarrow -\delta_{CP}$  is applied for  
<sup>486</sup> antineutrino propagation. Thus, a model of the Earth’s density is required for  
<sup>487</sup> neutrino propagation. Following the official SK-only methodology [79], this  
<sup>488</sup> analysis uses the Preliminary Reference Earth Model (PREM) [80] which provides  
<sup>489</sup> piecewise cubic polynomials as a function of the Earth’s radius. This density  
<sup>490</sup> profile is illustrated in Figure 2.8. As the propagator requires layers of constant  
<sup>491</sup> density, the SK methodology approximates the PREM model by using four layers  
<sup>492</sup> of constant density [79], detailed in Table 2.3.



**Figure 2.8:** The density of the Earth given as a function of the radius, as given by the PREM model (Black), and the constant density four-layer approximation (Blue), as used in the official SK-only analysis.

Layer	Outer Radius [km]	Density [g/cm <sup>3</sup> ]	Chemical composition (Z/A)
Inner Core	1220	13	$0.468 \pm 0.029$
Outer Core	3480	11.3	$0.468 \pm 0.029$
Lower Mantle	5701	5.0	0.496
Transition Zone	6371	3.3	0.496

**Table 2.3:** Description of the four layers of the Earth invoked within the constant density approximation of the PREM model [80].

The atmospheric neutrino oscillation probabilities can be presented as two dimensional “oscillograms” as illustrated in Figure 2.9. The distinct discontinuities, as a function of  $\cos(\theta_Z)$ , are due to the discontinuous density in the PREM model.

Atmospheric neutrinos have sensitivity to  $\delta_{CP}$  through the overall event rate. Figure 2.10 illustrates the difference in oscillation probability between CP-conserving ( $\delta_{CP} = 0.$ ) and a CP-violating ( $\delta_{CP} = -1.601$ ) value taken from Asimov A oscillation parameter set (Table 2.2). The result is a complicated oscillation pattern in the appearance probability for sub-GeV upgoing neutrinos. The detector does not have sufficient resolution to resolve these individual patterns so the sensitivity to  $\delta_{CP}$  for atmospheric neutrinos comes via the overall normalisation of these events.

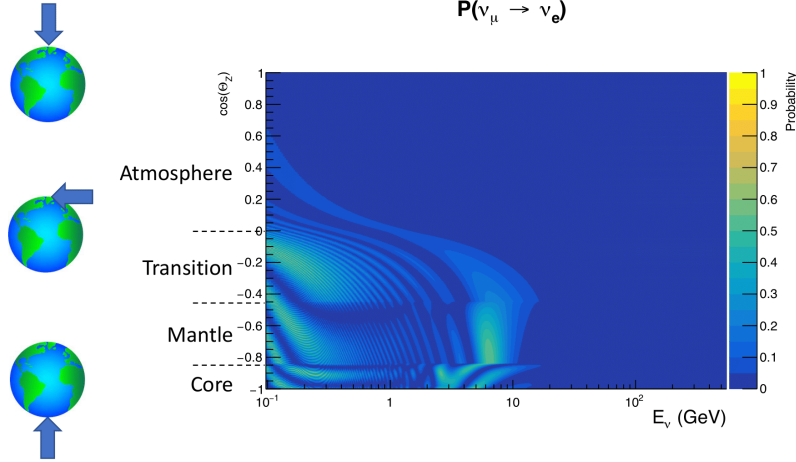


**Figure 2.9:** An “oscillogram” that depicts the  $P(\nu_\mu \rightarrow \nu_e)$  oscillation probability as a function of neutrino energy and cosine of the zenith angle. The zenith angle is defined such that  $\cos(\theta_Z) = 1.0$  represents neutrinos that travel from directly above the detector. The four-layer constant density PREM model approximation is used and Asimov A oscillation parameters are assumed (Table 2.2).

504     The presence of matter means that the effect  $\delta_{CP}$  has on the oscillation prob-  
 505     ability is not equal between neutrinos and antineutrinos. Furthermore, the  
 506     interaction cross-section for neutrinos is larger than for antineutrinos so the two  
 507     effects have to be disentangled. These effects are further convoluted by detector  
 508     efficiencies as SK cannot distinguish neutrinos and antineutrinos well. All of  
 509     these effects lead to a difference in the number of neutrinos detected compared  
 510     to antineutrinos. This changes how the  $\delta_{CP}$  normalisation term is observed,  
 511     resulting in a very complex sensitivity to  $\delta_{CP}$ .

512     The vacuum and matter oscillation probabilities for  $P(\nu_e \rightarrow \nu_e)$  and  $P(\bar{\nu}_e \rightarrow$   
 513      $\bar{\nu}_e)$  are presented in Figure 2.11, where the PREM model has been assumed. The  
 514     oscillation probability for both neutrinos and antineutrinos is affected in the  
 515     presence of matter. However, the resonance effects around  $O(5)\text{GeV}$  only occur  
 516     for neutrinos in the normal mass hierarchy and antineutrinos in the inverse mass  
 517     hierarchy. The exact position and amplitude of the resonance depend on  $\sin^2(\theta_{23})$ ,  
 518     further increasing the atmospheric neutrinos’ sensitivity to the parameter.

519     As the T2K beam flux is centered at the first oscillation maximum ( $E_\nu =$

$$\mathbf{P}(\nu_\mu \rightarrow \nu_e; \delta_{CP} = -1.601) - \mathbf{P}(\nu_\mu \rightarrow \nu_e; \delta_{CP} = 0)$$

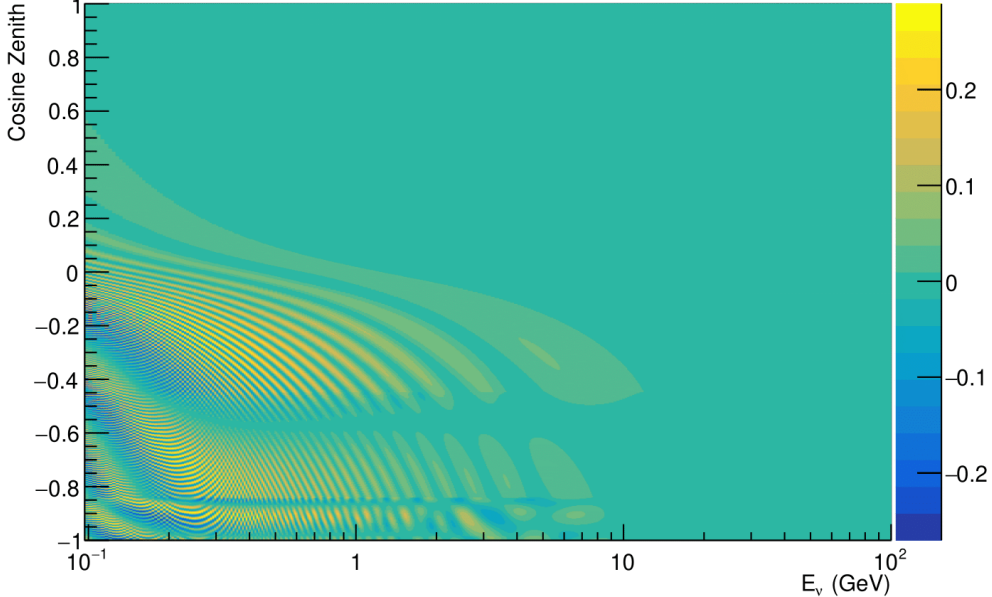


**Figure 2.10:** The effect of  $\delta_{CP}$  for atmospheric neutrinos given in terms of the neutrino energy and zenith angle. This oscillogram compares the  $P(\nu_\mu \rightarrow \nu_e)$  oscillation probability for a CP conserving ( $\delta_{CP} = 0.0$ ) and a CP violating ( $\delta_{CP} = -1.601$ ) value taken from the Asimov A parameter set. The other oscillation parameters assume the Asimov A oscillation parameter set given in Table 2.2.

520 0.6GeV) [43], the sensitivity to  $\delta_{CP}$  is predominantly observed as a change in the  
 521 event-rate of e-like samples in  $\nu/\bar{\nu}$  modes. Figure 2.12 illustrates the  $P(\nu_\mu \rightarrow \nu_e)$   
 522 oscillation probability for a range of  $\delta_{CP}$  values. A circular modulation of the  
 523 first oscillation peak (in both magnitude and position) is observed when varying  
 524 throughout the allowable values of  $\delta_{CP}$ . The CP-conserving values of  $\delta_{CP} = 0, \pi$   
 525 have a lower(higher) oscillation maximum than the CP-violating values of  $\delta_{CP} =$   
 526  $-\pi/2 (\delta_{CP} = \pi/2)$ . A sub-dominant shift in the energy of the oscillation peak is  
 527 also present, which aids in separating the two CP-conserving values of  $\delta_{CP}$ .

528 T2K's sensitivity to  $\sin^2(\theta_{23})$  and  $\Delta m_{32}^2$  is observed as a shape-based variation  
 529 of the muon-like samples, as illustrated in Figure 2.12. The value of  $\Delta m_{32}^2$  laterally  
 530 shifts the position of the oscillation dip (around  $E_\nu \sim 0.6\text{GeV}$ ) in the  $P(\nu_\mu \rightarrow \nu_\mu)$   
 531 oscillation probability. A variation of  $\sin^2(\theta_{23})$  is predominantly observed as  
 532 a vertical shift of the oscillation dip with second-order horizontal shifts being



**Figure 2.11:** An illustration of the matter-induced effects on the oscillation probability, given as a function of neutrino energy and zenith angle. The top row of panels gives the  $P(\nu_e \rightarrow \nu_e)$  oscillation probability and the bottom row illustrates the  $P(\bar{\nu}_e \rightarrow \bar{\nu}_e)$  oscillation probability. The left column highlights the oscillation probability in a vacuum, whereas the middle and right column represents the oscillation probabilities when the four-layer fixed density PREM model is assumed. All oscillation probabilities assume the “Asimov A” set given in Table 2.2, but importantly, the right column sets an inverted mass hierarchy. The “matter resonance” effects at  $E_\nu \sim 5\text{GeV}$  can be seen in the  $P(\nu_e \rightarrow \nu_e)$  for normal mass hierarchy and  $P(\bar{\nu}_e \rightarrow \bar{\nu}_e)$  for inverted hierarchy.

533 due to matter effects. The beam neutrinos have limited sensitivity to matter  
 534 effects due to the relatively shorter baseline as well as the Earth’s mantle being  
 535 a relatively low-density material (as compared to the Earth’s core). For some  
 536 values of  $\delta_{CP}$ , the degeneracy in the number of e-like events allows the mass  
 537 hierarchy to be broken. This leads to a  $\delta_{CP}$ -dependent mass hierarchy sensitivity  
 538 which can be seen in Figure 2.13.

539 Whilst all oscillation channels should be included for completeness, the

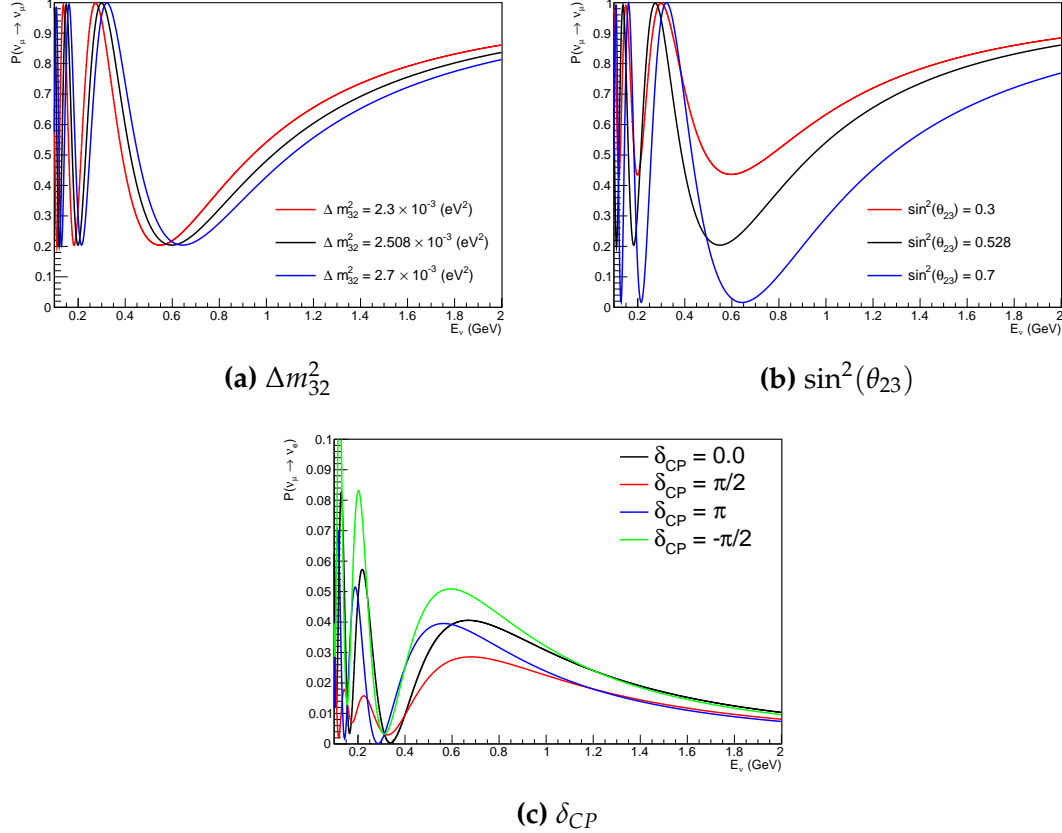


**Figure 2.12:** The oscillation probability for beam neutrino events given as a function of neutrino energy. All oscillation parameters assume the “Asimov A” set given in Table 2.2 unless otherwise stated. Each panel represents a change in one of the oscillation parameters whilst keeping the remaining parameters fixed.

computational resources required to run a fit are limited and any reasonable approximations which reduce the number of oscillation probability calculations that need to be made should be applied. The  $\nu_e \rightarrow \nu_{e,\mu,\tau}$  (and antineutrino equivalent) oscillations can be ignored for beam neutrinos as the  $\nu_e/\bar{\nu}_e$  fluxes are approximately two orders of magnitude smaller than the corresponding  $\nu_\mu/\bar{\nu}_\mu$  flux. Furthermore, as the peak neutrino energy of the beam is well below the threshold for charged current tau production ( $E_\nu = 3.5$  GeV [59]), only a small proportion of the neutrinos produced in the beam have the required energy. For the few neutrinos that have sufficient energy, the oscillation probability is very small due to their energy being well above the oscillation maximum (small value of  $L/E$ ). Whilst these approximations have been made for the beam



**Figure 2.13:** The number of electron-like events in the FHC and RHC operating mode of the beam, as a function of the oscillation probabilities. Both normal hierarchy (Solid) and inverse hierarchy (Dashed) values of  $\Delta m_{32}^2$  are given.

551 neutrinos, the atmospheric flux of  $\nu_e$  is of the same order of magnitude as the  $\nu_\mu$   
 552 flux and the energy distribution of atmospheric neutrinos extends well above  
 553 the tau production threshold. These events can have non-negligible oscillation  
 554 probabilities due to the further distance they travel.

# 3

555

556

## T2K and SK Experiment Overview

557 As the successor of the Kamiokande experiment, the Super-Kamiokande (SK)  
558 collaboration has been leading atmospheric neutrino oscillation analyses for  
559 over two decades. The detector has provided some of the strongest constraints  
560 on proton decay and the first precise measurements of the  $\Delta m_{32}^2$  and  $\sin^2(\theta_{23})$   
561 neutrino oscillation parameters. The history, detection technique, and operation  
562 of the SK detector is described in section 3.1.

563 The Tokai-to-Kamioka (T2K) experiment was one of the first long-baseline  
564 experiments to use both neutrino and antineutrino beams to precisely measure  
565 charge parity violation within the neutrino sector. The T2K experiment observed  
566 the first hints of a non-zero  $\sin^2(\theta_{13})$  measurement and continues to lead the  
567 field with the constraints it provides on  $\sin^2(\theta_{13})$ ,  $\sin^2(\theta_{23})$ ,  $\Delta m_{32}^2$  and  $\delta_{CP}$ . In  
568 section 3.2, the techniques that T2K use to generate the neutrino beam and  
569 constrain systematic parameter through near detector constraints are described.

### 570 3.1 The Super-Kamiokande Experiment

571 The SK experiment began taking data in 1996 [81] and has had many modifi-  
572 cations throughout its operation. There have been seven defined periods of  
573 data taking as noted in Table 3.1. Data taking began in SK-I which ran for five

574 years. Between the SK-I and SK-II periods, approximately 55% of the PMTs were  
 575 damaged during maintenance [82]. Those that survived were equally distributed  
 576 throughout the detector in the SK-II era, which resulted in a reduced 19% photo-  
 577 coverage. From SK-III onwards, repairs to the detector meant the full suite of  
 578 PMTs was operational recovering the 40% photo-coverage. Before the start of  
 579 SK-IV, the data acquisition and electronic systems were upgraded. Between  
 580 SK-IV and SK-V, a significant effort was placed into tank open maintenance and  
 581 repair/replacement of defective PMTs in preparation for the Gadolinium upgrade;  
 582 a task for which the author of this thesis was required. Consequently, the detector  
 583 conditions were significantly changed from this point. SK-VI marked the start of  
 584 the SK-Gd era, with the detector being doped with gadolinium at a concentration  
 585 of 0.01% by concentration. SK-VII, which started during the writing of this thesis,  
 586 has increased the gadolinium concentration to 0.03% for continued operation [83].

587 The oscillation analysis presented within this thesis focuses on the SK-IV  
 588 period of running and the data taken within it. This follows from the recent  
 589 SK analysis presented in [84]. Therefore, the information presented within this  
 590 section focuses on that period.

Period	Start Date	End Date	Live-time (days)
I	April 1996	July 2001	1489.19
II	October 2002	October 2005	798.59
III	July 2006	September 2008	518.08
IV	September 2008	May 2018	3244.4
V	January 2019	July 2020	461.02
VI	July 2020	May 2022	583.3
VII	May 2022	Ongoing	N/A

**Table 3.1:** The various SK periods and their respective live-time. The SK-VI live-time is calculated until 1<sup>st</sup> April 2022. SK-VII started during the writing of this thesis.

### 591 3.1.1 The SK Detector

592 The basic structure of the Super-Kamiokande (SK) detector is a cylindrical tank  
 593 with a diameter 39.3m and height 41.1m filled with ultrapure water [82]. A  
 594 diagram of the significant components of the SK detector is given in Figure 3.1.

595 The SK detector is situated in the Kamioka mine in Gifu, Japan. The mine  
 596 is underground with roughly 1km rock overburden (2.7km water equivalent  
 597 overburden) [85]. At this depth, the rate of cosmic ray muons is significantly  
 598 decreased to a value of  $\sim 2\text{Hz}$  (net rate) [86]. The top of the tank is covered  
 599 with stainless steel which is designed as a working platform for maintenance,  
 600 calibration, and location for high voltage and data acquisition electronics.



**Figure 3.1:** A schematic diagram of the Super-Kamiokande Detector. Taken from [87].

601 A smaller cylindrical structure (36.2m diameter, 33.8m height) is situated  
 602 inside the tank, with an approximate 2m gap between this structure and the outer  
 603 tank wall. The purpose of this structure is to support the photomultiplier tubes  
 604 (PMTs). The volume inside and outside the support structure is referred to as the  
 605 inner detector (ID) and outer detector (OD), respectively. In the SK-IV era, the  
 606 ID and OD are instrumented by 11,129 50cm and 1,885 20cm PMTs respectively  
 607 [82]. The ID contains a 32kton mass of water. Many analyses performed at SK  
 608 use a “fiducial volume” defined by the volume of water inside the ID excluding  
 609 some distance to the ID wall. This reduces the volume of the detector which is  
 610 sensitive to neutrino events but reduces radioactive backgrounds and allows for

611 better reconstruction performance. The nominal fiducial volume is defined as the  
612 area contained inside 2m from the ID wall for a total of 22.5kton water [88].

613 The two regions of the detector (ID and OD) are optically separated with  
614 opaque black plastic hung from the support structure. The purpose of this is  
615 to determine whether an event entered or exited the ID. This allows cosmic ray  
616 muons and partially contained events to be tagged and separated from neutrino  
617 events entirely contained within the ID. This black plastic is also used to cover  
618 the area between the ID PMTs to reduce photon reflection from the ID walls.  
619 Opposite to this, the OD is lined with a reflective material to allow photons to  
620 reflect around inside the OD until collected by one of the PMTs. Furthermore,  
621 each OD PMT is optically coupled with  $50 \times 50\text{cm}$  plates of wavelength shifting  
622 acrylic which increases the efficiency of light collection [85].

623 In the SK-IV data-taking period, the photocathode coverage of the detector, or  
624 the fraction of the ID wall instrumented with PMTs, is  $\sim 40\%$  [85]. The PMTs have  
625 a quantum efficiency (the ratio of detected electrons to incident photons) of  $\sim 21\%$   
626 for photons with wavelengths of  $360\text{nm} < \lambda < 390\text{nm}$  [89, 90]. The proportion  
627 of photoelectrons that produce a signal in the dynode of a PMT, termed the  
628 collection efficiency, is  $> 70\%$  [85]. The PMTs used within SK are most sensitive  
629 to photons with wavelength  $300\text{nm} \leq \lambda \leq 600\text{nm}$  [85]. One disadvantage of  
630 using PMTs as the detection media is that the Earth's geomagnetic field can  
631 modify its response. Therefore, a set of compensation coils is built around the  
632 inner surface of the detector to mitigate this effect [86].

633 The SK detector is filled with ultrapure water, which in a perfect world, con-  
634 tains no impurities. However, bacteria and organic compounds can significantly  
635 degrade the water quality. This decreases the attenuation length, which reduces  
636 the total number of photons that hit a PMT. To combat this, a sophisticated water  
637 treatment system has been developed [85, 91]. UV lights, mechanical filters, and  
638 membrane degasifiers are used to reduce the bacteria, suspended particulates,  
639 and radioactive materials from the water. The flow of water within the tank  
640 is also critical as it can remove stagnant bacterial growth or build-up of dust

641 on the surfaces within the tank. Gravity drifts impurities in the water towards  
642 the bottom of the tank which, if left uncontrolled, can create asymmetric water  
643 conditions between the top and bottom of the tank. Typically, the water entering  
644 the tank is cooled below the ambient temperature of the tank to control convection  
645 and inhibit bacteria growth. Furthermore, the rate of dark noise hits within PMTs  
646 is sensitive to the PMT temperature [92]. Therefore controlling the temperature  
647 gradients within the tank is beneficial for stable measurements.

648 SK-VI is the first phase of the SK experiment to use gadolinium dopants  
649 within the ultrapure water [83]. As such, the SK water system had to be replaced  
650 to avoid removing the gadolinium concentrate from the ultrapure water [93]. For  
651 an inverse  $\beta$ -decay (IBD) interaction on a water target, the emitted neutron is  
652 thermally captured on hydrogen. This process releases a 2.2MeV  $\gamma$  ray which is  
653 difficult to detect as the resulting Compton scattered electrons are very close to the  
654 Cherenkov threshold, limiting detection capability. Thermal capture of neutrons  
655 on gadolinium generates  $\gamma$  rays with higher energy (8MeV [68]) meaning they  
656 are more easily detected and reconstructed. SK-VI has 0.01% Gd loading (0.02%  
657 gadolinium sulphate by mass) which causes  $\approx$  50% of neutrons emitted by IBD to  
658 be captured on gadolinium[94, 95] . Whilst predominantly useful for low energy  
659 analyses, Gd loading allows better  $\nu/\bar{\nu}$  separation for atmospheric neutrino  
660 event selections [96]. Efforts are currently in place to increase the gadolinium  
661 concentrate to 0.03% for  $\approx$  75% neutron capture efficiency on gadolinium [97].  
662 The final stage of loading targets 0.1% concentrate for  $\approx$  90% neutron capture  
663 efficiency on gadolinium.

### 664 3.1.2 Calibration

665 The calibration of the SK detector is documented in [82] and summarised below.  
666 The analysis presented within this thesis is dependent upon ‘high energy events’  
667 (Charged particles with  $O(> 100)$ MeV momenta). These are events that are  
668 expected to generate a larger number of photons such that each PMT will  
669 be hit with multiple photons. The reconstruction of these events depends

upon the charge deposited within each PMT and the timing response of each individual PMT. Therefore, the most relevant calibration techniques to this thesis are outlined.

Before installation, 420 PMTs were calibrated to have identical charge responses and then distributed throughout the tank in a cross-shape pattern (As illustrated by Figure 3.2). These are used as a standardised measure for the rest of the PMTs installed at similar geometric positions within SK to be calibrated against. To perform this calibration, a xenon lamp is located at the center of the SK tank which flashes uniform light at 1Hz. This allows for geometrical effects, water quality variation, and timing effects to be measured in situ throughout normal data-taking periods.

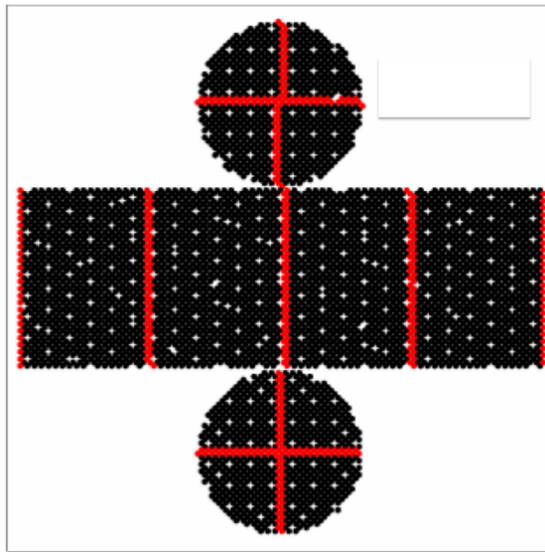


**Figure 3.2:** The location of “standard PMTs” (red) inside the SK detector. Taken from [82].

When specifically performing calibration of the detector (in out-of-data taking mode), the water in the tank was circulated to avoid top/bottom asymmetric water quality. Any non-uniformity within the tank significantly affects the PMT hit probability through scattering or absorption. This becomes a dominant effect for very low-intensity light sources that are designed such that only one photon is incident upon a given PMT.

687 The gain of a PMT is defined as the ratio of the total charge of the signal  
 688 produced compared to the charge of photoelectrons emitted by the photocathodes  
 689 within the PMT. To calibrate the signal of each PMT, the “relative” and “absolute”  
 690 gain values are measured. The relative gain is the variation of gain among each  
 691 of the PMTs whereas the absolute gain is the average gain of all PMTs.

692 The relative gain is calibrated as follows. A laser is used to generate two  
 693 measurements: a high-intensity flash that illuminates every PMT with a sufficient  
 694 number of photons, and a low-intensity flash in which only a small number  
 695 of PMTs collect light. The first measurement creates an average charge,  $Q_{obs}(i)$   
 696 on PMT  $i$ , whereas the second measurement ensures that each hit PMT only  
 697 generates a single photoelectron. For the low-intensity measurement, the number  
 698 of times each PMT records a charge larger than 1/4 photoelectrons,  $N_{obs}(i)$ , is  
 699 counted. The values measured can be expressed as

$$\begin{aligned} Q_{obs}(i) &\propto I_H \times f(i) \times \epsilon(i) \times G(i), \\ N_{obs}(i) &\propto I_L \times f(i) \times \epsilon(i). \end{aligned} \tag{3.1}$$

700 Where  $I_H$  and  $I_L$  is the intensity of the high and low flashes,  $f(i)$  is the  
 701 acceptance efficiency of the  $i^{\text{th}}$  PMT,  $\epsilon(i)$  is the product of the quantum and  
 702 collection efficiency of the  $i^{\text{th}}$  PMT and  $G(i)$  is the gain of the  $i^{\text{th}}$  PMT. The relative  
 703 gain for each PMT can be determined by taking the ratio of these quantities.

704 The absolute gain calibration is performed by observing fixed energy  $\gamma$ -rays  
 705 of  $E_\gamma \sim 9\text{MeV}$  emitted isotropically from neutron capture on a NiCf source  
 706 situated at the center of the detector. This generates a photon yield of about 0.004  
 707 photoelectrons/PMT/event, meaning that  $> 99\%$  of PMT signals are generated  
 708 from single photoelectrons. A charge distribution is generated by performing  
 709 this calibration over all PMTs, and the average value of this distribution is taken  
 710 to be the absolute gain value.

711 As mentioned in subsection 3.1.1, the average quantum and collection effi-  
 712 ciency for the SK detector PMTs is  $\sim 21\%$  and  $> 70\%$  respectively. However,  
 713 these values do differ between each PMT and need to be calibrated accordingly.

714 Consequently, the NiCf source is also used to calibrate the “quantum  $\times$  collection”  
715 efficiency (denoted “QE”) value of each PMT. The NiCf low-intensity source is  
716 used as the PMT hit probability is proportional to the QE ( $N_{obs}(i) \propto \epsilon(i)$  in  
717 Equation 3.1). A Monte Carlo prediction which includes photon absorption,  
718 scattering, and reflection is made to estimate the number of photons incident on  
719 each PMT and the ratio of the number of predicted to observed hits is calculated.  
720 The difference is attributed to the QE efficiency of that PMT. This technique is  
721 extended to calculate the relative QE efficiency by normalizing the average of  
722 all PMTs which removes the dependence on the light intensity.

723 Due to differing cable lengths and readout electronics, the timing response  
724 between a photon hitting the PMT and the signal being captured by the data  
725 acquisition can be different between each PMT. Due to threshold triggers (De-  
726 scribed in subsection 3.1.3), the time at which a pulse reaches a threshold is  
727 dependent upon the size of the pulse. This is known as the ‘time-walk’ effect  
728 and also needs to be accounted for in each PMT. To calibrate the timing response,  
729 a pulse of light with width 0.2ns is emitted into the detector through a diffuser.  
730 Two-dimensional distributions of time and pulse height (or charge) are made  
731 for each PMT and are used to calibrate the timing response. This is performed  
732 in-situ during data taking with the light source pulsing at 0.03Hz.

733 The top/bottom water quality asymmetry is measured using the NiCf calibra-  
734 tion data and cross-referencing these results to the “standard PMTs”. The water  
735 attenuation length is continuously measured by the rate of vertically-downgoing  
736 cosmic-ray muons which enter via the top of the tank.

737 Dark noise is where a PMT registers a pulse that is consistent with a single  
738 photoelectron emitted from photon detection despite the PMT being in complete  
739 darkness. This is predominately caused by two processes. Firstly there is  
740 intrinsic dark noise which is where photoelectrons gain enough thermal energy  
741 to be emitted from the photocathode, and secondly, the radioactive decay of  
742 contaminants inside the structure of the PMT. Typical dark noise rate for PMTs  
743 used within SK are  $O(3)\text{kHz}$  [85]. This is lower than the expected number of

744 photons generated for a ‘high energy event’ (As described in subsection 3.1.4)  
745 but instability in this value can cause biases in reconstruction. Dark noise is  
746 related to the gain of a PMT and is calibrated using hits inside a time window  
747 recorded before an event trigger [98].

### 748 3.1.3 Data Acquisition and Triggering

749 As the analysis presented in this thesis will only use the SK-IV period of the  
750 SK experiment so this subsection focuses on the relevant points of the data  
751 acquisition and triggering systems to that SK period. The earlier data acquisition  
752 and triggering systems are documented in [99, 100].

753 Before the SK-IV period started, the existing front-end electronics were re-  
754 placed with “QTC-Based Electronics with Ethernet, QBEE” systems [101]. When  
755 the QBEE observes a signal above a 1/4 photoelectron threshold, the charge-to-  
756 time (QTC) converter generates a rectangular pulse. The start of the rectangular  
757 pulse indicates the time at which the analog photoelectron signal was received  
758 and the width of the pulse indicates the total charge integrated throughout the  
759 signal. This is then digitized by time-to-digital converters and sent to the “front-  
760 end” PCs. The digitized signal from every QBEE is then chronologically ordered  
761 and sent to the “merger” PCs. It is the merger PCs that apply the software trigger.  
762 Any triggered events are passed to the “organizer” PC. This sorts the data stream  
763 of multiple merger PCs into chronologically ordered events, which are then saved  
764 to disk. The schematic of data flow from PMTs to disk is illustrated in Figure 3.3.

765 The software trigger (described in [103]) operates by determining the number  
766 of PMT hits within a 200ns sliding window,  $N_{200}$ . This window coincides with  
767 the maximum time that a Cherenkov photon would take to traverse the length  
768 of the SK tank [100]. For lower energy events that generate fewer photons, this  
769 technique is useful for eliminating background processes like dark noise and  
770 radioactive decay which would be expected to be separated in time. When the  
771 value of  $N_{200}$  exceeds some pre-defined threshold, a software trigger is issued.  
772 There are several trigger thresholds used within the SK-IV period which are

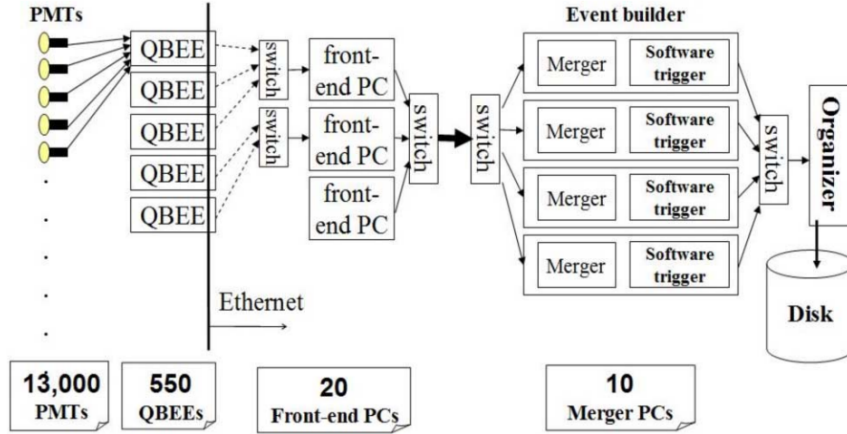


**Figure 3.3:** Schematic view of the data flow through the data acquisition and online system. Taken from [102].

773 detailed in Table 3.2. If one of these thresholds is met, the PMT hits within an  
 774 extended time window are also read out and saved to disk. In the special case  
 775 of an event that exceeds the SHE trigger but does not exceed the OD trigger,  
 776 the AFT trigger looks for delayed coincidences of 2.2MeV gamma rays emitted  
 777 from neutron capture in a  $535\mu\text{s}$  window after the SHE trigger. A similar but  
 778 more complex “Wideband Intelligent Trigger (WIT)” has been deployed and  
 779 is described in [104].

Trigger	Acronym	Condition	Extended time window ( $\mu\text{s}$ )
Super Low Energy	SLE	>34/31 hits	1.3
Low Energy	LE	>47 hits	40
High Energy	HE	>50 hits	40
Super High Energy	SHE	>70/58 hits	40
Outer Detector	OD	>22 hits in OD	N/A

**Table 3.2:** The trigger thresholds and extended time windows saved around an event which were utilised throughout the SK-IV period. The exact thresholds can change and the values listed here represent the thresholds at the start and end of the SK-IV period.

### 780 3.1.4 Cherenkov Radiation

781 Cherenkov light is emitted from any highly energetic charged particle traveling  
 782 with relativistic velocity,  $\beta$ , greater than the local speed of light in a medium [105].

783 Cherenkov light is formed at the surface of a cone with a characteristic pitch angle,

$$\cos(\theta) = \frac{1}{\beta n}. \quad (3.2)$$

784 Where  $n$  is the refractive index of the medium. Consequently, the Cherenkov  
 785 momentum threshold,  $P_{thres}$ , is dependent upon the mass,  $m$ , of the charged  
 786 particle moving through the medium,

$$P_{thres} = \frac{m}{\sqrt{n^2 - 1}}. \quad (3.3)$$

787 For water, where  $n = 1.33$ , the Cherenkov threshold momentum and energy  
 788 for various particles are given in Table 3.3. In contrast,  $\gamma$ -rays are detected  
 789 indirectly via the combination of photons generated by Compton scattering  
 790 and pair production. The threshold for detection in the SK detector is typically  
 791 higher than the threshold for photon production. This is due to the fact that the  
 792 attenuation of photons in the water means that typically  $\sim 75\%$  of Cherenkov  
 793 photons reach the ID PMTs. Then the collection and quantum efficiencies  
 794 described in subsection 3.1.1 result in the number of detected photons being  
 795 lower than the number of photons which reach the PMTs.

Particle	Threshold Momentum (MeV)	Threshold Energy (MeV)
Electron	0.5828	0.7751
Muon	120.5	160.3
Pion	159.2	211.7
Proton	1070.0	1423.1

**Table 3.3:** The threshold momentum and total energy for a particle to generate Cherenkov light in ultrapure water, as calculated in Equation 3.2 in ultrapure water which has refractive index  $n = 1.33$ .

796 The Frank-Tamm equation [106] describes the relationship between the num-  
 797 ber of Cherenkov photons generated per unit length,  $dN/dx$ , the wavelength of  
 798 the photons generated,  $\lambda$ , and the relativistic velocity of the charged particle,

$$\frac{d^2N}{dxd\lambda} = 2\pi\alpha \left(1 - \frac{1}{n^2\beta^2}\right) \frac{1}{\lambda^2}. \quad (3.4)$$

799 where  $\alpha$  is the fine structure constant. For a 100MeV momentum electron,  
 800 approximately 330 photons will be produced per centimeter in the  $300\text{nm} \leq \lambda \leq$   
 801  $700\text{nm}$  region which the ID PMTs are most sensitive to [85].

## 802 3.2 The Tokai to Kamioka Experiment

803 The Tokai to Kamioka (T2K) experiment is a long-baseline neutrino oscillation  
 804 experiment located in Japan. Proposed in the early 2000s [107, 108] to replace  
 805 K2K [109], T2K was designed to observe electron neutrino appearance whilst  
 806 precisely measuring the oscillation parameters associated with muon neutrino  
 807 disappearance [110]. The experiment consists of a neutrino beam generated  
 808 at the Japan Proton Accelerator Research Complex (J-PARC), a suite of near  
 809 detectors situated 280m from the beam target, and the Super Kamiokande far  
 810 detector positioned at a 295km baseline. The cross-section view of the T2K  
 811 experiment is drawn in Figure 3.4.

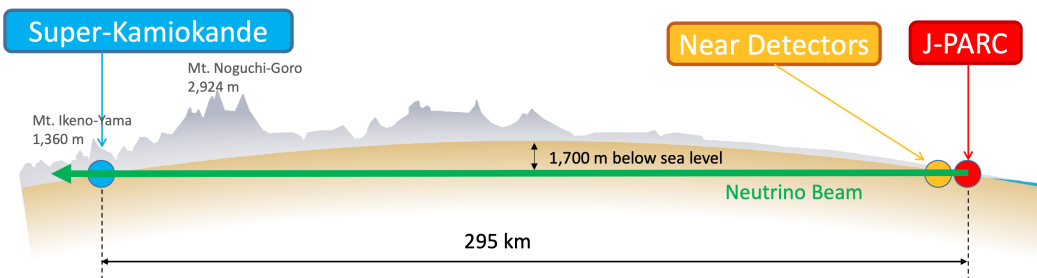


**Figure 3.4:** The cross-section view of the Tokai to Kamioka experiment illustrating the beam generation facility at J-PARC, the near detector situated at a baseline of 280m and the Super Kamiokande far detector situated 295km from the beam target.

812 The T2K collaboration makes world-leading measurements of the  $\sin^2(\theta_{23})$ ,  
 813  $\Delta m_{32}^2$ , and  $\delta_{CP}$  oscillation parameters. Improvements in the precision and accu-  
 814 racy of parameter estimates are still being made by including new data samples  
 815 and developing the models which describe the neutrino interactions and detector  
 816 responses [111]. Electron neutrino appearance was first observed at T2K in 2014  
 817 [112] with  $7.3\sigma$  significance.

818 The near detectors provide constraints on the beam flux and cross-section  
 819 model parameters used within the oscillation analysis by observing the unoscil-  
 820 lated neutrino beam. There are a host of detectors situated in the near detector hall  
 821 (As illustrated in Figure 3.5): ND280 (subsection 3.2.3), INGRID (subsection 3.2.4),  
 822 NINJA [113], WAGASCI [114], and Baby-MIND [115]. The latter three are not  
 823 currently used within the oscillation analysis presented in this thesis.

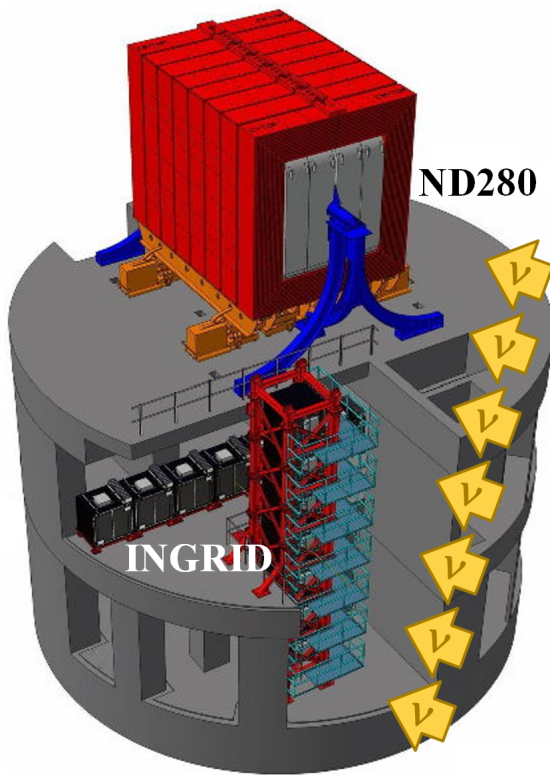


**Figure 3.5:** The near detector suite for the T2K experiment showing the ND280 and INGRID detectors. The distance between the detectors and the beam target is 280m.

824 Whilst this thesis presents the ND280 in terms of its purpose for the oscillation  
 825 analysis, the detector can also make many cross-section measurements at neutrino  
 826 energies of  $O(1)$ GeV for the different targets within the detector [116, 117]. These  
 827 measurements are of equal importance as they can lead the way in determining  
 828 the model parameters used in the interaction models for the future high-precision  
 829 era of neutrino physics.

### 3.2.1 Analysis Overview

There are two independent fitters, MaCh3 and BANFF, which perform the near detector fit. MaCh3 uses a bayesian Markov Chain Monte Carlo fitting technique, whereas BANFF uses a frequentist gradient descent technique. The output of each fitter is compared as a method of cross-checking the behaviour of the two fitters. This is done by comparing: the Monte Carlo predictions using various tunes, the likelihood that is calculated in each fitter and the post-fit constraint associated with every parameter used in the fit. Once validated, the output converted into a covariance matrix to describe the error and correlations between all the flux and cross-section parameters. This is then propagated to the far-detector oscillation analysis group.

The far detector group has three independent fitters: P-Theta, VALOR and MaCh3. The first two fitters use a hybrid frequentist fitting technique where the likelihood is minimised with respect to the parameters of interest and marginalised over all other parameters. These fitters use the covariance provided by the near detector fitters as a basis for implementing the near detector constraints. The MaCh3 fitter uses a simultaneous fit of all near and far detector samples. This removes any Gaussian assumptions when making the covariance matrix from the near detector results. The results for all three fitters are compares using a technique similar to the validation of the near detector fitters.

There are three particular tunes of the T2K flux and low energy cross section model typically considered. Firstly, the “generated” tune which is the set of dial values with which the Monte Carlo was generated. Secondly, the set of dial values which are taken from external data measurements and used as inputs. These are the “pre-fit” dial values. The reason these two sets of dial values are different is that the external data measurements are continually updated but it is very computationally intensive to regenerate a Monte Carlo prediction after each update. The final tune is the “post-fit”, “post-ND fit” or “post-BANFF” dial values. These are the values taken from the constraints provided by the near detector.

### 3.2.2 The Neutrino Beam

The neutrino beam used within the T2K experiment is described in [39, 43] and summarised below. The accelerator facility at J-PARC is composed of two sections; the primary and secondary beamlines. Figure 3.6 illustrates a schematic of the beamline, focusing mostly on the components of the secondary beamline. The primary beamline has three accelerators that progressively accelerate protons; a linear accelerator, a rapid-cycling synchrotron, and the main-ring (MR) synchrotron. Once fully accelerated by the MR, the protons have a kinetic energy of 30GeV. Eight bunches of these protons, separated by 500ns, are extracted per “spill” from the MR and directed towards a graphite target (a rod of length 91.4cm and diameter 2.6cm). Spills are extracted at 0.5Hz with  $\sim 3 \times 10^{14}$  protons contained per spill.

The secondary beamline consists of three main components: the target station, the decay volume, and the beam dump. The target station is comprised of the target, beam monitors, and three magnetic focusing horns. The proton beam interacts with the graphite target to form a secondary beam of mostly pions and kaons. The secondary beam travels through a 96m long decay volume, generating neutrinos through the following decays [39],

$$\begin{array}{ll}
\pi^+ \rightarrow \mu^+ + \nu_\mu & \pi^- \rightarrow \mu^- + \bar{\nu}_\mu \\
K^+ \rightarrow \mu^+ + \nu_\mu & K^- \rightarrow \mu^- + \bar{\nu}_\mu \\
\rightarrow \pi^0 + e^+ + \nu_e & \rightarrow \pi^0 + e^- + \bar{\nu}_e \\
\rightarrow \pi^0 + \mu^+ + \nu_\mu & \rightarrow \pi^0 + \mu^- + \bar{\nu}_\mu \\
K_L^0 \rightarrow \pi^- + e^+ + \nu_e & K_L^0 \rightarrow \pi^+ + e^- + \bar{\nu}_e \\
\rightarrow \pi^- + \mu^+ + \nu_\mu & \rightarrow \pi^+ + \mu^- + \bar{\nu}_\mu \\
\mu^+ \rightarrow e^+ + \bar{\nu}_\mu + \nu_e & \mu^- \rightarrow e^- + \nu_\mu + \bar{\nu}_e.
\end{array}$$

The electrically charged component of the secondary beam is focused towards the far detector by the three magnetic horns. These horns direct charged particles of a particular polarity towards SK whilst defocusing the oppositely charged particles. This allows a mostly neutrino or mostly antineutrino beam to be used within the experiment, denoted as “forward horn current (FHC)” or “reverse horn current (RHC)” respectively.

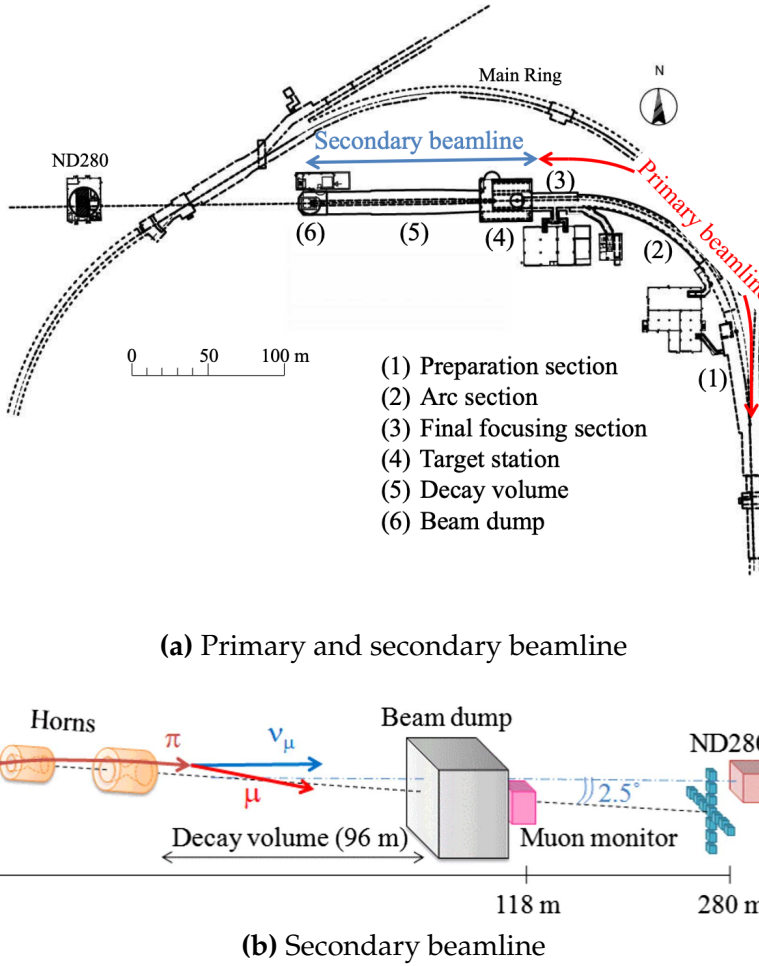


**Figure 3.6:** Top panel: Bird's eye view of the most relevant part of primary and secondary beamline used within the T2K experiment. The primary beamline is the main-ring proton synchrotron, kicker magnet, and graphite target. The secondary beamline consists of the three focusing horns, decay volume, and beam dump. Figure taken from [43]. Bottom panel: The side-view of the secondary beamline including the focusing horns, beam dump and neutrino detectors. Figure taken from [118].

885     Figure 3.7 illustrates the different contributions to the FHC and RHC neutrino  
 886     flux. The low energy flux is dominated by the decay of pions whereas kaon  
 887     decay becomes the dominant source of neutrinos for  $E_\nu > 3\text{GeV}$ . The “wrong-  
 888     sign” component, which is the  $\bar{\nu}_\mu$  background in a  $\nu_\mu$  beam, and the intrinsic  
 889     irreducible  $\nu_e$  background, are predominantly due to muon decay for  $E_\nu <$   
 890      $2\text{GeV}$ . As the antineutrino production cross-section is smaller than the neutrino  
 891     cross-section, the wrong-sign component is more dominant in the RHC beam  
 892     as compared to that in the FHC beam.



**Figure 3.7:** The Monte Carlo prediction of the energy spectrum for each flavour of neutrino ( $\nu_e$ ,  $\bar{\nu}_e$ ,  $\nu_\mu$  and  $\bar{\nu}_\mu$ ) in the neutrino dominated beam FHC mode (Left) and antineutrino dominated beam RHC mode (Right) expected at SK. Taken from [119].

893     The beam dump, situated at the end of the decay volume, stops all charged  
 894     particles other than highly energetic muons ( $p_\mu > 5\text{GeV}$ ). The MuMon detector  
 895     monitors the penetrating muons to determine the beam direction and inten-  
 896     sity which is used to constrain some of the beam flux systematics within the  
 897     analysis [118, 120].

898     The T2K experiment uses an off-axis beam to narrow the neutrino energy  
 899     distribution. This was the first implementation of this technique in a long-  
 900     baseline neutrino oscillation experiment after its original proposal [121]. Pion  
 901     decay,  $\pi \rightarrow \mu + \nu_\mu$ , is a two-body decay. Consequently, the neutrino energy,  
 902      $E_\nu$ , can be determined based on the pion energy,  $E_\pi$ , and the angle at which  
 903     the neutrino is emitted,  $\theta$ ,

$$E_\nu = \frac{m_\pi^2 - m_\mu^2}{2(E_\pi - p_\pi \cos(\theta))}, \quad (3.5)$$

904     where  $m_\pi$  and  $m_\mu$  are the mass of the pion and muon respectively. For a fixed  
 905     energy pion, the neutrino energy distribution is dependent upon the angle at  
 906     which the neutrinos are observed from the initial pion beam direction. For the  
 907     295km baseline at T2K,  $E_\nu = 0.6\text{GeV}$  maximises the electron neutrino appearance  
 908     probability,  $P(\nu_\mu \rightarrow \nu_e)$ , whilst minimising the muon disappearance probability,

909  $P(\nu_\mu \rightarrow \nu_\mu)$ . Figure 3.8 illustrates the neutrino energy distribution for a range of  
 910 off-axis angles, as well as the oscillation probabilities most relevant to T2K.

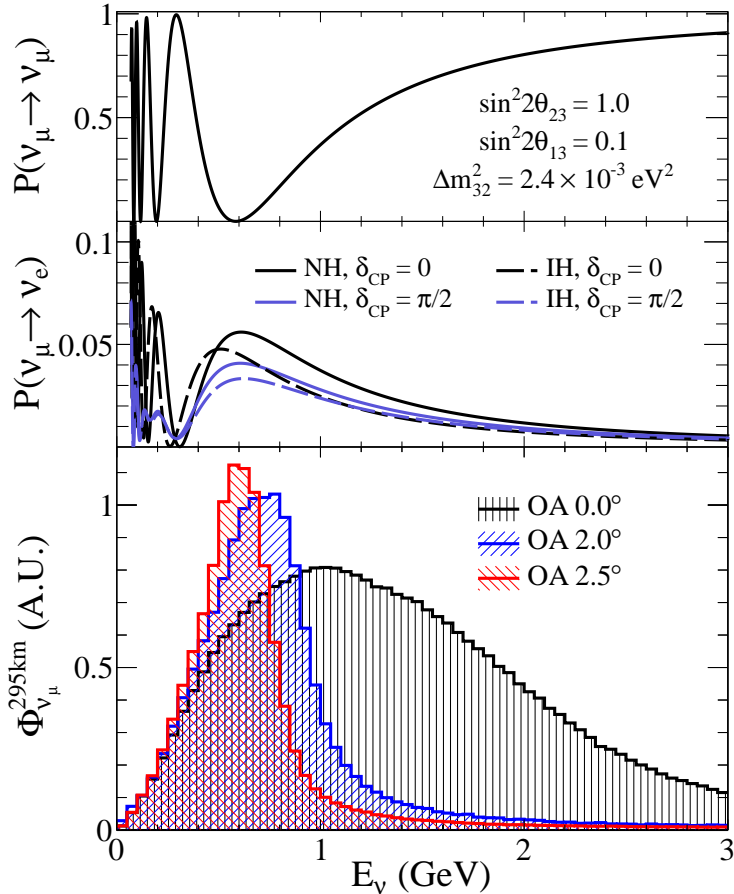


**Figure 3.8:** Top panel: T2K muon neutrino disappearance probability as a function of neutrino energy. Middle panel: T2K electron neutrino appearance probability as a function of neutrino energy. Bottom panel: The neutrino flux distribution for three different off-axis angles (Arbitrary units) as a function of neutrino energy.

### 911 3.2.3 The Near Detector at 280m

912 Whilst all the near detectors are situated in the same “pit” located at 280m from  
 913 the beamline, the “ND280” detector is the off-axis detector which is situated at  
 914 the same off-axis angle as the Super-Kamiokande far detector. It has two primary  
 915 functions; firstly it measures the neutrino flux and secondly, it counts the event  
 916 rates of different types of neutrino interactions. Both of these constrain the flux  
 917 and cross-section systematics invoked within the model for a more accurate  
 918 prediction of the expected event rate at the far detector.



**Figure 3.9:** The components of the ND280 detector. The neutrino beam travels from left to right. Taken from [43].

As illustrated in Figure 3.9, the ND280 detector consists of several sub-detectors. The most important part of the detector for this analysis is the tracker region. This is comprised of two-time projection chambers (TPCs) sandwiched between three fine grain detectors (FGDs). The FGDs contain both hydrocarbon plastics and water targets for neutrino interactions and provide track reconstruction near the interaction vertex. The emitted charged particles can then propagate into the TPCs which provide particle identification and momentum reconstruction. The FGDs and TPCs are further described in subsubsection 3.2.3.1 and subsubsection 3.2.3.2 respectively. The electromagnetic calorimeter (ECAL) encapsulates the tracker region alongside the  $\pi^0$  detector (P0D). The ECAL measures the deposited energy from photons emitted from interactions within the FGD. The P0D constrains the cross-section of neutral current interactions which generate neutral pions, which is one of the largest backgrounds in the electron neutrino appearance oscillation channel. The P0D and ECAL detectors are detailed in subsubsection 3.2.3.3 and subsubsection 3.2.3.4 respectively. The entire detector is located within a large yoke magnet which produces a 0.2T magnetic field.

935 field. This design of the magnet also includes a scintillating detector called the  
936 side muon range detector (SMRD), which is used to track high-angle muons as  
937 well as acting as a cosmic veto. The SMRD is described in subsubsection 3.2.3.5.

938 **3.2.3.1 Fine Grained Detectors**

939 The T2K tracker region is comprised of two fine-grained detectors (FGD) and  
940 three Time Projection Chambers (TPC). A detailed description of the FGD design,  
941 construction, and assembly is found in [122] and summarised below. The FGDS  
942 are the primary target for neutrino interactions with a mass of 1.1 tonnes per FGD.  
943 Alongside this, the FGDS are designed to be able to track short-range particles  
944 which do not exit the FGD. Typically, short-range particles are low momentum  
945 and are observed as tracks that deposit a large amount of energy per unit length.  
946 This means the FGD needs good granularity to resolve these particles. The  
947 FGDS have the best timing resolution ( $\sim 3\text{ns}$ ) of any of the sub-detectors of the  
948 ND280 detector. As such, the FGDS are used for time of flight measurements  
949 to distinguish forward-going positively charged particles from backward-going  
950 negatively charged particles. Finally, any tracks which pass through multiple  
951 sub-detectors are required to be track matched to the FGD.

952 Both FGDS are made from square scintillator planes of side length 186cm and  
953 width 2.02cm. Each plane consists of two layers of 192 scintillator bars in an  
954 X or Y orientation. A wavelength-shifting fiber is threaded through the center  
955 of each bar and is read out by a multi-pixel photon counter (MPPC). FGD1 is  
956 the most upstream of the two FGDS and contains 15 planes of carbon plastic  
957 scintillator which is a common target in external neutrino scattering data. As  
958 the far detector is a pure water target, 7 of the 15 scintillator planes in FGD2  
959 have been replaced with a hybrid water-scintillator target. Due to the complexity  
960 of the nucleus, nuclear effects can not be extrapolated between different nuclei.  
961 Therefore having the ability to take data on one target which is the same as  
962 external data and another target which is the same as the far detector target is  
963 beneficial for reliable model parameter estimates.

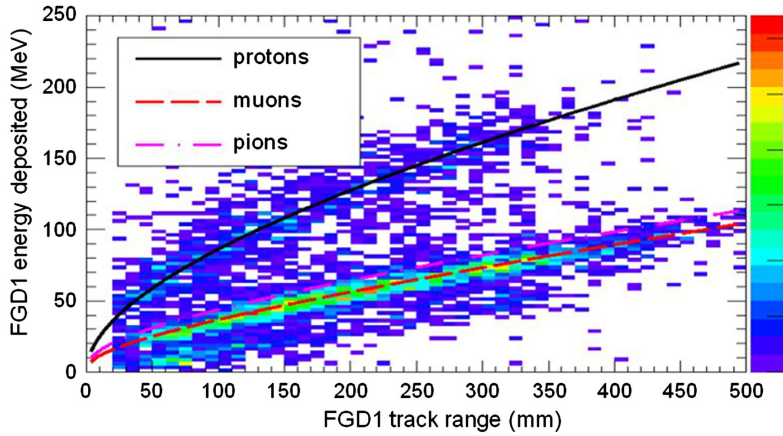


**Figure 3.10:** Comparison of data to Monte Carlo prediction of integrated deposited energy as a function of track length for particles that stopped in FGD1. Taken from [122].

964     The integrated deposited energy is used for particle identification. The FGD  
965     can distinguish protons from other charged particles by comparing the integrated  
966     deposited energy from data to Monte Carlo prediction as seen in Figure 3.10.

### 967     3.2.3.2 Time Projection Chambers

968     The majority of particle identification and momentum measurements within  
969     ND280 are provided by three Time Projection Chambers (TPCs) [123]. The  
970     TPCs are located on either side of the FGDs. They are located inside of the  
971     magnetic field meaning the momentum of a charged particle can be determined  
972     from the bending of the track.

973     Each TPC module consists of two gas-tight boxes, as shown in Figure 3.11,  
974     which are made of non-magnetic material. The outer box is filled with CO<sub>2</sub> which  
975     acts as an electrical insulator between the inner box and the ground. The inner box  
976     forms the field cage which produces a uniform electric drift field of  $\sim 275\text{V/cm}$   
977     and is filled with an argon gas mixture. Charged particles moving through this  
978     gas mixture ionize the gas and the ionised charge is drifted towards micromegas  
979     detectors which measure the ionization charge. The time and position information  
980     in the readout allows a three-dimensional image of the neutrino interaction.

981     The particle identification of tracks that pass through the TPCs is performed  
982     using dE/dx measurements. Figure 3.12 illustrates the data to Monte Carlo



**Figure 3.11:** Schematic design of a Time Projection Chamber detector. Taken from [123].

983 distributions of the energy lost by a charged particle passing through the TPC as  
 984 a function of the reconstructed particle momentum. The resolution is  $7.8 \pm 0.2\%$   
 985 meaning that electrons and muons can be distinguished. This allows reliable  
 986 measurements of the intrinsic  $\nu_e$  component of the beam.

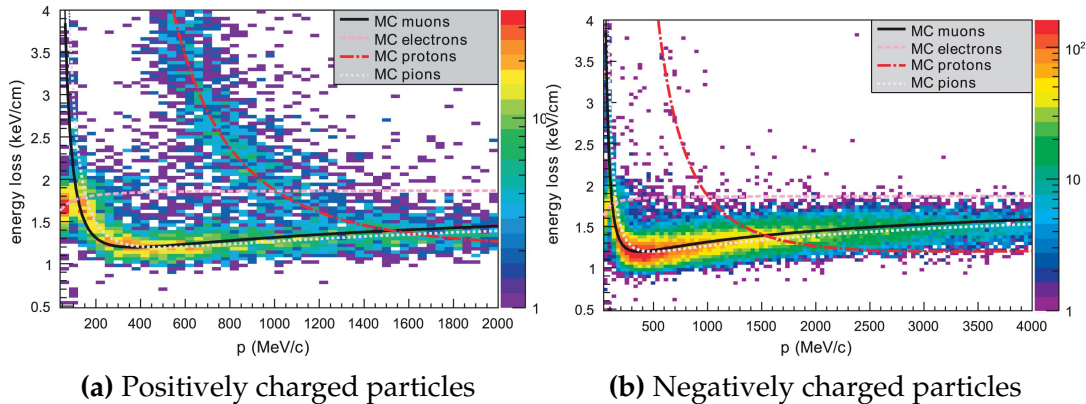


**Figure 3.12:** The distribution of energy loss as a function of reconstructed momentum for charged particles passing through the TPC, comparing data to Monte Carlo prediction. Taken from [123].

987 **3.2.3.3  $\pi^0$  Detector**

988 If one of the  $\gamma$ -rays from a  $\pi^0 \rightarrow 2\gamma$  decay is missed at the far detector, the  
 989 reconstruction will determine that event to be a charge current  $\nu_e$ -like event.  
 990 This is one of the main backgrounds hindering the electron neutrino appearance

991 searches. The  $\pi^0$  detector (P0D) measures the cross-section of the neutral current  
 992 induced neutral pion production on a water target to constrain this background.

993 The P0D is a cube of approximately 2.5m length consisting of layers of scin-  
 994 tillating bars, brass and lead sheets, and water bags as illustrated in Figure 3.13.  
 995 Two electromagnetic calorimeters are positioned at the most upstream and most  
 996 downstream position in the sub-detector and the water target is situated in  
 997 between them. The scintillator layers are built from two triangular bars orientated  
 998 in opposite directions to form a rectangular layer. Each triangular scintillator bar  
 999 is threaded with optical fiber which is read out by MPPCs. The high-Z brass and  
 1000 lead regions produce electron showers from the photons emitted in  $\pi^0$  decay.

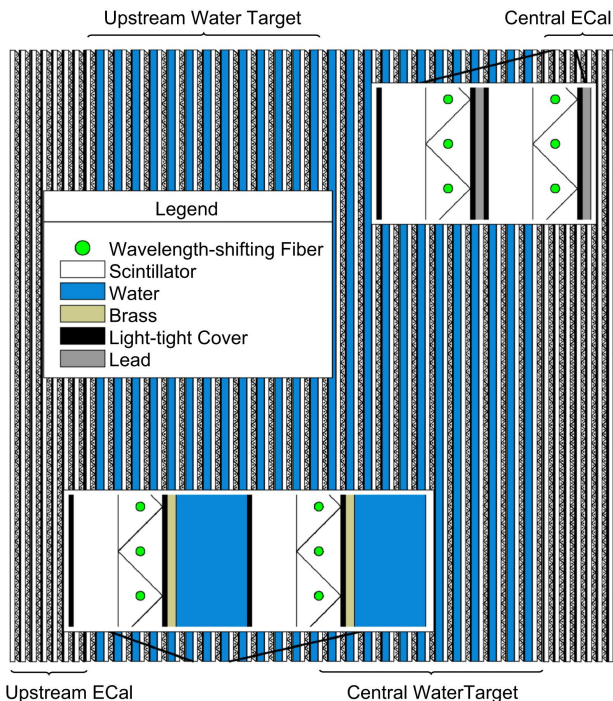


**Figure 3.13:** A schematic of the P0D side-view. Taken from [124].

1001 The sub-detector can generate measurements of NC1 $\pi^0$  cross-sections on a  
 1002 water target by measuring the event rate both with and without the water target,  
 1003 with the cross-section on a water target being determined as the difference. The to-  
 1004 tal active mass is 16.1 tonnes when filled with water and 13.3 tonnes when empty.

**1005 3.2.3.4 Electromagnetic Calorimeter**

**1006** The electromagnetic calorimeter [125] (ECal) encapsulates the P0D and tracking  
**1007** sub-detectors. Its primary purpose is to aid  $\pi^0$  reconstruction from any interac-  
**1008** tion in the tracker. To do this, it measures the energy and direction of photon  
**1009** showers from  $\pi^0 \rightarrow 2\gamma$  decay. It can also distinguish pion and muon tracks  
**1010** depending on the shape of the photon shower deposited.

**1011** The ECal is comprised of three sections; the P0D ECal which surrounds the  
**1012** P0D, the barrel ECal which encompasses the tracking region, and the downstream  
**1013** ECal which is situated downstream of the tracker region. The barrel and down-  
**1014** stream ECals are tracking calorimeters that focus on electromagnetic showers  
**1015** from high-angle particles emitted from the tracking sub-detectors. Particularly in  
**1016** the TPC, high-angle tracks (those which travel perpendicularly to the beam-axis)  
**1017** can travel along a single scintillator bar resulting in very few hits. The width of  
**1018** the barrel and downstream ECal corresponds to  $\sim 11$  electron radiation lengths  
**1019** to ensure a significant amount of the  $\pi^0$  energy is contained. As the P0D has  
**1020** its own calorimetry which reconstructs showers, the P0D ECal determines the  
**1021** energy which escapes the P0D.

**1022** Each ECal is constructed of multiple layers of scintillating bars sandwiched  
**1023** between lead sheets. The scintillating bars are threaded with optical fiber and read  
**1024** out by MPPCs. Each sequential layer of the scintillator is orientated perpendicular  
**1025** to the previous which allows a three-dimensional event reconstruction. The  
**1026** target mass of the P0D ECal, barrel ECal, and downstream ECal are 1.50, 4.80,  
**1027** and 6.62 tonnes respectively.

**1028 3.2.3.5 Side Muon Range Detector**

**1029** As illustrated in Figure 3.9, the ECal, FGDs, P0D, and TPCs are enclosed within  
**1030** the UA1 magnet. Reconditioned after use in the UA1 [126] and NOMAD [127]  
**1031** experiments, this magnet provides a uniform horizontal magnetic field of 0.2T  
**1032** with an uncertainty of  $2 \times 10^{-4}$ T.

1033     Built into the UA1 magnet, the side muon range detector (SMRD)[128] monitors  
1034     high-energy muons which leave the tracking region and permeate through  
1035     the ECal. It additionally acts as a cosmic muon veto and trigger.

### 1036     **3.2.4 The Interactive Neutrino GRID**

1037     The Interactive Neutrino GRID (INGRID) detector is situated within the same  
1038     “pit” as the other near detectors. It is aligned with the beam in the “on-axis”  
1039     position and measures the beam direction, spread, and intensity. The detector  
1040     was originally designed with 16 identical modules [43] (two modules have since  
1041     been decommissioned) and a “proton” module. The design of the detector is 14  
1042     modules oriented in a cross with length and height 10m × 10m, as illustrated  
1043     in Figure 3.14.

1044     Each module is composed of iron sheets interlaced with eleven tracking  
1045     scintillator planes for a total target mass of 7.1 tonnes per module. The scintillator  
1046     design is an X-Y pattern of 24 bars in both orientations, where each bar contains  
1047     wave-length shifting fibers which are connected to multi-pixel photon counters  
1048     (MPPCs). Each module is encapsulated inside veto planes to aid the rejection  
1049     of charged particles entering the module.

1050     The proton module is different from the other modules in that it consists  
1051     of entirely scintillator planes with no iron target. The scintillator bars are also  
1052     smaller than those used in the other modules to increase the granularity of  
1053     the detector and improve tracking capabilities. The module sits in the center  
1054     of the beamline and is designed to give precise measurements of quasi-elastic  
1055     charged current interactions to evaluate the performance of the Monte Carlo  
1056     simulation of the beamline.

1057     The INGRID detector can measure the beam direction to an uncertainty of  
1058     0.4mrad and the beam centre within a resolution of 10cm [43]. The beam direction  
1059     in both the vertical and horizontal directions is discussed in [129] and it is found  
1060     to be in good agreement with the MUMON monitor described in subsection 3.2.2.



**Figure 3.14:** Left panel: The Interactive Neutrino GRID on-axis Detector. 14 modules are arranged in a cross-shape configuration, with the center modules being directly aligned with the on-axis beam. Right panel: The layout of a single module of the INGRID detector. Both figures are recreated from [43].

# 4

1061

1062

1063

## Bayesian Statistics and Markov Chain Monte Carlo Techniques

1064 This thesis presents a Bayesian oscillation analysis. To extract the oscillation  
1065 parameters, a Markov Chain Monte Carlo (MCMC) method is used. This chapter  
1066 explains the theory of how parameter estimates can be determined using this  
1067 technique and condenses the material found in the literature [130–133].

1068 The oscillation parameter determination presented here is built upon a si-  
1069 multaneous fit to neutrino beam data in the near detector, beam data at SK, and  
1070 atmospheric data at SK. In total, there are four oscillation parameters of interest  
1071 ( $\sin^2(\theta_{23})$ ,  $\sin^2(\theta_{13})$ ,  $\Delta m_{32}^2$ , and  $\delta_{CP}$ ), two oscillation parameters to which this  
1072 study will not be sensitive ( $\sin^2(\theta_{12})$ ,  $\Delta m_{21}^2$ ) and many nuisance parameters that  
1073 control the systematic uncertainty models.

1074 This analysis uses a Monte Carlo technique to generate a multi-dimensional  
1075 probability distribution across all of the model parameters used in the fit. To  
1076 determine an estimate for each parameter, this multi-dimensional object is in-  
1077 tegrated over all other parameters. This process is called Marginalisation and  
1078 is described in subsection 4.3.1. Monte Carlo techniques approximate the prob-  
1079 ability distribution of each parameter within the limit of generating infinite  
1080 samples. As ever, generating a large number of samples is time and resource-

1081 dependent. Therefore, an MCMC technique is utilised within this analysis to  
1082 reduce the required number of steps to sufficiently sample the parameter space.  
1083 This technique is described in further detail in subsection 4.2.1.

1084 The Bayesian analysis techniques used within this thesis are built within the  
1085 MaCh3 framework [134]. This uses a custom MCMC library package exclusively  
1086 supported and developed by the MaCh3 collaborators (which includes the author  
1087 of this thesis).

1088 **4.1 Bayesian Statistics**

1089 Bayesian inference treats observable data,  $D$ , and model parameters,  $\vec{\theta}$ , on equal  
1090 footing such that a probability model of both data and parameters is required.  
1091 This is the joint probability distribution  $P(D, \vec{\theta})$  and can be described by the  
1092 prior distribution for model parameters  $P(\vec{\theta})$  and the likelihood of the data given  
1093 the model parameters  $P(D|\vec{\theta})$ ,

$$P(D, \vec{\theta}) = P(D|\vec{\theta})P(\vec{\theta}). \quad (4.1)$$

1094 The prior distribution,  $P(\vec{\theta})$ , describes all previous knowledge about the  
1095 parameters within the model. For example, if the risk of developing health  
1096 problems is known to increase with age, the prior distribution would describe the  
1097 increase. For the purpose of this analysis, the prior distribution is typically  
1098 the best-fit values taken from external data measurements with a Gaussian  
1099 uncertainty. The prior distribution can also contain correlations between model  
1100 parameters. In an analysis using Monte Carlo techniques, the likelihood of  
1101 measuring some data assuming some set of model parameters is calculated  
1102 by comparing the Monte Carlo prediction generated at that particular set of  
1103 model parameters to the data.

1104 It is parameter estimation that is important for this analysis and as such, Bayes'  
1105 theorem [135] is applied to calculate the probability for each parameter to have a

1106 certain value given the observed data,  $P(\vec{\theta}|D)$ , which is known as the posterior  
1107 distribution (often termed the posterior). This can be expressed as

$$P(\vec{\theta}|D) = \frac{P(D|\vec{\theta})P(\vec{\theta})}{\int P(D|\vec{\theta})P(\vec{\theta})d\vec{\theta}}. \quad (4.2)$$

1108 The denominator in Equation 4.2 is the integral of the joint probability distri-  
1109 bution over all values of all parameters used within the fit. For brevity, the  
1110 posterior distribution is

$$P(\vec{\theta}|D) \propto P(D|\vec{\theta})P(\vec{\theta}). \quad (4.3)$$

1111 For the purposes of this analysis, it is acceptable to neglect the normalisation  
1112 term and focus on this proportional relationship.

### 1113 4.1.1 Application of Prior Knowledge

1114 The posterior distribution is proportional to the prior uncertainty applied to  
1115 each parameter, as illustrated by Equation 4.3. This means that it is possible  
1116 to change the prior after the posterior distribution has been determined. The  
1117 prior uncertainty of a particular parameter can be ‘divided’ out of the posterior  
1118 distribution and the resulting distribution can be reweighted using the new  
1119 prior uncertainty that is to be applied. The methodology and implementation  
1120 of changing the prior follows that described in [136].

1121 An example implementation that is useful for this analysis is the application  
1122 of the “reactor constraint”. As discussed in section 2.4, an external constraint  
1123 on  $\sin^2(\theta_{13})$  is determined from measurements taken from reactor experiments.  
1124 However, the sensitivities from just using the T2K and SK samples is equally  
1125 as important. Without this technique, two fits would have to be run, doubling  
1126 the required resources. Therefore, the key benefit for this analysis is the fact that  
1127 only a single ‘fit’ has to be performed and can be used to build the two posterior  
1128 distributions of the with and without reactor constraint applied.

## 1129 4.2 Monte Carlo Simulation

1130 Monte Carlo techniques are used to numerically solve a complex problem that  
1131 does not necessarily have an analytical solution. These techniques rely on  
1132 building a large ensemble of samples from an unknown distribution and then  
1133 using the ensemble to approximate the properties of the distribution.

1134 An example that uses Monte Carlo techniques is to calculate the area under-  
1135 neath a curve. For example, take the problem of calculating the area under a  
1136 straight line with gradient  $M = 0.4$  and intercept  $C = 1.0$ . Analytically, one can  
1137 calculate the area under the line is equal to 30 units for  $0 \leq x \leq 10$ . Using Monte  
1138 Carlo techniques, one can calculate the area under this line by throwing many  
1139 random values for the  $x$  and  $y$  components of each sample and then calculating  
1140 whether that point falls below the line. The area can then be calculated by the  
1141 ratio of points below the line to the total number of samples thrown multiplied by  
1142 the total area in which samples were scattered. The study is shown in Figure 4.1  
1143 highlights this technique and finds the area under the curve to be 29.9 compared  
1144 to an analytical solution of 30.0. The deviation of the numerical to analytical  
1145 solution can be attributed to the number of samples used in the study. The  
1146 accuracy of the approximation in which the properties of the Monte Carlo samples  
1147 replicate those of the desired distribution is dependent on the number of samples  
1148 used. Replicating this study with a differing number of Monte Carlo samples  
1149 used in each study (As shown in Figure 4.2) highlights how the Monte Carlo  
1150 techniques are only accurate within the limit of a high number of samples.

1151 Whilst the above example has an analytical solution, these techniques are just  
1152 as applicable to complex solutions. Clearly, any numerical solution is only as  
1153 useful as its efficiency. As discussed, the accuracy of the Monte Carlo technique is  
1154 dependent upon the number of samples generated to approximate the properties  
1155 of the distribution. Furthermore, if the positions at which the samples are  
1156 evaluated are not ‘cleverly’ picked, the efficiency of the Monte Carlo technique  
1157 significantly drops. Given the example in Figure 4.1, if the region in which the

1158 samples are scattered significantly extends passed the region of interest, many  
1159 calculations will be calculated but do not add to the ability of the Monte Carlo  
1160 technique to achieve the correct result. For instance, any sample evaluated at  
1161 a  $y \geq 5$  could be removed without affecting the final result. This does bring in  
1162 an aspect of the ‘chicken and egg’ problem in that to achieve efficient sampling,  
1163 one needs to know the distribution beforehand.

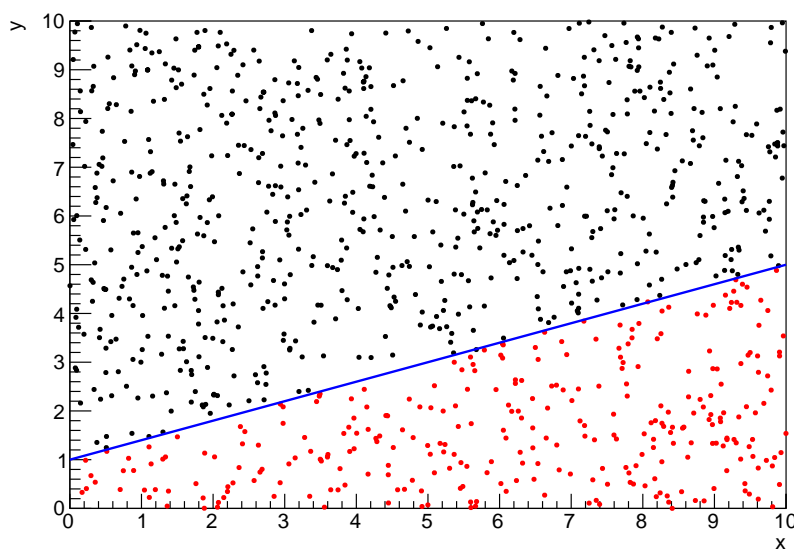


**Figure 4.1:** Example of using Monte Carlo techniques to find the area under the blue line. The gradient and intercept of the line are 0.4 and 1.0 respectively. The area found to be under the curve using one thousand samples is 29.9 units.

### 1164 4.2.1 Markov Chain Monte Carlo

1165 This analysis utilises a multi-dimensional probability distribution, with some  
1166 dimensions being significantly more constrained than others. These constraints  
1167 can be from prior knowledge of parameter distributions from external data or  
1168 un-physical regions in which parameters can not exist. To maximise the efficiency  
1169 of building the posterior distribution, a Markov Chain Monte Carlo (MCMC)  
1170 technique is used. This employs a Markov chain to select the points at which  
1171 to sample the posterior distribution. It performs a semi-random stochastic walk  
1172 through the allowable parameter space. This builds a posterior distribution

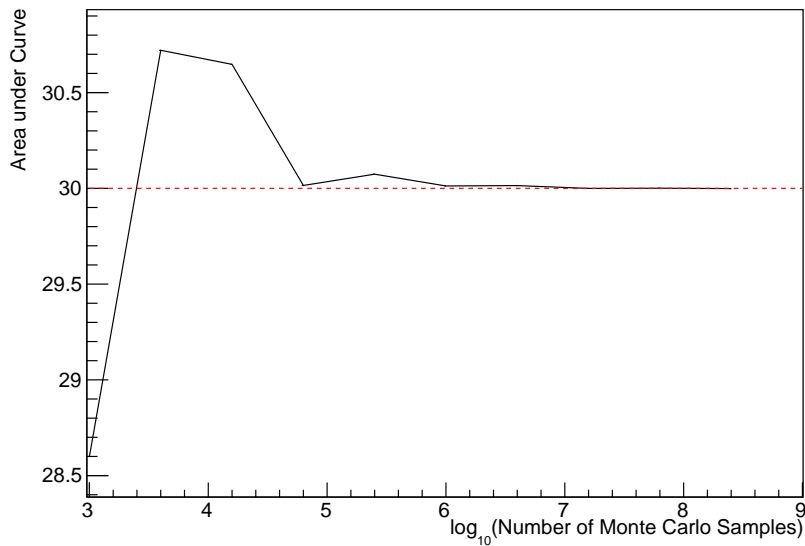


**Figure 4.2:** The area under a line of gradient 0.4 and intercept 1.0 for the range  $0 \leq x \leq 10$  as calculated using Monte Carlo techniques as a function of the number of samples used in each repetition. The analytical solution to the area is 30 units as given by the red line.

1173 which has the property that the density of sampled points is proportional to the  
 1174 probability density of that parameter. This means that the samples produced by  
 1175 this technique are not statistically independent but they will cover the space  
 1176 of the distribution.

1177 A Markov chain functions by selecting the position of step  $\vec{x}_{i+1}$  based on the  
 1178 position of  $\vec{x}_i$ . The space in which the Markov chain selects samples is dependent  
 1179 upon the total number of parameters utilised within the fit, where a discrete point  
 1180 in this space is described by the N-dimensional space  $\vec{x}$ . In a perfectly operating  
 1181 Markov chain, the position of the next step depends solely on the previous step  
 1182 and not on the further history of the chain ( $\vec{x}_0, \vec{x}_1$ , etc.). However, in solving  
 1183 the multi-dimensionality of the fit used within this analysis, each step becomes  
 1184 correlated with several of the steps preceding itself. Providing the MCMC chain is  
 1185 well optimised, it will begin to converge towards a unique stationary distribution.  
 1186 The period between the chain's initial starting point and the convergence to the  
 1187 unique stationary distribution is colloquially known as the burn-in period. Once  
 1188 the chain reaches the stationary distribution, all points sampled after that point

1189 will look like samples from that distribution.

1190 Further details of the theories underpinning MCMC techniques are discussed  
1191 in [131] but can be summarised by the requirement that the chain satisfies the  
1192 three ‘regularity conditions’:

- 1193 • Irreducibility: From every position in the parameter space  $\vec{x}$ , there must  
1194 exist a non-zero probability for every other position in the parameter space  
1195 to be reached.
- 1196 • Recurrence: Once the chain arrives at the stationary distribution, every step  
1197 following from that position must be samples from the same stationary  
1198 distribution.
- 1199 • Aperiodicity: The chain must not repeat the same sequence of steps at any  
1200 point throughout the sampling period.

1201 The output of the chain after burn-in (i.e. the sampled points after the chain  
1202 has reached the stationary distribution) can be used to approximate the posterior  
1203 distribution and model parameters  $\vec{\theta}$ . To achieve the requirement that the unique  
1204 stationary distribution found by the chain be the posterior distribution, one  
1205 can use the Metropolis-Hastings algorithm. This guides the stochastic process  
1206 depending on the likelihood of the current proposed step compared to that  
1207 of the previous step.

### 1208 4.2.2 Metropolis-Hastings Algorithm

1209 As a requirement for MCMCs, the Markov chain implemented in this technique  
1210 must have a unique stationary distribution that is equivalent to the posterior  
1211 distribution. To ensure this requirement and that the regularity conditions are  
1212 met, this analysis utilises the Metropolis-Hastings (MH) algorithm [137, 138].  
1213 For the  $i^{th}$  step in the chain, the MH algorithm determines the position in the  
1214 parameter space to which the chain moves to based on the current step,  $\vec{x}_i$ , and  
1215 the proposed step,  $\vec{y}_{i+1}$ . The proposed step is randomly selected from some

1216 proposal function  $f(\vec{x}_{i+1}|\vec{x}_i)$ , which depends solely on the current step (ie. not  
1217 the further history of the chain). The next step in the chain  $\vec{x}_{i+1}$  can be either the  
1218 current step or the proposed step determined by whether the proposed step is  
1219 accepted or rejected. To decide if the proposed step is selected, the acceptance  
1220 probability,  $\alpha(\vec{x}_i, \vec{y}_i)$ , is calculated as

$$\alpha(\vec{x}_i, \vec{y}_{i+1}) = \min\left(1, \frac{P(\vec{y}_{i+1}|D)f(\vec{x}_i|\vec{y}_{i+1})}{P(\vec{x}_i|D)f(\vec{y}_{i+1}|\vec{x}_i)}\right). \quad (4.4)$$

1221 Where  $P(\vec{y}_{i+1}|D)$  is the posterior distribution as introduced in section 4.1. To  
1222 simplify this calculation, the proposal function is required to be symmetric such  
1223 that  $f(\vec{x}_i|\vec{y}_{i+1}) = f(\vec{y}_{i+1}|\vec{x}_i)$ . In practice, a multi-variate Gaussian distribution  
1224 centered on  $\vec{x}_i$  is used to throw parameter proposals. This reduces Equation 4.4 to

$$\alpha(\vec{x}_i, \vec{y}_{i+1}) = \min\left(1, \frac{P(\vec{y}_{i+1}|D)}{P(\vec{x}_i|D)}\right). \quad (4.5)$$

1225 DB: Figure out what Giles means

1226 After calculating this quantity, a random number,  $\beta$ , is generated uniformly  
1227 between 0 and 1. If  $\beta \leq \alpha(\vec{x}_i, \vec{y}_{i+1})$ , the proposed step is accepted. Otherwise,  
1228 the chain sets the next step equal to the current step. This procedure is repeated  
1229 for subsequent steps. This can be interpreted as if the posterior probability  
1230 of the proposed step is greater than that of the current step, ( $P(\vec{y}_{i+1}|D) \geq$   
1231  $P(\vec{x}_i|D)$ ), the proposed step will always be accepted. If the opposite is true,  
1232 ( $P(\vec{y}_{i+1}|D) \leq P(\vec{x}_i|D)$ ), the proposed step will be accepted with probability  
1233  $P(\vec{x}_i|D)/P(\vec{y}_{i+1}|D)$ . This ensures that the Markov chain does not get trapped  
1234 in any local minima in the potentially non-Gaussian posterior distribution. The  
1235 outcome of this technique is that the density of steps taken in a discrete region  
1236 is directly proportional to the probability density in that region.

### 1237 4.2.3 MCMC Optimisation

1238 As discussed in subsection 4.2.2, the proposal function invoked within the MH  
1239 algorithm can take any form and the chain will still converge to the stationary  
1240 distribution. At each set of proposed parameter values, a prediction of the same

1241 spectra has to be generated which requires significant computational resources.  
1242 Therefore, the number of steps taken before the unique stationary distribution  
1243 is found should be minimised as only steps after convergence add information  
1244 to the oscillation analysis. Furthermore, the chain should entirely cover the  
1245 allowable parameter space to ensure that all values have been considered. Tuning  
1246 the distance that the proposal function jumps between steps on a parameter-by-  
1247 parameter basis can both minimise the length of the burn-in period and ensure  
1248 that the correlation between step  $\vec{x}_i$  and  $\vec{x}_j$  is sufficiently small.

1249 The effect of changing the width of the proposal function is highlighted in  
1250 Figure 4.3. Three scenarios, each with the same underlying stationary distribution  
1251 (A Gaussian of width 1.0 and mean 0.), are presented. The only difference between  
1252 the three scenarios is the width of the proposal function, colloquially known as  
1253 the ‘step size  $\sigma$ ’. Each scenario starts at an initial parameter value of 10.0 which  
1254 would be considered an extreme variation. For the case where  $\sigma = 0.1$ , it is  
1255 clear to see that the chain takes a long time to reach the expected region of the  
1256 parameter. This indicates that this chain would have a large burn-in period and  
1257 does not converge to the stationary distribution until step  $\sim 500$ . Furthermore,  
1258 whilst the chain does move towards the expected region, each step is significantly  
1259 correlated with the previous. Considering the case where  $\sigma = 5.0$ , the chain  
1260 approaches the expected parameter region almost instantly meaning that the  
1261 burn-in period is not significant. However, there are clearly large regions of steps  
1262 where the chain does not move. This is likely due to the chain proposing steps  
1263 in the tails of the distribution which have a low probability of being accepted.  
1264 Consequently, this chain would take a significant number of steps to fully span  
1265 the allowable parameter region. For the final scenario, where  $\sigma = 0.5$ , you can  
1266 see a relatively small burn-in period of approximately 100 steps. Once the chain  
1267 reaches the stationary distribution, it moves throughout the expected region of  
1268 parameter values many times, sufficiently sampling the full parameter region.  
1269 This example is a single parameter varying across a continuous distribution and  
1270 does not fully reflect the difficulties in the many-hundred multi-variate parameter

1271 distribution used within this analysis. However, it does give a conceptual idea of  
1272 the importance of selecting the proposal function and associated step size.



**Figure 4.3:** Three MCMC chains, each with a stationary distribution equal to a Gaussian centered at 0 and width 1 (As indicated by the black dotted lines). All of the chains use a Gaussian proposal function but have different widths (or ‘step size  $\sigma$ ’). The top panel has  $\sigma = 0.1$ , middle panel has  $\sigma = 0.5$  and the bottom panel has  $\sigma = 5.0$ .

1273 As discussed, step size tuning directly correlates to the average step accep-  
1274 tance rate. If the step size is too small, many steps will be accepted but the  
1275 chain moves slowly. If the opposite is true, many steps will be rejected as the  
1276 chain proposes steps in the tails of the distribution. Discussion in [139] suggests  
1277 that the ‘ideal’ acceptance rate of a high dimension MCMC chain should be

<sub>1278</sub> approximately  $\sim 25\%$ . An “ideal” step size [139] of

$$\sigma = \frac{2.4}{N_p}, \quad (4.6)$$

<sub>1279</sub> where  $N_p$  is the number of parameters included in the MCMC fit. However,  
<sub>1280</sub> the complex correlations between systematics mean that some parameters have  
<sub>1281</sub> to be hand-tuned and many efforts have been taken to select a set of parameter-  
<sub>1282</sub> by-parameter step sizes to approximately reach the ideal acceptance rate.

<sub>1283</sub> Figure 4.4 highlights the likelihood as calculated by the fit in subsection 8.2.4  
<sub>1284</sub> as a function of the number of steps in each chain. In practice, many independent  
<sub>1285</sub> MCMC chains are run simultaneously to parallelise the task of performing the  
<sub>1286</sub> fit. This figure overlays the distribution found in each chain. As seen, the  
<sub>1287</sub> likelihood decreases from its initial value and converges towards a stationary  
<sub>1288</sub> distribution after  $\sim 1 \times 10^5$  steps.

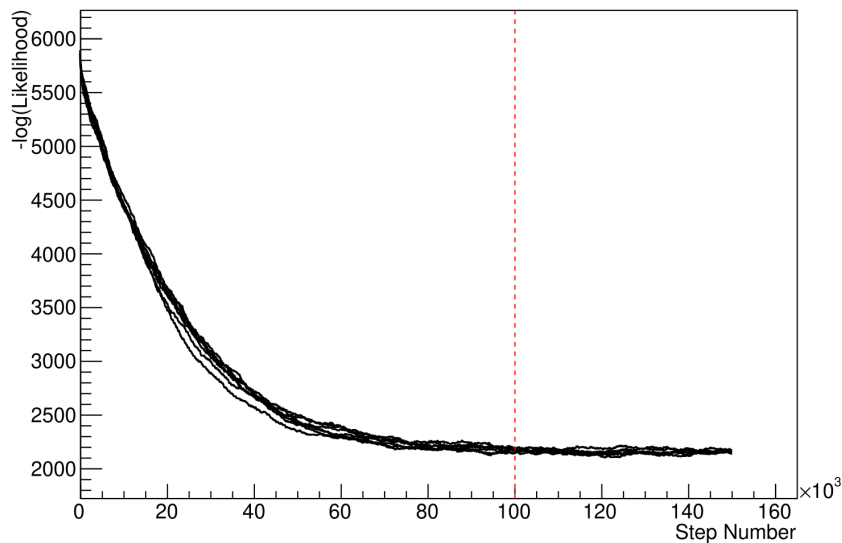


**Figure 4.4:** The log-likelihood from the fit detailed in subsection 8.2.4 as a function of the number of steps accumulated in each fit. Many independent MCMC chains were run in parallel and overlaid on this plot. The red line indicates the  $1 \times 10^5$  step burn-in period after which the log-likelihood becomes stable.

<sub>1289</sub> Multiple configurations of this analysis have been performed throughout this  
<sub>1290</sub> thesis where different samples or systematics have been used. For all of these con-  
<sub>1291</sub> figurations, it was found that a burnin period of  $1 \times 10^5$  was sufficient in all cases.

## 1292 4.3 Understanding the MCMC Results

1293 The previous sections have described how to generate the posterior probability  
1294 distribution using Bayesian MCMC techniques. However, this analysis focuses  
1295 on oscillation parameter determination. The posterior distribution output from  
1296 the chain is a high-dimension object, with as many dimensions as there are  
1297 parameters included in the oscillation analysis. However, this multi-dimensional  
1298 object is difficult to conceptualize so parameter estimations are often presented  
1299 in one or two-dimensional projections of this probability distribution. To do  
1300 this, marginalisation techniques are invoked.

### 1301 4.3.1 Marginalisation

1302 The output of the MCMC chain is a highly dimensional probability distribution  
1303 which is very difficult to interpret. From the standpoint of an oscillation analysis  
1304 experiment, the one or two-dimensional ‘projections’ of the oscillation parameters  
1305 of interest are most relevant. Despite this, the best fit values and uncertainties on  
1306 the oscillation parameters of interest should correctly encapsulate the correlations  
1307 to the other systematic uncertainties (colloquially called ‘nuisance’ parameters).  
1308 For this joint beam and atmospheric analysis, the oscillation parameters of  
1309 interest are  $\sin^2(\theta_{23})$ ,  $\sin^2(\theta_{13})$ ,  $\Delta m_{32}^2$ , and  $\delta_{CP}$ . All other parameters (includ-  
1310 ing the oscillation parameters this fit is insensitive to) are deemed nuisance  
1311 parameters. To generate these projections, the posterior distribution is integrated  
1312 over all nuisance parameters. This is called marginalisation. This technique  
1313 also explains why it is acceptable to neglect the normalisation constant of the  
1314 posterior distribution, which was discussed in section 4.1.

1315 A simple example of the marginalisation technique is to imagine the scenario  
1316 where two coins are flipped. To determine the probability that the first coin  
1317 returned a ‘head’, the exact result of the second coin flip is disregarded and  
1318 simply integrated over. For the parameters of interest,  $\vec{\theta}_i$ , the marginalised

1319 posterior is calculated by integrating over the nuisance parameters,  $\vec{\theta}_n$ . In this  
1320 case, Equation 4.2 becomes

$$P(\vec{\theta}_i|D) = \frac{\int P(D|\vec{\theta}_i, \vec{\theta}_n)P(\vec{\theta}_i, \vec{\theta}_n)d\vec{\theta}_n}{\int P(D|\vec{\theta})P(\vec{\theta})d\vec{\theta}}. \quad (4.7)$$

1321 Where  $P(\vec{\theta}_i, \vec{\theta}_n)$  encodes the prior knowledge about the uncertainty and  
1322 correlations between the parameters of interest and the nuisance parameters.  
1323 In practice, this is simply taking the one or two-dimensional projection of the  
1324 multi-dimensional probability distribution.

1325 While in principle an easy solution to a complex problem, correlations be-  
1326 tween the interesting and nuisance parameters can bias the marginalised results.  
1327 A similar effect is found when the parameters being marginalised over have  
1328 non-Gaussian probability distributions. For example, Figure 4.5 highlights the  
1329 marginalisation bias in the probability distribution found for a parameter when  
1330 requiring a correlated parameter to have a positive parameter value. Due to  
1331 the complex nature of the oscillation parameter fit presented in this thesis, there  
1332 are correlations occurring between the oscillation parameters of interest and the  
1333 other nuisance parameters included in the fit.



**Figure 4.5:** Left: The two-dimensional probability distribution for two correlated parameters  $x$  and  $y$ . The red distribution shows the two-dimensional probability distribution when  $0 \leq x \leq 5$ . Right: The marginalised probability distribution for the  $y$  parameter found when requiring the  $x$  to be bound between  $-5 \leq x \leq 5$  and  $0 \leq x \leq 5$  for the black and red distribution, respectively.

### **4.3.2 Parameter Estimation and Credible Intervals**

The purpose of this analysis is to determine the best fit values for the oscillation parameters that the beam and atmospheric samples are sensitive to:  $\sin^2(\theta_{23})$ ,  $\sin^2(\theta_{13})$ ,  $\Delta m_{32}^2$ , and  $\delta_{CP}$ . The posterior probability density, taken from the output MCMC chain, is binned in these parameters. The parameter best-fit point is then taken to be the value that has the highest posterior probability. This is performed in both one and two-dimensional projections.

However, the single best-fit point in a given parameter is not of much use on its own. The uncertainty on the best-fit point must also be presented using credible intervals. The definition of the  $1\sigma$  credible interval is that there is 68% belief that the parameter is within those bounds. For a more generalised definition, the credible interval is the region,  $R$ , of the posterior distribution that contains a specific fraction of the total probability, such that

$$\int_R P(\theta|D)d\theta = \alpha. \quad (4.8)$$

Where  $\theta$  is the parameter being evaluated. This technique then calculates the  $\alpha \times 100\%$  credible interval.

In practice, this analysis uses the highest posterior density (HPD) credible intervals which are calculated through the following method. First, the probability distribution is area-normalised such that it has an integrated area equal to 1.0. The bins of probability are then summed from the highest to lowest until the sum exceeds the  $1\sigma$  level (0.68 in this example). This process is repeated for a range of credible intervals, notably the  $1\sigma$ ,  $2\sigma$  and  $3\sigma$  along with other levels where the critical values for each level can be found in [76]. This process can be repeated for the two-dimensional probability distributions by creating two-dimensional contours of credible intervals rather than a one-dimensional result.

### 1358 4.3.3 Bayesian Model Comparisons

1359 Due to the matter resonance, this analysis has some sensitivity to the mass  
 1360 hierarchy of neutrino states (whether  $\Delta m_{32}^2$  is positive or negative) and the  
 1361 octant of  $\sin^2(\theta_{23})$ . The Bayesian approach utilised within this analysis gives an  
 1362 intuitive method of model comparison by determining which hypothesis is most  
 1363 favourable. Taking the ratio of Equation 4.3 for the two hypotheses of normal  
 1364 hierarchy,  $NH$ , and inverted hierarchy,  $IH$ , gives

$$\frac{P(\vec{\theta}_{NH}|D)}{P(\vec{\theta}_{IH}|D)} = \frac{P(D|\vec{\theta}_{NH})}{P(D|\vec{\theta}_{IH})} \times \frac{P(\vec{\theta}_{NH})}{P(\vec{\theta}_{IH})}. \quad (4.9)$$

1365 The middle term defines the Bayes factor,  $B(NH/IH)$ , which is a data-driven  
 1366 interpretation of how strong the data prefers one hierarchy to the other. For this  
 1367 analysis, equal priors on both mass hierarchy hypotheses are chosen ( $P(\vec{\theta}_{NH}) =$   
 1368  $P(\vec{\theta}_{IH}) = 0.5$ ). In practice, the MCMC chain proposes a value of  $|\Delta m_{32}^2|$  and  
 1369 then applies a 50% probability that the value is sign flipped. Consequently,  
 1370 the Bayes factor can be calculated from the ratio of the probability density in  
 1371 either hypothesis. This equates to counting the number of steps taken in the  
 1372 normal and inverted hierarchies and taking the ratio. The same approach can be  
 1373 taken to compare the upper octant (UO) compared to the lower octant (LO)  
 1374 hypothesis of  $\sin^2(\theta_{23})$ .

$\log_{10}(B_{AB})$	$B_{AB}$	Strength of Preference
< 0.0	< 1	No preference for hypothesis A (Supports hypothesis B)
0.0 – 0.5	1.0 – 3.16	Preference for hypothesis A is weak
0.5 – 1.0	3.16 – 10.0	Preference for hypothesis A is substantial
1.0 – 1.5	10.0 – 31.6	Preference for hypothesis A is strong
1.5 – 2.0	31.6 – 100.0	Preference for hypothesis A is very strong
> 2.0	> 100.0	Decisive preference for hypothesis A

**Table 4.1:** Jeffreys scale for strength of preference for two models  $A$  and  $B$  as a function of the calculated Bayes factor ( $B_{AB} = B(A/B)$ ) between the two models [140]. The original scale is given in terms of  $\log_{10}(B(A/B))$  but converted to linear scale for easy comparison throughout this thesis.

1375 Whilst the value of the Bayes factor should always be shown, the Jeffreys scale  
 1376 [140] (highlighted in Table 4.1) gives an indication of the strength of preference

1377 for one model compared to the other. Other interpretations of the strength of  
1378 preference of a model exist, e.g. the Kass and Raferty Scale [141].

#### 1379 4.3.4 Comparison of MCMC Output to Expectation

1380 To ensure the fit is performing well, a best-fit spectrum is produced using the  
1381 posterior probability distribution and compared with the data, allowing easy  
1382 by-eye comparisons to be made. A simple method of doing this is to perform a  
1383 comparison in the fitting parameters (For instance, the reconstructed neutrino  
1384 energy and lepton direction for T2K far detector beam samples) of the spectra  
1385 generated by the MCMC chain to ‘data’. This ‘data’ could be true data or some  
1386 variation of Monte Carlo prediction. This allows easy comparison of the MCMC  
1387 probability distribution to the data. To perform this,  $N$  steps from the post-burnin  
1388 MCMC chain are randomly selected. From these, the Monte Carlo prediction  
1389 at each step is generated by reweighting the model parameters to the values  
1390 specified at that step. Due to the probability density being directly correlated  
1391 with the density of steps in a certain region, parameter values close to the best  
1392 fit value are most likely to be selected.

1393 In practice, for each bin of the fitting parameters has a probability distribution  
1394 of event rates, with one entry per sampled MCMC step. This distribution is  
1395 binned where the bin with the highest probability is selected as the mean and an  
1396 error on the width of this probability distribution is calculated using the approach  
1397 highlighted in subsection 4.3.2. Consequently, the best fit distribution in the fit  
1398 parameter is not necessarily that which would be attained by reweighting the  
1399 Monte Carlo prediction to the most probable parameter values.

1400 A similar study can be performed to illustrate the freedom of the model  
1401 parameter space prior to the fit. This can be done by throwing parameter values  
1402 from the prior uncertainty of each parameter.

# 5

1403

1404

1405

## Simulation, Reconstruction, and Event Reduction

1406 As a crucial part of the oscillation analysis, an accurate prediction of the expected  
1407 neutrino spectrum at the far detector is required. This includes modeling the  
1408 flux generation, neutrino interactions, and detector effects. All of the simulation  
1409 packages required to do this are briefly described in section 5.1. The reconstruc-  
1410 tion of neutrino events in the far detector, including the `fitQun` algorithm, is  
1411 documented in section 5.2. This also includes data quality checks of the SK-V  
1412 data which the author performed for the T2K oscillation analysis presented at the  
1413 Neutrino 2020 conference [75]. Finally, section 5.3 describes the steps taken in the  
1414 SK detector to trigger on events of interest whilst removing the comparatively  
1415 large rate of cosmic ray muon events.

### 1416 5.1 Simulation

1417 In order to generate a Monte Carlo prediction of the expected event rate at  
1418 the far detector, all the processes in the beam and atmospheric fluxes, neutrino  
1419 interaction, and detector need to be modeled.

### 1420 5.1.1 Neutrino Flux

1421 The beamline simulation consists of three distinct parts: the initial hadron  
 1422 interaction modeled by FLUKA [142], the target station geometry and particle  
 1423 tracking performed by JNUBEAM, [143, 144] and any hadronic re-interactions  
 1424 simulated by GCALOR [145]. The primary hadronic interactions are  $O(10)\text{GeV}$ ,  
 1425 where FLUKA matches external cross-section data better than GCALOR [146].  
 1426 However, FLUKA is not very adaptable so a small simulation is built to model  
 1427 the interactions in the target and the output is then passed to JNUBEAM and  
 1428 GCALOR for propagation. The hadronic interactions are tuned to data from the  
 1429 NA61/SHINE [147–149] and HARP [150] experiments. The tuning is done by  
 1430 reweighting the FLUKA and GCALOR predictions to match the external data  
 1431 multiplicity and cross-section measurements, based on final state particle kine-  
 1432 matics [146]. The culmination of this simulation package generates the predicted  
 1433 flux for neutrino and antineutrino beam modes which are illustrated in Figure 3.7.

1434 The atmospheric neutrino flux is simulated by the HKKM model [51, 53]. The  
 1435 primary cosmic ray flux is tuned to AMS [151] and BESS [152] data assuming  
 1436 the US-standard atmosphere '76 [153] density profile and includes geomagnetic  
 1437 field effects. The primary cosmic rays interact to generate pions and muons.  
 1438 The interaction of these secondary particles to generate neutrinos is handled by  
 1439 DPMJET-III [154] for energies above 32GeV and JAM [53, 155] for energies below  
 1440 that value [49]. These hadronic interactions are tuned to BESS and L3 data [156,  
 1441 157] using the same methodology as the tuning of the beamline simulation. The  
 1442 energy and cosine zenith predictions of  $\nu_e, \bar{\nu}_e, \nu_\mu, \bar{\nu}_\mu$  flux are given in Figure 2.3  
 1443 and Figure 2.5, respectively. The flux is approximately symmetrical and peaked  
 1444 around the horizon ( $\cos(\theta_Z) = 0.0$ ). This is because horizontally-going pions  
 1445 and kaons can travel further than their vertically-going counterparts resulting  
 1446 in a larger probability of decaying to neutrinos. The symmetry is broken in  
 1447 lower-energy neutrinos due to geomagnetic effects, which modify the track of the  
 1448 primary cosmic rays. Updates to the HKKM model are currently ongoing [158].

### **5.1.2 Neutrino Interaction**

Once a flux prediction has been made for all three detectors, NEUT 5.4.0 [159, 160] models the interactions of the neutrinos in the detectors. For the purposes of this analysis, quasi-elastic (QE), meson exchange (MEC), single meson production (PROD), coherent pion production (COH), and deep inelastic scattering (DIS) interactions are simulated. These interaction categories can be further broken down by whether they were propagated via a  $W^\pm$  boson in Charged Current (CC) interactions or via a  $Z^0$  boson in Neutral Current (NC) interactions. CC interactions have a charged lepton in the final state, which can be flavour-tagged in reconstruction to determine the flavour of the neutrino. In contrast, NC interactions have a neutrino in the final state so no flavour information can be determined from the observables left in the detector after an interaction. This is the reason why neutrinos that interact through NC modes are assumed to not oscillate within this analysis. Both CC and NC interactions are modeled for all the above interaction categories, other than MEC interactions which are only modeled for CC events.

As illustrated in Figure 5.1, CCQE interactions dominate the cross-section of neutrino interactions around  $E_\nu \sim 0.5\text{GeV}$ . The NEUT implementation adopts the Llewellyn Smith [161] model for neutrino-nucleus interactions, where the nuclear ground state of any bound nucleons (neutrino-oxygen interactions) is approximated by a spectral-function [162] model that simulates the effects of Fermi momentum and Pauli blocking. The cross-section of QE interactions is controlled by vector and axial-vector form factors parameterised by the BBBA05 [163] model and a dipole form factor with  $M_A^{QE} = 1.21\text{GeV}$  fit to external data [164], respectively. NEUT implements the Valencia [165] model to simulate MEC events, where two nucleons and two holes in the nuclear target are produced (often called 2p2h interactions).

For neutrinos of energy  $O(1)\text{GeV}$ , PROD interactions become dominant. These predominantly produce charged and neutral pions although  $\gamma$ , kaon,



**Figure 5.1:** The NEUT prediction of the  $\nu_\mu$ -H<sub>2</sub>O cross-section overlaid on the T2K  $\nu_\mu$  flux. The charged current (black, solid) and neutral current (black, dashed) inclusive, charged current quasi-elastic (blue, solid), charged current 2p2h (blue, dashed), charged current single pion production (pink), and charged current multi- $\pi$  and DIS (Purple) cross-sections are illustrated. Figure taken from [159].

and  $\eta$  production is also considered. To simulate these interactions, the Berger-Sehgal [166] model is implemented within NEUT. It simulates the excitation of a nucleon from a neutrino interaction, production of an intermediate baryon, and the subsequent decay to a single meson or  $\gamma$ . Pions can also be produced through COH interactions, which occur when the incoming neutrino interacts with the entire oxygen nucleus leaving a single pion outside of the nucleus. NEUT utilises the Berger-Sehgal [167] model to simulate these COH interactions.

DIS and multi- $\pi$  producing interactions become the most dominant for energies  $> O(5)\text{GeV}$ . PYTHIA [168] is used to simulate any interaction with invariant mass  $W > 2\text{GeV}/c^2$ , which produces at least one meson. For any interaction which produces at least two mesons but has  $W < 2\text{GeV}/c^2$ , the

<sup>1489</sup> Bronner model is used [169]. Both of these models use Parton distribution  
<sup>1490</sup> functions based on the Bodek-Yang model [170–172].

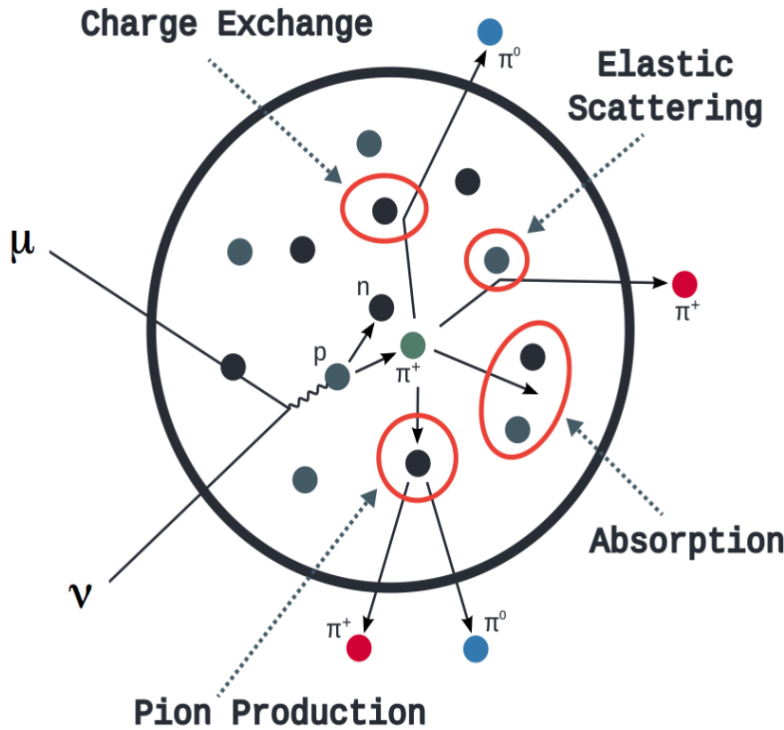


**Figure 5.2:** Illustration of the various processes which a pion can undergo before exiting the nucleus. Taken from [173].

<sup>1491</sup> Any pion that is produced within the nucleus can re-interact through final  
<sup>1492</sup> state interactions before it exits, as illustrated by the scattering, absorption,  
<sup>1493</sup> production, and exchange interactions in Figure 5.2. These re-interactions alter  
<sup>1494</sup> the observable particles within the detector. For instance, if the charged pion  
<sup>1495</sup> from a CC PROD interaction is absorbed, the observables would mimic a CC QE  
<sup>1496</sup> interaction. To simulate these effects, NEUT uses a semi-classical intranuclear  
<sup>1497</sup> cascade model [159]. This cascade functions by stepping the pion through the  
<sup>1498</sup> nucleus in fixed-length steps equivalent to  $dx = R_N/100$ , where  $R_N$  is the radius  
<sup>1499</sup> of the nucleus. At each step, the simulation allows the pion to interact through  
<sup>1500</sup> scattering, charged exchange, absorption, or production with an interaction-  
<sup>1501</sup> dependent probability calculated from a fit to external data [174]. This cascade  
<sup>1502</sup> continues until the pion is absorbed or exits the nucleus.

**5.1.3 Detector**

Once the final state particle kinematics have been determined by NEUT, they are passed into the detector simulation. The near detectors, ND280 and INGRID, are simulated using a GEANT4 package [43, 175] to simulate the detector geometry, particle tracking, and energy deposition. The response of the detectors is simulated using the elecSim package [43].

The far detector simulation is based upon the original Kamiokande experiment software which uses the GEANT3-based SKDETSIM [43, 176] package. This simulates the interactions of particles in the water as well as Cherenkov light production. The water quality and PMT calibration measurements detailed in subsection 3.1.2 are also used within this simulation to make accurate predictions of the detector response.

Any event which generates optical photons that occurs in SK will be observed by the PMT array, where each PMT records the time and accumulated charge. This recorded information is shown in event displays similar to those illustrated in Figure 5.3 for simulated Monte Carlo events. To be useful for physics analyses, this series of PMT hit information needs to be reconstructed to determine the number and identity of particles and their kinematics (or track parameters): four-vertex, direction, and momentum. The reconstruction uses the fact that the charge and timing distribution of photons generated by a particular particle in an event is dependent upon its initial kinematics. Electron and muon rings are distinguished by their “fuzziness”. Muons are heavier and less affected by scattering or showering meaning they typically produce “crisp” rings. Electrons are more likely to interact via electromagnetic showering or scattering which results in larger variations of their direction from the initial direction. Consequently, electrons typically produce “fuzzier” rings compared to muons.



**Figure 5.3:** Event displays from Monte Carlo simulation at Super Kamiokande illustrating the “crisp” ring from a muon and the typically “fuzzy” electron ring. Each pixel represents a PMT and the color scheme denotes the accumulated charge deposited on that PMT. Figures taken from [177].

## 5.2 Event Reconstruction at SK

For the purposes of this analysis, the `fitQun` reconstruction algorithm [178] is utilised. Its core function is to compare a prediction of the accumulated charged and timing distribution from each PMT, generated for a particular particle identity and track parameters, to that observed in the neutrino event. It determines the preferred values by maximising a likelihood function (or minimising a log-likelihood function) which includes information from PMTs which were hit and those that were not hit. The `fitQun` algorithm is based on the key concepts of the MiniBooNE reconstruction algorithm [179].

The `fitQun` algorithm improves upon the previous `APFit` algorithm [180] which has been used for many previous SK analyses. `APFit` fits the vertex from timing information and then fits the direction of the particle from PMT hits within a 43 deg Cherenkov cone (assuming an ultra-relativistic particle) using a fitting estimator. A Hough transformation is used to find the radius of a ring (related to the momentum through Equation 3.2) as well as the number of rings contained within the event. The analysis presented here uses the `fitQun` algorithm as it improves both the accuracy of the fit parameters and the rejection of neutral

1546 current  $\pi^0$  events as compared to APFit [181, 182].

1547 Any event in SK can consist of prompt (or primary) and decay (or secondary)  
1548 particles. For example, a charged current muon neutrino interaction can gen-  
1549 erate two particles that have the potential of generating Cherenkov photons  
1550 (assuming the proton is below the Cherenkov threshold): the prompt muon,  
1551 and the secondary decay-electron from the muon, approximately  $2\mu\text{s}$  later. To  
1552 reconstruct all particles within an event, it is divided into time clusters which are  
1553 called “subevents”. Subevents after the primary subevent are considered to  
1554 be decay electrons.

1555 The main steps of the `fitQun` reconstruction algorithm are:

- 1556 • **Vertex pre-fitting:** An estimate of the vertex is made using a goodness-of-fit  
1557 metric based on PMT hit times
- 1558 • **Peak finding:** The initial time of each subevent is determined by clustering  
1559 events by time residuals
- 1560 • **Single-ring fits:** Given the pre-fit vertex and estimated time of interaction,  
1561 a maximum likelihood technique searches for a single particle generating  
1562 light. Electron, muon, charged pion, and proton hypotheses are considered
- 1563 • **Multi-ring fits:** Seeded from the single-ring fits, hypotheses with multiple  
1564 light-producing particles are considered using the same maximum likeli-  
1565 hood technique. Electron-like or charged pion-like rings are added until  
1566 the likelihood stops improving

1567 To find all the subevents in an event, a vertex goodness metric is calculated  
1568 for some vertex position  $\vec{x}$  and time  $t$ ,

$$G(\vec{x}, t) = \sum_i^{\text{hit PMTs}} \exp \left( -\frac{1}{2} \left( \frac{T_{Res}^i(\vec{x}, t)}{\sigma} \right)^2 \right), \quad (5.1)$$

1569 where

$$T_{Res}^i(\vec{x}, t) = t^i - t - |R_{PMT}^i - \vec{x}| / c_n, \quad (5.2)$$

1570 is the residual hit time. It is the difference in time between the PMT hit time  
 1571  $t^i$ , of the  $i^{th}$  PMT, and the expected time of the PMT hit if the photon was at  
 1572 the vertex.  $R_{PMT}^i$  is the position of the  $i^{th}$  PMT,  $c_n$  is the speed of light in water  
 1573 and  $\sigma = 4\text{ns}$  which is comparable to the time resolution of the PMT. When the  
 1574 proposed fit values of time and vertex are close to the true values,  $T_{Res}^i(\vec{x}, t)$  tends  
 1575 to zero resulting in subevents appearing as spikes in the goodness metric. The  
 1576 proposed fit vertex and time are grid-scanned, and the values which maximise  
 1577 the goodness metric are selected as the “pre-fit vertex”. Whilst this predicts a  
 1578 vertex for use in the clustering algorithm, the final vertex is fit using the higher-  
 1579 precision maximum likelihood method described below.

1580 Once the pre-fit vertex has been determined, the goodness metric is scanned as  
 1581 a function of  $t$  to determine the number of subevents. A peak-finding algorithm  
 1582 is then used on the goodness metric, requiring the goodness metric to exceed  
 1583 some threshold and drop below a reduced threshold before any subsequent  
 1584 additional peaks are considered. The thresholds are set such that the rate of  
 1585 false peak finding is minimised while still attaining good data to Monte Carlo  
 1586 agreement. To improve performance, the pre-fit vertex for each delayed subevent  
 1587 is re-calculated after PMT hits from the previous subevent are masked. This  
 1588 improves the decay-electron tagging performance. Once all subevents have  
 1589 been determined, the time window around each subevent is then defined by the  
 1590 earliest and latest time which satisfies  $-180 < T_{Res}^i < 800\text{ns}$ . The subevents and  
 1591 associated time windows are then used as seeds for further reconstruction.

1592 For a given subevent, the `fitQun` algorithm constructs a likelihood based on  
 1593 the accumulated charge  $q_i$  and time information  $t_i$  from the  $i^{th}$  PMT,

$$L(\Gamma, \vec{\theta}) = \prod_j^{\text{unhit}} P_j(\text{unhit}|\Gamma, \vec{\theta}) \prod_i^{\text{hit}} \{1 - P_i(\text{unhit}|\Gamma, \vec{\theta})\} f_q(q_i|\Gamma, \vec{\theta}) f_t(t_i|\Gamma, \vec{\theta}). \quad (5.3)$$

1594 Where  $\vec{\theta}$  defines the track parameters; vertex position, direction vector and  
 1595 momenta, and  $\Gamma$  represents the particle hypothesis.  $P_i(\text{unhit}|\Gamma, \vec{\theta})$  is the proba-  
 1596 bility of the  $i^{\text{th}}$  tube to not register a hit given the track parameters and particle  
 1597 hypothesis. The charge likelihood,  $f_q(q_i|\Gamma, \vec{\theta})$ , and time likelihood,  $f_t(t_i|\Gamma, \vec{\theta})$ ,  
 1598 represents the probability density function of observing charge  $q_i$  and time  $t_i$  on  
 1599 the  $i^{\text{th}}$  PMT given the specified track parameters and particle hypothesis.

1600 The predicted charge is calculated based on contributions from both the  
 1601 direct light and the scattered light. The direct light contribution is determined  
 1602 based on the integration of the Cherenkov photon profile along the track. PMT  
 1603 angular acceptance, water quality, and calibration measurements discussed in  
 1604 subsection 3.1.2 are included to accurately predict the charge probability density  
 1605 at each PMT. The scattered and reflected light is calculated in a similar way,  
 1606 although it includes a scattering function that depends on the vertex of the  
 1607 particle and the position of the PMT. The charge likelihood is calculated by  
 1608 comparing the prediction to the observed charge in the PMT which is tuned  
 1609 to the PMT simulation.

1610 The time likelihood is approximated to depend on the vertex  $\vec{x}$ , direction  $\vec{d}$ ,  
 1611 and time  $t$  of the track as well as the particle hypothesis. The expected time  
 1612 for PMT hits is calculated by assuming unscattered photons being emitted from  
 1613 the midpoint of the track,  $S_{\text{mid}}$ ,

$$t_{\text{exp}}^i = t + S_{\text{mid}}/c + |R_{\text{PMT}}^i - \vec{x} - S_{\text{mid}}\vec{d}|/c_n, \quad (5.4)$$

1614 where  $c$  is the speed of light in a vacuum. The time likelihood is then expressed  
 1615 in terms of the residual difference between the PMT hit time and the expected  
 1616 hit time,  $t_{\text{Res}}^i = t^i - t_{\text{exp}}^i$ . The particle hypothesis and momentum also affect the  
 1617 Cherenkov photon distribution. These parameters modify the shape of the time  
 1618 likelihood density since in reality not all photons are emitted at the midpoint of  
 1619 the track. As with the charge likelihood, the contributions from both the direct  
 1620 and scattered light to the time likelihood density are calculated separately, which  
 1621 are both calculated from particle gun Monte Carlo studies.

The track parameters and particle identity which maximise  $L(\Gamma, \vec{\theta})$  are defined as the best-fit parameters. In practice MINUIT [183] is used to minimise the value of  $-\ln L(\Gamma, \vec{\theta})$ . The `fitQun` algorithm considers an electron-like, muon-like, and charged pion-like hypothesis for events with a single final state particle, denoted “single-ring events”. The particle’s identity is determined by taking the ratio of the likelihood of each of the hypotheses. For instance, electrons and muons are distinguished by considering the value of  $\ln(L(e, \vec{\theta}_e)/L(\mu, \vec{\theta}_\mu))$  in comparison to the reconstructed momentum of the electron hypothesis, as illustrated by Figure 5.4. The coefficients of the discriminator between electron-like and muon-like events are determined from Monte Carlo studies [178]. Similar distributions exist for distinguishing electron-like events from  $\pi^0$ -like events, and muon-like events from pion-like events. The cuts are defined as,

$$\begin{aligned} \text{Electron/Muon} : & \ln(L_e/L_\mu) > 0.2 \times p_e^{rec} [\text{MeV}], \\ \text{Electron}/\pi^0 : & \ln(L_e/L_{\pi^0}) < 175 - 0.875 \times m_{\gamma\gamma} [\text{MeV}], \\ \text{Muon/Pion} : & \ln(L_\mu/L_{\pi^\pm}) < 0.15 \times p_\mu^{rec} [\text{MeV}], \end{aligned} \quad (5.5)$$

as taken from [184], where  $p_e^{rec}$  and  $p_\mu^{rec}$  are the reconstructed momentum of the single-ring electron and muon fits, respectively.  $m_{\gamma\gamma}$  represents the reconstructed invariant mass of the two photons emitted from  $\pi^0$  decay. Typically, the distance between a particular entry in these two-dimensional distributions and the cut-line is termed the PID parameter and is illustrated in Figure 5.5.

The `fitQun` algorithm also considers a  $\pi^0$  hypothesis. To do this, it performs a fit looking for two standard electron-hypothesis tracks which point to the same four-vertex. This assumes the electron tracks are generated from photon-conversion so the electron tracks actually appear offset from the proposed  $\pi^0$  vertex. For these fits, the conversion length, direction, and momentum of each photon are also considered as track parameters which are then fit in the same methodology as the standard single-ring hypotheses.

Whilst lower energy events are predominantly single-ring events, higher energy neutrino events can generate final states with multiple particles which

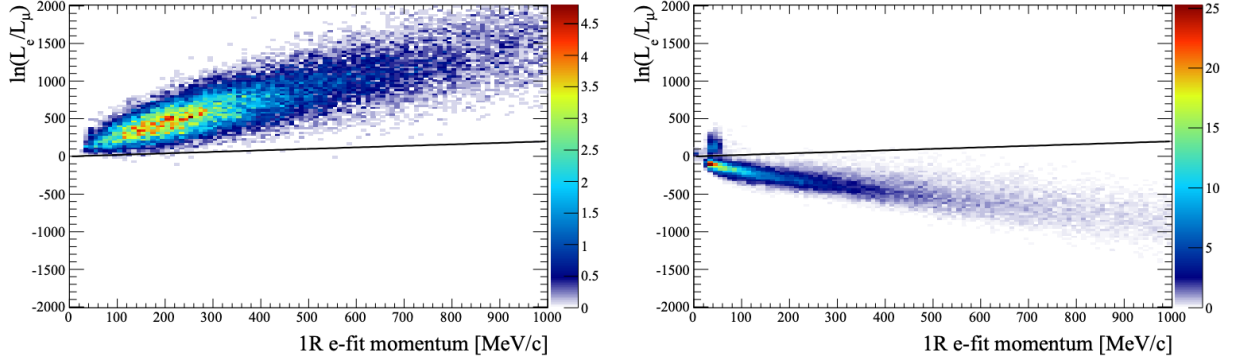


**Figure 5.4:** The difference of the electron-like and muon-like log-likelihood compared to the reconstructed single-ring fit momentum for atmospheric  $\nu_e$  (left) and  $\nu_\mu$  (right) samples. The black line represents the cut used to discriminate electron-like and muon-like events, with coefficients obtained from Monte Carlo studies. Figures from [178].

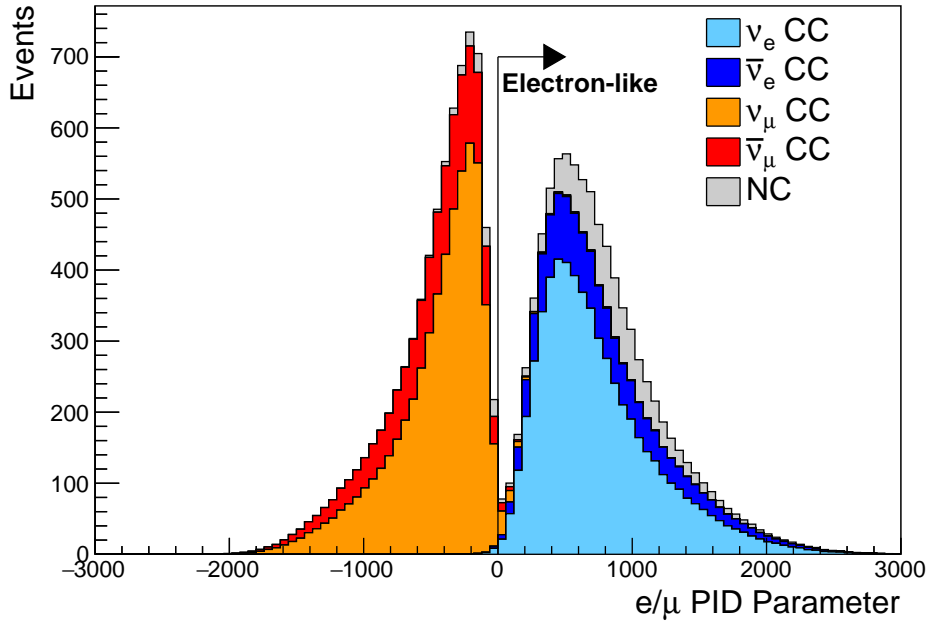


**Figure 5.5:** The electron/muon PID separation parameter for all sub-GeV single-ring events in SK-IV. The charged current (CC) component is broken down in four flavours of neutrino ( $\nu_\mu$ ,  $\bar{\nu}_\mu$ ,  $\nu_e$  and  $\bar{\nu}_e$ ). Events with positive values of the parameter are determined to be electron-like.

1648 generate Cherenkov photons. These “multi-ring” hypotheses are also considered  
 1649 in the `fitQun` algorithm. When calculating the charge likelihood density, the  
 1650 predicted charge associated with each ring is calculated separately and then  
 1651 summed to calculate the total accumulated charge on each PMT. Similarly, the  
 1652 time likelihood for the multi-ring hypothesis is calculated assuming each ring

is independent. Each track is time-ordered based on the time of flight from the center of the track to the PMT and the direct light from any ring incident on the PMT is assumed to arrive before any scattered light. To reduce computational resource usage, the multi-ring fits only consider electron-like and charged pion-like rings as the pion fit can be used as a proxy for a muon fit due to their similar mass. Due to the pions ability to interact through the strong force, they are more likely to hard-scatter. That means a single charged pion can produce multiple rings in different directions. There is an additional freedom, the fraction of kinetic energy lost in a single ring segment, which is added into the `fitQun` pion fit to cover this difference. Pion and muon rings are indistinguishable when this fraction tends to unity.

Multi-ring fits proceed by proposing another ring to the previous fit and then fitting the parameters in the method described above. Typically, multi-ring fits have the largest likelihood because of the additional degrees of freedom introduced. A likelihood value is calculated for the  $n$ -ring and  $(n + 1)$ -ring hypotheses, where the additional ring is only included if the likelihood value is above 9.35, based on Monte Carlo studies in [185].

### 5.2.1 Validation of Reconstruction in SK-V

Understanding how the modelling of the detector conditions and stability effects the reconstruction is critical for ensuring accurate measurements. It is important to note that the detector systematics used in the 2020 T2K-only [75] oscillation analysis are determined using data-to-Monte Carlo comparisons of the SK-IV data [186]. Due to tank-open maintenance occurring between SK-IV and SK-V, the dark rate of each PMT was observed to increase in SK-V due to light exposure for a significant time during the repairs. This increase can be seen in Figure 5.6. Run-10 of the T2K experiment was conducted in the SK-V period, so the consistency of SK-IV and SK-V data needs to be studied to determine whether the SK-IV-defined systematics can be applied to the run-10 data. Consequently, the author of this thesis assessed the quality of `fitQun` event reconstruction for SK-V data.

This comparison study was performed using the stopping muon data set for both the SK-IV and SK-V periods. This data sample is used due to the high rate of interactions ( $O(200)$  events per hour) as well as having similar energies to muons from CCQE  $\nu_\mu$  interactions from beam interactions. The rate of cosmic muons does depend on the solar activity cycle [187] but has been neglected in this comparison study. This is because the shape of the distributions is most important for the purposes of being compared to the detector systematics. The SK-IV and SK-V data samples consist of 2398.42 and 626.719 hours of data which equates to 686k and 192k events respectively. These samples do not correspond to the full data sets of either period but do contain enough events to be systematics limited rather than statistics limited.

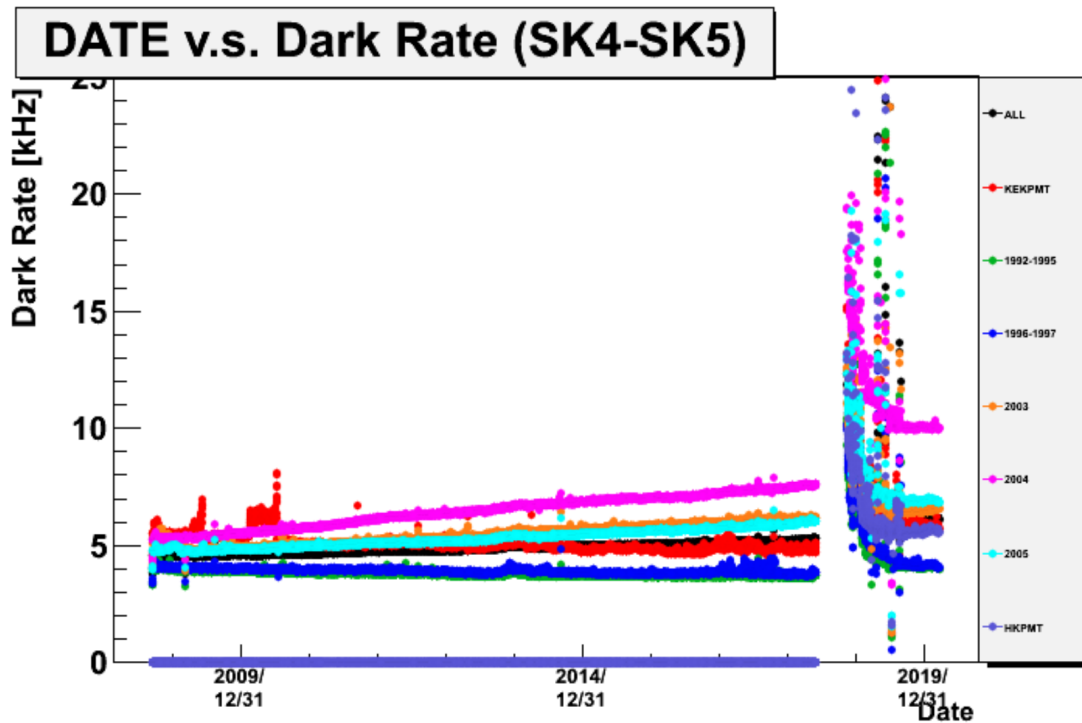


**Figure 5.6:** The variation of the measured dark rate as a function of date, broken down by PMT type. The SK-IV and SK-V periods span September 2008 to May 2018 and January 2019 to July 2020, respectively. The break in measurement in 2018 corresponds to the period of tank repair and refurbishment. Figure adapted from [186].

The predicted charge calculated in the `fitQun` algorithm includes a contribution from the photoelectron emission due to dark noise. Therefore, the increase

in the SK-V dark rate needs to be accounted for. In practice, the average dark rate in each SK period is calculated and used as an input in the reconstruction. This is calculated by averaging the dark rate per run for each period separately, using the calibration measurements detailed in subsection 3.1.2. The average dark rate from SK-IV and SK-V were found to be 4.57kHz and 6.30kHz, respectively. The charges associated with the muon and decay electron subevents are illustrated in Figure 5.7. The photoelectron emission from dark noise is more significant for events that have lower energy. This is because this contribution becomes more comparable to the number of photoelectrons emitted from incident photons in lower-energy events. This behaviour is observed in the data, where the charge deposited by the muon subevent is mostly unaffected by the increase in dark rate, whilst the charge associated with the decay-electron is clearly affected.

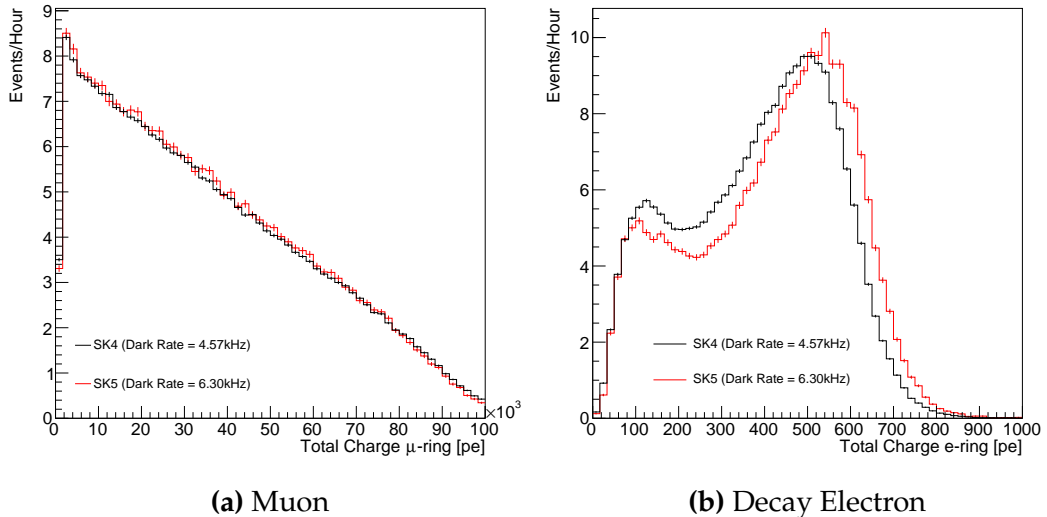


**Figure 5.7:** Comparison of the measured raw charge deposited per event from the stopping muon data samples between SK-IV (Blue) and SK-V (Red), split by the primary muon subevent (left) and the associated decay electron subevent (right).

The energy scale systematic is estimated from data-to-Monte Carlo differences in the stopping muon sample in [188] and found to be 2.1%. To determine the consistency of SK-IV and SK-V with respect to the energy scale systematic, the muon momentum distribution is compared between the two SK periods. As the total number of Cherenkov photons is integrated across the track length,

<sub>1712</sub> the reconstructed momentum divided by track length (or range) is compared  
<sub>1713</sub> between SK-IV and SK-V as illustrated in Figure 5.8.

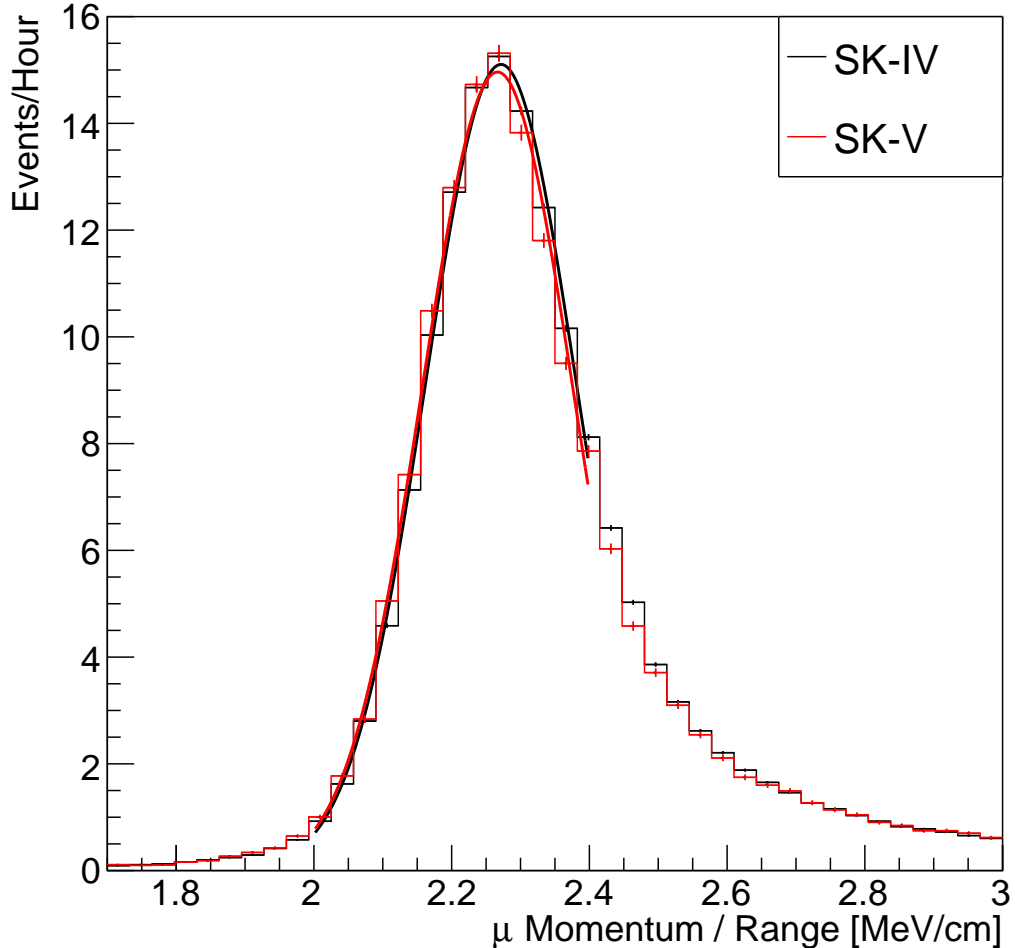


**Figure 5.8:** The distribution of the reconstructed momentum from the muon ring divided by the distance between the reconstructed muon and decay electron vertices as found in the stopping muon data sets of SK-IV (Black) and SK-IV (Red). Only events with one tagged decay electron are considered. A Gaussian fit is considered in the range [2.0, 2.4] MeV/cm and illustrated as the solid curve.

<sub>1714</sub> The consistency between these muon distributions has been computed in two  
<sub>1715</sub> ways. Firstly, a Gaussian is fit to the peak of each distribution separately, whose  
<sub>1716</sub> mean is found to be  $(2.272 \pm 0.003)$  MeV/cm and  $(2.267 \pm 0.006)$  MeV/cm for SK-  
<sub>1717</sub> IV and SK-V respectively. The ratio of these is equal to  $1.002 \pm 0.003$ . The means of  
<sub>1718</sub> the Gaussian fits are consistent with the expected stopping power of a minimum

ionising muon for a target material (water) with  $Z/A \sim 0.5$  [189]. The second consistency check is performed by introducing a nuisance parameter,  $\alpha$ , which modifies the SK-V distribution. The value of  $\alpha$  which minimises the  $\chi^2$  value between the SK-IV and SK-V is determined by scanning across a range of values. This is repeated by applying the nuisance parameter as both a multiplicative factor and an additive shift. The  $\chi^2$  distributions for different values of  $\alpha$  is illustrated in Figure 5.9. The values which minimise the  $\chi^2$  are found to be 0.0052 and 1.0024 for the additive and multiplicative implementations, respectively. No evidence of shifts larger than the 2.1% uncertainty on the energy scale systematic has been found in the reconstructed momentum distribution of SK-IV and SK-V.

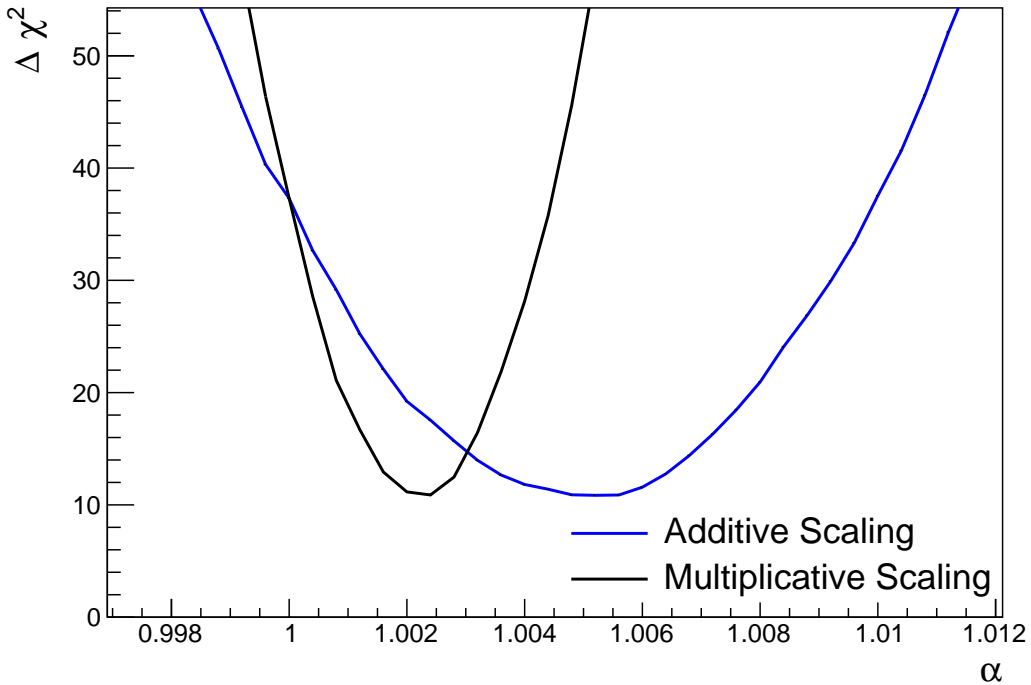


**Figure 5.9:** The  $\chi^2$  difference between the SK-IV and SK-V reconstructed muon momentum divided by range when the SK-V is modified by the scaling parameter  $\alpha$ . Both additive (Blue) and multiplicative (Black) scaling factors have been considered. In practice, the additive scaling factor actually uses the value of  $(\alpha - 1.0)$  but is illustrated like this so the results can be shown on the same axis range.

### **5.3 Event Reduction at SK**

1729     5.3 Event Reduction at SK

1730     In normal data-taking operations, the SK detector observes many background  
 1731     events alongside the beam and atmospheric neutrino signal events of physics  
 1732     interest for this thesis. Cosmic ray muons and flasher events, which are the spon-  
 1733     taneous discharge of a given PMT, contribute the largest amount of background  
 1734     events in the energy range relevant to this thesis. Therefore the data recorded  
 1735     is reduced with the aim of removing these background events. The reduction  
 1736     process is detailed in [55, 88] and briefly summarised below.

1737       Atmospheric neutrino events observed in the SK detector are categorised  
 1738       into three different types of samples: fully contained (FC), partially contained  
 1739       (PC) and up-going muon (Up- $\mu$ ), using PMT hit signatures in the inner and  
 1740       outer detector (ID and OD, respectively). To identify FC neutrino events, it is  
 1741       required that the neutrino interacts inside the fiducial volume of the ID and that  
 1742       no significant OD activity is observed. For this analysis, an event is defined to be  
 1743       in the fiducial volume provided the event vertex is at least 0.5m away from the  
 1744       ID walls. PC events have the same ID requirements but can have a larger signal  
 1745       present inside the OD. Typically, only high energy muons from  $\nu_\mu$  interactions can  
 1746       penetrate the ID wall. The Up- $\mu$  sample contains events where muons are created  
 1747       from neutrino interactions in the OD water or rock below the tank. They then  
 1748       propagate upwards through the detector. Downward-going muons generated  
 1749       from neutrino interactions above the tank are neglected because of the difficulty  
 1750       in separating their signature from the cosmic muon shower background. The  
 1751       sample categories are visually depicted in Figure 5.10.

1752       Based on the event characteristics, as defined by the `fitQun` event reconstruc-  
 1753       tion software, the FC events are categorised by

- 1754       • **Visible Energy:** equal to the sum of the reconstructed kinetic energy of  
 1755       particles above the Cerenkov threshold for all rings present in the event.  
 1756       The purpose is to separate events into sub-GeV and multi-GeV categories.

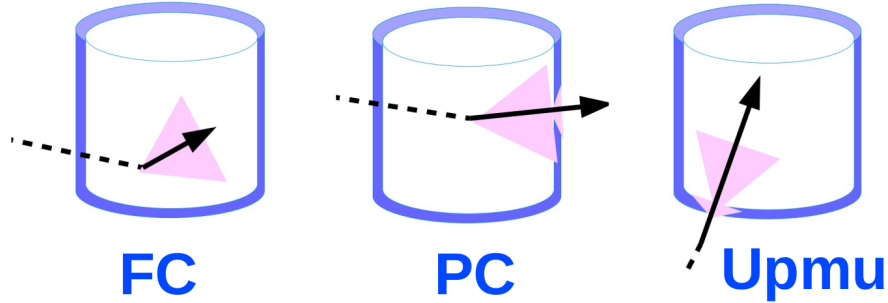


**Figure 5.10:** A depiction of the topology patterns for fully-contained (FC), partially-contained (PC), and up-going muon ( $\text{Up-}\mu$ ) samples included in this analysis.

- **Number of observed Cerenkov rings.** The purpose is to separate single-ring and multi-ring events, where single-ring events predominantly consist of quasi-elastic interactions and multi-ring events are typically resonant pion production or deep inelastic scattering events.
- **Particle identification parameter of the most energetic ring:** A value determined from the maximum likelihood value based on `fitQun`'s electron, muon, or pion hypothesis. The purpose is to separate electron-like and muon-like events.
- **Number of decay electrons:** The purpose is to separate quasi-elastic events (which have one decay electron emitted from the muon decay) and resonant pion production events (which have two decay electrons emitted from the muon and pion).

The PC and Up- $\mu$  categories are broken down into “through-going” and “stopping” samples depending on whether the muon leaves the detector. This is because the PC stopping events deposit the entire energy of the interaction into the detector, resulting in better reconstruction. The energy of events that exit the detector has to be estimated, with a typically worse resolution, which introduces much larger systematic uncertainties. Through-going Up- $\mu$  samples are further broken down by whether any hadronic showering was observed in the event which typically indicates DIS interactions. The expected neutrino energy for the different categories is given in Figure 5.11. FC sub-GeV and multi-GeV events

<sup>1778</sup> peak around 0.7GeV and 3GeV respectively, with slightly different peak energies  
<sup>1779</sup> for  $\nu_e$  and  $\nu_\mu$  oscillation channels. PC and Up- $\mu$  are almost entirely comprised  
<sup>1780</sup> of  $\nu_\mu$  events and peak around 7GeV and 100GeV, respectively.

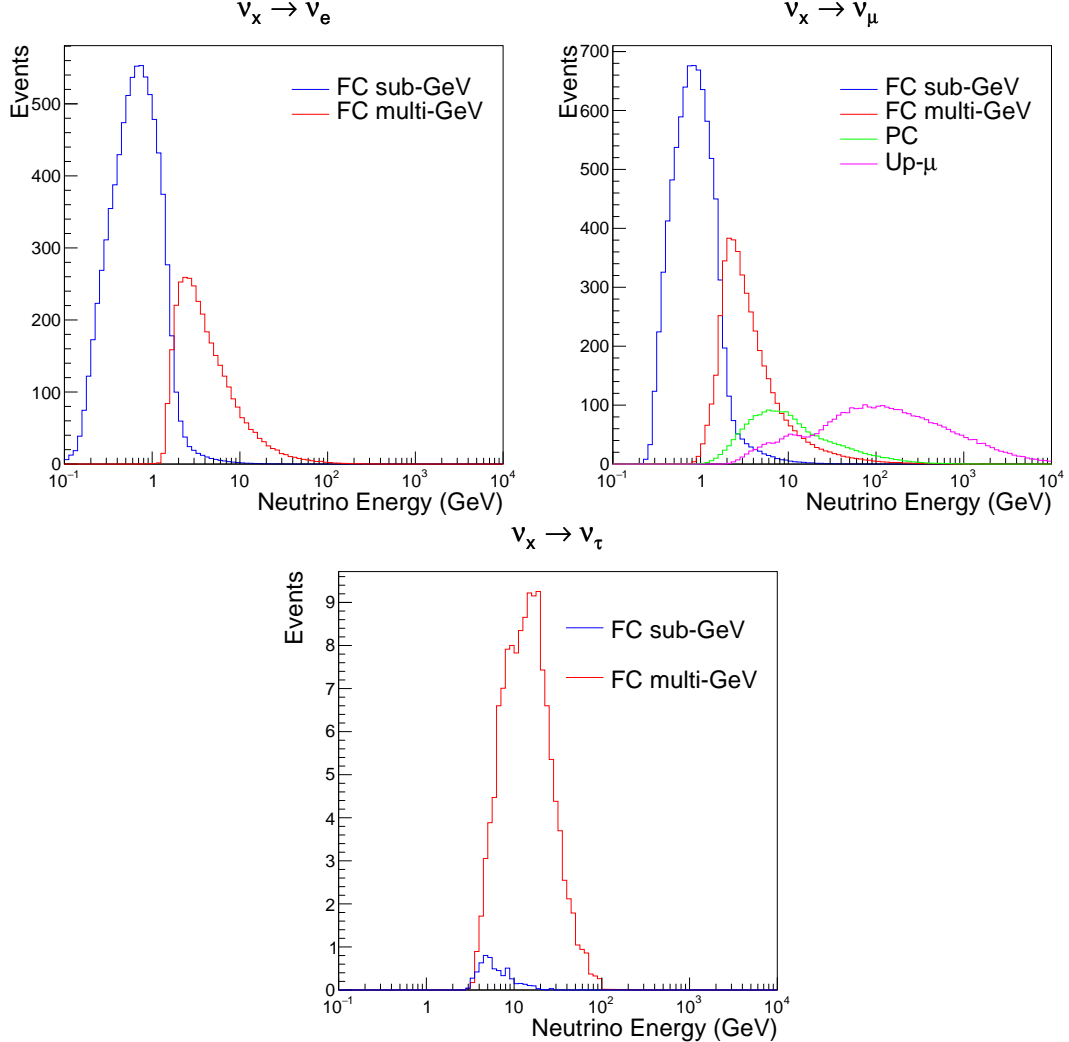


**Figure 5.11:** The predicted neutrino flux of the fully contained (FC) sub-GeV and multi-GeV, partially contained (PC), and upward-going muon (Up- $\mu$ ) events. The prediction is broken down by the  $\nu_x \rightarrow \nu_e$  prediction (top left),  $\nu_x \rightarrow \nu_\mu$  prediction (top right) and  $\nu_x \rightarrow \nu_\tau$  prediction (bottom).  $\nu_x$  represents the flavours of neutrinos produced in the cosmic ray showers (electron and muon). Asimov A oscillation parameters are assumed (given in Table 2.2).

<sup>1781</sup> The first two steps in the FC reconstruction remove the majority of cosmic  
<sup>1782</sup> ray muons by requiring a significant amount of ID activity compared to that  
<sup>1783</sup> measured in the OD. Events that pass this cut are typically very high momentum  
<sup>1784</sup> muons or events that leave very little activity in the OD. Consequently, a third

reduction step is then applied to select cosmic-ray muons that pass the initial reduction step. A purpose-built cosmic muon fitter is used to determine the entrance (or exit) position of the muon and a cut is applied to OD activity contained within 8m of this position. Flasher events are removed in the fourth reduction step which is based on the close proximity of PMT hits surrounding the PMT producing the flash. Events that pass all these reduction steps are reconstructed with the APFit algorithm. The fifth step of the reduction uses information from the more precise fitter to repeat the previous two steps with tighter cuts. Muons below the Cherenkov threshold can not generate optical photons in the ID but the associated decay electron can due to its lower mass. These are the types of events targeted in the fifth reduction step. The final cuts require the event vertex to be within the fiducial volume (0.5m from the wall although the nominal distance is 2.0m), visible energy  $E_{vis} > 30\text{MeV}$  and fewer than 16 hits within the higher energy OD cluster. The culmination of the fully contained reduction results in 8.09 events/day in the nominal fiducial volume [84]. The uncertainty in the reconstruction is calculated by comparing Monte Carlo prediction to data. The largest discrepancy is found to be 1.3% in the fourth reduction step.

The PC and Up- $\mu$  events are processed through their own reduction processes detailed in [55]. Both of these samples are reconstructed with the APFit algorithm rather than `fiTQun`. This is because the efficiency of reconstructing events that leave the detector has not been sufficiently studied for reliable systematic uncertainties with `fiTQun`. The PC and Up- $\mu$  samples acquire events at approximately 0.66 and 1.44 events/day.

Beam neutrinos events undergo the same reduction steps as FC events and are then subject to further cuts [190]. The GPS system that links the timing between the beam facility and SK needs to be operating correctly and there should be no activity within the detector in the previous  $100\mu\text{s}$  before the trigger. The events then need to triggered between  $-2\mu\text{s}$  and  $10\mu\text{s}$  of the expected spill timing.

1814      The beam neutrino samples are not split by visible energy since their energy  
 1815      range is smaller than the atmospheric neutrino events. Following the T2K  
 1816      analysis in [75], only single-ring beam neutrino events are considered. Similar to  
 1817      atmospheric event selection, the number of decay electrons is used as a proxy for  
 1818      distinguishing CCQE and CCRES events. The expected neutrino energy, broken  
 1819      down by the number of decay electrons, is given in Figure 5.12.

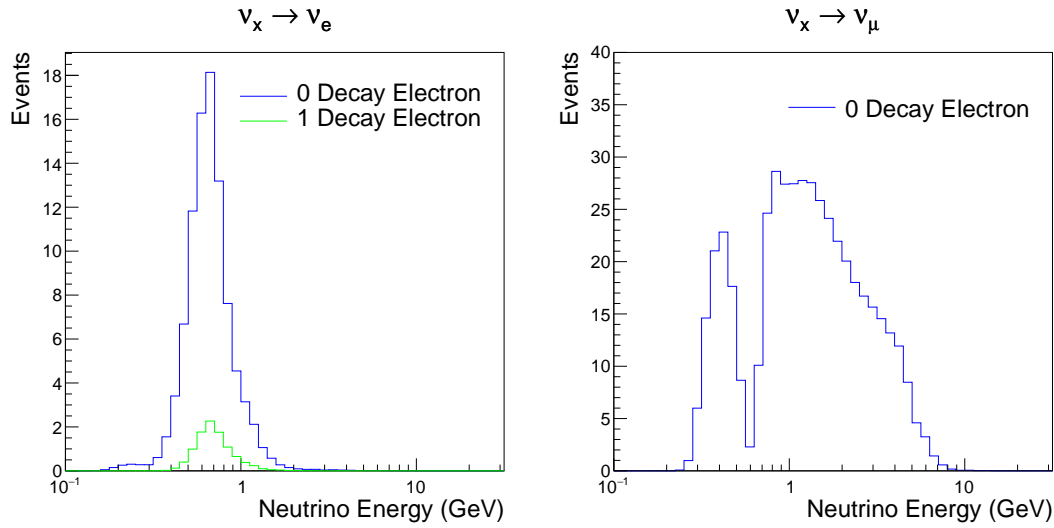


**Figure 5.12:** The predicted flux of beam neutrinos, as a function of neutrino energy. The predictions are broken down by the number of decay electrons associated with the particular events. Asimov A oscillation parameters are assumed (given in Table 2.2).

# 6

1820

1821

## Sample Selections and Systematics

1822 The oscillation analysis presented within this thesis is built upon a simultaneous  
1823 fit to atmospheric data at SK, neutrino beam data in the near detector, and  
1824 beam data measured at SK. This is the first simultaneous oscillation analysis  
1825 of beam and atmospheric samples supported by the T2K and SK collaborations.  
1826 Notably, the author of this thesis has been responsible for the building and  
1827 developing the MaCh3 framework to support all sets of samples simultaneously.  
1828 The definitions of the samples are documented in section 6.1, section 6.2, and  
1829 section 6.3, respectively. The data collected and used within this analysis is  
1830 detailed in Table 6.1. The near and far detector data corresponds to T2K runs  
1831 2-9 and runs 1-10, respectively. The accumulated POT and beam power for runs  
1832 1 – 10 are illustrated in Figure 6.1.

Data Type	Total
Near Detector FHC	$1.15 \times 10^{21}$ POT
Near Detector RHC	$8.34 \times 10^{20}$ POT
Far Detector FHC	$1.97 \times 10^{21}$ POT
Far Detector RHC	$1.63 \times 10^{21}$ POT
Atmospheric SK-IV	3244.4 days

**Table 6.1:** The amount of data collected in each detector used within this analysis. The data collected at the near and far detector, for both neutrino beam (FHC) and antineutrino beam (RHC), is measured as the number of protons on target (POT).

The difference in POT recorded at the near and far detector is due to the difference in downtime. The SK detector is very stable with almost 100% of data recorded during beam operation. Due to various technical and operational issues, the downtime of the near detector is significantly higher due to its more complex design and operating requirements.

The systematic parameters invoked within the flux, detector, and interaction models used within this analysis are documented in section 6.4. The standard configuration of the joint beam and atmospheric data fit utilises far detector systematics provided in the official inputs from the two experiments. Additionally, a correlated detector model which fits the parameters used in sample selections to data has been developed and documented in subsection 6.4.5.

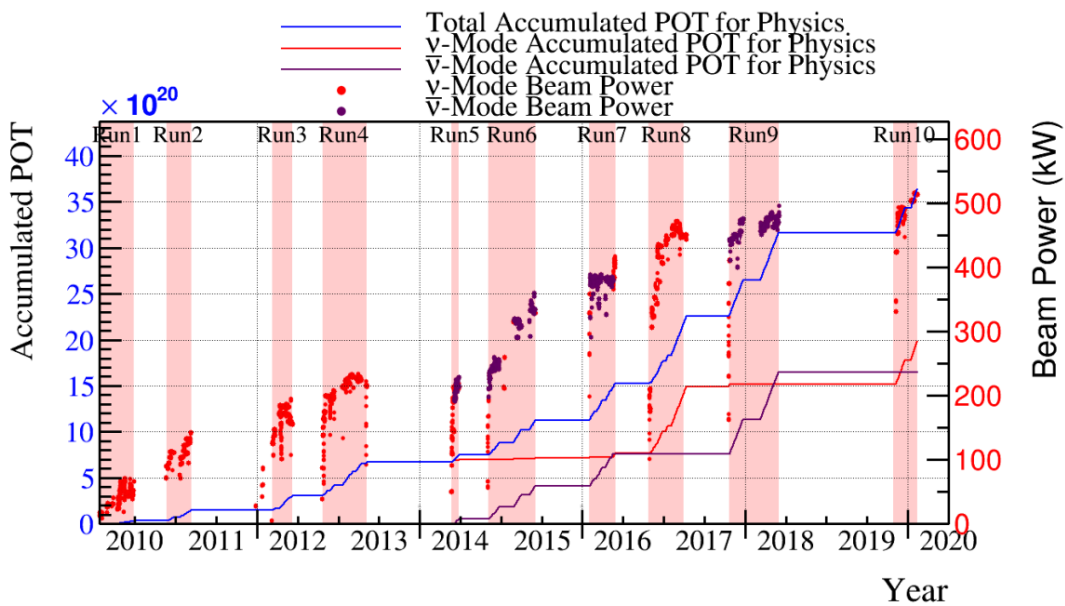


**Figure 6.1:** The accumulated beam data, measured as the number of protons on target (POT). The total data (blue) is given which comprises of the neutrino beam (red) and antineutrino (purple) components. The beam power for neutrino and antineutrino beams is given as the markers using the same colour scheme. The timescale runs from Run 1 which started in January 2010 until Run 10 which ended in February 2020. The ratio of accumulated data in neutrino and antineutrino beam is 54.7% : 45.3%.

## 1844 6.1 Atmospheric Samples

1845 The atmospheric event selection follows the official SK-IV analysis presented  
1846 in [88] and is documented below. The Monte Carlo prediction used within this  
1847 analysis corresponds to 500 years worth of neutrino events, which is scaled down  
1848 to match the SK-IV livetime of 3244.4 days.

1849 The fully contained (FC), partially contained (PC), and upward going muon  
1850 events ( $\text{up-}\mu$ ) which pass the reduction cuts discussed in section 5.3 are further  
1851 broken down into different samples based on reconstruction information. This  
1852 section details the samples used within this oscillation analysis, alongside the  
1853 chosen binning.

1854 FC events are first separated by the visible energy deposited within the  
1855 detector. This is calculated as the sum of the reconstructed kinetic energy  
1856 above the Cherenkov threshold for all rings present in the event. Events are  
1857 separated by whether they were above or below  $E_{\text{vis}} = 1.33\text{GeV}$ . This separates  
1858 “subGeV” and “multiGeV” events. Typically, lower energy events consist of  
1859 charged current quasi-elastic (CCQE) interactions which are better understood  
1860 and simpler to reconstruct resulting in smaller systematic uncertainties. Events  
1861 are further separated by the number of rings associated with the event due to  
1862 similar reasoning. As the oscillation probability is dependant upon the flavour  
1863 of neutrino, electron and muon events are separated using a similar likelihood  
1864 method to that discussed in section 5.2. To reduce computational resources  
1865 required for the reconstruction, only electron and pion hypotheses are considered  
1866 so this separation cut depends on the ratio of the electron to pion likelihoods,  
1867  $\log(L_e/L_\pi)$ . Finally, the number of decay electrons is used to classify events.  
1868 Charged current resonant pion production (CCRES) interactions generate a final-  
1869 state pion. This can decay, mostly likely through a muon, into a decay electron.  
1870 Therefore any electron-like event with one decay electron or muon-like event  
1871 with two decay electrons was most likely produced by a CCRES interaction.  
1872 Consequently, the number of decay electrons can be used to distinguish CCQE

<sup>1873</sup> and CCRES interaction modes. Ultimately, FC subGeV events are separated  
<sup>1874</sup> into the samples listed in Table 6.2.

Sample Name	Description
SubGeV- <i>e</i> like-0dcy	Single ring <i>e</i> -like events with zero decay electrons
SubGeV- <i>e</i> like-1dcy	Single ring <i>e</i> -like events with one or more decay electrons
SubGeV- <i>μ</i> like-0dcy	Single ring <i>μ</i> -like events with zero decay electrons
SubGeV- <i>μ</i> like-1dcy	Single ring <i>μ</i> -like events with one decay electrons
SubGeV- <i>μ</i> like-2dcy	Single ring <i>μ</i> -like events with two or more decay electrons
SubGeV- <i>π</i> 0like	Two <i>e</i> -like ring events with zero decay electrons and reconstructed $\pi^0$ mass $85 \leq m_{\pi^0} < 215$ MeV

**Table 6.2:** The fully contained subGeV samples, defined as events with visible energy  $E_{vis} < 1.33$  GeV, used within this oscillation analysis.

<sup>1875</sup> In addition to the cuts discussed above, multiGeV samples also have addi-  
<sup>1876</sup> tional cuts to separate samples which target neutrino and antineutrino events.  
<sup>1877</sup> As discussed in section 2.5, the matter resonance only occurs for neutrinos in the  
<sup>1878</sup> normal hierarchy and antineutrinos in the inverted mass hierarchy. Therefore,  
<sup>1879</sup> having flavour-enriched samples aids in the determination of the mass hierarchy.  
<sup>1880</sup> For a CCRES interaction,

$$\begin{aligned}
 \bar{\nu}_e + N &\rightarrow e^+ + N' + \pi^-, \\
 \nu_e + N &\rightarrow e^- + N' + \pi^+ \\
 &\quad \downarrow \mu^+ + \nu_\mu \\
 &\quad \downarrow e^+ + \nu_e + \bar{\nu}_\mu.
 \end{aligned} \tag{6.1}$$

<sup>1881</sup> The  $\pi^-$  emitted from a  $\bar{\nu}_e$  interaction is more likely to be captured by an  
<sup>1882</sup> oxygen nucleus than the  $\pi^+$  from  $\nu_e$  interactions [191]. These pions then decay,  
<sup>1883</sup> mostly through muons, to electrons. Therefore the number of tagged decay  
<sup>1884</sup> electrons associated with an event gives an indication of whether the interaction  
<sup>1885</sup> was due to a neutrino or antineutrino: zero for  $\bar{\nu}_e$  events, and one for  $\nu_e$  events.  
<sup>1886</sup> The ability to separate neutrino from antineutrino events is illustrated in Table 6.4,  
<sup>1887</sup> where the MultiGeV-*e*like-nue has 78% purity of CC neutrino interactions with  
<sup>1888</sup> only 7% antineutrino background, the rest consisting of NC backgrounds.

1889     The number of decay electrons discriminator works reasonably well for single-  
 1890     ring events. However, this is not the case for multi-ring events. A multiGeV  
 1891     multiring electron-like (MME) likelihood cut was introduced in [192, 193]. This  
 1892     is a two-stage likelihood selection cut. Four observables are used in the first  
 1893     likelihood cut to distinguish  $CC\nu_e$  and  $CC\bar{\nu}_e$  events from background:

- 1894     • The number of decay electrons  
 1895     • The maximum distance between the vertex of the neutrino and the decay  
 1896        electrons  
 1897     • The energy deposited by the highest energy ring  
 1898     • The particle identification of that highest energy ring

1899     Background events consist of  $CC\nu_\mu$  and NC interactions. Typically, the  
 1900     majority of the energy in these background events is carried by the hadronic  
 1901     system. Additionally, muons tend to travel further than the pions from  $CC\nu_e$   
 1902     before decaying. Thus, the parameters used within the likelihood cut target these  
 1903     typical background interaction kinematics.

Sample Name	Description
MultiGeV-elike-nue	Single ring $e$ -like events with zero decay electrons
MultiGeV-elike-nuebar	Single ring $e$ -like events with one or more decay electrons
MultiGeV-mulike	Single ring $\mu$ -like events
MultiRing-elike-nue	Two or more ring events with leading energy $e$ -like ring and passed both MME and $\nu/\bar{\nu}$ separation cuts
MultiRing-elike-nuebar	Two or more ring events with leading energy $e$ -like ring and passed MME and failed $\nu/\bar{\nu}$ separation cuts
MultiRing-mulike	Two or more ring events with leading energy $\mu$ -like ring and only requires $E_{vis} > 0.6\text{GeV}$
MultiRing-Other1	Two or more ring events with leading energy $e$ -like ring and failed the MME likelihood cut

**Table 6.3:** The fully contained multiGeV samples used within this oscillation analysis. Both the sample name and description are given.

1904     Neutrino and antineutrino events are then separated by a second likelihood  
 1905     method ( $\nu/\bar{\nu}$  separation) detailed in [60]. This uses the number of decay electrons,

1906 the number of reconstructed rings, and the event’s transverse momentum. The  
1907 last two parameters are used because higher-energy samples tend to have more  
1908 pions produced above the Cherenkov threshold which results in more rings  
1909 compared to an antineutrino interaction. Furthermore, the angular distribution  
1910 also tends to be more forward peaked in antineutrino interactions as compared  
1911 to neutrino interactions [88]. These FC multiGeV sample definitions are de-  
1912 tailed in Table 6.3.

1913 The PC and up- $\mu$  samples are split by the amount of energy deposited within  
1914 the outer detector, into “stopping” and “through-going” samples. If an event  
1915 leaves the detector, the energy it takes with it has to be estimated which increases  
1916 the systematic uncertainty compared to events entirely contained within the  
1917 inner detector. This estimation is particularly poor at high energies, thus the  
1918 up- $\mu$  through-going events are not binned in reconstructed momentum. The  
1919 through-going up- $\mu$  are further separated by the presence of any electromagnetic  
1920 showering in the event, as the assumption of non-showering muon does not give  
1921 reliable reconstruction for these types of events [55]. In total, 13 FC, 2 PC, and  
1922 3 up- $\mu$  atmospheric samples are included within this analysis.

1923 The atmospheric samples are binned in direct observables: reconstructed  
1924 lepton momentum and direction, as given by Table A.1. The distribution of  
1925 the reconstructed lepton momentum (for samples that only have one bin in  
1926 reconstructed zenith angle) and reconstructed direction for each atmospheric  
1927 sample used within this analysis is illustrated in Figure 6.2. The by-mode  
1928 breakdown of each of the atmospheric samples is given in Appendix A.

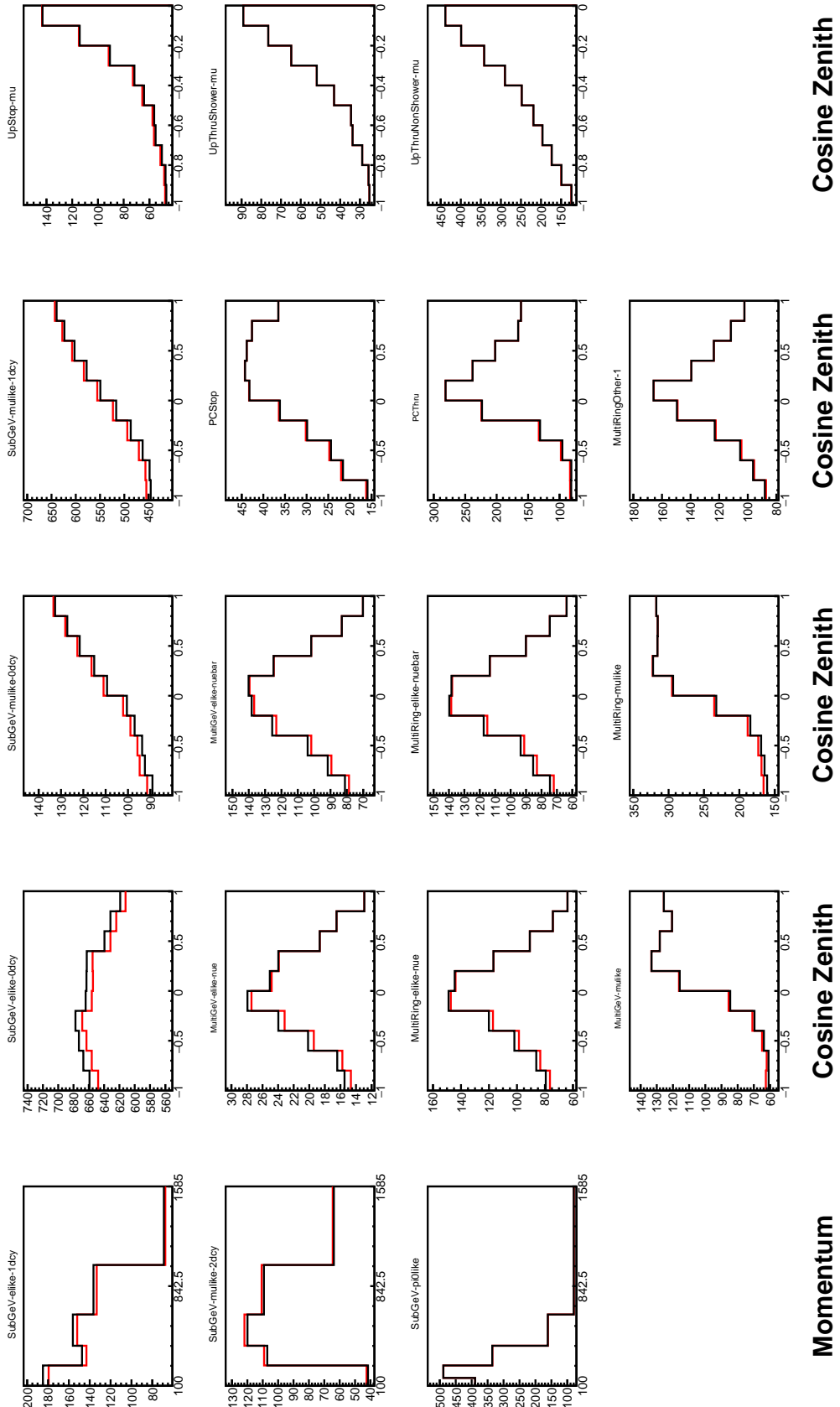


**Figure 6.2:** Comparison of the SK-IV atmospheric samples between predictions made with the CP-violating Asimov A (Black) and CP-conserving Asimov B (Red) oscillation parameter sets (given in Table 2.2). The subGeV samples CCRES and  $\pi^0$ -like samples are given in their reconstructed lepton momentum. All other samples are presented in their reconstructed zenith angle projection.

Sample	$CC\nu_e$	$CC\bar{\nu}_e$	$CC(\nu_\mu + \bar{\nu}_\mu)$	$CC(\nu_\tau + \bar{\nu}_\tau)$	NC
SubGeV- <i>elike</i> -0dcy	72.17	23.3	0.724	0.033	3.77
SubGeV- <i>elike</i> -1dcy	86.81	1.773	7.002	0.062	4.351
SubGeV- <i>mulike</i> -0dcy	1.003	0.380	90.07	0.036	8.511
SubGeV- <i>mulike</i> -1dcy	0.023	0.	98.46	0.029	1.484
SubGeV- <i>mulike</i> -2dcy	0.012	0.	99.25	0.030	0.711
SubGeV- <i>pi0like</i>	6.923	2.368	0.928	0.011	89.77
MultiGeV- <i>elike</i> -nue	78.18	7.041	3.439	1.886	9.451
MultiGeV- <i>elike</i> -nuebar	56.68	37.81	0.174	0.614	4.718
MultiGeV- <i>mulike</i>	0.024	0.005	99.67	0.245	0.058
MultiRing- <i>elike</i> -nue	59.32	12.39	4.906	3.385	20
MultiRing- <i>elike</i> -nuebar	52.39	31.03	1.854	1.585	13.14
MultiRing- <i>mulike</i>	0.673	0.080	97.33	0.342	1.578
MultiRingOther-1	27.98	2.366	34.93	4.946	29.78
PCStop	8.216	3.118	84.45	0.	4.214
PCThru	0.564	0.207	98.65	0.	0.576
UpStop-mu	0.829	0.370	98.51	0.	0.289
UpThruNonShower-mu	0.206	0.073	99.62	0.	0.103
UpThruShower-mu	0.128	0.054	99.69	0.	0.132

**Table 6.4:** The purity of each atmospheric sample used within this analysis, broken down by charged current (CC) and neutral current (NC) interactions and which neutrino flavour interacted within the detector. Each row sums to 100% by definition. Asimov A oscillation parameter sets are assumed (given in Table 2.2). Electron neutrino and antineutrino events are separated to illustrate the ability of the separation likelihood cuts used within the multiGeV and multiring sample selections.

## 1929 6.2 Near Detector Beam Samples

1930 The near detector sample selections are documented in detail within [194] and  
1931 summarised below. Samples are selected based upon which of the two Fine  
1932 Grained Detector (FGD) the vertex is reconstructed in as well as the operating  
1933 mode of the beam: FHC or RHC. Wrong-sign neutrino background samples are  
1934 considered in the RHC mode in order to add additional constraints on model  
1935 parameters. Samples from the wrong-sign component of the FHC beam mode  
1936 are not included as they are statistically insignificant compared to those samples  
1937 already listed.

1938 The reconstruction algorithm uses a clustering algorithm to group hits within  
1939 the TPC. It then adds information from the upstream FGD to form a track  
1940 that passes through both sub-detectors. In FHC(RHC), the highest momentum  
1941 negative(positive) curvature track is defined as the muon candidate. Before  
1942 being assigned a sample, these candidate muon events must pass CC-inclusive  
1943 cuts, as defined in [195]:

- 1944 • Event Timing: The DAQ must be operational and the event must occur  
1945 within the expected beam time window consistent with the beam spill
- 1946 • TPC Requirement: The muon-candidate track path must intercept one or  
1947 more TPCs
- 1948 • Fiducial volume: The event must originate from within the fiducial volume  
1949 defined in [196]
- 1950 • Upstream Background: Remove events that have muon tracks that originate  
1951 upstream of the FGDs by requiring no high-momentum tracks within  
1952 150mm upstream of the candidate vertex. Additionally, events that occur  
1953 within the downstream FGD are vetoed if a secondary track starts within  
1954 the upstream FGD

- <sup>1955</sup> • Broken track removal: All candidates where the muon candidate is broken  
<sup>1956</sup> in two are removed

- <sup>1957</sup> • Muon PID: Measurements of  $dE/dx$  in a TPC are used to distinguish muon-  
<sup>1958</sup> like events, from electron-like or proton-like, using a likelihood cut

<sup>1959</sup> In addition to these cuts, RHC neutrino events also have to undergo the  
<sup>1960</sup> following cuts to aid in the separation of neutrino and antineutrino [197]:

- <sup>1961</sup> • TPC Requirement: The track path must intercept TPC2  
<sup>1962</sup> • Positive Track: The highest momentum track must have a positive recon-  
<sup>1963</sup> structed charge  
<sup>1964</sup> • TPC1 Veto: Remove any events originating upstream of TPC1

<sup>1965</sup> Once all CC-inclusive events have been determined, they are further split  
<sup>1966</sup> by pion multiplicity: CC0 $\pi$ , CC1 $\pi$ , and CCOther. This breakdown targets the  
<sup>1967</sup> specific interaction modes CCQE, CCRES, and other CC background interactions,  
<sup>1968</sup> respectively. Pions in the TPCs are selected by requiring a second track to be  
<sup>1969</sup> observed, which is separate from the muon track and is in the same beam spill  
<sup>1970</sup> window and sub-detector. The number of FGD pions is equal to the number  
<sup>1971</sup> of Michel electrons which were tagged within the same sub-detector and spill  
<sup>1972</sup> window. If this value is equal to zero, the number of FGD pions is equivalent  
<sup>1973</sup> to the number of pion-like tracks which have  $dE/dx$  measurements consistent  
<sup>1974</sup> with the pion hypothesis and have a vertex consistent with that of the muon  
<sup>1975</sup> candidate. This pion track also pass through the sequential downstream TPC  
<sup>1976</sup> (TPC2 for FGD1, TPC3 for FGD2). The Michel electron tagging is preferential as  
<sup>1977</sup> a delayed Michel is almost always a pion meaning this cut has a higher purity  
<sup>1978</sup> [195, 198], whereas a track in the FGD that is consistent with a pion could be  
<sup>1979</sup> another particle resulting in a lower purity. Michel electrons are neglected in the  
<sup>1980</sup> TPC as the pions very rarely stop due to the low density.

<sup>1981</sup> CC0 $\pi$ , CC1 $\pi$ , and CCOther samples are defined with the following cuts:

- $\nu_\mu$ **CC0 $\pi$  Selection:** No electrons in TPC and no charged pions or decay electrons within the TPC or FGD
  - $\nu_\mu$ **CC1 $\pi$  Selection:** Exactly one charged pion in either the TPC or FGD
  - $\nu_\mu$ **CCOther Selection:** All events which are not classified into the above two selections
- Counting the three selections for each FGD in FHC and RHC running, including the wrong-sign background in RHC, 18 near detector samples are used within this analysis. These samples are binned in reconstructed lepton momentum (illustrated in Figure 6.3) and direction with respect to the beam. The binning is chosen such that each event has at least 20 Monte Carlo events in each bin [196]. This is to ensure that the bins are coarse enough to ensure the reduction of statistical errors, whilst also being fine enough to sample the high-resolution peak regions. The exact binning is detailed in [196].

### 6.3 Far Detector Beam Samples

The beam neutrino events which occur at the SK detector, which pass the reduction cuts detailed in section 5.3, are separated based on whether the beam was operating in FHC or RHC mode. The events are then separated into three samples: electron-like (1Re), muon-like (1R $\mu$ ), and CC1 $\pi^+$ -like (1Re1de) which are observed as electron-like events with an associated decay electron [186]. As discussed in section 6.1, positively charged pions emitted from neutrino interactions are more likely to produce decay electrons than negatively charged pions. Consequently, the CC1 $\pi^+$ -like sample is only selected when the beam is operating in FHC mode. Therefore, five beam samples measured at SK are used in this analysis.

The fiducial volume definition for beam samples is slightly different from that used for the atmospheric samples. It uses both the distance to the closest wall (dWall) and the distance to the wall along the trajectory of the particle (toWall).

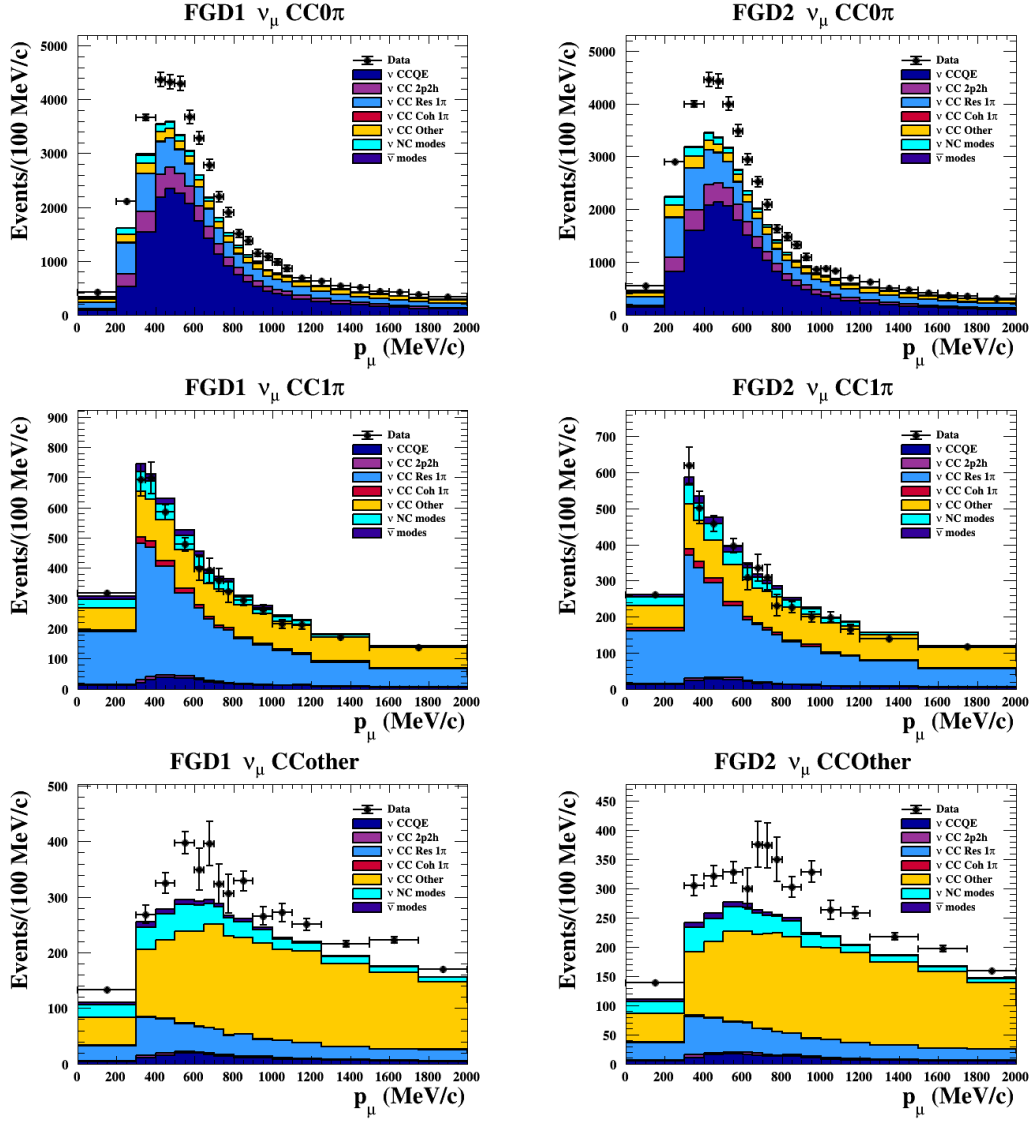


**Figure 6.3:** The nominal Monte Carlo predictions compared to data for the FGD1 and FGD2 samples in neutrino beam mode, broken down into the  $CC\nu_\mu 0\pi$ ,  $CC\nu_\mu 1\pi$  and  $CC\nu_\mu$  Other categories. Figures taken from [194].

- 2009 This allows events that originate close to the wall but are facing into the tank to be  
 2010 included within the analysis, which would have otherwise been removed. These  
 2011 additional events are beneficial for a statistics-limited experiment. The exact  
 2012 cut values for both `dWall` and `toWall` are different for each of the three types of  
 2013 sample and are optimised based on T2K sensitivity to  $\delta_{CP}$  [184, 199]. They are:  
 2014 **1Re event selection** For an event to be classified as a 1Re-like, the event must sat-  
 2015 isfy:

- 2016     • Fully-contained and have  $d_{\text{Wall}} > 80\text{cm}$  and  $t_{\text{Wall}} > 170\text{cm}$
- 2017     • Total of one ring which is reconstructed as electron-like with reconstructed momentum  $P_e > 100\text{MeV}$
- 2018     • Zero decay electrons are associated with the event
- 2019     • Passes  $\pi^0$  rejection cut discussed in section 5.2
- 2020     The zero decay electron cut removes non-CCQE interactions and the  $\pi^0$  rejection cut is designed to remove neutral current  $\pi^0$  background events which can be easily reconstructed as 1Re-like events.
- 2021     The zero decay electron cut removes non-CCQE interactions and the  $\pi^0$  rejection cut is designed to remove neutral current  $\pi^0$  background events which can be easily reconstructed as 1Re-like events.
- 2022     The zero decay electron cut removes non-CCQE interactions and the  $\pi^0$  rejection cut is designed to remove neutral current  $\pi^0$  background events which can be easily reconstructed as 1Re-like events.
- 2023     The zero decay electron cut removes non-CCQE interactions and the  $\pi^0$  rejection cut is designed to remove neutral current  $\pi^0$  background events which can be easily reconstructed as 1Re-like events.
- 2024     The zero decay electron cut removes non-CCQE interactions and the  $\pi^0$  rejection cut is designed to remove neutral current  $\pi^0$  background events which can be easily reconstructed as 1Re-like events.
- 2025     The zero decay electron cut removes non-CCQE interactions and the  $\pi^0$  rejection cut is designed to remove neutral current  $\pi^0$  background events which can be easily reconstructed as 1Re-like events.
- 2026     The zero decay electron cut removes non-CCQE interactions and the  $\pi^0$  rejection cut is designed to remove neutral current  $\pi^0$  background events which can be easily reconstructed as 1Re-like events.
- 2027     **CC1 $\pi^+$  event selection** This event selection is very similar to that of the 1Re sample. The only differences are that the  $d_{\text{Wall}}$  and  $t_{\text{Wall}}$  criteria are changed to  $> 50\text{cm}$  and  $> 270\text{cm}$ , respectively, and exactly one decay electron is required from the  $\pi^+$  decay.

2031     **1R $\mu$  event selection** A 1R $\mu$ -like event is determined by the following cuts:

- 2032     • Fully-contained and have  $d_{\text{Wall}} > 50\text{cm}$  and  $t_{\text{Wall}} > 250\text{cm}$
- 2033     • Total of one ring which is reconstructed as muon-like with reconstructed momentum  $P_\mu > 200\text{MeV}$
- 2034     • Fewer than two decay electrons are associated with the event
- 2035     • Passes  $\pi^+$  rejection cut discussed in section 5.2

2037 All of these samples are binned in reconstructed neutrino energy. This is  
 2038 possible under a particular interaction mode assumption, as the direction from  
 2039 the source is known extremely well. For the 1Re-like and 1R $\mu$ -like samples,

$$E_{\nu}^{rec} = \frac{(M_N - V_{nuc})E_l - m_l^2/2 + M_N V_{nuc} - V_{nuc}^2/2 + (M_P^2 + M_N^2)/2}{M_N - V_{nuc} - E_l + P_l \cos(\theta_{beam})}. \quad (6.2)$$

2040 Where  $M_N$ ,  $M_P$  and  $m_l$  are the masses of the neutron, proton and outgoing  
 2041 lepton, respectively.  $V_{nuc} = 27\text{MeV}$  is the binding energy of the oxygen nucleus  
 2042 [186],  $\theta_{beam}$  is the angle between the beam and the direction of the outgoing  
 2043 lepton, and  $E_l$  and  $P_l$  are the energy and momentum of that outgoing lepton.

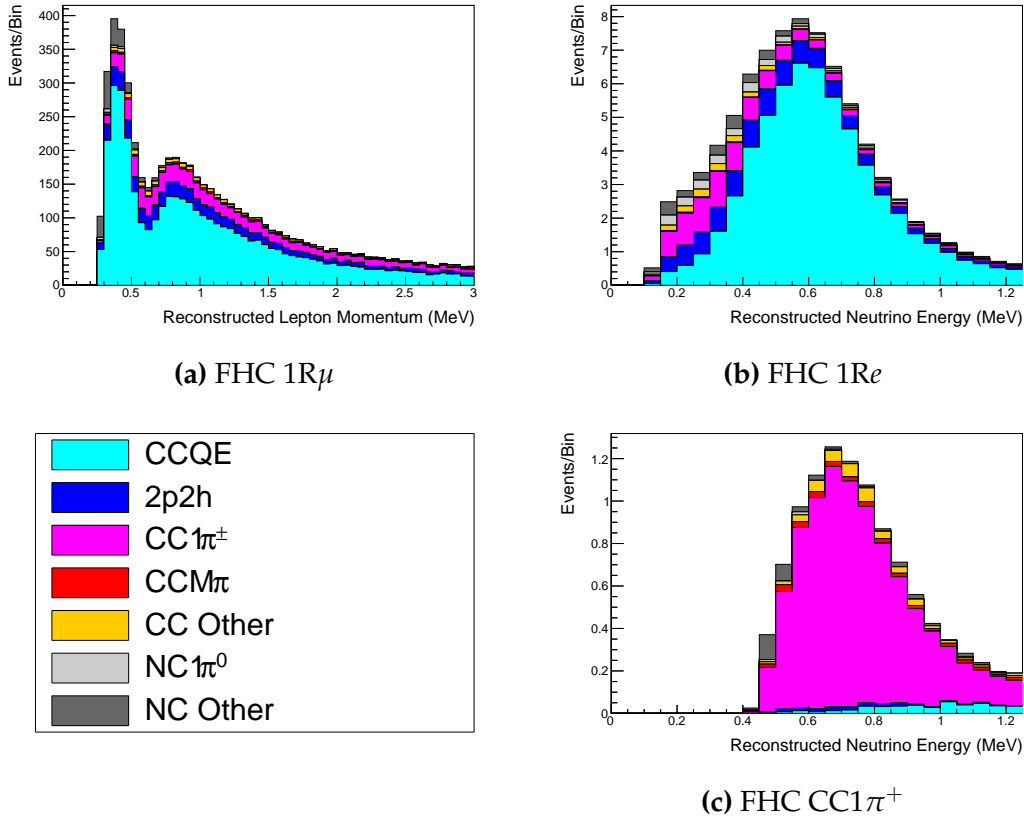


**Figure 6.4:** The reconstructed neutrino energy, as defined by Equation 6.2 and Equation 6.3, for the 1R $\mu$ -like, 1Re-like, and CC1 $\pi^+$ -like samples. The AsimovA oscillation parameters are assumed (given in Table 2.2). These samples are the FHC mode samples. For ease of viewing, the 1R $\mu$  sample only shows the  $0. \leq E_{\nu}^{rec} < 3.0\text{GeV}$  but the binning extends to 30.0GeV.

2044 The reconstructed neutrino energy of the CC1 $\pi^+$ -like events also accounts  
2045 for the delta resonance produced within the interaction,

$$E_\nu^{rec} = \frac{2M_N E_l + M_{\Delta^{++}}^2 - M_N^2 - m_l^2}{2(M_N - E_l + P_l \cos(\theta_{beam}))}. \quad (6.3)$$

2046 Where  $M_{\Delta^{++}}$  is the mass of the delta baryon. Binding energy effects are not  
2047 considered as a two-body process, with the delta baryon, is assumed. This follows  
2048 the T2K oscillation analysis presented in [75], although recent developments of  
2049 the interaction model in the latest T2K oscillation analysis do include effects  
2050 from binding energy in this calculation [200].

2051 The reconstructed neutrino energy for the FHC samples is illustrated in  
2052 Figure 6.4. As expected, the 1R $\mu$ -like and 1Re-like samples are heavily dominated  
2053 by CCQE interactions, with smaller contributions from 2p2h meson exchange and  
2054 resonant pion production interactions. The CC1 $\pi^+$ -like sample predominantly  
2055 consists of charged current resonant pion production interactions. The 1Re-like  
2056 and CC1 $\pi^+$ -like samples are also binned by the angle between the neutrino beam  
2057 and the reconstructed lepton momentum. This is to aid in charged current and  
2058 neutral current separation, as indicated in Figure 6.5. This is because the neutral  
2059 current backgrounds are predominantly due to  $\pi^0$ -decays, which decay into two  
2060  $\gamma$  rays. The opening angle of which (alongside the different final state kinematics)  
2061 can produce a slightly broader angular distribution compared to the final state  
2062 particles originating from charged current  $\nu_e$  interactions.

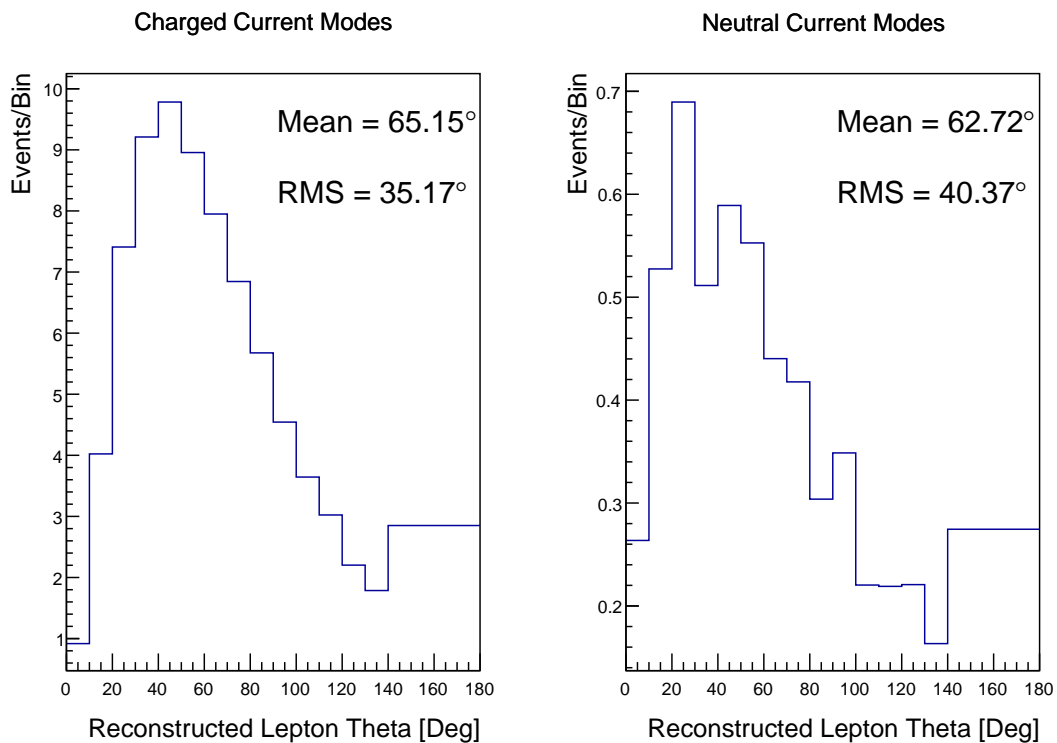


**Figure 6.5:** The distribution of the angle between the neutrino beam direction and the reconstructed final state lepton, for the FHC 1Re-like sample. The distribution is broken down by neutrino interaction mode into charged current (left) and neutral current (right) components. Asimov A oscillation parameter sets are assumed (given in Table 2.2). The RMS of the charged and neutral current plots are  $35.17^\circ$  and  $40.37^\circ$ , respectively.

## 6.4 Systematic Uncertainties

The systematic model parameters for this analysis are split into groups, or blocks, depending on their purpose. They consist of flux uncertainties, neutrino-matter interaction systematics, and detector efficiencies. There are also uncertainties on the oscillation parameters to which this analysis is not sensitive, namely  $\Delta m_{21}^2$  and  $\sin^2(\theta_{12})$ . These oscillation parameter uncertainties are taken from the 2020 PDG measurements [76]. As described in chapter 4, each model parameter used within this analysis requires a prior uncertainty. This is provided via separate covariance matrices for each block. The covariance matrices can include prior correlations between parameters within a single block, but the separate treatment means prior correlations can not be included for parameters in different groups. Some parameters in these models have no reasonably motivated uncertainties and are assigned flat priors which do not modify the likelihood penalty. In practice, these flat prior parameters are actually assigned a Gaussian with a very large width to ensure the covariance matrix is positive definite. They are then checked at run time to determine if they contribute to the likelihood. The flux, neutrino interaction, and detector modeling simulations have already been discussed in section 5.1 and section 5.2. The uncertainties invoked within each of these models are described below.

### 6.4.1 Beam Flux

The neutrino beam flux systematics are based upon the uncertainty in the modeling of the components of the beam simulation. This includes the model of hadron productions and reinteractions, the shape, intensity, and alignment of the beam with respect to the target, and the uniformity of the magnetic field produced by the horn, alongside other effects. The uncertainty, as a function of neutrino energy, is illustrated in Figure 6.6 which includes a depiction of the total uncertainty as well as the contribution from individual components. The uncertainty around the peak of the energy distribution ( $E_\nu \sim 0.6\text{GeV}$ ) is

2091 dominated by uncertainties in the beam profile and alignment. Outside of this  
2092 region, uncertainties on hadron production dominate the error.

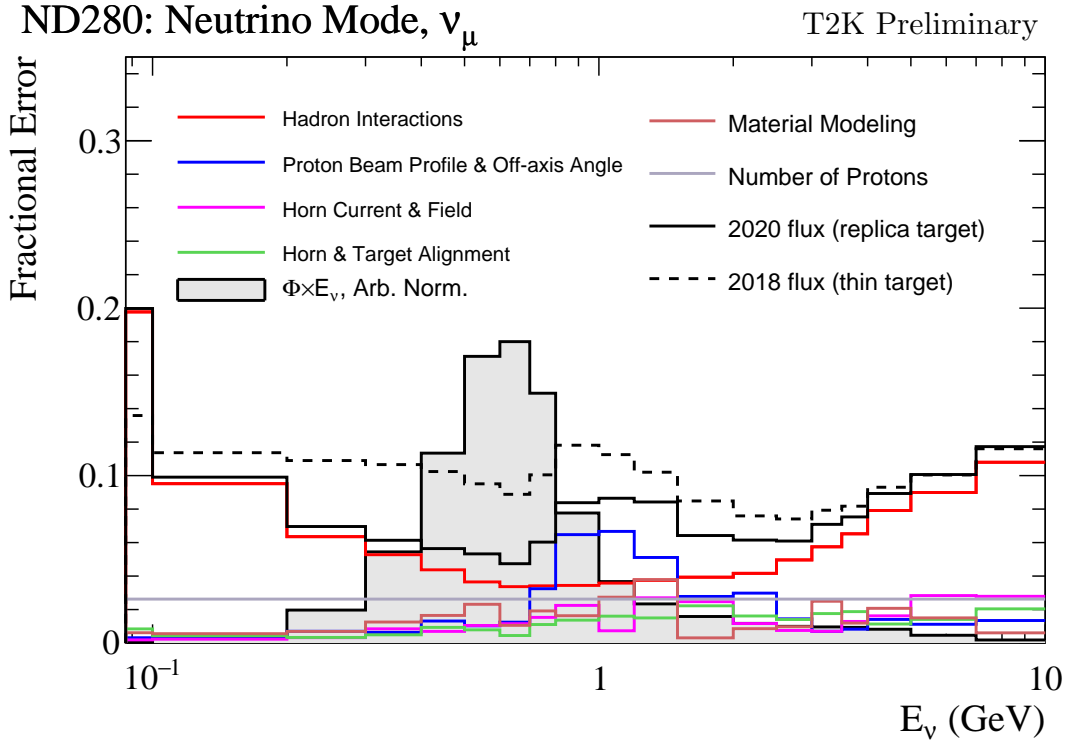


**Figure 6.6:** The total uncertainty evaluated on the near detector  $\nu_\mu$  flux prediction constrained by the replica-target data, illustrated as a function of neutrino energy. The solid(dashed) line indicates the uncertainty used within this analysis(the T2K 2018 analysis [201]). The solid histogram indicates the neutrino flux as a function of energy. Figure taken from [202].

2093 The beam flux uncertainties are described by one hundred parameters. They  
2094 are split between the ND280 and SK detectors and binned by neutrino flavour:  
2095  $\nu_\mu$ ,  $\bar{\nu}_\mu$ ,  $\nu_e$  and  $\bar{\nu}_e$ . The response is then broken down as a function of neutrino  
2096 energy. The bin density in the neutrino energy is the same for the  $\nu_\mu$  in FHC  
2097 and  $\bar{\nu}_\mu$  in RHC beams, and narrows for neutrino energies close to the oscillation  
2098 maximum of  $E_\nu = 0.6\text{GeV}$ . This binning is specified in Table 6.5. All of these  
2099 systematic uncertainties are applied as normalisation parameters with Gaussian  
2100 priors centered at 1.0 and error specified from a covariance matrix provided  
2101 by the T2K beam group [202].

Neutrino Flavour	Sign	Neutrino Energy Bin Edges (GeV)
$\mu$	Right	0., 0.4, 0.5, 0.6, 0.7, 1., 1.5, 2.5, 3.5, 5., 7., 30.
$\mu$	Wrong	0., 0.7, 1., 1.5, 2.5, 30.
$e$	Right	0., 0.5, 0.7, 0.8, 1.5, 2.5, 4., 30.
$e$	Wrong	0., 2.5, 30.

**Table 6.5:** The neutrino energy binning for the different neutrino flavours. “Right” sign indicates neutrinos in the FHC beam and antineutrinos in the RHC beam. “Wrong” sign indicates antineutrinos in the FHC beam and neutrinos in the RHC beam. The binning of the detector response is identical for the FHC and RHC modes as well as at ND280 and SK.

## 2102 6.4.2 Atmospheric Flux

2103 The atmospheric neutrino flux is modeled by the HKKM model [51]. 16 systematic  
 2104 uncertainties are applied to control the normalisation of each neutrino flavour,  
 2105 energy, and direction. They are summarised below:

- 2106 • **Absolute Normalisation:** The overall normalisation of each neutrino flavour  
 2107 is controlled by two independent systematic uncertainties, for  $E_\nu < 1\text{GeV}$   
 2108 and  $E_\nu > 1\text{GeV}$ , respectively. This is driven mostly by hadronic interaction  
 2109 uncertainties for the production of pions and kaons [51]. The strength of  
 2110 the response is dependent upon the neutrino energy. The uncertainty is  
 2111 parameterized following Figure 11 in [51].
- 2112 • **Relative Normalisation:** Uncertainties on the ratio of  $(\nu_\mu + \bar{\nu}_\mu) / (\nu_e + \bar{\nu}_e)$   
 2113 are controlled by the difference between the HKKM model [51], FLUKA  
 2114 [54] and Bartol models [50]. Three independent parameters are applied in  
 2115 the energy ranges:  $E_\nu < 1\text{GeV}$ ,  $1\text{GeV} < E_\nu < 10\text{GeV}$ , and  $E_\nu > 10\text{GeV}$ .
- 2116 •  **$\nu/\bar{\nu}$  Normalisation:** The uncertainties in the  $\pi^+/\pi^-$  (and kaon equivalent)  
 2117 production uncertainties in the flux of  $\nu/\bar{\nu}$ . The response is applied using  
 2118 the same methodology as the relative normalisation parameters.
- 2119 • **Up/Down and Vertical/Horizontal Ratio:** Similar to the above two sys-  
 2120 tematics, the difference between the HKKM, FLUKA, and Bartol model

2121 predictions, as a function of  $\cos(\theta_Z)$ , is used to control the normalisation of  
2122 events as a function of zenith angle.

- 2123 • **K/ $\pi$  Ratio:** Higher energy neutrinos ( $E_\nu > 10\text{GeV}$ ) mostly originate in  
2124 kaon decay. Measurements of the ratio of K/ $\pi$  production [203] are used to  
2125 control the systematic uncertainty of the expected ratio of pion and kaon  
2126 production.
- 2127 • **Solar Activity:** As the 11-year solar cycle can affect the Earth's magnetic  
2128 field, the flux of primary cosmic rays varies across the same period. The  
2129 uncertainty is calculated by taking a  $\pm 1$  year variation, equating to a 10%  
2130 uncertainty for the SK-IV period.
- 2131 • **Atmospheric Density:** The height of the interaction of the primary cosmic  
2132 rays is dependent upon the atmospheric density. The HKKM assumes the  
2133 US standard 1976 [153] profile. This systematic controls the uncertainty in  
2134 that model.

2135 The total uncertainty is dominated by the absolute and relative normalisation  
2136 parameters. The effect of which is illustrated in Figure 6.7. Generally, the  
2137 uncertainty is large at low energy, reducing to  $O(10\%)$  around the peak of the  
2138 flux distribution and then increasing once the neutrino energy exceeds 10GeV.

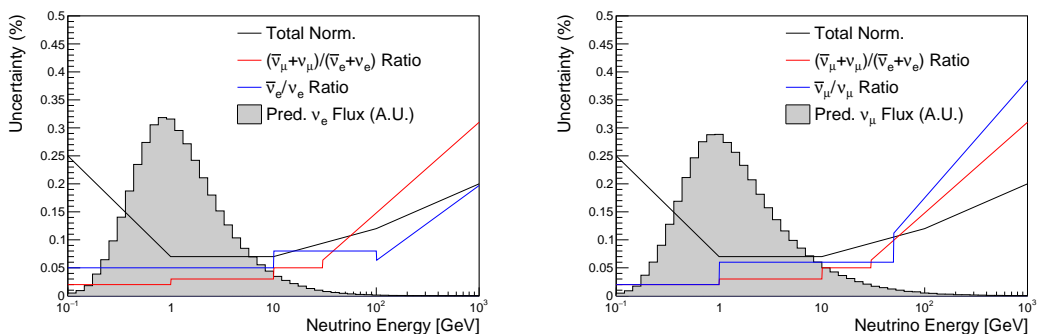


**Figure 6.7:** The uncertainty evaluated on the atmospheric  $\nu_e$  (left) and  $\nu_\mu$  (right) flux predictions. The absolute normalisation and flavour ratio uncertainties are given. The solid histogram indicates the neutrino flux as a function of energy.

2139      Updates to the HKKM and Bartol models are underway [158] to use a similar  
2140      tuning technique to that used in the beam flux predictions. After those updates,  
2141      it may be possible to include correlations in the hadron production uncertainty  
2142      systematics for beam and atmospheric flux predictions.

### 2143      6.4.3 Neutrino Interaction

2144      Neutrino interactions in the detectors are modeled by NEUT. The two indepen-  
2145      dent oscillation analyses, T2K-only [204] and the SK-only [60], have developed  
2146      separate interaction models. To maximise sensitivity out of this simultaneous  
2147      beam and atmospheric analysis, a correlated interaction model has been defined  
2148      in [205]. Where applicable, correlations allow the systematic uncertainties applied  
2149      to the atmospheric samples to be constrained by near detector neutrino beam  
2150      measurements. This can lead to stronger sensitivity to oscillation parameters  
2151      as compared to an uncorrelated model.

2152      The low-energy T2K systematic model has a more sophisticated treatment  
2153      of CCQE, 2p2h, and CCRES uncertainties, where extensive comparisons of  
2154      this model have been performed to external data [204]. However, the model  
2155      is not designed for high-energy atmospheric events, like those illustrated in  
2156      Figure 5.11. Therefore the high energy systematic model from the SK-only  
2157      analysis is implemented for the relevant multi-GeV, PC, and up- $\mu$  samples.  
2158      The T2K CCQE model is more sophisticated so it has been implemented for  
2159      all samples within this analysis, where separate low-energy and high-energy  
2160      dials have been implemented. The low-energy dials are constrained by the near  
2161      detector measurements and are uncorrelated to their high-energy counterparts.  
2162      The author of this thesis was responsible for implementing and validating the  
2163      combined cross-section model as documented in [205, 206].

2164      The high energy systematic model includes parameters developed from  
2165      comparisons of Nieves and Rein-Seghal models which affect resonant pion  
2166      producing interactions, comparisons of the GRV98 and CKMT models which  
2167      control DIS interactions, and hadron multiplicity measurements which modulate

the normalisation of multi-pion producing events. The uncertainty on the  $\nu_\tau$  cross-section is particularly large and is controlled by a 25% normalisation uncertainty. These uncertainties are applied via normalisation or shape parameters. The former linearly scales the weight of all affected Monte-Carlo events, whereas the latter can increase or decrease a particular event's weight depending on its neutrino energy and mode of interaction. The response of the shape parameters is defined by third-order polynomial splines which return a weight for a particular neutrino energy. To reduce computational resources for the far detector fit, the response is binned by neutrino energy and sample binning: lepton momentum and cosine zenith binning for atmospheric splined responses and reconstructed neutrino energy and direction binning for beam samples. In total, 17 normalisation and 15 shape parameters are included in the high-energy model within this analysis.

Figure 6.8 indicates the predicted neutrino energy distribution for both beam and subGeV atmospheric samples. There is clearly significant overlap in neutrino energy between the subGeV atmospheric and beam samples, allowing similar kinematics in the final state particles. Figure 6.9 illustrates the fractional contribution of the different interaction modes per sample.

Comparing beam and atmospheric samples which target CCQE interactions (S.G. e-like 0de, S.G.  $\mu$ -like [0,1]de, [FHC,RHC] 1R  $\mu$ -like and [FHC,RHC] 1R e-like samples), there is a very similar contribution of CCQE, CC 2p2h, and CC1 $\pi^\pm$  interactions. The samples which target CC1 $\pi^\pm$  interactions, (S.G. e-like 0de, S.G.  $\mu$ -like 2de and FHC 1R+1d.e e-like) also consist of very similar mode interactions.

As a consequence of the similarity in energy and mode contributions, correlating the systematic model between the beam and subGeV atmospheric samples ensures that this analysis attains the largest sensitivity to oscillation parameters while still ensuring neutrino interaction systematics are correctly accounted for. Due to its more sophisticated CCQE and 2p2h model, the T2K systematic model was chosen as the basis of the correlated model.

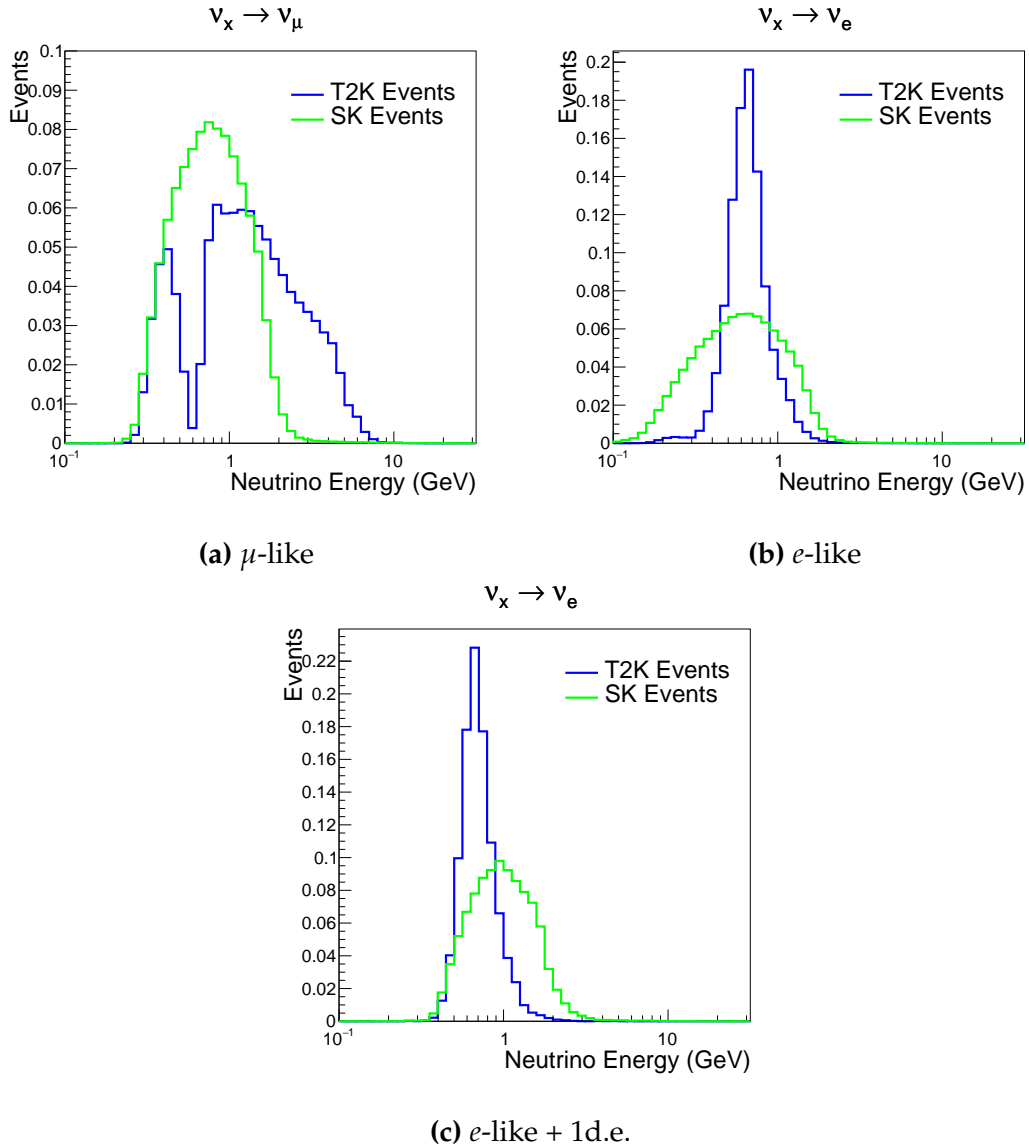


**Figure 6.8:** The predicted neutrino energy distribution for subGeV atmospheric and beam samples. FHC and RHC beam samples are summed together Asimov A oscillation parameters are assumed (given in Table 2.2). Beam and atmospheric samples with similar cuts are compared against one another.

2198     The T2K systematic model [204] is applied in a similar methodology to the  
 2199     SK model parameters. It consists of 19 shape parameters and 24 normalisation  
 2200     parameters. Four additional parameters, which model the uncertainty in the  
 2201     binding energy, are applied in a way to shift the momentum of the lepton emitted  
 2202     from a nucleus. This controls the uncertainty specified on the 27MeV binding  
 2203     energy assumed within Equation 6.2. The majority of these parameters are

	CC QE	CC 2p2h	CC $1\pi^\pm$	CC $M\pi$	CC Other	NC $1\pi^0$	NC $1\pi^\pm$	NC $M\pi$	NC Coh.	NC Other
FHC 1R+1d.e. e-like	<b>0.04</b>	0.02	<b>0.83</b>	0.03	0.04	0.01	0.01	0.01	0.00	0.01
RHC 1R e-like	<b>0.62</b>	0.12	0.11	0.01	0.02	0.06	0.01	0.01	0.01	0.04
FHC 1R e-like	<b>0.68</b>	0.12	0.10	0.00	0.02	0.04	0.01	0.00	0.00	0.02
RHC 1R $\mu$ -like	<b>0.62</b>	0.13	0.17	0.02	0.03	0.00	0.02	0.00	0.00	0.00
FHC 1R $\mu$ -like	<b>0.62</b>	0.12	0.16	0.02	0.03	0.00	0.03	0.00	0.00	0.00
S.G. $\pi^0$ -like	<b>0.05</b>	0.01	0.02	0.00	0.01	<b>0.68</b>	0.06	0.07	0.06	0.04
S.G. $\mu$ -like 2de	<b>0.04</b>	0.01	<b>0.80</b>	0.10	0.04	0.00	0.00	0.00	0.00	0.00
S.G. $\mu$ -like 1de	<b>0.72</b>	0.11	0.12	0.01	0.02	0.00	0.01	0.00	0.00	0.00
S.G. $\mu$ -like 0de	<b>0.68</b>	0.11	0.10	0.01	0.02	0.01	0.05	0.01	0.00	0.02
S.G. e-like 1de	<b>0.05</b>	0.01	<b>0.75</b>	0.10	0.05	0.00	0.01	0.02	0.00	0.01
S.G. e-like 0de	<b>0.73</b>	0.11	0.10	0.01	0.02	0.02	0.00	0.00	0.00	0.00

**Figure 6.9:** The interaction mode contribution of each sample given as a fraction of the total event rate in that sample. Asimov A oscillation parameters are assumed (given in Table 2.2). The Charged Current (CC) modes are broken into quasi-elastic (QE), 2p2h, resonant charged pion production ( $1\pi^\pm$ ), multi-pion production ( $M\pi$ ), and other interaction categories. Neutral Current (NC) interaction modes are given in interaction mode categories:  $\pi^0$  production, resonant charged pion production, multi-pion production, and others.

2204 assigned a Gaussian prior uncertainty. Those that have no reasonably motivated  
 2205 uncertainty, or those which have not been fit to external data, are assigned a  
 2206 flat prior which does not affect the penalty term.

2207 On top of the combination of the SK and T2K interaction models, several  
 2208 other parameters have been specifically developed for the joint oscillation anal-  
 2209 ysis. The majority of the atmospheric samples'  $\delta_{CP}$  sensitivity comes from the  
 2210 normalisation of subGeV electron-like events. These are modeled using a spectral  
 2211 function to approximate the nuclear ground state. However, the near detector is  
 2212 not able to constrain the model so an additional systematic is introduced which  
 2213 models an alternative Continous Random Phase Approximation (CRPA) nuclear  
 2214 ground state. This dial approximates the event weights if a CRPA model had

been assumed rather than a spectral function. This dial only applies to  $\nu_e$  and  $\bar{\nu}_e$  as the near detector does not constraint  $\nu_e$  cross-section measurements. It is applied as a shape parameter.

Further additions to the model have been introduced due to the inclusion of the subGeV  $\pi^0$  atmospheric sample. This particularly targets charged current and neutral current  $\pi^0$  producing interactions to help constrain the systematic uncertainties. Therefore, an uncertainty that affects neutral current resonant  $\pi^0$  production is incorporated into this analysis. Comparisons of NEUT's NC resonant pion production predictions have been made to MiniBooNE [207] data and a consistent 16% to 21% underprediction is observed [205]. Consequently, a conservative 30% normalisation parameter is invoked.

Down-going events are mostly insensitive to oscillation parameters and can act similar to the near detector within an accelerator experiment (Details will be discussed in chapter 7). This region of phase space can act as a sideband and allows the cross-section model and near detector constraint to be studied. The distribution of events in this region is calculated using the technique outlined in subsection 4.3.4. The results are illustrated in Figure 6.10. For CCQE-targeting samples, the application of the near detector constraint is well within the statistical fluctuation of the down-going data. This means there is no significant tension is observed between the data and the Monte Carlo prediction after the near detector constraint is applied. This is not the case for samples with target CCRES interactions. The electron-like data is consistent with the constrained prediction at high reconstructed momenta but diverges at lower momentum, whereas the muon-like sample is under-predicted throughout the range of momenta. To combat this disagreement, an additional cross-section systematic dial, specifically designed to inflate the low pion momentum systematics was developed in [205]. This is a shape parameter implemented through a splined response.

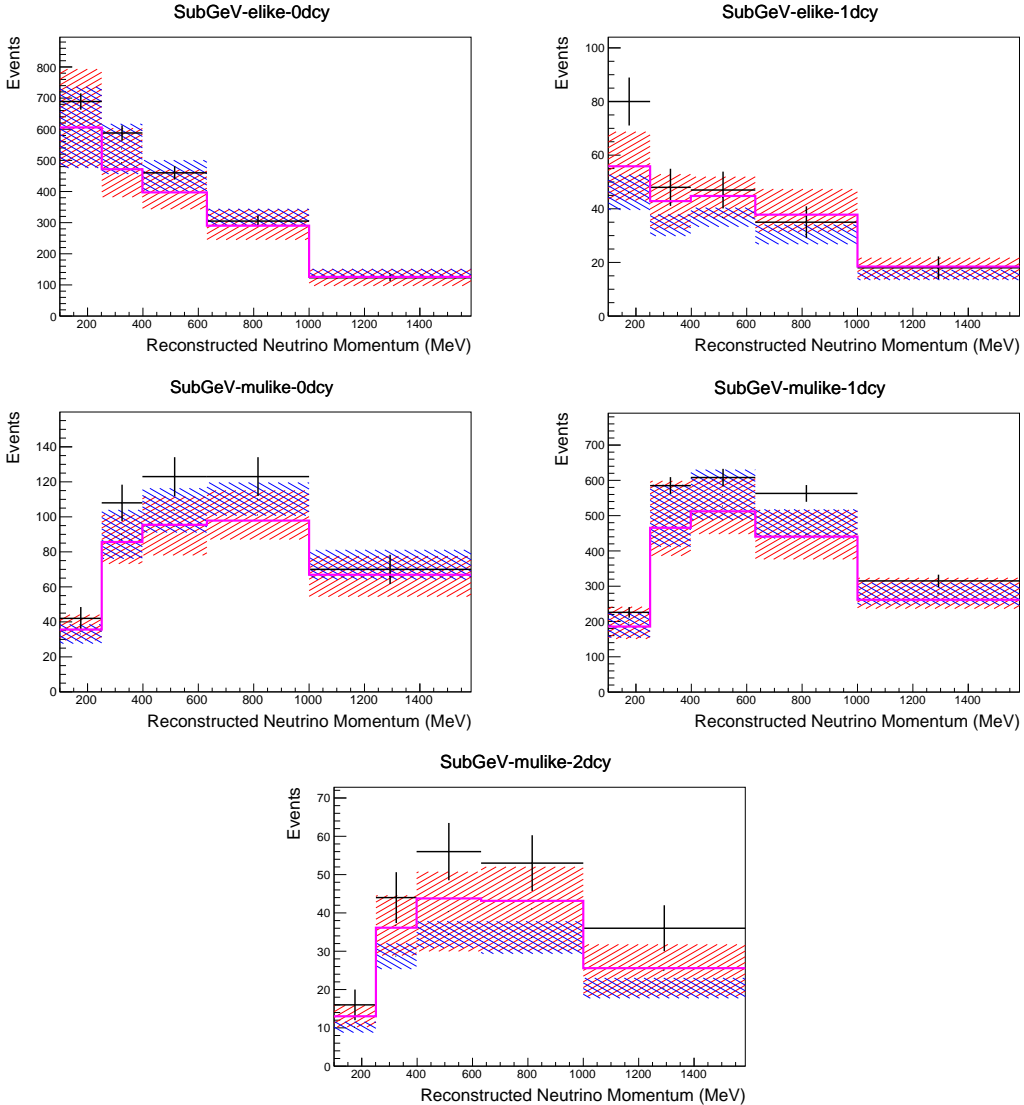


**Figure 6.10:** Down-going atmospheric subGeV single-ring samples comparing the mean and error of the pre-fit and post-fit Monte Carlo predictions in red and blue, respectively. The magenta histogram illustrates the Monte Carlo prediction using the generated dial values. The black points illustrate the down-going data with statistical errors given. The mean and errors of the Monte Carlo predictions are calculated by the techniques documented in subsection 4.3.4. The pre-fit spectrum is calculated by throwing the cross-section and atmospheric flux dial values from the pre-fit covariance matrix. The post-fit spectrum is calculated by sampling the cross-section dial values from an ND fit MCMC chain, whilst still throwing the atmospheric flux dials from the pre-fit covariance.

#### 2242 6.4.4 Near Detector

2243 The systematics applied due to uncertainties arising from the response of the near  
 2244 detector is documented in [132]. The response is described by 574 normalisation  
 2245 parameters binned in the selected sample as well as momentum and angle,

2246  $P_\mu$  and  $\cos(\theta_\mu)$ , of the final-state muon. These are applied via a covariance  
2247 matrix with each parameter being assigned a Gaussian prior from that covariance  
2248 matrix. These normalisation parameters are built from underlying systematics,  
2249 e.g. pion secondary interaction systematics, which are randomly thrown and  
2250 the variation in each  $P_\mu \times \cos(\theta_\mu)$  bin is determined. Two thousand throws are  
2251 evaluated and a covariance matrix response is created. This allows significant  
2252 correlations between FGD1 and FGD2 samples, as well as adjacent  $P_\mu \times \cos(\theta_\mu)$   
2253 bins. Statistical uncertainties are accounted for by including fluctuations of each  
2254 event's weight from a Poisson distribution.

2255 Similar to the cross-section systematics, MaCh3 and BANFF are used to  
2256 constrain the uncertainty of these systematics through independent validations.  
2257 Each fitter generates a post-fit covariance matrix which is compared and passed  
2258 to the far-detector oscillation analysis working group. As the analysis presented  
2259 within this thesis uses the MaCh3 framework, a joint oscillation analysis fit of all  
2260 three sets of samples and their respective systematics is performed.

#### 2261 6.4.5 Far Detector

2262 Two configurations of the far detector systematic model implementation have  
2263 been considered. Firstly, the far detector systematic uncertainties for beam and  
2264 atmospheric samples are taken from their respective analysis inputs, denoted  
2265 “official inputs” analysis, with no correlations assumed between the beam and at-  
2266 mospheric samples. The beam- and atmospheric-specific inputs are documented  
2267 in subsubsection 6.4.5.1 and subsubsection 6.4.5.2. Secondly, an alternative  
2268 detector model has been developed which correlates the response of the SK  
2269 detector systematics between the beam and atmospheric samples. Here, the  
2270 distribution of parameters used for applying event cuts (e.g. electron-muon  
2271 PID separation) is modified within the fit. It follows a similar methodology to  
2272 the beam far detector systematics implementation but performs a joint fit of  
2273 the beam and atmospheric data. This alternative implementation is detailed  
2274 in subsubsection 6.4.5.3.

2275 **6.4.5.1 Beam Samples**

2276 There are 45 systematics which describe the response of the far detector to  
2277 beam events [186], split into 44 normalisation parameters and one energy scale  
2278 systematic. The energy scale systematic is applied as a multiplicative scaling  
2279 of the reconstructed neutrino energy. It is estimated from data-to-Monte Carlo  
2280 differences in the stopping muon sample in [188] and found to be 2.1%. The  
2281 normalisation parameters are assigned a Gaussian error centered at one with  
2282 width taken from a covariance matrix. A detailed breakdown of the generation  
2283 of the covariance matrix is found in [199]. To build the covariance matrix, a fit  
2284 is performed on atmospheric data which has been selected using beam sample  
2285 selection cuts. These cuts use the variables,  $L^i$ , where the index  $i$  is detailed in  
2286 Table 6.6. Each  $L^i$  is a smear,  $\alpha$ , and shift,  $\beta$  parameter such that,

$$L_j^i \rightarrow \bar{L}_j^i = \alpha_j^i L + \beta_j^i \quad (6.4)$$

2287 Where  $L_j^i$  ( $\bar{L}_j^i$ ) correspond to nominal(varied) PID cut parameters given in  
2288 Table 6.6. The shift and smear parameters are nuisance parameters with no prior  
2289 constraints. They are binned by final-state topology,  $j$ , where the binning is given  
2290 in Table 6.7. The final-state topology binning is because the detector will respond  
2291 differently to events that have one or multiple rings. For example, the detector  
2292 will be able to distinguish single-ring events better than two overlapping ring  
2293 events, resulting in different systematic uncertainty for one-ring events compared  
2294 to two-ring events. This approach is used to allow the cut parameter distributions  
2295 to be modified within the fit, allowing for better data to Monte Carlo agreement.

Cut Variable	Parameter Name
0	<code>fitQun e/mu PID</code>
1	<code>fitQun e/pi0 PID</code>
2	<code>fitQun mu/pi PID</code>
3	<code>fitQun Ring-Counting Parameter</code>

**Table 6.6:** List of cut variables that are included within the shift/smear fit documented in [199].

Category	Description
1e	Only one electron above Cherenkov threshold in the final state
1 $\mu$	Only one muon above Cherenkov threshold in the final state
1e+other	One electron and one or more other charged particles above Cherenkov threshold in the final state
1 $\mu$ +other	One muon and one or more other charged particles above Cherenkov threshold in the final state
1 $\pi^0$	Only one $\pi^0$ in the final state
1 $\pi^\pm$ or 1p	Only one hadron (typically charged pion or proton) in the final state
Other	Any other final state

**Table 6.7:** Reconstructed event topology categories on which the SK detector systematics [199] are based.

2296        The mis-modeling of  $\pi^0$  events is also considered. If one of the two rings  
 2297 from a  $\pi^0$  event is missed, this will be reconstructed as a CC $\nu_e$ -like event. This  
 2298 is one of the largest systematics hindering the electron neutrino appearance  
 2299 analyses. Consequently, additional systematics have been introduced to con-  
 2300 strain the mis-modeling of  $\pi^0$  events in SK, binned by reconstructed neutrino  
 2301 energy. To evaluate this systematic uncertainty, a set of “hybrid- $\pi^0$ ” samples is  
 2302 constructed. These events are built by overlaying one electron-like ring from  
 2303 the SK atmospheric neutrino samples or decay electron ring from a stopping  
 2304 cosmic ray muon with one simulated photon ring. Both rings are chosen so  
 2305 that momenta and opening angle follow the decay kinematics of NC  $\pi^0$  events  
 2306 from the T2K-MC. Hybrid- $\pi^0$  Monte Carlo samples with both rings from the  
 2307 SK Monte Carlo are produced to compare with the hybrid- $\pi^0$  data samples and  
 2308 the difference in the fraction of events that pass the  $\nu_e$  selection criteria is used  
 2309 to assign the systematic errors. In order to investigate any data to Monte Carlo  
 2310 differences that may originate from either the higher energy ring or lower energy  
 2311 ring, two samples are built; a sample in which the electron constitutes the higher  
 2312 energy ring from the  $\pi^0$  decay (called the primary sample) and another one in  
 2313 which it constitutes the lower energy ring (called the secondary sample). The  
 2314 standard T2K  $\nu_e$  fitQun event selection criteria are used to select events.

2315        Final contributions to the covariance matrix are determined by supplemen-  
 2316 tary uncertainties obtained by comparing stopping muon data to Monte Carlo

prediction, as first introduced in section 5.2. The efficiency of tagging decay electrons is estimated by the stopping muon data to Monte Carlo differences by comparing the number of one decay electron events to the number of events with one or fewer decay electrons. Similarly, the rate at which fake decay electrons are reconstructed by `fiTQun` is estimated by comparing the number of two decay electron events to the number of events with one or two reconstructed decay electrons. The two sources of systematics are added in quadrature weighted by the number of events with one true decay electron yielding a 0.2% systematic uncertainty. A fiducial volume systematic of  $\pm 2.5\text{cm}$  which corresponds to a 0.5% shift in the normalisation of events is also applied. Additional normalisation uncertainties based on neutrino flavour and interaction mode are also defined in [186, 208, 209].

Two additional sources of uncertainty are included: secondary and photo-nuclear interactions. These are estimated by varying the underlying parameters are building a distribution of sample event rates. These contributions are then added in quadrature to the above covariance matrix. The final uncertainty on the SK detector systematics are provided in Figure 6.11.

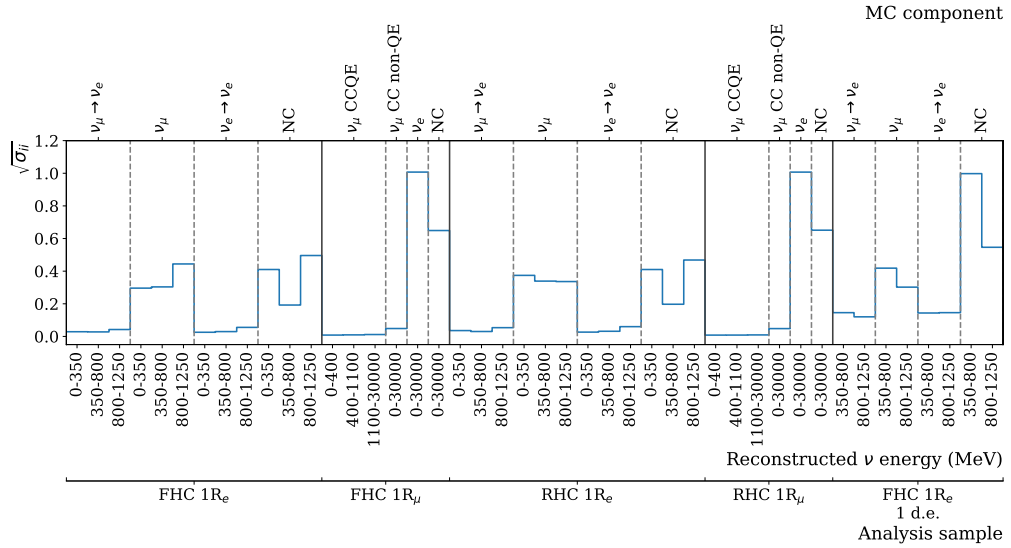


**Figure 6.11:** The uncertainty on each of the 44 parameters describing the SK detector systematics (The energy scale systematic is neglected). The parameters are split by sample, oscillation channel, interaction mode and reconstructed neutrino energy.

#### 2334 6.4.5.2 Atmospheric Samples

2335 The detector systematics for atmospheric samples, documented in [88], are split  
2336 into two sub-groups: those which are related to particle identification and ring  
2337 counting systematics, and those which are related to calibration, separation,  
2338 and reduction uncertainties.

2339 The particle identification systematics consist of five parameters. The ring sep-  
2340 aration systematic enforces an anti-correlated response between the single-ring  
2341 and multi-ring samples. This is implemented as a fractional increase/decrease  
2342 in the overall normalisation of each sample, depending on the distance to the  
2343 nearest wall from an event's vertex. The coefficients of the normalisation are  
2344 estimated prior to the fit and depend on the particular atmospheric sample. Two  
2345 electron-muon separation systematics are included within this model which  
2346 anti-correlates the response of the electron-like and muon-like samples: one for  
2347 single-ring events and another for multi-ring events.

2348 The multi-ring electron-like separation likelihood, discussed in section 6.1,  
2349 encodes the ability of the detector to separate neutrino from anti-neutrino events.  
2350 Two normalisation parameters vary the relative normalisation of multi-ring  $\nu_e$   
2351 and  $\bar{\nu}_e$  samples whilst keeping a consistent overall event rate.

2352 There are 22 systematics related to calibration measurements, including effects  
2353 from backgrounds, reduction, and showering effects. They are documented in  
2354 [88] and are briefly summarised in Table 6.8. They are applied via normalisation  
2355 parameters, with the separation systematics requiring the conservation of event  
2356 rate across all samples.

#### 2357 6.4.5.3 Correlated Detector Model

2358 A complete uncertainty model of the SK detector would be able to determine  
2359 the systematic shift on the sample spectra for a variation of the underlying  
2360 parameters, e.g. PMT angular acceptance. However, this is computationally  
2361 intensive, requiring Monte Carlo predictions to be made for each plausible  
2362 variation. Consequently, an effective parameter model has been utilised for

Index	Description
0	Partially contained reduction
1	Fully contained reduction
2	Separation of fully contained and partially contained events
3	Separation of stopping and through-going partially contained events in top of detector
4	Separation of stopping and through-going partially contained events in barrel of detector
5	Separation of stopping and through-going partially contained events in bottom of detector
6	Background due to cosmic rays
7	Background due to flasher events
8	Vertex systematic moving events into and out of fiducial volume
9	Upward going muon event reduction
10	Separation of stopping and through-going in upward going muon events
11	Energy systematic in upward going muon events
12	Reconstruction of the path length of upward going muon events
13	Separation of showering and non-showering upward going muon events
14	Background of stopping upward going muon events
15	Background of non-showering through-going upward going muon events
16	Background of showering through-going upward going muon events
17	Efficiency of tagging two rings from $\pi^0$ decay
18	Efficiency of decay electron tagging
19	Background from downgoing cosmic muons
20	Asymmetry of energy deposition in tank
21	Energy scale deposition

**Table 6.8:** Sources of systematic errors specified within the grouped into the “calibration” systematics model.

2363 a correlated detector model following from the T2K-only model implementation  
 2364 documented in subsubsection 6.4.5.1. It correlates the detector systematics  
 2365 between the far-detector beam and subGeV atmospheric samples due to their  
 2366 similar energies and interaction types. As there are no equivalent beam samples,  
 2367 the multi-GeV, multiring, PC, and Up- $\mu$  samples will be subject to the particle  
 2368 identification systematics implementation as described in subsubsection 6.4.5.2  
 2369 rather than using this correlated detector model. The calibration systematics also  
 2370 described in the aforementioned chapter still apply to all atmospheric samples.  
 2371 The correlated detector model utilises the same smear and shift parameters  
 2372 documented in subsubsection 6.4.5.1, split by final state topology. Beyond this,

the shift and smear parameters are split by visible energy deposited within the detector, with binning specified in Table 6.9. This is because atmospheric events are categorised by subGeV and multi-GeV events based on visible energy, so this splitting is required when correlating the systematic model for beam and atmospheric events. Alongside the technical requirement, higher energy events will be better reconstructed due to fractionally less noise within the detector. As a result of the inclusion of visible energy binning, Equation 6.4 becomes

$$L_{jk}^i \rightarrow \bar{L}_{jk}^i = \alpha_{jk}^i L + \beta_{jk}^i, \quad (6.5)$$

where  $k$  is the visible energy bin.

Index	Range (MeV)
0	$30 \geq E_{vis} > 300$
1	$300 \geq E_{vis} > 700$
2	$700 \geq E_{vis} > 1330$
3	$E_{vis} \geq 1330$

**Table 6.9:** Visible energy binning for which the correlated SK detector systematics are based

The implementation of this systematic model takes the events reconstructed values of the cut parameters, modifies them by the particular shift and smear parameter for that event, and then re-applies event selection. This causes event migration, which is a new feature incorporated into the MaCh3 framework which is only achievable due to the event-by-event reweighting scheme.

Particular care has to be taken when varying the ring counting parameter. This is because the number of rings is a finite value (one-ring, two-ring, etc.) which can not be continuously varied through this shift and smear technique. Consequently a continuous ring counting parameter,  $RC_i$ , is calculated for the  $i^{th}$  event, following the definition in [185]: the preferred likelihoods from all considered one-ring ( $L_{1R}$ ) and two-ring ( $L_{2R}$ ) fits are determined. The difference

is computed as  $\Delta_{LLH} = \log(L_{1R}) - \log(L_{2R})$ . The ring counting parameter is then defined as

$$RC_i = \text{sgn}(\Delta_{LLH}) \times \sqrt{|\Delta_{LLH}|}, \quad (6.6)$$

where  $\text{sgn}(x) = x/|x|$ . This ring counting parameter corresponds to an intermediate likelihood value used within the `fitQun` algorithm to decide the number of rings associated with a particular event. However, fake-ring merging algorithms are applied after this likelihood value is used. Consequently, this ring counting parameter does not always exactly correspond to the number of reconstructed rings. This can be seen in Figure 6.12.

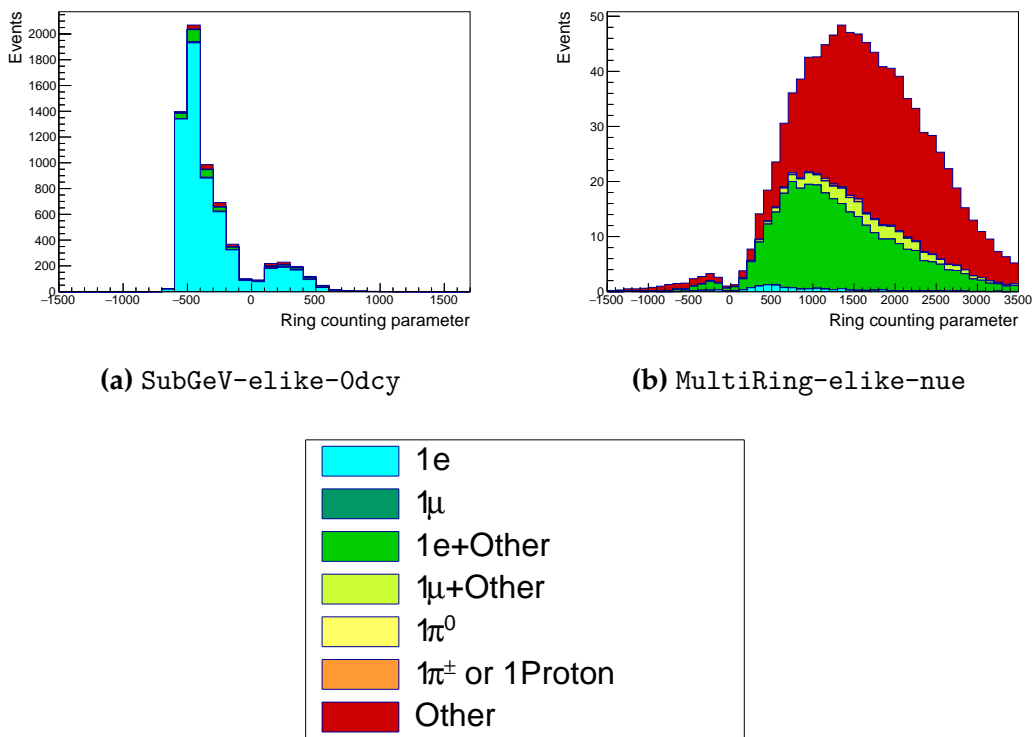


**Figure 6.12:** The ring counting parameter as defined in Equation 6.6 for the SubGeV-elike-0dcy and MultiRing-elike-nue samples.

As the `fitQun` algorithm does not provide a likelihood value after the fake-ring algorithms have been applied, the ring counting parameter distribution is correlated to the final number of reconstructed rings through “maps”. These

2403 are two-dimensional distributions of the ring counting parameter and the final  
 2404 number of reconstructed rings. An example is illustrated in Figure 6.13. In  
 2405 principle, the `fitQun` reconstruction algorithm should be re-run after the variation  
 2406 in the ring counting parameter. However, this is not computationally viable.  
 2407 Therefore the “maps” are used as a reweighting template.

2408 The maps are split by final state topology and true neutrino flavour and  
 2409 all `fitQun`-reconstructed Monte Carlo events are used to fill them. The maps  
 2410 are row-normalised to represent the probability of  $X$  rings for a given  $RC_i$   
 2411 value. Prior to the oscillation fit, an event’s nominal weight is calculated as  
 2412  $W^i(N_{Rings}^i, L_{jk}^i)$ , where  $N_{Rings}^i$  is the reconstructed number of rings for the  $i^{th}$   
 2413 event and  $W^i(x, y)$  is the bin content in map associated with the  $i^{th}$  event, where  
 2414  $x$  number of rings and  $y$  is ring counting parameter. Then during the fit, the  
 2415 value of  $R = W^i(N_{Rings}^i, \bar{L}_{jk}^i) / W^i(N_{Rings}^i, L_{jk}^i)$  is calculated as the event weight  
 2416 for the  $i^{th}$  event. This is the only cut variable that uses a reweighting technique  
 2417 rather than event migration.

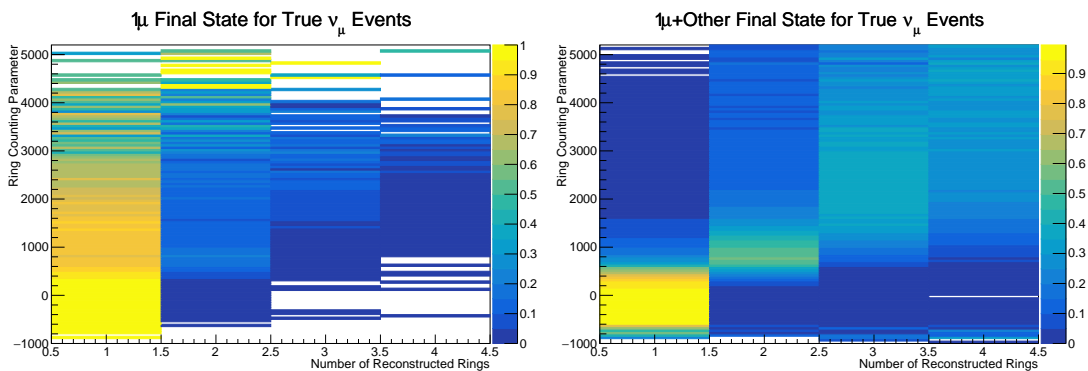


**Figure 6.13:** The ring counting parameter, defined in Equation 6.6, as a function of the number of reconstructed rings as found by the `fitQun` reconstruction algorithm. Left: true  $\nu_\mu$  events with only one muon above the Cherenkov threshold in the final state. Right: true  $\nu_\mu$  events with one muon and at least one other charged particle above the Cherenkov threshold in the final state.

2418 The  $\pi^0$  systematics introduced in subsection 6.4.4 are applied via a covariance  
 2419 matrix. This is not possible in the alternative model as no covariance matrix  
 2420 is used. Thus, the implementation of the  $\pi^0$  systematics has been modified.  
 2421 The inputs from the hybrid  $\pi^0$  sample are included via the use of “ $\chi^2$  maps”,

which are two-dimensional histograms in  $\alpha_{jk}^i$  and  $\beta_{jk}^i$  parameters over some range. Illustrative examples of the  $\chi^2$  maps are given in Figure 6.14. Due to their nature, the shift and smear parameters are typically very correlated. A map is produced for each cut parameter given in Table 6.6 and for each visible energy bin given in Table 6.9.

The maps are filled through the  $\chi^2$  comparison of the hybrid  $\pi^0$  Monte Carlo and data in the particle identification parameters documented in Table 6.6. The Monte Carlo distribution is modified by the  $\alpha_{jk}^i$  and  $\beta_{jk}^i$  scaling, whilst cross-section and flux nuisance parameters are thrown from their prior uncertainties. The  $\chi^2$  between the scaled Monte Carlo and data is calculated and the relevant point in the  $\chi^2$  map is filled.

The implementation within this alternative detector model is to add the bin contents of the maps, for the relevant values of the  $\alpha_{jk}^i$  and  $\beta_{jk}^i$  parameters, to the likelihood penalty. Only  $1\pi^0$  final state topology shift and smear parameters use this prior uncertainty.

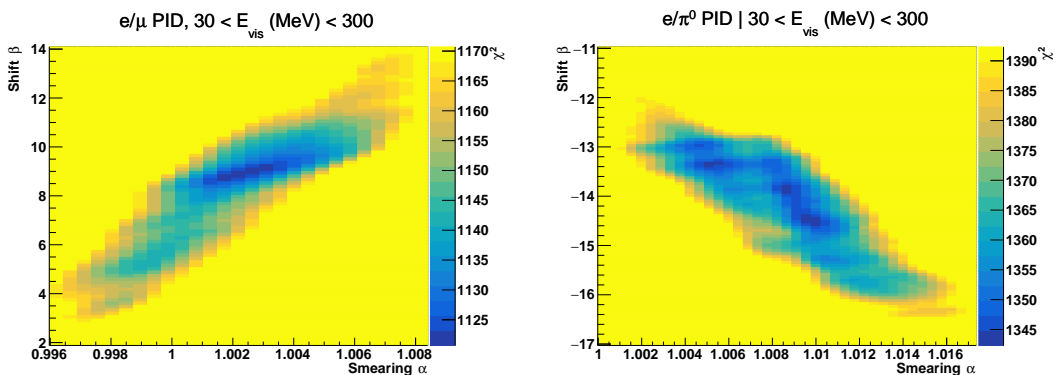


**Figure 6.14:** The  $\chi^2$  between the hybrid- $\pi^0$  Monte Carlo and data samples, as a function of smear ( $\alpha$ ) and shift ( $\beta$ ) parameters, for events which have  $1\pi^0$  final state topology. Left: Electron-muon separation PID parameter for events with  $30 \leq E_{\text{vis}}(\text{MeV}) < 300$ . Right: Electron- $\pi^0$  separation PID parameter for events with  $30 \leq E_{\text{vis}}(\text{MeV}) < 300$ .

Similarly, the implementation of the supplementary systematics documented in subsubsection 6.4.5.1 needs to be modified. A new framework [210] was built in tandem with the T2K-SK working group [186] so the additional parameters can be incorporated into the MaCh3 framework. These are applied as normalisation parameters, depending on the particular interaction mode, number of tagged

2442 decay electrons, and whether the primary particle generated Cherenkov light.  
2443 They are assigned Gaussian uncertainties with widths described by a covariance  
2444 matrix. Furthermore, the secondary interaction and photo-nuclear effects need to  
2445 be accounted for in this detector model using a different implementation than  
2446 that in subsubsection 6.4.5.1. This was done by including a shape parameter for of  
2447 each of the secondary interactions and the photo-nuclear systematic parameters.

2448 There are a total of 224  $\alpha_{jk}^i$  and  $\beta_{jk}^i$  parameters, of which 32 have prior  
2449 constraints from the hybrid  $\pi^0$  samples.

2450 One final complexity of this correlated detector model is that the two sets  
2451 of samples, beam and subGeV atmospheric, use slightly different parameters  
2452 to distinguish electron and muon-like events. The T2K samples use the value  
2453 of  $\log(L_e/L_\mu)$  whereas the atmospheric samples use the value of  $\log(L_e/L_\pi)$ ,  
2454 where  $L_X$  is the likelihood for hypothesis X. This is because the T2K fits use  
2455 single-ring fiTQun fitting techniques, whereas multi-ring fits are applied to the  
2456 atmospheric samples where only the electron and pion hypothesis are considered.  
2457 The correlation between the two likelihood ratios is illustrated in Figure 6.15. As  
2458 discussed in section 5.2, the pion hypothesis is a very good approximation of the  
2459 muon hypothesis due to their similar mass. Consequently, using the same shift  
2460 and smear parameters correlated between the beam and subGeV atmospheric  
2461 samples is deemed a good approximation.

## 2462 6.5 Likelihood Calculation

2463 This analysis performs a joint oscillation parameter fit of the ND280 beam  
2464 samples, the T2K far detector beam samples, and the SK atmospheric samples  
2465 introduced in this chapter.

2466 Once the Monte Carlo predictions of each beam and atmospheric sample  
2467 have been built, a likelihood needs to be constructed. This is done by comparing  
2468 the binned Monte Carlo prediction to binned data. The Monte Carlo prediction  
2469 is calculated at a particular point,  $\vec{\theta}$ , in the model parameter space such that  
2470  $N_i^{MC} = N_i^{MC}(\vec{\theta})$ , where  $N_i$  represents the bin content of the  $i^{th}$  bin. The data

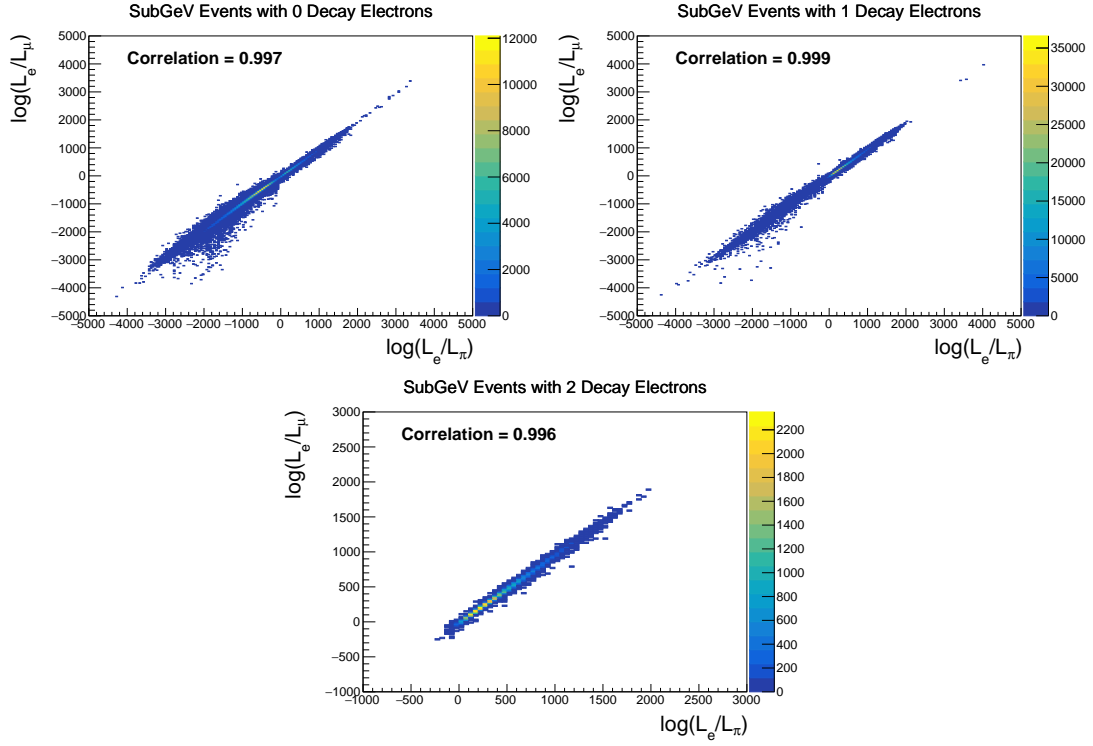


**Figure 6.15:** The distribution of  $\log(L_e/L_\mu)$  compared to  $\log(L_e/L_\pi)$  for subGeV events with zero (top left), one (top right) or two (bottom) decay electrons. The correlation in the distribution is calculated as 0.997, 0.999 and 0.996, respectively.

and Monte Carlo spectra are represented by  $N_i^D$  and  $N_i^{MC}$ , respectively. The bin contents for the beam near detector, beam far detector and atmospheric samples are denoted with  $ND$ ,  $FD$ , and  $Atm$ , respectively. The binning index,  $i$ , runs over all the bins within a sample. Taking the FHC1Rmu far detector sample as an example, the binning index runs over all the reconstructed neutrino energy bins. The likelihood calculation between the data and the Monte Carlo prediction for a particular bin follows a Poisson distribution, where the data is treated as a fluctuation of the simulation.

The data can consist of either real data or an ‘Asimov’ Monte Carlo prediction, which is typically used for sensitivity studies and denoted ‘Asimov data’. The process for building Asimov data is as follows. The Monte Carlo prediction is reweighted using a particular set of oscillation parameters (potentially those listed in Table 2.2) and systematic parameter tune. The resulting spectra for each sample is then defined to be the Asimov data for that sample. Whilst this results

2485 in unphysical non-integer data predictions, it eliminates statistical fluctuations  
 2486 from the data. Therefore, the results of a fit to Asimov data should not include any  
 2487 biases from statistical fluctuations. Furthermore, these results should produce  
 2488 posterior probability distributions consistent with the parameters which were  
 2489 used to make the data prediction. That is to say, the fit results should return the  
 2490 known parameters. Any biases seen would be attributed to correlations between  
 2491 each oscillation parameter and correlations between oscillation and systematic  
 2492 parameters. Consequently, Asimov fit results present the maximum precision  
 2493 at which the oscillation parameters could be measured to.

2494 Following the T2K analysis presented in [75], the likelihood contribution for  
 2495 the near detector samples also includes a Monte Carlo statistical uncertainty term,  
 2496 derived from the Barlow and Beeston statistical treatment [211, 212]. In addition  
 2497 to treating the data as a Poisson fluctuation of the Monte Carlo prediction, it  
 2498 includes a contribution to the likelihood that which treats the generated Monte  
 2499 Carlo prediction as a statistical fluctuation of the actual true simulation assuming  
 2500 an infinite amount of statistics had been created. The technical implementation  
 2501 of this additional likelihood term is documented in [194] and briefly summarised  
 2502 as follows. The term is defined as,

$$\frac{(\beta_i - 1)^2}{2\sigma_{\beta_i}^2}, \quad (6.7)$$

2503 where  $\beta_i$  represents a scaling parameter for the  $i^{th}$  bin that relates the bin  
 2504 content for the amount of Monte Carlo actually generated  $N_i^{MC}$  to the bin content  
 2505 if an infinite amount of Monte Carlo statistics had been generated  $N_{i,true}^{MC}$ , such  
 2506 that  $N_{i,true}^{MC} = \beta_i \times N_i^{MC}$ . In the case where a sufficient amount of Monte Carlo  
 2507 statistics had been generated,  $\beta_i = 1$ . An analytical solution for  $\beta_i$  is given in  
 2508 [194]. Additionally,  $\sigma_{\beta_i} = \sqrt{\sum_i w_i^2 / N_i^{MC}}$  where  $\sqrt{\sum_i w_i^2}$  represents the sum of  
 2509 the square of the weights of the Monte Carlo events which fall into bin  $i$ .

2510 An additional contribution to the likelihood comes from the variation of  
 2511 the systematic model parameters. For those parameters with well-motivated  
 2512 uncertainty estimates, a covariance matrix,  $V$ , describes the prior knowledge of

each parameter as well as any correlations between the parameters. Due to a technical implementation, a single covariance matrix describes each “block” of model parameters, e.g. beam flux systematics. The covariance matrix associated with the  $k^{th}$  block is denoted  $V^k$ . This substitution results in  $\vec{\theta} = \sum_k^{N_b} \vec{\theta}^k$  and  $V = \sum_k^{N_b} V^k$  where  $N_b$  denotes the number of blocks. A single covariance matrix is provided for: the oscillation parameters, the beam flux parameters, the atmospheric flux parameters, the neutrino interaction systematics, the near detector parameters, the beam far detector systematics, and the atmospheric far detector systematics. The number of parameters in the  $k^{th}$  block is defined as  $n(k)$ .

The equation for the likelihood  $\mathcal{L}$  includes all the terms discussed above. It is defined as,

$$\begin{aligned}
-\ln(\mathcal{L}) = & \\
& \sum_i^{\text{NDbins}} N_i^{\text{ND},MC}(\vec{\theta}) - N_i^{\text{ND},D} + N_i^{\text{ND},D} \times \ln \left[ N_i^{\text{ND},D} / N_i^{\text{ND},MC}(\vec{\theta}) \right] + \frac{(\beta_i - 1)^2}{2\sigma_{\beta_i}^2} \\
& + \sum_i^{\text{FDbins}} N_i^{\text{FD},MC}(\vec{\theta}) - N_i^{\text{FD},D} + N_i^{\text{FD},D} \times \ln \left[ N_i^{\text{FD},D} / N_i^{\text{FD},MC}(\vec{\theta}) \right] \\
& + \sum_i^{\text{Atmbins}} N_i^{\text{Atm},MC}(\vec{\theta}) - N_i^{\text{Atm},D} + N_i^{\text{Atm},D} \times \ln \left[ N_i^{\text{Atm},D} / N_i^{\text{Atm},MC}(\vec{\theta}) \right] \\
& + \frac{1}{2} \sum_k^{N_b} \sum_i^{n(k)} \sum_j^{n(k)} (\vec{\theta}^k)_i (V^k)_{ij}^{-1} (\vec{\theta}^k)_j.
\end{aligned} \tag{6.8}$$

The negative log-likelihood value is determined at each step of the MCMC to build the posterior distribution defined in chapter 4. This value is minimised when the Monte Carlo prediction tends towards the data spectrum.

# 7

2527

2528

## Oscillation Probability Calculation

2529 It is important to understand how and where the sensitivity to the oscillation  
2530 parameters comes from for both atmospheric and beam samples. An  
2531 overview of how these samples respond to changes in  $\delta_{CP}$ ,  $\Delta m_{32}^2$ , and  $\sin^2(\theta_{23})$   
2532 is given in section 2.5. This section also explains the additional complexities  
2533 involved when performing an atmospheric neutrino analysis as compared to  
2534 a beam-only analysis.

2535 Without additional techniques, atmospheric sub-GeV upward-going neutrinos ( $E_\nu < 1.33\text{GeV}, \cos(\theta_Z) < 0.$ ) can artificially inflate the sensitivity to  $\delta_{CP}$   
2536 due to the quickly varying oscillation probability in this region. Therefore, a  
2537 “sub-sampling” approach has been developed to reduce these biases ensuring  
2538 accurate and reliable sensitivity measurements. This technique ensures that small-  
2539 scale unresolvable features of the oscillation probability have been averaged over  
2540 whilst the large-scale features in the oscillation probability are unaffected. The  
2541 documentation and validation of this technique are found in section 7.1. The  
2542 oscillation probability calculation is computationally intensive due to the large  
2543 number of matrix multiplications needed. Consequently, the CUDAProb3 imple-  
2544 mentation choice made within the fitting framework, as detailed in section 7.2,  
2545 ensures that the analysis can be done in a timely manner.

Whilst the beam neutrinos are assumed to propagate through a constant density slab of material, the density variations through the Earth result in more complex oscillation patterns for atmospheric neutrinos. Furthermore, the uncertainty in the electron density can modify the oscillation probability for the denser core layers of the Earth. The model of the Earth used within this analysis is detailed in section 7.3. This includes information about the official SK-only methodology as well as improvements that have been made to remove some of the approximations used in that analysis. Another complexity of atmospheric neutrino oscillation studies is that the height of production in the atmosphere is not known on an event-by-event basis. An analytical averaging technique that approximates the uncertainty of the oscillation probability has been followed, with the author of this thesis being responsible for the implementation and validation. This implementation of an external technique is described in section 7.4.

## 7.1 Treatment of Fast Oscillations

As shown in Figure 7.1, atmospheric neutrino oscillations have a significantly more complex structure for upgoing neutrinos with energy below 1GeV. This is because the  $L/E$  dependence of the oscillation probability in this region induces rapid variations for small changes in  $L$  or  $E$ . As discussed in section 2.5, this is also the region in which atmospheric neutrinos have sensitivity to  $\delta_{CP}$ . In practice, the direction of the neutrino is inferred from the direction of the final state particles traveling in the detector. The correlation between these two directions can be particularly weak for low-energy neutrino interactions. This creates a distinct difference from the beam neutrinos where the position of the source is very precisely known.

As a consequence of the unresolvable structure, an event rate consistent with the averaged oscillation probability is observed in the subGeV upgoing region. This creates a computational problem: A significantly large amount of Monte Carlo statistics would be required to accurately predict the number of events if Monte Carlo averaging was the only technique used. This section describes

2576 the ‘sub-sampling’ approach developed for this analysis and compares it to the  
2577 methodology used within the SK-only analysis.

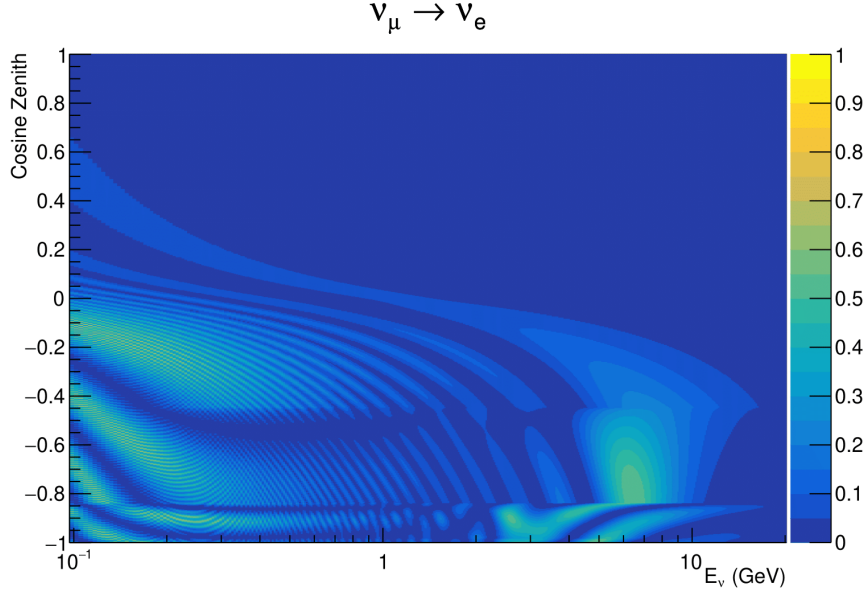


**Figure 7.1:** The oscillation probability  $P(\nu_\mu \rightarrow \nu_e)$ , given as a function of neutrino energy and zenith angle, which highlights an example of the “fast” oscillations in the sub-GeV upgoing region.

2578 The official SK-only analysis uses the osc3++ oscillation parameter fitter  
2579 [79]. To perform the fast oscillation averaging, it uses a ‘nearest-neighbour’  
2580 technique. For a given Monte Carlo neutrino event, the nearest twenty Monte  
2581 Carlo neighbours in reconstructed lepton momentum and zenith angle are  
2582 found and a distribution of their neutrino energies is built. The RMS,  $\sigma$ , of  
2583 this distribution is then used to compute an average oscillation probability for  
2584 the given neutrino Monte Carlo event.

2585 For the  $i^{th}$  event, the oscillation weight is calculated as

$$W_i = \frac{1}{5}P(E_i, \bar{L}_i) + \frac{1}{5}\sum_{\beta=-1, -0.5, 0.5, 1} P(E_i + \beta\sigma_i, L_\beta), \quad (7.1)$$

2586 where  $P(E, L)$  is the oscillation probability calculation for neutrino energy  $E$   
2587 and path length  $L$  and the two path lengths,  $\bar{L}_i$  and  $L_\beta$  are described below. All  
2588 of the oscillation probability calculations are performed with a fixed zenith angle  
2589 such that the same density profile is used. The uncertainty in the production

height is controlled by using an “average” production height,  $\bar{L}_i$ , which represents the average path length computed using twenty production heights taken from the Honda flux model’s prediction [53]. These inputs are provided in 5% intervals of the cumulative distribution function. The value of  $\bar{L}_i$  is calculated as:

$$\bar{L}_i = \frac{1}{20} \sum_{j=1}^{20} \sqrt{(R_E + h_j)^2 - R_E^2 (1 - \cos^2 \theta_i)} - R_E \cos \theta_i. \quad (7.2)$$

Where  $R_E$  is the Earth’s radius and  $\theta_i$  is the zenith angle of the  $i^{th}$  event. The production heights  $h_j$  represent the  $(j \times 5)^{th}$  percentile of the cumulative distribution function.  $L_\beta$  values (where the values of  $\beta$  are given in Equation 7.1) are similarly calculated but instead use different combinations of four production heights,

$$\begin{aligned} L_{-1.0} &= \frac{1}{4} L(45, 50, 55, 60), \\ L_{-0.5} &= \frac{1}{4} L(35, 40, 65, 70), \\ L_{+0.5} &= \frac{1}{4} L(25, 30, 75, 68), \\ L_{+1.0} &= \frac{1}{4} L(15, 20, 85, 89). \end{aligned} \quad (7.3)$$

Where  $L(i, j, k, l)$  represents the sum of the path lengths with fixed zenith angle and production heights corresponding to the  $i^{th}$ ,  $j^{th}$ ,  $k^{th}$  and  $l^{th}$  percentile of the cumulative distribution function. The values that are taken as  $\beta$  (and values for  $L_\beta$ ) are chosen to smooth the oscillation contours in  $\Delta m_{32}^2$  without incurring loss of sensitivity [213].

This averaging technique works because of the inference between the zenith angle and the reconstructed direction of final state particles in the detector. For low-energy neutrinos, where the resolution of the true neutrino direction is poor,  $\sigma_i$  will be large, resulting in significant averaging effects. Contrary to this, the inferred direction of high-energy neutrinos will be much closer to the true value, meaning that  $\sigma_i$  will be smaller, culminating in small averaging effects.

In practice, these calculations are performed prior to the fit as only oscillation parameters at fixed points are considered. The MCMC technique used in this thesis requires oscillation probabilities to be evaluated at arbitrary parameter values, not known *a priori*. Calculating the five oscillation probabilities per event required by the SK technique is computationally infeasible, so a different averaging technique is used. However, the concept of the averaging technique can be taken from it.

To perform a similar averaging as the SK analysis, a sub-sampling approach using binned oscillograms has been devised. A coarsely binned oscillogram is defined in  $\cos(\theta_Z)$  and  $E_\nu$ . For a given set of oscillation parameters, a single oscillation probability will be assigned to each coarse bin. This value will then apply to all Monte Carlo events which fall into that bin. To assign these oscillation probabilities, the probability is calculated at  $N \times N$  points on a grid within a particular bin. This ensemble of oscillation probabilities is averaged to define the coarse bin's oscillation probability, assuming a flat prior in  $E_\nu$  and  $\cos(\theta_Z)$  within the bin. Figure 7.2 illustrates the  $N = 2$  example where the assigned value to a coarse bin is the average of the four fine bins which fall in that coarse bin. Whilst the coarse bin edges do not have to be linear on either axis, the sub-division of the fine bins is linear within the range of a coarse bin.

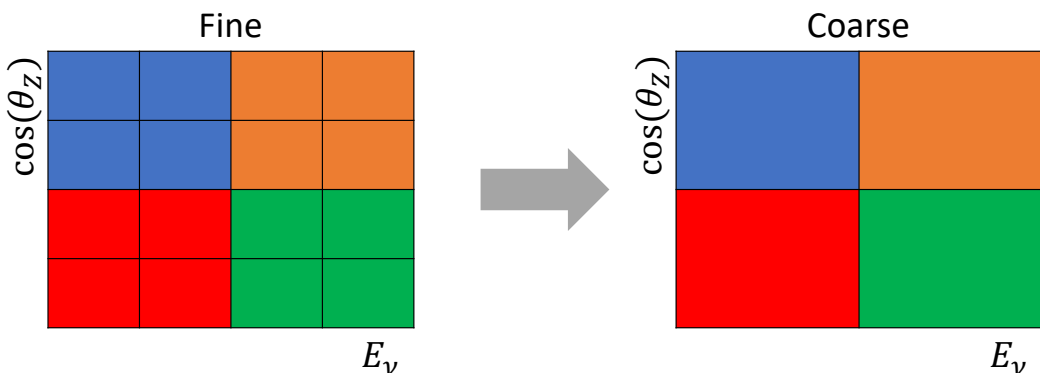


**Figure 7.2:** Illustration of the averaging procedure for  $N = 2$ . The oscillation probabilities calculated on the finer left binning are averaged to obtain the oscillation probabilities in the coarser right binning. These averaged oscillation probabilities with the coarser binning are then applied to each event during the fit.

The coarse binning is defined with  $67 \times 52$  bins in true neutrino energy  $\times$  cosine zenith. It is picked to be identical to that provided in [213]. In general, the binning is logarithmically spaced in neutrino energy but has some hand-picked bin edges around the matter resonance to smoothly increased the bin density. This is to avoid smearing this region which can be well sampled by the Monte Carlo. The cosine zenith binning is approximately linearly spaced across the allowable range but the values of layer transitions are hit precisely:  $-0.8376$  (core-mantle) and  $-0.4464$  (mantle/transition zone). Bins are spread further apart for downgoing events as this is a region unaffected by the fast oscillation wavelengths and reduces the total number of calculations required to perform the calculation.

The choice of  $N$  is justified based on two studies. Firstly, the variation of event rates of each sample is studied as a function of  $N$ . For a given set of oscillation parameters thrown from the PDG prior constraints (detailed in Table 2.1), the oscillation probabilities are calculated using a given value of  $N$ . Each sample is re-weighted and the event rate is stored. The value of  $N$  is scanned from 1, which corresponds to no averaging, to 19, which corresponds to the largest computationally viable subdivision binning. The event rate of each sample at large  $N$  is expected to converge to a stationary value due to the fine binning fully sampling the small-scale structure. Figure 7.3 illustrates this behaviour for the SubGeV\_elike\_0dcy sample for 9 different throws of the oscillation parameters.

Denoting the event rate for one sample for a given throw  $t$  at each  $N$  by  $\lambda_t^N$ , the average over all considered  $N$  values ( $\bar{\lambda}_t = \frac{1}{24} \sum_{N=1}^{24} \lambda_t^N$ ) is computed. The variance in the event rate at each  $N$  is then calculated as

$$\text{Var}[\lambda^N] = \frac{1}{N_{\text{throws}}} \sum_{t=1}^{N_{\text{throws}}} \left( \lambda_t^N - \bar{\lambda}_t \right)^2 - \left[ \frac{1}{N_{\text{throws}}} \sum_{t=1}^{N_{\text{throws}}} \left( \lambda_t^N - \bar{\lambda}_t \right) \right]^2. \quad (7.4)$$

In practice, the following procedure is undertaken. For a particular throw, the difference between the event rate at a particular choice of  $N$  and the mean of the distribution is calculated. This is illustrated in Figure 7.4. This value is then calculated for all the 2000 throws, generating a distribution of  $\lambda_t^N - \bar{\lambda}_t$ .

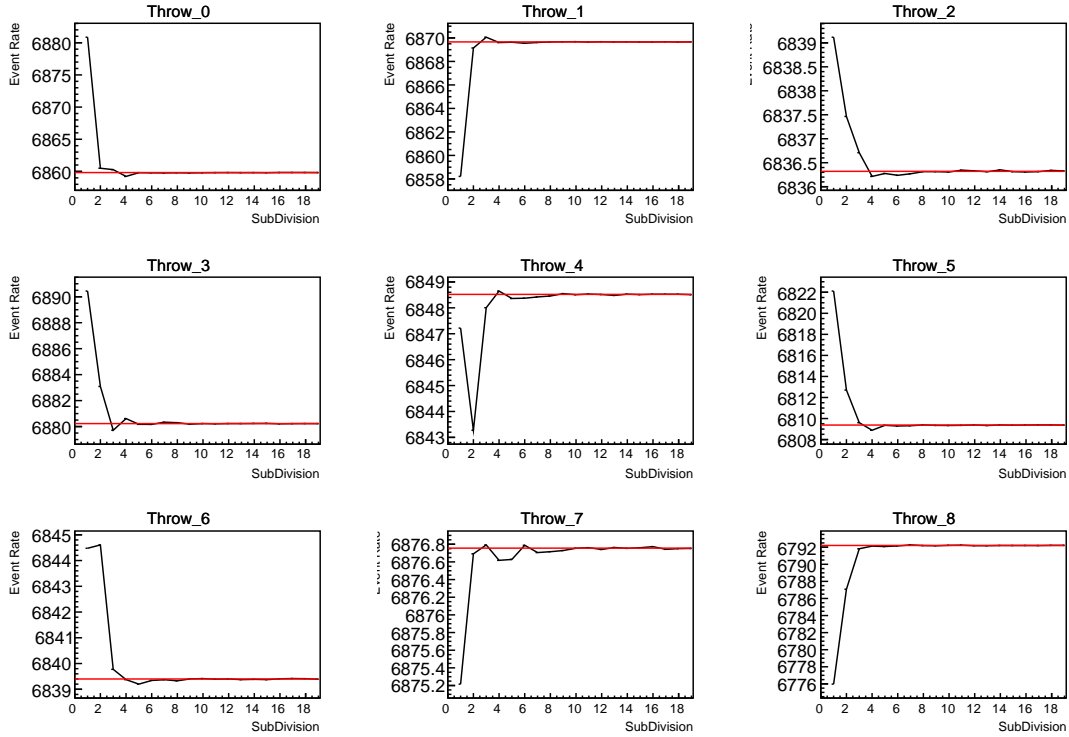


**Figure 7.3:** Event rate of the SubGeV\_elike\_0dcy sample as a function of the number of sub-divisions per coarse bin. Each subplot represents the event rate of the sample at a different oscillation parameter set thrown from the PDG priors detailed in Table 2.1. The red line in each subplot represents the mean of the event rate over the different values of sub-divisions for that particular oscillation parameter throw.

2656 This is repeated for each of the values of  $N$  considered within this study. The  
 2657 distributions of this value, for  $N = \{1, 5\}$ , are given in Figure 7.5. As expected,  
 2658 the distribution gets narrower and tends towards zero for the higher values of  $N$ .

2659 The aim of the study is to find the lowest value of  $N$  such that this variance  
 2660 is below 0.001. This utilises the width of the distributions given in Figure 7.5.  
 2661 This is the typical threshold used by T2K fitters to validate systematic imple-  
 2662 mentation so has been set as the same criteria. The results of this study for  
 2663 each atmospheric sample used within this thesis are illustrated in Figure 7.6 for  
 2664 2000 throws of the oscillation parameters. As can be seen, the variance is below  
 2665 the threshold at  $N = 10$ , and is driven primarily by the SubGeV\_mulike\_1dcy  
 2666 and SubGeV\_elike\_0dcy samples.

2667 The second study to determine the value of  $N$  is as follows. The likelihood  
 2668 for each sample is computed against an Asimov data set created with Asimov A

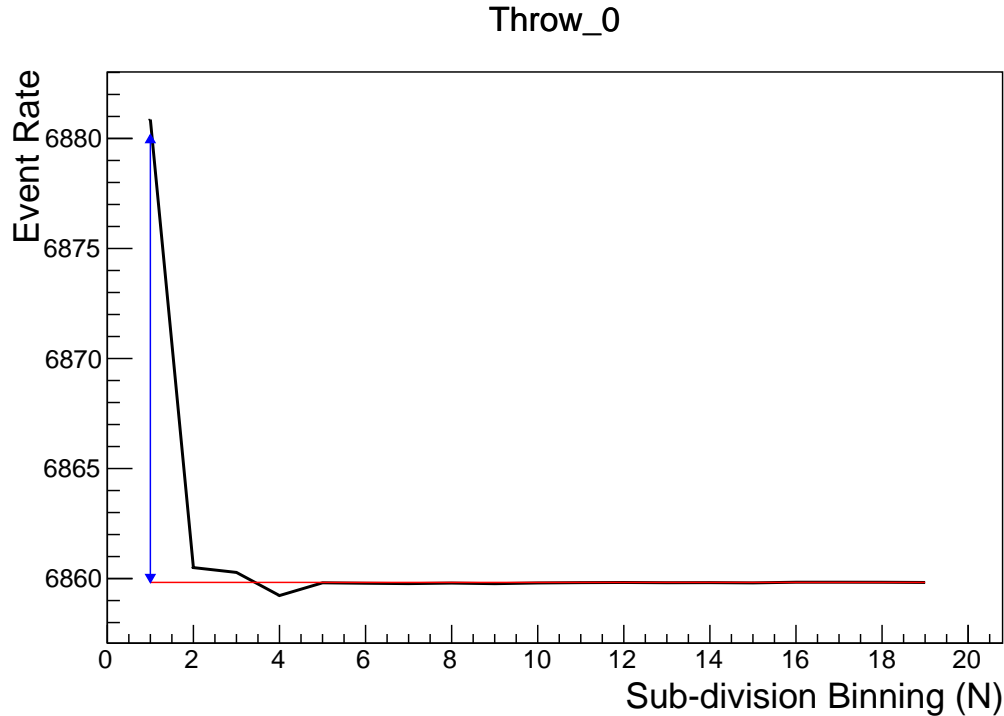


**Figure 7.4:** Event rate of the SubGeV\_elike\_0dcy sample, for a particular oscillation parameter throw, as a function of the number of sub-divisions,  $N$ , per coarse bin. The difference between the mean event rate (red),  $\bar{\lambda}$ , and the event rate at  $N = 1$ ,  $\lambda^{N=1}$  is defined as  $\lambda^N - \bar{\lambda}$  and illustrated by the blue arrow.

oscillation parameters (Table 2.2). Following Equation 7.4, the variance of the log-likelihood over all considered  $N$  is computed. The results are shown in Figure 7.7.

A choice of  $N = 10$  sub-divisions per coarse bin has a variance in both event rate and log-likelihood residuals less than the required threshold of 0.001. The largest value of the likelihood variance is of order  $10^{-7}$ , corresponding to an error on the log-likelihood of about  $3 \times 10^{-4}$  which is small enough to be negligible for the oscillation analysis.

Figure 7.8 illustrates the effect of the smearing using  $N = 10$ . The fast oscillations in the sub-GeV upgoing region have been replaced with a normalisation effect whilst the large matter resonance structure remains.

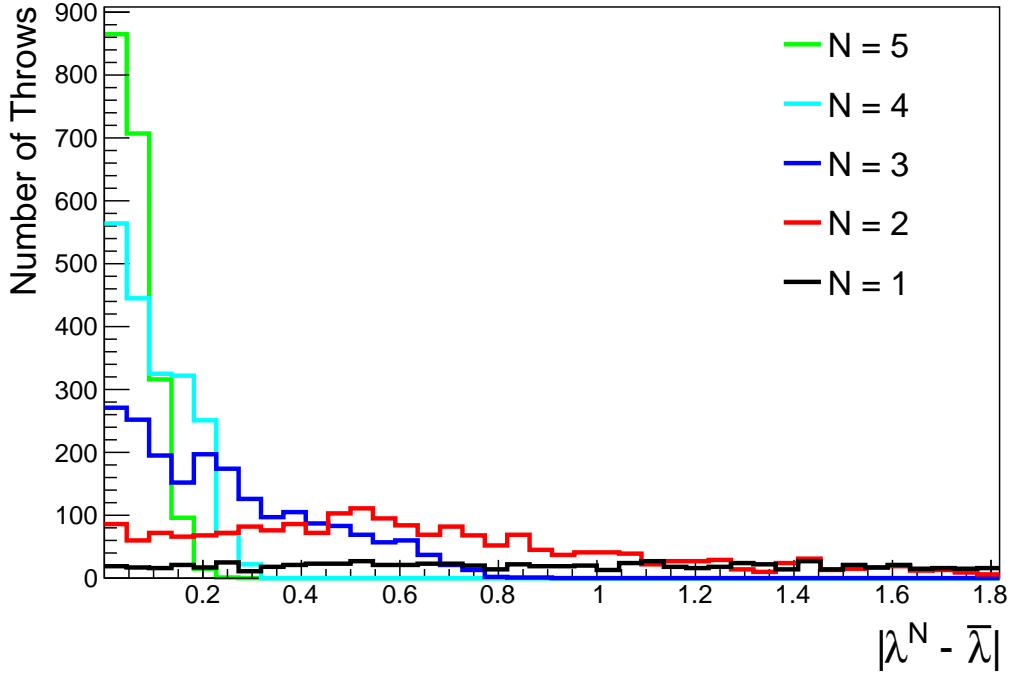


**Figure 7.5:** The distribution of  $\lambda^N - \bar{\lambda}$  for various values of  $N$ . As expected, the distribution gets narrower for larger values of  $N$ .

## 2679 7.2 Calculation Engine

2680 As previously discussed in section 7.1, the calculation of oscillation probabilities  
 2681 is performed at run-time. Consequently, the time per calculation is crucial for fit  
 2682 performance. The initial fitting framework used for this analysis was developed  
 2683 with ProbGPU [214]. This is a GPU-only implementation of the prob3 engine  
 2684 [215]. It is primarily designed for neutrino propagation in a beam experiment  
 2685 (single layer of constant density) with the atmospheric propagation code not  
 2686 being used prior to the analysis in this thesis.

2687 Another engine, CUDAProb3 [216], has been interfaced with the fitting frame-  
 2688 work used in this analysis. This interfacing was done by the author of this  
 2689 thesis. It has been specifically optimised for atmospheric neutrino oscillation  
 2690 calculation so does not contain the code to replace the beam oscillation calculation.  
 2691 The engine utilises object-orientated techniques as compared to the functional  
 2692 implementation of ProbGPU. This allows the energy and cosine zenith arrays to

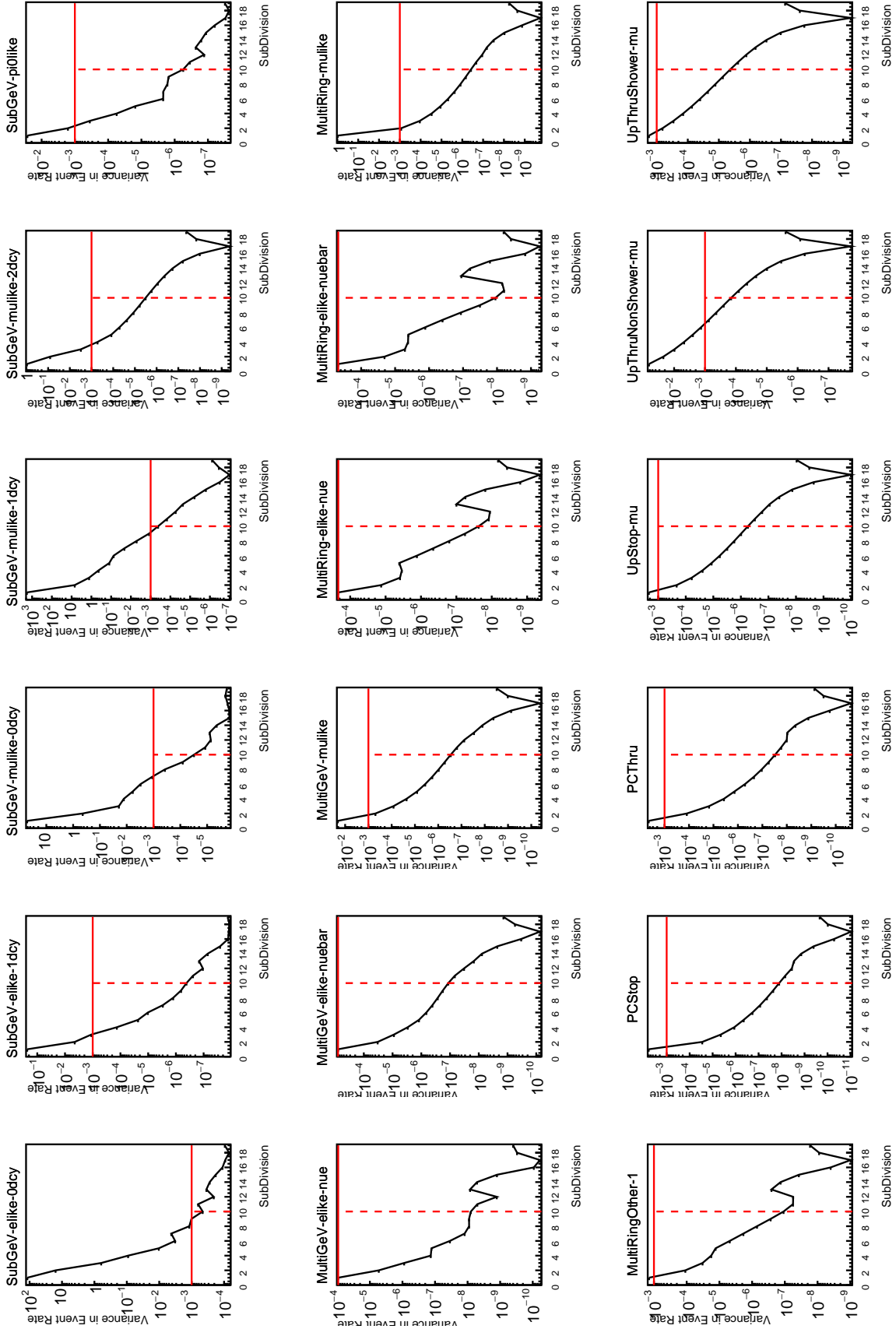


**Figure 7.6:** Variance of event rate for each atmospheric sample as a function of the number of sub-divisions per coarse bin. The solid red line indicates the 0.1% threshold and the dashed red line indicates the variance at a sub-division  $N = 10$ .

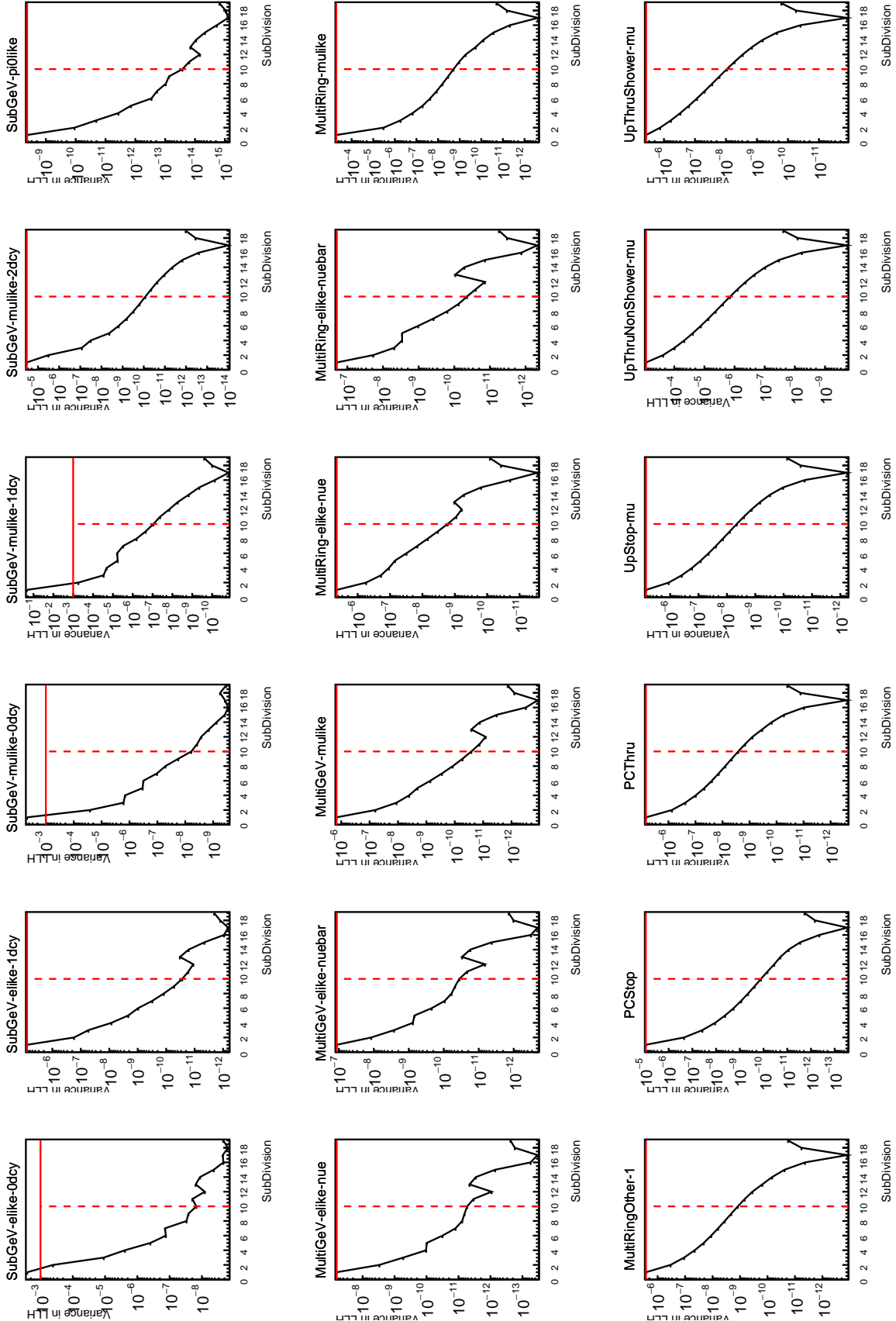


**Figure 7.7:** Variance of sample likelihood, when compared to 'Asimov data' set at Asimov A, for each atmospheric sample as a function of the number of sub-divisions per coarse bin. The solid red line indicates the 0.1% threshold and the dashed red line is a graphical indication of the variance at a sub-division  $N = 10$ .

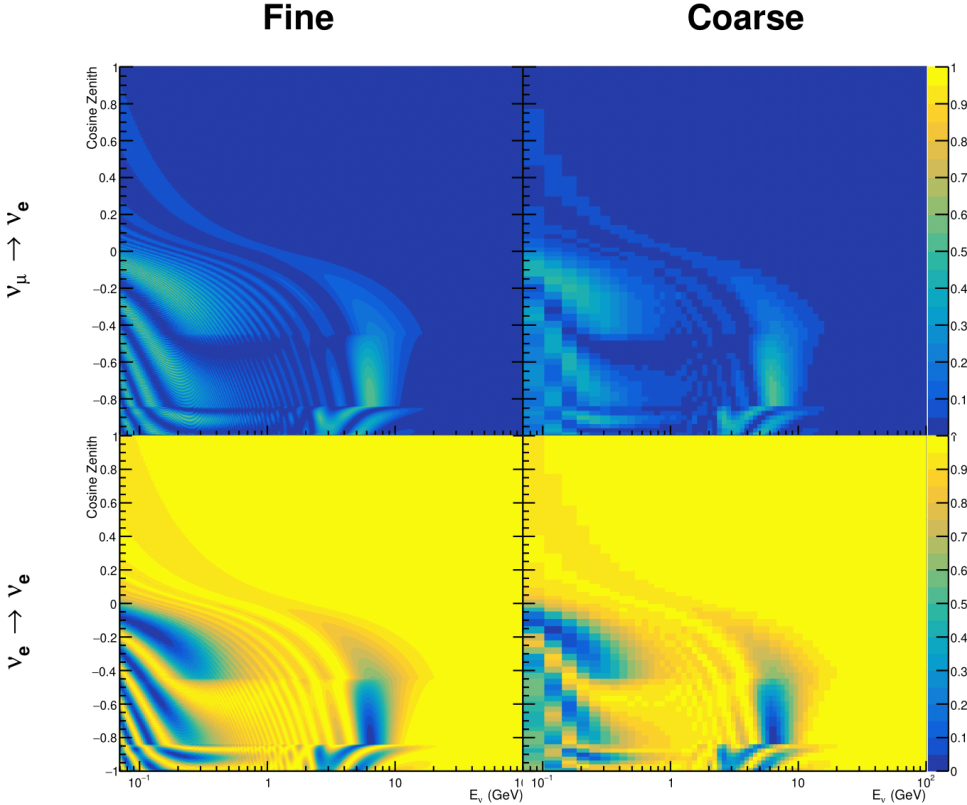


**Figure 7.8:** The oscillation probability,  $P(\nu_\mu \rightarrow \nu_e)$  (top row) and  $P(\nu_e \rightarrow \nu_e)$  (bottom row), given as a function of neutrino energy and zenith angle. The left column gives the “fine” binning used to calculate the oscillation probabilities and the right column illustrates the “coarse” binning used to reweight the Monte Carlo events. The fine binning choice is given with  $N = 10$ , which was determined to be below the threshold from Figure 7.6 and Figure 7.7.

2693 be kept on GPU memory, rather than having to load these arrays onto GPU  
 2694 memory for each calculation. Reducing the memory transfer between CPU and  
 2695 GPU significantly reduces the time required for calculation. This can be seen  
 2696 in Figure 7.9, where the GPU implementation of CUDAProb3 is approximately  
 2697 three times faster than the ProbGPU engine.

2698 Another significant advantage of CUDAProb3 is that it contains a CPU multi-  
 2699 threaded implementation which is not possible with the ProbGPU or prob3 engines.  
 2700 This eliminates the requirement for GPU resources when submitting jobs to batch  
 2701 systems. As illustrated in Figure 7.9, the calculation speed depends on the number

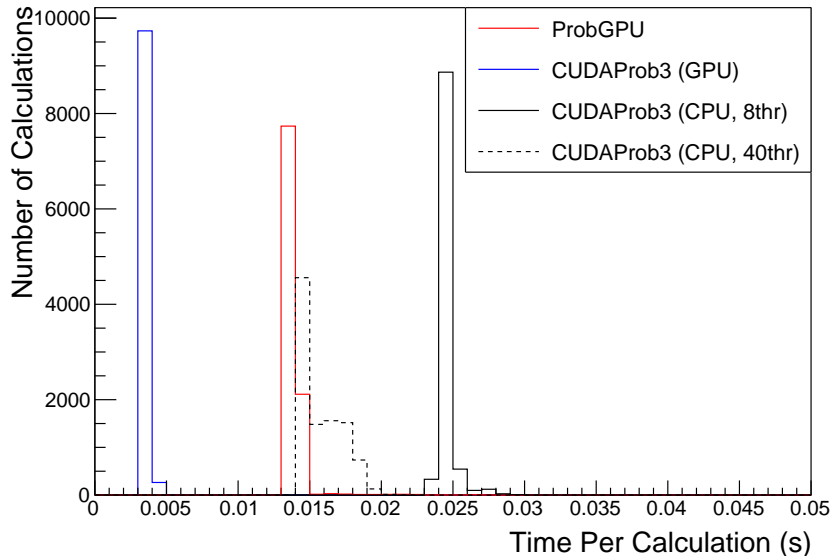


**Figure 7.9:** The calculation time taken to both calculate the oscillation probabilities and fill the “coarse” oscillograms, following the technique given in section 7.1, for the CUDAProb3 and ProbGPU (Red) calculation engines. CUDAProb3 has both a GPU (Blue) and CPU (Black) implementation, where the CPU implementation is multi-threaded. Therefore, 8-threads (solid) and 40-threads (dashed) configurations have been tested. Prob3, which is a CPU single-thread implementation has a mean step time of 1.142s.

of available threads. Using 8 threads (which is typical of the batch systems being used) is approximately twice as slow as the ProbGPU engine implementation, but would allow the fitting framework to be run on many more resources. This fact is utilised for any SK-only fits but GPU resources are required for any fits which include beam samples due to the ProbGPU requirement. Based on the benefits shown by the implementation in this section, efforts are being placed into including linear propagation for beam neutrino propagation into the engine [217].

### 7.3 Matter Density Profile

For an experiment observing neutrinos propagating through the Earth, a model of the Earth’s density profile is required. The model used within this analysis is based on the Preliminary Reference Earth Model (PREM) [80], as illustrated in Figure 2.8. Table 2.3 documents the density and radii of the layers used within the constant density approximation used by the SK-only analysis [79]. The

density measurements provided in the PREM model are provided in terms of mass density, whereas neutrino oscillations are sensitive to the electron number density. This value can be computed as the product of the chemical composition, or the  $Z/A$  value, and the mass density of each layer. Currently, the only way to measure the chemical composition value for layers close to the Earth's core is through neutrino oscillations. The chemical composition of the upper layers of the Earth's Mantle and the Transition zone is well known due to it being predominantly pyrolite which has a chemical composition value of 0.496 [218]. The chemical composition dial for the core layers is set to a value of 0.468, as calculated in [219]. As this value is less well known, it is assigned a Gaussian error with a standard deviation equivalent to the difference in chemical composition in core and mantle layers. Figure 7.10 illustrates the effect of moving from the  $Z/A = 0.5$  method which is used in the official SK-only analysis to these more precise values.

The beam oscillation probability in this thesis uses a baseline of 295km, density  $2.6\text{g/cm}^3$ , and chemical composition 0.5 as is done by the official T2K-only analysis [220].

For a neutrino with given  $E_\nu, \cos(\theta_Z)$ , the oscillation probability calculation engine must be passed a list of the matter regions that the neutrino traversed, with the path length and fixed density in each region. However, a neutrino passing through the earth experiences a range of radii, and thus a range of densities, in each region. In the SK-only analysis, the earth density model used is piecewise-constant, thereby ignoring this effect. For this thesis, the density values for the calculation engine are found by averaging the earth density along the neutrino's path in each layer,

$$\langle \rho \rangle_i = \frac{1}{t_{i+1} - t_i} \int_{t_i}^{t_{i+1}} \rho(t) dt \quad (7.5)$$

where  $t_i$  are the intersection points between each layer and  $t$  is the path length of the trajectory across the layer. This leads to an improved approximation. For this averaging, the simplification of the PREM model developed in [221] is

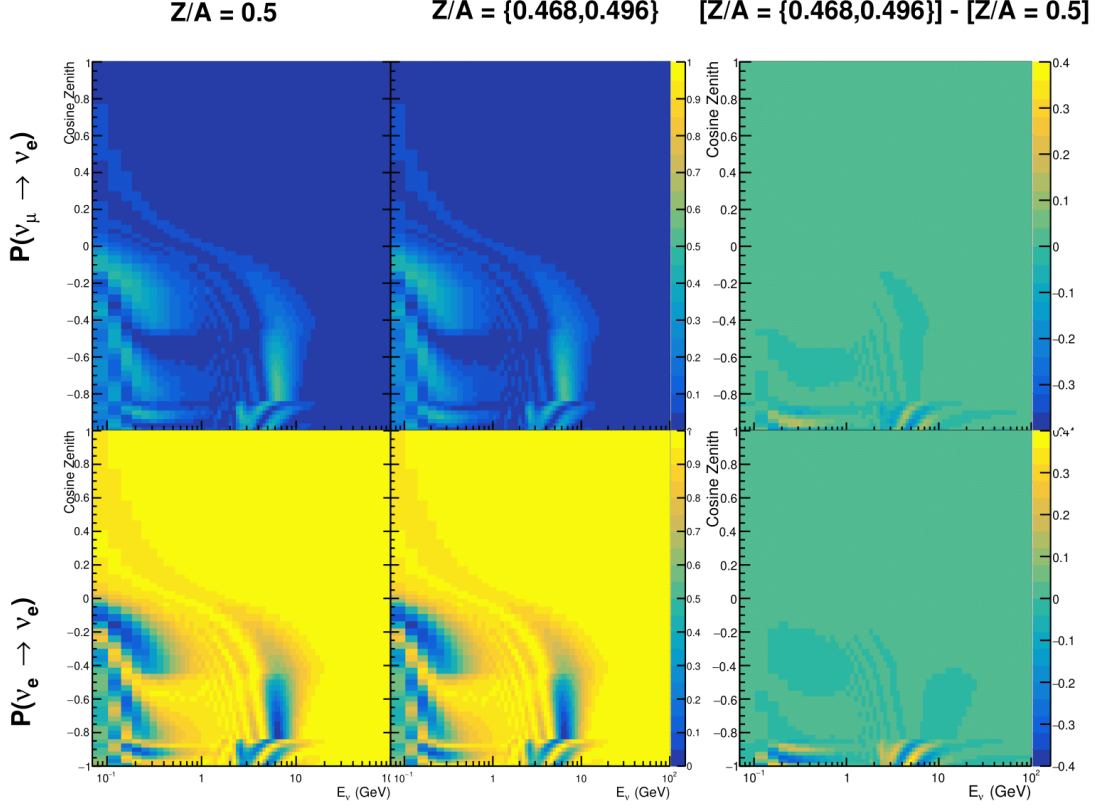


**Figure 7.10:** The oscillation probability,  $P(\nu_\mu \rightarrow \nu_e)$  (top row) and  $P(\nu_e \rightarrow \nu_e)$  (bottom row), given as a function of neutrino energy and zenith angle. The left column gives probabilities where the constant  $Z/A = 0.5$  approximation which is used in the official SK-only analysis. The middle column gives the probabilities where  $Z/A = [0.468, 0.498]$  values are used, as given in Table 2.3. The right column illustrates the difference in oscillation probability between the two different techniques.

used. The layers of the prem model are combined into four to reduce calculation time, with a quadratic fit to each section. This fit was not performed by the author of the thesis and is documented in [213]. The coefficients of the quadratic fit to each layer are given in Table 7.1 with the final distribution illustrated in Figure 7.11. The quadratic approximation is clearly much closer to the PREM model as compared to the constant density approximation.

The effect of using the quadratic density per  $\cos(\theta_Z)$  model is highlighted in Figure 7.12. The slight discontinuity in the oscillation probability around  $\cos(\theta_Z) \sim -0.45$  in the fixed density model, which is due to the transition to

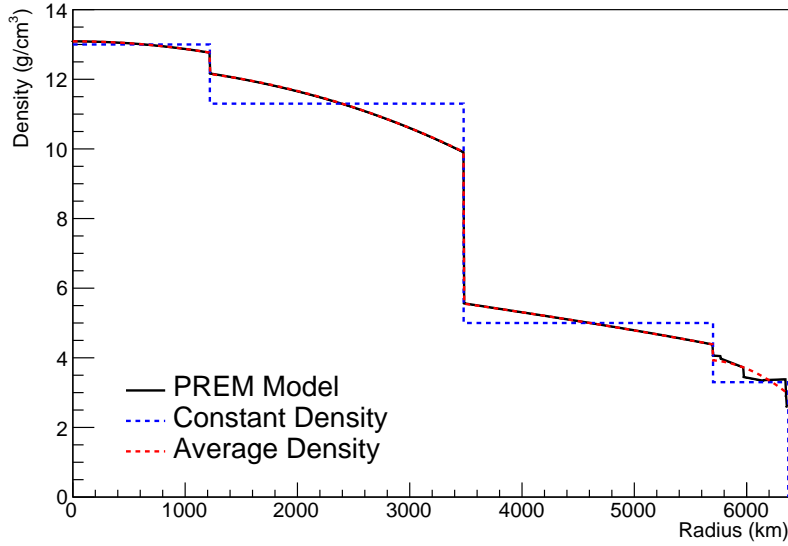


**Figure 7.11:** The density of the Earth given as a function of the radius, as given by the PREM model (Black), the constant density four-layer approximation (Blue), as used in the official SK-only analysis, and the quadratic approximation of the PREM model (Red).

Layer	Outer Radius [km]	Density [g/cm <sup>3</sup> ]
Inner Core	1220	$13.09 - 8.84x^2$
Outer Core	3480	$12.31 + 1.09x - 10.02x^2$
Lower Mantle	5701	$6.78 - 1.56x - 1.25x^2$
Transition Zone	6371	$-50.42 + 123.33x - 69.95x^2$

**Table 7.1:** The quadratic polynomial fits to the PREM model for four assumed layers of the PREM model. The fit to calculate the coefficients is given in [213], where  $x = R / R_{\text{Earth}}$ .

mantle layer boundary, has been reduced. This is expected as the difference in the density across this boundary is significantly smaller in the quadratic density model as compared to the constant density model. Whilst the difference in density across the other layer transitions is reduced, there is still a significant difference. This means the discontinuities in the oscillation probabilities remain but are significantly reduced. However, as the quadratic density approximation matches the PREM model well in this region, these discontinuities are due to the Earth model rather than an artifact of the oscillation calculation.

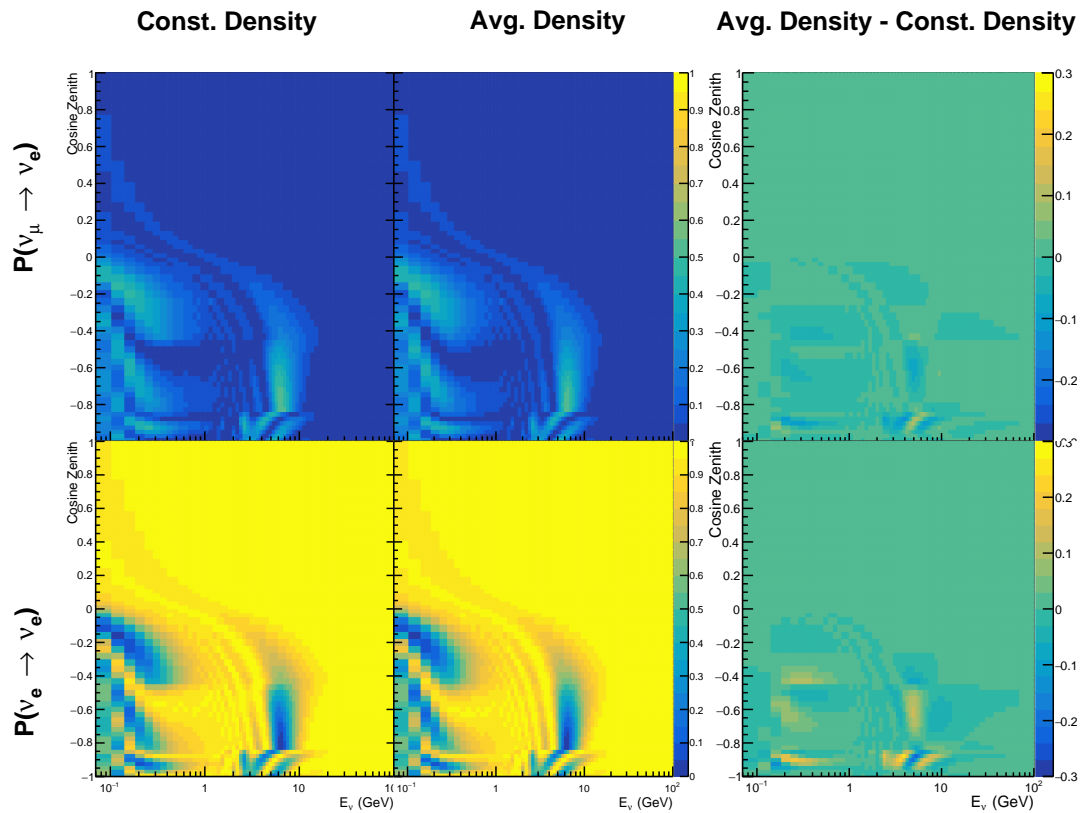


**Figure 7.12:** The oscillation probability,  $P(\nu_\mu \rightarrow \nu_e)$  (top row) and  $P(\nu_e \rightarrow \nu_e)$  (bottom row), given as a function of neutrino energy and zenith angle. The left column gives probabilities where the four-layer constant density approximation is used. The middle column gives the probabilities where the density is integrated over the trajectory, using the quadratic PREM approximation, for each  $\cos(\theta_Z)$  is used. The right column illustrates the difference in oscillation probability between the two different techniques.

## 2760 7.4 Production Height Averaging

2761 As discussed in section 2.5, the height at which the cosmic ray flux interacts  
 2762 in the atmosphere is not known on an event-by-event basis. The production  
 2763 height can vary from the Earth’s surface to  $\sim 50\text{km}$  above that. The SK-only  
 2764 analysis methodology (described in section 7.1) for including the uncertainty  
 2765 on the production height is to include variations from the Honda model when  
 2766 pre-calculating the oscillation probabilities prior to the fit. This technique is not  
 2767 possible for this analysis which uses continuous oscillation parameters that can  
 2768 not be known prior to the fit. Consequently, an analytical averaging technique  
 2769 was developed in [213]. The author of this thesis was not responsible for the  
 2770 derivation of the technique but has performed the implementation and validation  
 2771 of the technique for this analysis alone.

2772 Using the 20 production heights per Monte Carlo neutrino event, provided  
 2773 as 5% percentiles from the Honda flux model, a production height distribution  
 2774  $p_j(h|E_\nu, \cos \theta_Z)$  is built for each neutrino flavour  $j = \nu_e, \bar{\nu}_e, \nu_\mu, \bar{\nu}_\mu$ . In practice, a  
 2775 histogram is filled with 20 evenly spaced bins in production height  $h$  between  
 2776 0 and 50km. The neutrino energy and cosine zenith binning of the histogram  
 2777 are the same as that provided in section 7.1. The average production height,  
 2778  $\bar{h} = \int dh \frac{1}{4} \sum_j p_j(h|E_\nu, \cos(\theta_Z))$ , is calculated. This assumes a linear average over  
 2779 the four flavours of neutrino which are considered to be generated in cosmic ray  
 2780 showers. The production height binning of this histogram is then translated into  
 2781  $\delta t(h) = t(\bar{h}) - t(h)$ , where  $t(h)$  is the distance travelled along the trajectory.

2782 For the  $i^{\text{th}}$  traversed layer, the transition amplitude,  $D_i(t_{i+1}, t_i)$ , is computed.  
 2783 The time-ordered product of these is then used as the overall transition amplitude  
 2784 via

$$A(t_{n+1}, t_0) = D_n(t_{n+1}, t_n) \dots D_1(t_2, t_1) D_0(t_1, t_0), \quad (7.6)$$

2785 where,

$$\begin{aligned} D_n(t_{n+1}, t_n) &= \exp[-iH_n(t_{n+1} - t_n)] \\ &= \sum_{k=1}^3 C_k \exp[ia_k(t_{n+1} - t_n)] \end{aligned} \quad (7.7)$$

2786 is expressed as a diagonalised time-dependent solution to the Schrodinger  
 2787 equation. The  $0^{th}$  layer is the propagation through the atmosphere and is the  
 2788 only term that depends on the production height. Using the substitution  $t_0 =$   
 2789  $t(\bar{h}) - \delta t(h)$ , it can be shown that

$$D_0(t_1, t_0) = D_0(t_1, \bar{h})D_0(\delta t). \quad (7.8)$$

2790 Thus Equation 7.6 becomes

$$\begin{aligned} A(t_{n+1}, t_0) &= D_n(t_{n+1}, t_n) \dots D_1(t_2, t_1)D_0(t_1, \bar{h})D(\delta t) \\ &= A(t_{n+1}, \bar{h}) \sum_{k=1}^3 C_k \exp[ia_k \delta t], \\ &= \sum_{k=1}^3 B_k \exp[ia_k \delta t]. \end{aligned} \quad (7.9)$$

2791 The oscillation probability averaged over production height is then calculated  
 2792 as

$$\begin{aligned} \bar{P}(\nu_j \rightarrow \nu_i) &= \int d(\delta t) p_j(\delta t | E_\nu, \cos \theta_Z) P(\nu_j \rightarrow \nu_i) \\ &= \int d(\delta t) p_j(\delta t | E_\nu, \cos \theta_Z) A(t_{n+1}, t_0) A^*(t_{n+1}, t_0) \\ &= \sum_{km} (B_k)_{ij} (B_m)^*_{ij} \int d(\delta t) p_j(\delta t | E_\nu, \cos \theta_Z) \exp[i(a_k - a_m) \delta t] \end{aligned} \quad (7.10)$$

2793 It is important to note that the exact value of  $\bar{h}$  used does not matter as the  
 2794 values of  $\delta t$  would change to compensate for any modification to the value of  $\bar{h}$ .

2795 In practice, implementation in CUDAProb3 [216] is relatively straightforward  
 2796 as the majority of these terms are already calculated in the standard oscillation  
 2797 calculation. Figure 7.13 illustrates the results of the production height averaging.

2798 As expected, the main effect is observed in the low-energy downward-going  
 2799 and horizontal-going events. Upward-going events have to travel the radius  
 2800 of the Earth,  $R_E = 6371\text{km}$ , where the production height uncertainty is a small  
 2801 fraction of the total path length.

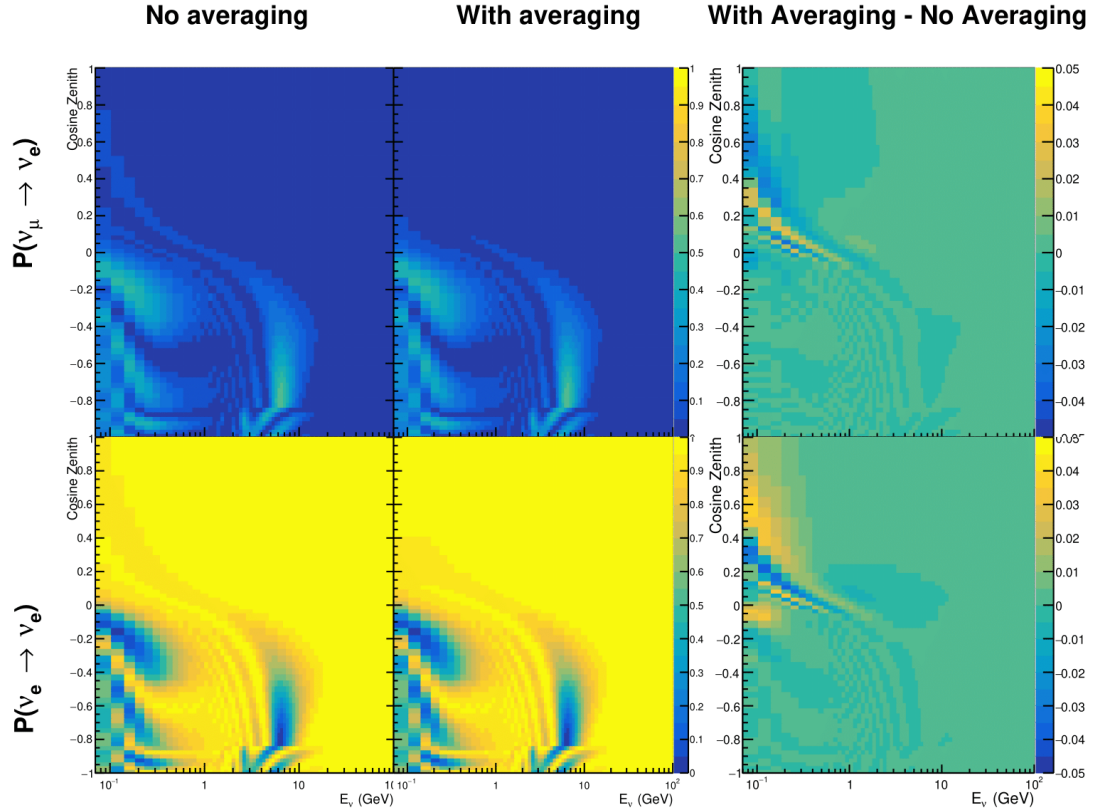


**Figure 7.13:** The oscillation probability,  $P(\nu_\mu \rightarrow \nu_e)$  (top row) and  $P(\nu_e \rightarrow \nu_e)$  (bottom row), given as a function of neutrino energy and zenith angle. The left column gives probabilities where a fixed production height of 25km is used. The middle column gives the probabilities where the production height is analytically averaged. The right column illustrates the difference in oscillation probability between the two different techniques.

# 8

2802

2803

## Oscillation Analysis

2804 Using the samples and systematics defined in chapter 6, this chapter documents  
2805 a simultaneous beam and atmospheric oscillation analysis from the T2K and SK  
2806 experiments. The MaCh3 Bayesian MCMC framework introduced in chapter 4  
2807 is used for all studies performed within this thesis.

2808 The MaCh3 framework used throughout this thesis has been validated through  
2809 many tests. The code which handles the beam far detector samples was developed  
2810 by the author and validated by comparison to the 2020 T2K analysis [75]. The  
2811 sample event rates and likelihood evaluations of beam samples generated by  
2812 the framework used within this thesis were compared to those from the T2K  
2813 analysis by the author of this thesis. Variations of the sample predictions were  
2814 compared at  $\pm 1\sigma$  and  $\pm 3\sigma$  and good agreement was found in all cases. A similar  
2815 study, led by Dr. C. Wret was used to validate the near detector portion of  
2816 the code [206]. The implementation of the atmospheric samples within MaCh3  
2817 was completed and cross-checked by the author of this thesis against the P-  
2818 Theta framework (Introduced in section 3.2). Both fitters are provided with  
2819 the same inputs and can therefore cross-validate each other. These validations  
2820 compared the event rate and likelihood calculation. Documentation of all the  
2821 above validations can be found in [206].

## 8.1 Monte Carlo Prediction

Using the three sets of dial values (generated, pre-BANFF, and post-BANFF tunes) defined in subsection 6.4.3, the predicted event rates for each sample are defined in Table 8.1. The oscillated (AsimovA defined in Table 2.2) and un-oscillated event rates are calculated for each tune.

Sample	Total Predicted Events					
	Generated		Pre-fit		Post-fit	
	Osc	UnOsc	Osc	UnOsc	Osc	UnOsc
SubGeV- <i>elike</i> -0dcy	7121.0	7102.6	6556.8	6540.0	7035.2	7015.7
SubGeV- <i>elike</i> -1dcy	704.8	725.5	693.8	712.8	565.7	586.0
SubGeV- <i>mulike</i> -0dcy	1176.5	1737.2	1078.6	1588.1	1182.7	1757.1
SubGeV- <i>mulike</i> -1dcy	5850.7	8978.1	5351.7	8205.1	5867.0	9009.9
SubGeV- <i>mulike</i> -2dcy	446.9	655.2	441.6	647.7	345.9	505.6
SubGeV- <i>pi0like</i>	1438.8	1445.4	1454.9	1461.1	1131.1	1136.2
MultiGeV- <i>elike</i> -nue	201.4	195.6	201.1	195.3	202.6	196.7
MultiGeV- <i>elike</i> -nuebar	1141.5	1118.3	1060.7	1039.5	1118.5	1095.7
MultiGeV- <i>mulike</i>	1036.7	1435.8	963.1	1334.1	1015.2	1405.9
MultiRing- <i>elike</i> -nue	1025.1	982.2	1026.8	984.3	1029.8	986.4
MultiRing- <i>elike</i> -nuebar	1014.8	984.5	991.0	962.0	1008.9	978.5
MultiRing- <i>mulike</i>	2510.0	3474.4	2475.6	3425.8	2514.6	3480.4
MultiRingOther-1	1204.5	1279.1	1205.8	1280.3	1207.4	1281.0
PCStop	349.2	459.2	338.4	444.7	346.8	456.1
PCThru	1692.8	2192.5	1661.5	2149.8	1689.2	2187.8
UpStop-mu	751.2	1295.0	739.7	1271.6	750.4	1293.0
UpThruNonShower-mu	2584.4	3031.6	2577.9	3019.4	2586.8	3034.0
UpThruShower-mu	473.0	488.6	473.2	488.7	473.8	489.4
FHC1Rmu	328.0	1409.2	301.1	1274.7	345.1	1568.0
RHC1Rmu	133.0	432.3	122.7	396.2	135.0	443.9
FHC1Re	84.6	19.2	77.4	18.2	93.7	19.7
RHC1Re	15.7	6.4	14.6	6.1	15.9	6.3
FHC1Re1de	10.5	3.2	10.3	3.1	8.8	2.9

**Table 8.1:** The Monte Carlo predicted event rate of each far detector sample used within this analysis. Three model parameter tunes are considered, as defined in subsection 6.4.3. Un-oscillated and oscillated predictions are given, where the oscillated predictions assume Asimov A oscillation parameters provided in Table 2.2.

Generally, the samples which target CCQE interaction modes observe a decrease in prediction when using the pre-fit dial values. This is in accordance with the Monte Carlo being produced assumed  $M_A^{QE} = 1.21\text{GeV}$  [164] whilst

the pre-fit dial value is set to  $M_A^{QE} = 1.03\text{GeV}$  as suggested by [204]. Furthermore, the predicted event rates of samples that target CCRES interaction modes are significantly reduced when considering the post-BANFF fit. This follows the observations in subsection 6.4.3. The strength of the accelerator neutrino experiment can be seen in the remarkable difference between the oscillated and unoscillated predictions in the FHC1Rmu and RHC1Rmu samples. There is a very clear decrease in the expected event rate between the oscillated and un-oscillated predictions which is not as obvious as in the atmospheric samples. This is due to the fact that the beam energy is tuned to the maximum disappearance probability which is not the case for the naturally generated atmospheric neutrinos.

### 8.1.1 Likelihood Scans

Using the definition of the likelihood presented in section 6.5, the response of each sample to a variation of a particular parameter can be studied. Figure 8.1 presents the variation of all the samples (beam and atmospheric) at the far detector to the oscillation parameters of interest:  $\delta_{CP}$ ,  $\sin^2(\theta_{13})$ ,  $\sin^2(\theta_{23})$ , and  $\Delta m_{32}^2$ . These plots are colloquially called ‘likelihood scan’ (or ‘log-likelihood scans’). The process of making these plots is as follows. An Asimov data set (following technique detailed in section 6.5) is built using the AsimovA oscillation parameters and pre-fit systematic tune. The Monte Carlo is then reweighted using the value of the oscillation parameter at each point on the x-axis of the scan. The likelihood is then calculated between the Asimov data and Monte Carlo prediction and plotted. This process identifies which samples drive the determination of the oscillation parameters in the joint fit.

Due to the caveat of fixed systematic parameters and the correlations between oscillation parameters being ignored when creating these likelihood scans, the value of  $\chi^2 = 1$  (or  $-2 \times \ln(\text{Likelihood}) = 1$ ) does not equate to the typical  $1\sigma$  sensitivity. However, it does give an indication of which samples respond the strongest to a variation in a particular oscillation parameter. The point at

2858 which the likelihood tends to zero illustrates the value of the parameter used  
 2859 to build the Asimov data prediction.

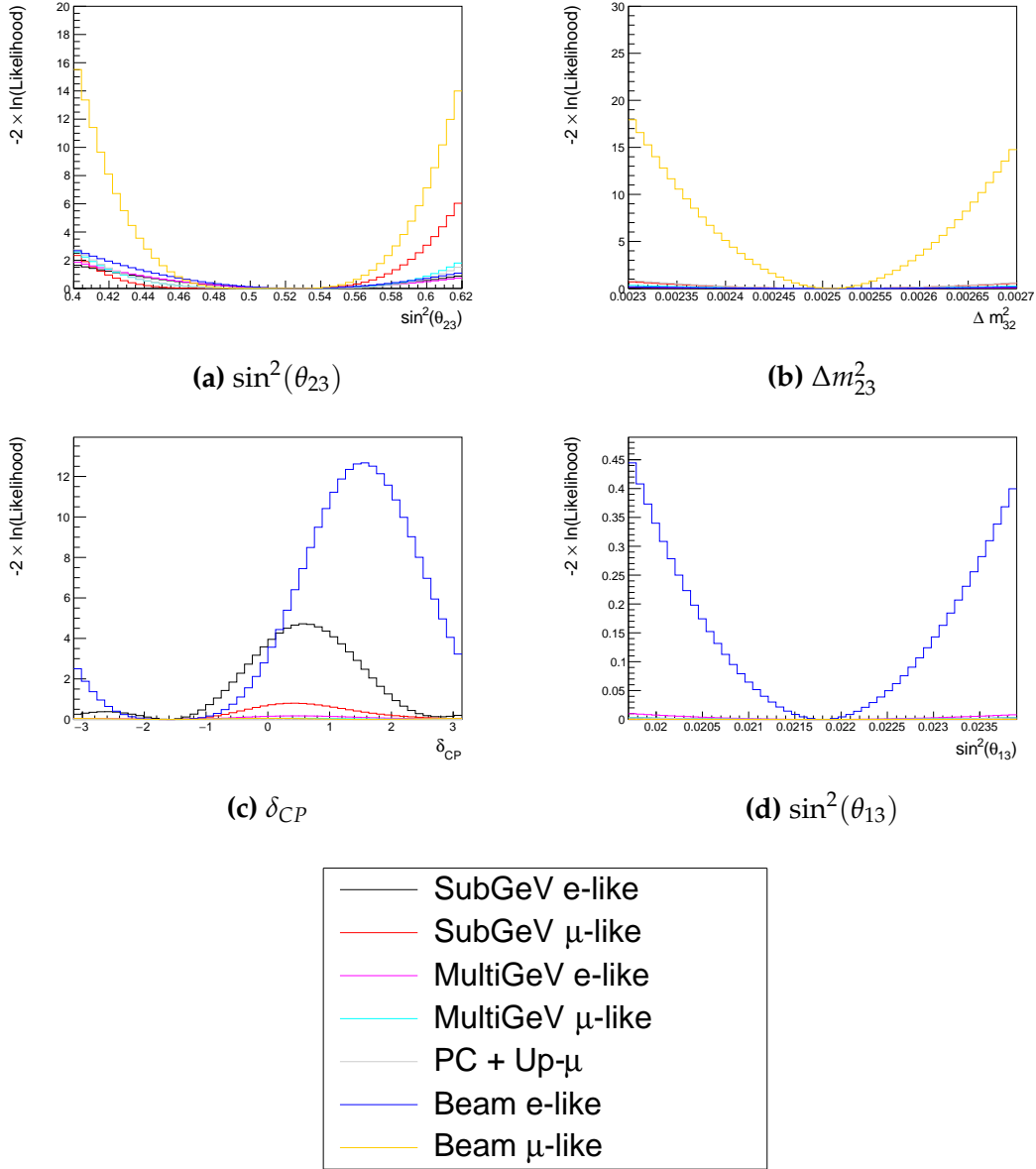


**Figure 8.1:** The response of the likelihood, as defined in section 6.5, illustrating the response of the samples to a variation of an oscillation parameter.

2860 The sensitivity to  $\sin^2(\theta_{23})$  is mostly dominated by the beam muon-like  
 2861 samples. The response of an individual atmospheric sample is small but non-  
 2862 negligible such that the summed response over all atmospheric samples becomes  
 2863 comparable to that of the muon-like beam samples. Consequently, the sensitivity

2864 of the joint fit to  $\sin^2(\theta_{23})$  would be expected to be greater than the beam-only  
2865 analysis. The only sample which respond to the  $\sin^2(\theta_{13})$  oscillation parameter is  
2866 the electron-like beam samples. Consequently, no increase in sensitivity beyond  
2867 that of the T2K-only analysis would be expected from the joint fit. Regardless, the  
2868 sensitivity of the beam sample is significantly weaker than the external reactor  
2869 constraint so prior knowledge will dominate any measurement that is included  
2870 within this thesis. The  $\Delta m_{21}^2$  and  $\sin^2(\theta_{12})$  parameters are not considered as  
2871 there is simply no sensitivity in any sample considered within this analysis.  
2872 The response to  $\Delta m_{32}^2$  is completely dominated by the beam muon-like samples.  
2873 This is because the beam neutrino energy can be specifically tuned to match the  
2874 maximal disappearance probability. Despite this, improvements to the  $|\Delta m_{32}^2|$   
2875 sensitivity may be expected due to additional mass hierarchy determination  
2876 added by the atmospheric samples.

2877 Two-dimensional scans of the appearance ( $\sin^2(\theta_{13})$ - $\delta_{CP}$ ) and disappearance  
2878 ( $\sin^2(\theta_{23})$ - $\Delta m_{32}^2$ ) parameters are illustrated in Figure 8.2 and Figure 8.3, respec-  
2879 tively. The caveat of fixed systematic parameters and correlations between other  
2880 oscillation parameters being neglected still apply.

2881 The appearance log-likelihood scans show the distinct difference in how  
2882 the beam and atmospheric samples respond. The beam samples have an ap-  
2883 proximately constant width of the  $2\sigma$  and  $3\sigma$  contours, throughout all ranges  
2884 of  $\delta_{CP}$ . The response of the atmospheric samples to  $\sin^2(\theta_{13})$  is very strongly  
2885 correlated to the value of  $\delta_{CP}$  being evaluated, with the strongest constraints  
2886 around  $\delta_{CP} \sim 1$ . Consequently, this difference allows some of the degeneracy in  
2887 a beam-only fit to be broken. Comparing the beam-only and joint fit likelihood  
2888 scans, the  $2\sigma$  continuous contour in  $\delta_{CP}$  for beam samples is broken when the  
2889 atmospheric samples are added. This may result in a stronger sensitivity to  
2890  $\delta_{CP}$ . Similarly, the width of the  $3\sigma$  contours also becomes dependent upon the  
2891 value of  $\delta_{CP}$ . Whilst these are encouraging results for the joint fit, these are  
2892 not sensitivity measurements as the systematic parameters are fixed and the  
2893 correlation between oscillation parameters is neglected. An interesting point to

note is that the atmospheric samples have little sensitivity to  $\sin^2(\theta_{13})$  on their own, as evidenced in Figure 8.1, but can improve sensitivity to the parameter when combined within the simultaneous fit.

The response of the atmospheric samples in Figure 8.2 shows an interesting behaviour when considering the application of the reactor constraint. At higher values of  $\sin^2(\theta_{13})$ , two lobes appear around  $\delta_{CP} \sim -\pi/2$  and  $\delta_{CP} \sim 2.4$ . If this distribution was projected onto the  $\delta_{CP}$  axis, these lobes would mean the posterior distribution would have a significant dip between these values. However, the region of  $\sin^2(\theta_{13})$  near the reactor constraint ( $\sin^2(\theta_{13}) = (2.18 \pm 0.08) \times 10^{-2}$ ) is flatter across the range of  $\delta_{CP}$ . Therefore, if we were to project only this region onto the  $\delta_{CP}$  axis, the dip between the peaks would not be as significant. If this behaviour was to be seen in the results of a fit, these marginalisation effects would actually conspire to reduce the sensitivity to  $\delta_{CP}$  if the reactor constraint was to be applied.

The disappearance log-likelihood scans in  $\sin^2(\theta_{23})$ - $\Delta m_{32}^2$  space (Figure 8.3) show the expected behaviour when considering the one-dimensional scans already discussed. The uncertainty on the width of  $|\Delta m_{32}^2|$  is mostly driven by the beam-only sensitivities. However, the width of this contour in the inverted mass region ( $\Delta m_{32}^2 < 0$ ) is significantly reduced due to the ability of the atmospheric samples to select the correct (normal) mass hierarchy. The width of the uncertainty in  $\sin^2(\theta_{23})$  is also reduced compared to the beam-only sensitivities, with a further decrease in the inverted hierarchy region due to the better mass hierarchy determination.

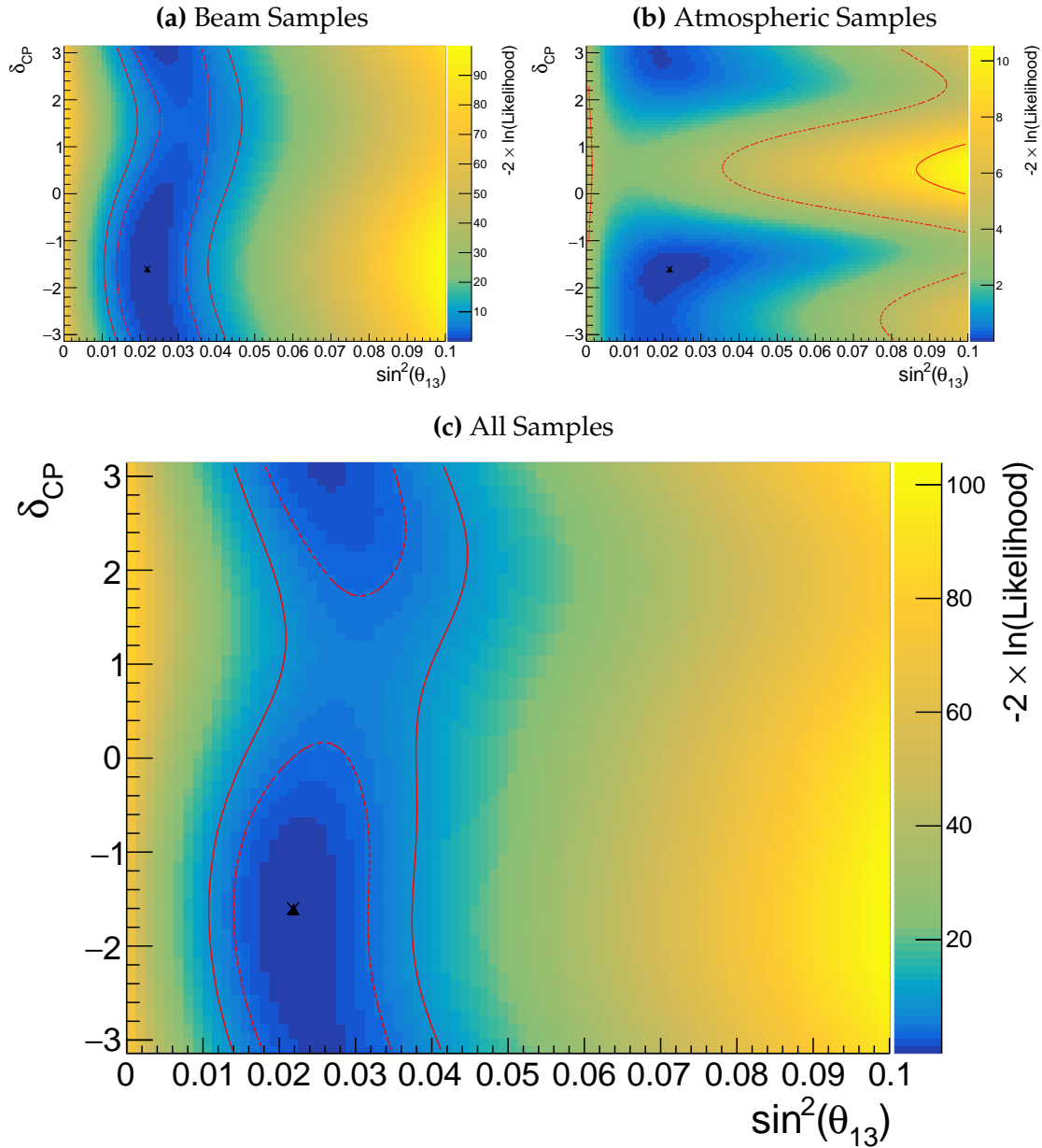


**Figure 8.2:** Two-dimensional log-likelihood scan of the appearance ( $\sin^2(\theta_{13})$ - $\delta_{CP}$ ) parameters showing the response of the beam samples (top left), atmospheric samples (top right) and the summed response (bottom). The Asimov A oscillation parameters, defined in Table 2.2, are known to be the true point (Black Cross). The position of the smallest log-likelihood is highlighted with the triangle. Prior uncertainty terms of the oscillation parameters are neglected. The two(three) sigma contour levels are illustrated with the dashed(solid) red line.

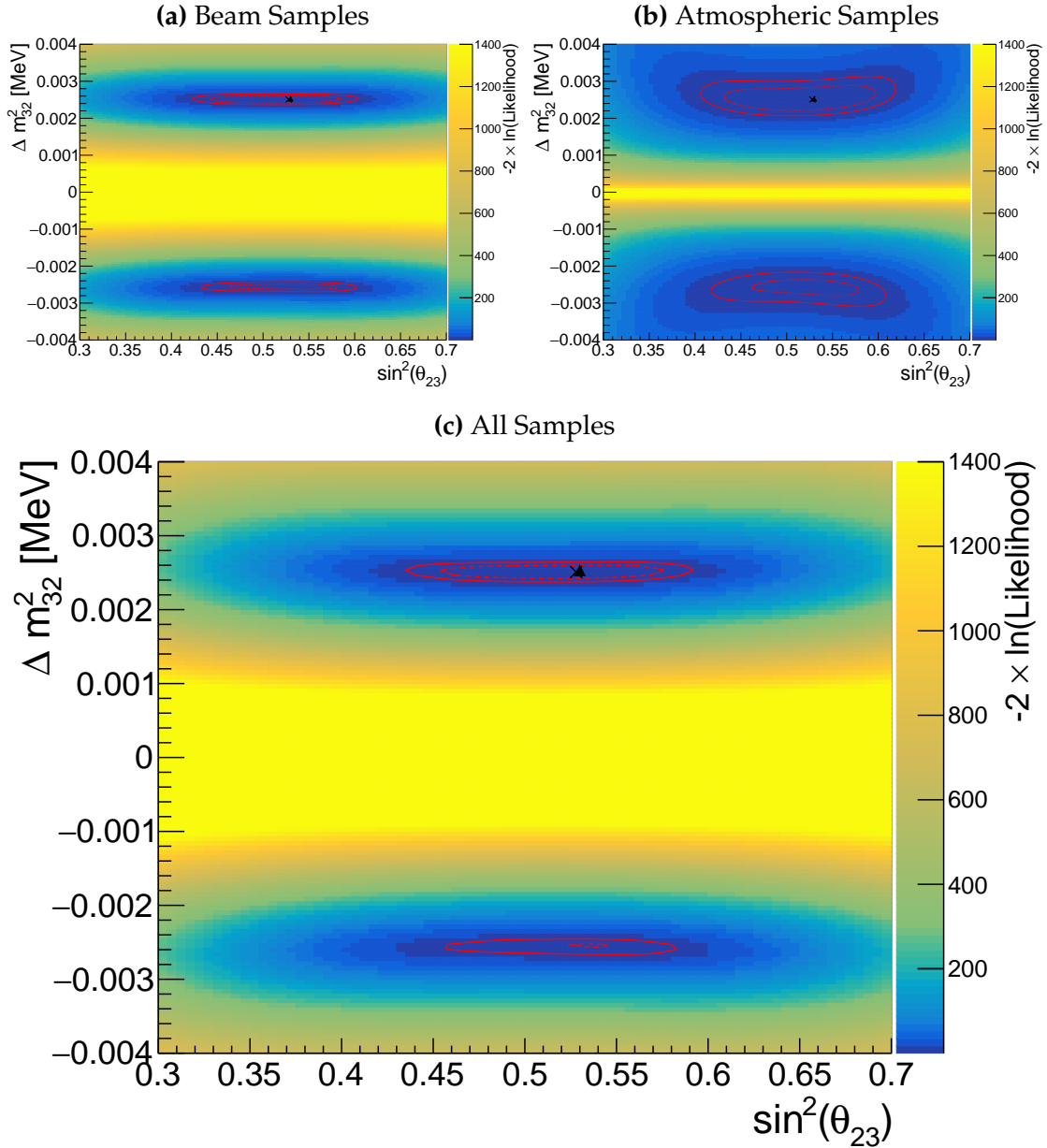


**Figure 8.3:** Two-dimensional log-likelihood scan of the disappearance ( $\sin^2(\theta_{23})$ )- $\Delta m_{32}^2$ ) parameters showing the response of the beam samples (top left), atmospheric samples (top right) and the summed response (bottom). The Asimov A oscillation parameters, defined in Table 2.2, are known to be the true point (Black Cross). The position of the smallest log-likelihood is highlighted with the triangle. Prior uncertainty terms of the oscillation parameters are neglected. The two(three) sigma contour levels are illustrated with the dashed(solid) red line.

2917 The likelihood scans illustrated thus far only consider the sensitivity of this  
2918 analysis for a fixed set of true oscillation parameters, namely Asimov A defined in  
2919 Table 2.2. Whilst computational infeasible to run many fits at different parameter  
2920 sets, it is possible to calculate the likelihood response to different Asimov data  
2921 sets. Figure 8.4 and Figure 8.5 illustrate how the sensitivity changes for differing  
2922 true values of  $\delta_{CP}$  and  $\sin^2(\theta_{23})$ , respectively. For both of these plots, the other  
2923 oscillation parameters are fixed at their Asimov A values. Consequently, the  
2924 caveat of fixed systematic parameters and correlations between other oscillation  
2925 parameters being neglected still applies.

2926 To explain how these plots are made, consider Figure 8.4. This plot is built  
2927 by considering multiple one-dimensional log-likelihood scans, each creating  
2928 an Asimov data with the value of  $\delta_{CP}$  taken from the x-axis. The likelihood to  
2929 a particular Asimov data set is calculated after reweighting the Monte Carlo  
2930 prediction to each value of  $\delta_{CP}$  on the y-axis.

2931 Figure 8.4 illustrates the sensitivity to  $\delta_{CP}$ . Notably, the  $1\sigma$  intervals contain  
2932 regions in the off-diagonal for which the beam and atmospheric samples have  
2933 broken and discontinuous contours. This indicates that there are regions of  $\delta_{CP}$   
2934 which are degenerate. For example, for the x-axis value of  $\delta_{CP} = 0$ , the beam  
2935 samples sensitivity would include two discontinuous regions excluded from  
2936 the  $1\sigma$  interval:  $\delta_{CP} \sim 0$  and  $\delta_{CP} \sim \pi$ . The offset in  $\delta_{CP}$  between the beam  
2937 and atmospheric samples allows the joint fit to have increased sensitivity in  
2938 these regions. Consequently, the difference between the beam-only and joint  
2939 beam-atmospheric fit should be studied using multiple Asimov data sets.

2940 Despite the increased sensitivity at  $1\sigma$ , the  $2\sigma$  intervals from the joint fit  
2941 are more similar to the two independent sensitivities and the off-diagonal de-  
2942 generacies mostly remain. This indicates that the joint fit has the strength to  
2943 aid parameter determination but can not entirely break the degeneracies in  $\delta_{CP}$   
2944 at higher confidence levels.

2945 Figure 8.5 illustrates a similar analysis as above, although the value of  $\sin^2(\theta_{23})$   
2946 is varied and  $\delta_{CP}$  is fixed to the Asimov A parameter value. Due to the beam

<sup>2947</sup> parameters and baseline being tuned to specifically target this oscillation parameter, the average sensitivity of the beam samples is stronger than the atmospheric  
<sup>2948</sup> samples. However, the degeneracy around maximal mixing ( $\sin^2(\theta_{23}) = 0.5$ ) is  
<sup>2949</sup> significantly more peaked in the beam samples compared to the atmospheric  
<sup>2950</sup> samples. This behaviour is strengthened when considering the  $2\sigma$  intervals, to the  
<sup>2951</sup> point where two distinct discontinuous regions of the  $2\sigma$  intervals exist around  
<sup>2952</sup> the Asimov point  $\sin^2(\theta_{23}) \sim 0.41, 0.6$ . Given the caveat of only considering  
<sup>2953</sup> likelihood scans, the joint analysis would mostly eliminate the discontinuous  
<sup>2954</sup> intervals in these regions. This means that the joint fit could feasibly have an  
<sup>2955</sup> increased preference for the correct octant hypothesis.  
<sup>2956</sup>

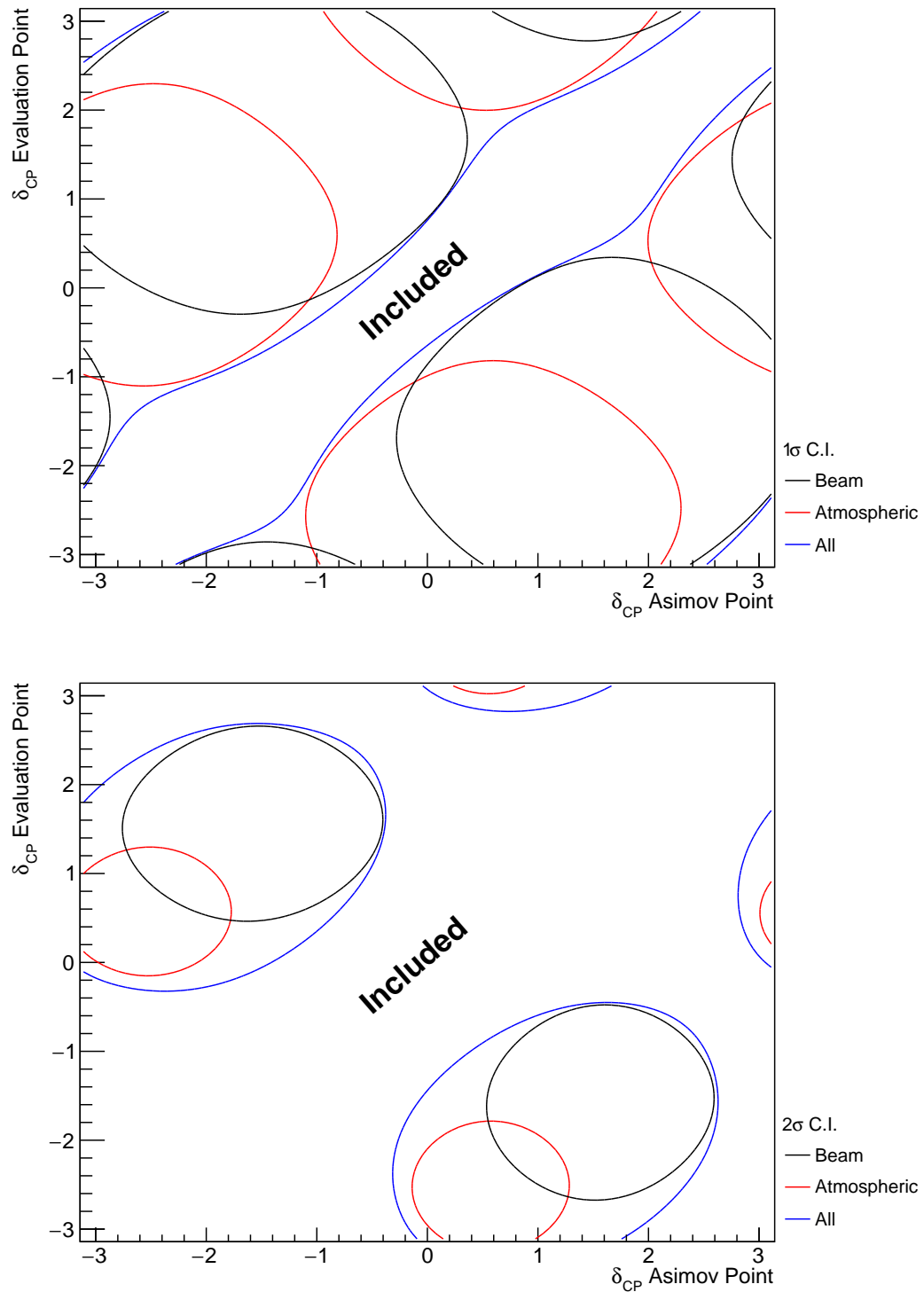


**Figure 8.4:** A series of one-dimensional likelihood scans over  $\delta_{CP}$ , where an Asimov data set is built for each value of  $\delta_{CP}$  on the x-axis and the likelihood is evaluated for each value of  $\delta_{CP}$  on the y-axis. The diagonal represents the minimum log-likelihood and defines the region included within the  $1\sigma$  (Top) and  $2\sigma$  (Bottom) confidence intervals. The beam (black) and atmospheric (red) samples are individually plotted and the joint fit (blue) is the sum of the two.

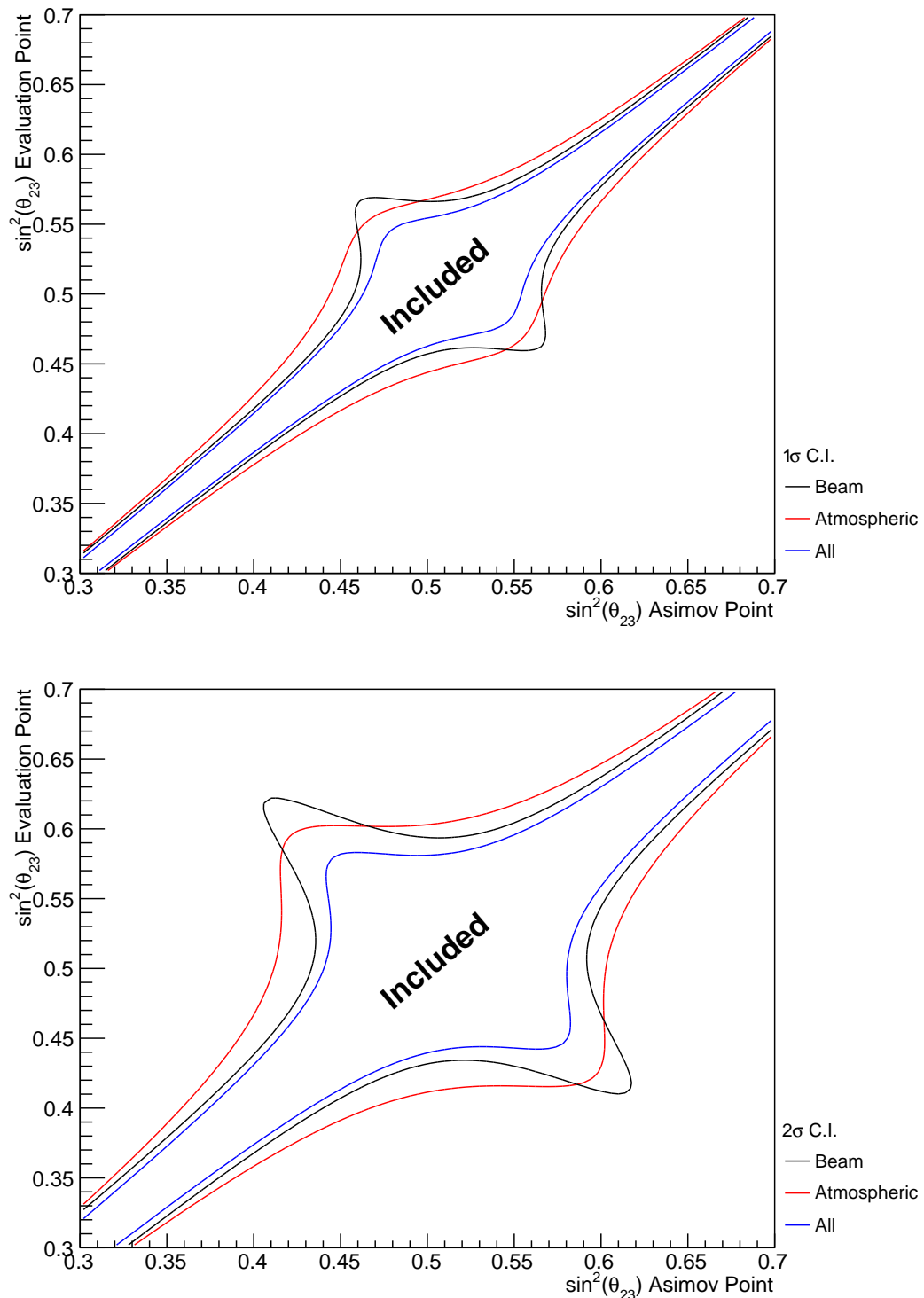


**Figure 8.5:** A series of one-dimensional likelihood scans over  $\sin^2(\theta_{23})$ , where an Asimov data set is built for each value of  $\sin^2(\theta_{23})$  on the x-axis and the likelihood is evaluated for each value of  $\sin^2(\theta_{23})$  on the y-axis. The diagonal represents the minimum log-likelihood and defines the region included within the  $1\sigma$  (Top) and  $2\sigma$  (Bottom) confidence intervals. The beam (black) and atmospheric (red) samples are individually plotted and the joint fit (blue) is the sum of the two.

Alongside oscillation parameters (Figure 8.1), the sensitivity to systematic parameters can also be studied for the joint fit. As some of these parameters are correlated between the beam and atmospheric events, the response of the atmospheric samples can modify the constraint. This means the systematics can have additional constraints than what they would from a beam-only analysis. Therefore, the response from the beam and the atmospheric samples to various systematic parameters has been compared in Figure 8.6. The Asimov data set has been created using the AsimovA oscillation parameter and the pre-fit systematic tune. For example, the systematic parameter controlling the effective axial mass coupling in CCQE interactions,  $M_A^{QE}$ , is clearly dominated by the ND constraint. An example where the response of the atmospheric sample is approximately similar to the near detector constraint is the 2p2h\_Cto0 normalisation systematic. This systematic models the scaling of the 2p2h interaction cross-section on a carbon target to an oxygen target. There are also systematics which have no near detector constraint. For example, the systematic parameters which describe the normalisation of the NC1Gamma and NCOther interaction modes. The atmospheric samples are significantly more sensitive to these systematics than the beam samples due to their similar interaction contributions but relatively higher statistics (Table 8.1). As an example of how the atmospheric samples can help constrain systematic parameters used within the T2K-only analysis, these NC background events in beam electron-like samples will be considerably more constrained with the additional sensitivity of atmospheric samples. This would be expected to reduce the overall uncertainty of the beam electron-like event rates in the joint analysis compared to the beam-only studies. This could modify the sensitivity of the beam samples due to the more constrained background events.

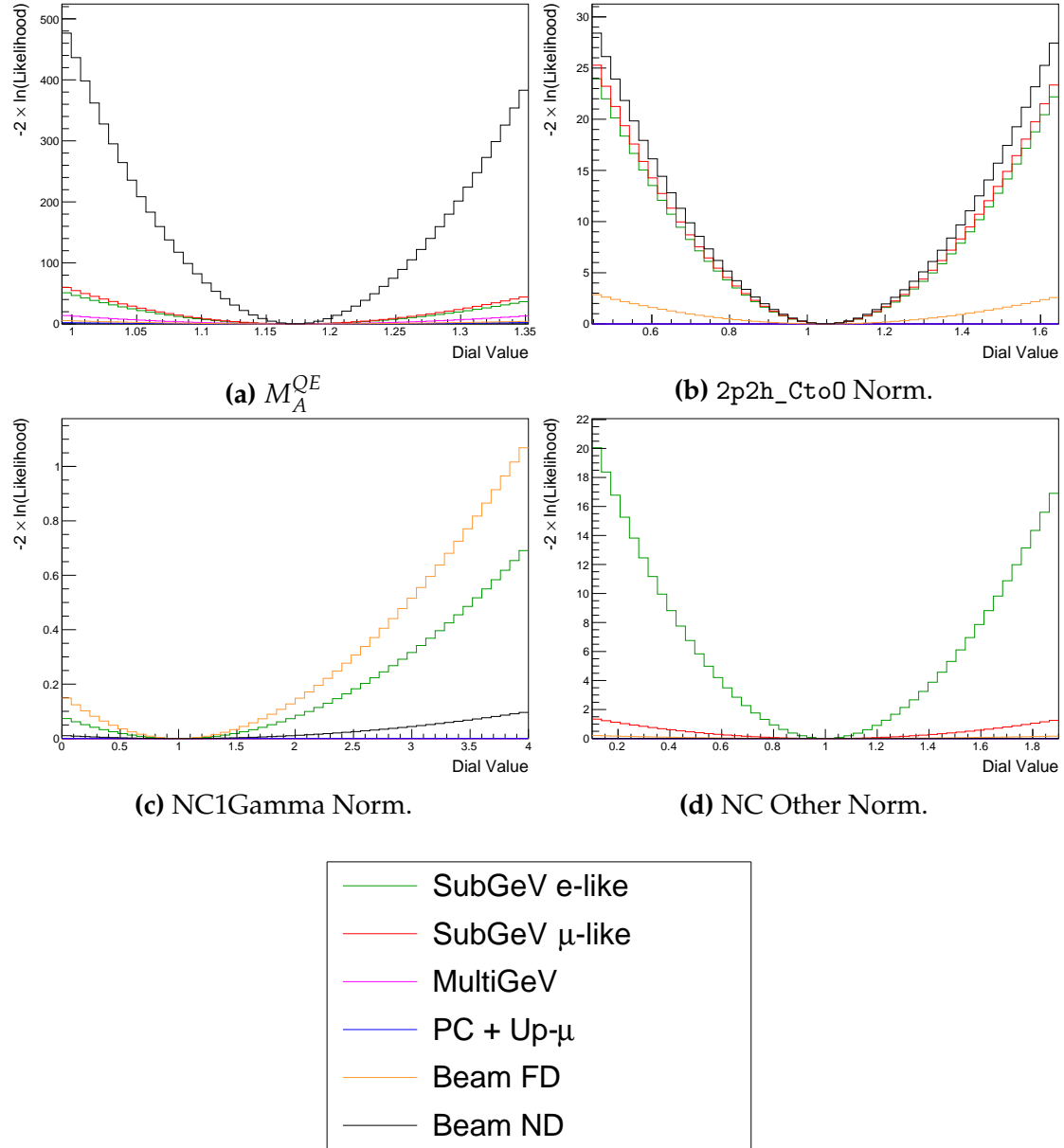


**Figure 8.6:** The response of the likelihood, as defined in section 8.2, illustrating the response of the samples to the various cross-section systematic parameters.

## 2982 8.2 Sensitivities

2983 The sensitivities of the joint T2K and SK oscillation analysis are presented in  
2984 the form of Asimov fits. This technique builds an Asimov data set (follow-  
2985 ing section 6.5) using the AsimovA oscillation parameters and post-BANFF  
2986 systematic tune.

2987 In practice, the Asimov fits presented within this analysis are modified from  
2988 the above definition. An Asimov prediction of both beam and atmospheric far  
2989 detector samples is fit whilst the true data is used for near detector samples.  
2990 The Asimov predictions at the far detector are built using the BANFF tuning (as  
2991 discussed in section 3.2). These modifications mean that the results are equivalent  
2992 to performing a far detector Asimov fit using inputs from the BANFF data fit.  
2993 Consequently, this allows the results to be cross-checked with the results from  
2994 the P-Theta analysis. The comparison has been performed and is documented in  
2995 [222]. No significant discrepancies were found between the fitters.

2996 This section proceeds with the following studies. Firstly, the sensitivity of  
2997 the atmospheric samples after the T2K cross-section has been applied to the low-  
2998 energy events is detailed in subsection 8.2.1. This includes studying the choice of  
2999 applying the 2020 PDG reactor constraint [76] to the atmospheric samples, which  
3000 is documented in subsection 8.2.2. Additionally, the effect of applying the near-  
3001 detector constraints onto the atmospheric samples is discussed in subsection 8.2.3.  
3002 The main result is the sensitivity of the simultaneous beam and atmospheric fit.  
3003 The sensitivities, both with and without the application of the reactor constraint,  
3004 are presented in subsection 8.2.4 and subsection 8.2.5, respectively. To indicate  
3005 the benefit of the joint analysis, the sensitivities are compared to the 2020 T2K  
3006 sensitivities [75, 186] in subsection 8.2.6 and subsection 8.2.7. As shown in  
3007 subsection 8.1.1, the response of the beam and atmospheric samples change  
3008 depending upon the true set of oscillation parameters assumed. Therefore,  
3009 subsection 8.2.8 documents the sensitivities at an alternative oscillation parameter

<sup>3010</sup> set. It is important to note that these results have been published at the Neutrino  
<sup>3011</sup> 2022 conference on behalf of the T2K and SK collaborations [111].

### 3012 8.2.1 Atmospheric-Only Sensitivity Without Reactor Constraint

3013 This section presents the results of an Asimov fit using samples from the near  
 3014 detector and only atmospheric samples from the far detector. The results are  
 3015 presented as one-dimensional or two-dimensional histograms which have been  
 3016 marginalised over all other parameters using the technique outlined in sub-  
 3017 section 4.3.1. Each histogram displays the posterior probability density and  
 3018 illustrates the credible intervals, calculated using the technique in subsection 4.3.2.  
 3019 For these fits in this subsection, a flat penalty term is used for  $\sin^2(\theta_{13})$  such the  
 3020 reactor constraint is not applied. The Asimov data is generated assuming the  
 3021 AsimovA oscillation parameter set defined in Table 2.2 and the post-BANFF  
 3022 systematic parameter tune.

Without Reactor Constraint, Both Hierarchies

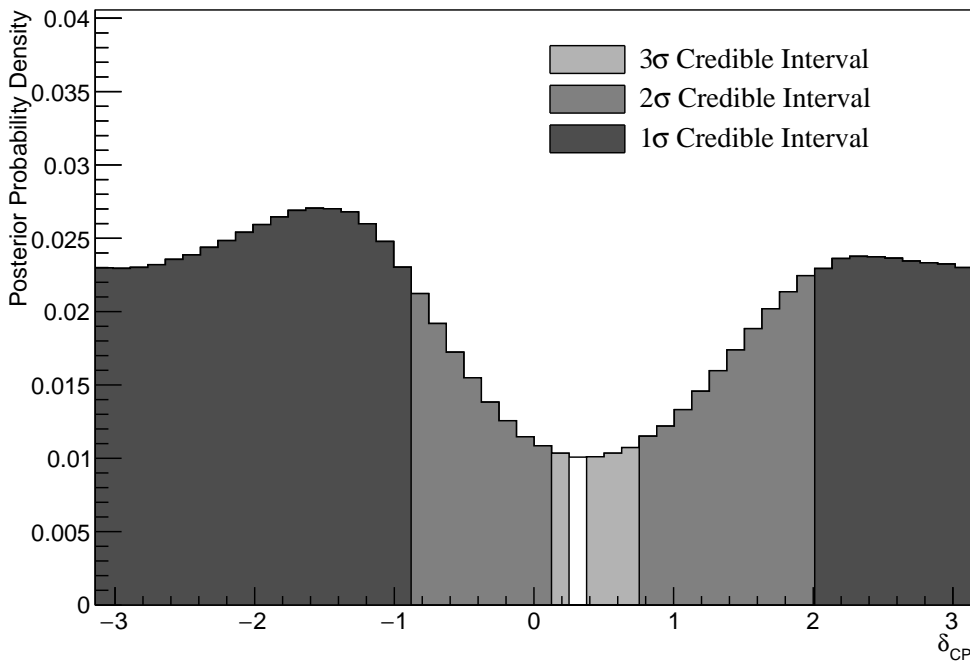


**Figure 8.7:** The one-dimensional posterior probability density distribution in  $\delta_{CP}$ , marginalised over both hierarchies, from the SK atmospheric-only fit. The reactor constraint is not applied.

3023 Figure 8.7 illustrates the posterior probability density for  $\delta_{CP}$ , marginalised  
 3024 over both hierarchies. If instead, only steps in the normal hierarchy were  
 3025 considered, the shape of the contours would change. The fit favours the known

oscillation parameter ( $\delta_{CP} = -1.601$ ) although the posterior probability is very flat through the range of  $-\pi < \delta_{CP} < -1$  and  $2 < \delta_{CP} < \pi$ . There is also a region around  $\delta_{CP} \sim 0.4$  which is disfavoured at  $2\sigma$ . This indicates that the SK samples can rule out some parts of the CP conserving parameter space reasonably well, near  $\delta_{CP} \sim 0.4$ , when the true value of  $\delta_{CP} \sim \pi/2$ .

### Without Reactor Constraint, Both Hierarchies

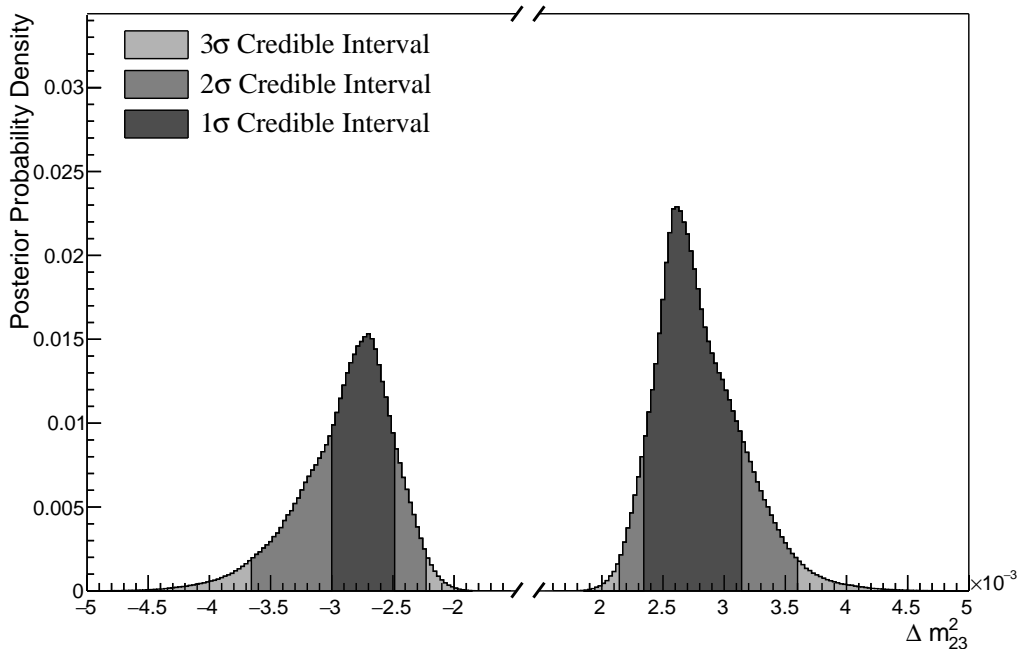


**Figure 8.8:** The one-dimensional posterior probability density distribution in  $\Delta m_{32}^2$ , marginalised over both hierarchies, from the SK atmospheric-only fit. The reactor constraint is not applied.

The posterior probability density in  $\Delta m_{32}^2$  is given in Figure 8.8. This distribution includes steps in both the normal hierarchy (NH,  $\Delta m_{32}^2 > 0$ ) and the inverse hierarchy (IH,  $\Delta m_{32}^2 < 0$ ). The highest posterior probability density is found within the NH, which agrees with the known oscillation parameter value. However, all of the credible intervals span both of the hierarchies hypotheses. If instead, only steps in the normal hierarchy were considered, the shape of the contours would change. The known oscillation parameter is  $2.509 \times 10^{-3} \text{ eV}^2$ , which is contained within the  $1\sigma$  credible interval.

	LO ( $\sin^2 \theta_{23} < 0.5$ )	UO ( $\sin^2 \theta_{23} > 0.5$ )	Sum
NH ( $\Delta m_{32}^2 > 0$ )	0.17	0.40	0.58
IH ( $\Delta m_{32}^2 < 0$ )	0.13	0.29	0.42
Sum	0.31	0.69	1.00

**Table 8.2:** The distribution of steps in an SK atmospheric-only fit, presented as the fraction of steps in the upper (UO) and lower (LO) octants and the normal (NH) and inverted (IH) hierarchies. The reactor constraint is not applied. The Bayes factors are calculated as  $B(\text{NH}/\text{IH}) = 1.37$  and  $B(\text{UO}/\text{LO}) = 2.24$ .

Following the discussion in subsection 4.3.3, the Bayes factor for hierarchy preference can be calculated by determining the fraction of steps that fall into the NH and the IH regions, as an equal prior is placed on both hypotheses. A similar calculation can be performed by calculating the fraction of steps which fall in the lower octant (LO,  $\sin^2 \theta_{23} < 0.5$ ) or upper octant (UO,  $\sin^2 \theta_{23} > 0.5$ ). The fraction of steps, broken down by hierarchy and octant, are given in Table 8.2. The Bayes factor for preferred hierarchy model is  $B(\text{NH}/\text{IH}) = 1.37$ . Table 4.1 states this value of the Bayes factor indicates a weak preference for the normal hierarchy model. The Bayes factor for choice of octant is  $B(\text{UO}/\text{LO}) = 2.24$ . This is also classified as a weak preference for the UO. Both of these show that the fit is returning the correct choice of models (NH and UO) for the known Asimov A oscillation parameters defined in Table 2.2.

The  $1\sigma$  credible intervals, broken down by hierarchy, and position in parameter space of the highest posterior probability density is given in Table 8.3. These are taken from the one-dimensional projections of the oscillation parameters, marginalised over all other parameters within the fit. For the known Asimov value of  $\delta_{CP} = -1.601$ , the  $1\sigma$  credible interval rules out a region between  $\delta_{CP} = -0.86$  and  $\delta_{CP} = 1.96$ , when marginalising over both hierarchies. The position of the highest posterior density is  $\delta_{CP} = -1.57$  which is clearly compatible with the known oscillation parameter value.

The sensitivity of the atmospheric samples to  $\sin^2(\theta_{13})$  is presented in Figure 8.9. The likelihood scans presented in Figure 8.1 suggest that the sensitivity

Parameter	Interval	HPD
$\delta_{CP}$ , (BH)	$[-\pi, -0.86], [1.96, \pi]$	-1.57
$\delta_{CP}$ , (NH)	$[-\pi, -0.86], [1.88, \pi]$	-1.57
$\delta_{CP}$ , (IH)	$[-\pi, -0.94], [1.96, \pi]$	-1.57
$\Delta m_{32}^2$ (BH) [ $\times 10^{-3}\text{eV}^2$ ]	$[-3.00, -2.50], [2.35, 3.15]$	2.65
$\Delta m_{32}^2$ (NH) [ $\times 10^{-3}\text{eV}^2$ ]	$[2.39, 3.04]$	2.64
$\Delta m_{32}^2$ (IH) [ $\times 10^{-3}\text{eV}^2$ ]	$[-3.15, -2.45]$	-2.70
$\sin^2(\theta_{23})$ (BH)	$[0.476, 0.59]$	0.542
$\sin^2(\theta_{23})$ (NH)	$[0.476, 0.59]$	0.554
$\sin^2(\theta_{23})$ (IH)	$[0.476, 0.59]$	0.542

**Table 8.3:** The position of the highest posterior probability density (HPD) and width of the  $1\sigma$  credible interval for the SK atmospheric-only fit. The reactor constraint is not applied. The values are presented by which hierarchy hypothesis is assumed: marginalised over both hierarchies (BH), normal hierarchy only (NH), and inverted hierarchy only (IH).

3061 to  $\sin^2(\theta_{13})$  will be small. This behaviour is also seen in the fit results, where the  
 3062 width of the  $1\sigma$  credible intervals span the region of  $\sin^2(\theta_{13}) = [0.008, 0.08]$ . This  
 3063 is more than an order of magnitude worse than the constraint from reactor  
 3064 experiments [76].

3065 As previously discussed, the correlations between oscillation parameters are  
 3066 also important to understand how the atmospheric samples respond. Figure 8.10  
 3067 illustrates the two dimensional  $\sin^2(\theta_{13}) - \delta_{CP}$  sensitivity, marginalised over all  
 3068 other parameters. The displayed contours are calculated by marginalising over  
 3069 both hierarchies. The shape of the  $1\sigma$  credible interval shows that the constraining  
 3070 power of the fit on  $\delta_{CP}$  is dependent upon the value of  $\sin^2(\theta_{13})$ . Furthermore,  
 3071 they show a strong resemblance to the likelihood scans illustrated in Figure 8.2.  
 3072 Whilst the atmospheric samples do not strongly constrain the value of  $\sin^2(\theta_{13})$ ,  
 3073 the value of  $\sin^2(\theta_{13})$  does impact the atmospheric sensitivity to  $\delta_{CP}$ . A value of  
 3074  $\sin^2(\theta_{13}) \sim 0.02$  would select a continuous contour over all values of  $\delta_{CP}$ . This  
 3075 shows the effect of the marginalisation effect previously described.

### Without Reactor Constraint, Both Hierarchies

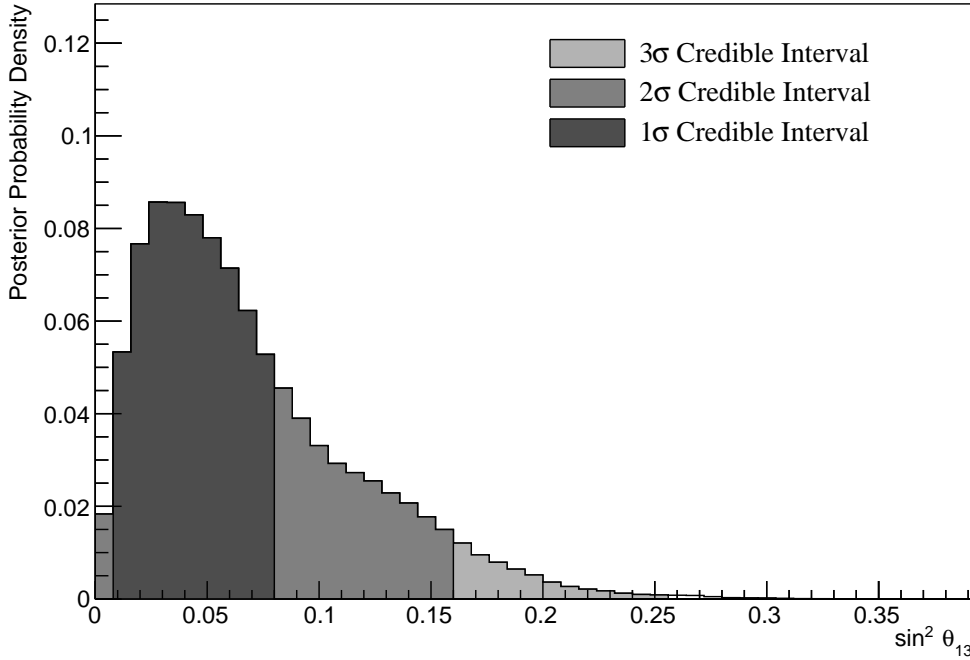


**Figure 8.9:** The one-dimensional posterior probability density distribution in  $\sin^2(\theta_{13})$ , marginalised over both hierarchies, from the SK atmospheric-only fit. The reactor constraint is not applied.

3076     The  $\sin^2(\theta_{23}) - \Delta m_{32}^2$  disappearance contours are illustrated in Figure 8.11.  
 3077     As expected, the area contained in the inverted hierarchy  $1\sigma$  credible interval is  
 3078     slightly smaller than that in the normal hierarchy. This follows from the Bayes  
 3079     factor showing a weak preference for NH meaning that more of the steps will exist  
 3080     in the  $\Delta m_{32}^2 > 0$  region. The known oscillation parameters of  $\sin^2(\theta_{23}) = 0.528$   
 3081     and  $\Delta m_{32}^2 = 2.509 \times 10^{-3} \text{ eV}^2$  are contained within the  $1\sigma$  credible interval.

3082     Figure 8.12 illustrates the two-dimensional projections for each permutation of  
 3083     oscillation parameters which this analysis is sensitive to:  $\delta_{CP}$ ,  $\sin^2(\theta_{13})$ ,  $\sin^2(\theta_{23})$ ,  
 3084     and  $\Delta m_{32}^2$ . The purpose of this plot is to illustrate the correlations between the  
 3085     oscillation parameters. The contours are calculated whilst marginalising over  
 3086     both hierarchies, however, only the NH is illustrated when plotting the  $\Delta m_{32}^2$   
 3087     parameter. As expected the correlations play a significant role in these sensitivity  
 3088     measurements, especially the choice of the  $\sin^2(\theta_{13})$  constraint. The application  
 3089     of reactor constraint would be expected to alter both the width and position of the

### Without Reactor Constraint, Both Hierarchies

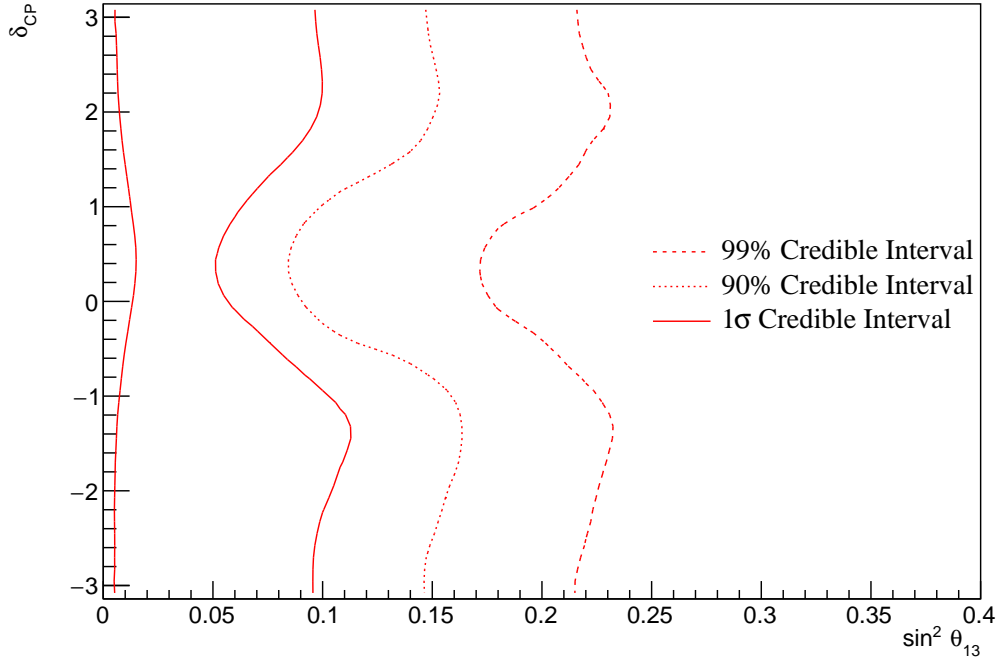


**Figure 8.10:** The two-dimensional posterior probability density distribution in  $\delta_{CP}$  –  $\sin^2(\theta_{13})$ , marginalised over both hierarchies, from the SK atmospheric-only fit. The reactor constraint is not applied.

3090  $\Delta m_{32}^2$ ,  $\delta_{CP}$ , and  $\sin^2(\theta_{23})$  constraints. The majority of the octant model preference  
 3091 comes from the region of  $\sin^2(\theta_{13}) \sim 0.03$  such that the application of the reactor  
 3092 constraint would not be expected to significantly change the octant preference.  
 3093 The reactor constraint would result in lower values of  $|\Delta m_{32}^2|$ . Interestingly, the  
 3094 distribution of steps in the  $\delta_{CP}$ - $\sin^2(\theta_{13})$  plot is slightly flatter in the region of the  
 3095 reactor constraint. Both the posterior distribution from this fit and the distribution  
 3096 in Figure 8.2 show a region of low negative log-likelihood extending out towards  
 3097 higher values of  $\sin^2(\theta_{13})$  in the  $\delta_{CP} \sim -\pi/2$  and  $\delta_{CP} \sim 2$  region. Consequently,  
 3098 the reactor constraint could feasibly reduce the sensitivity of the atmospheric  
 3099 samples to  $\delta_{CP}$ , due to the previously discussed marginalisation effects.

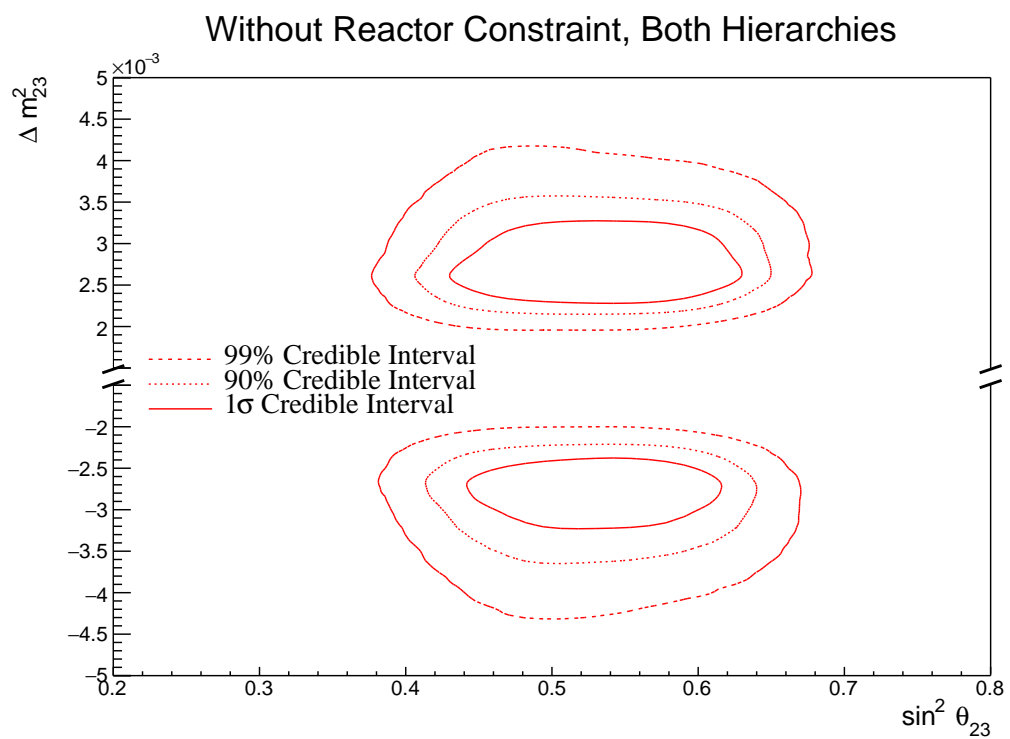


**Figure 8.11:** The two-dimensional posterior probability density distribution in  $\Delta m_{32}^2 - \sin^2(\theta_{23})$ , marginalised over both hierarchies, from the SK atmospheric-only fit. The reactor constraint is not applied.

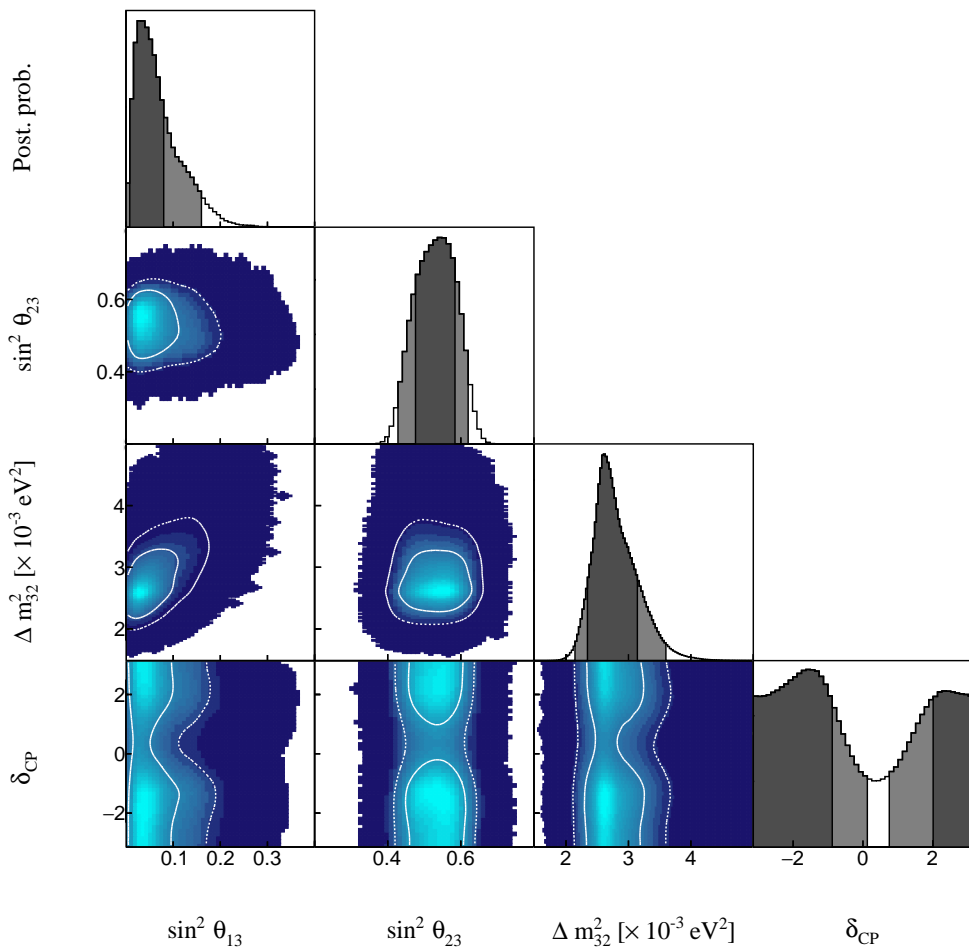


**Figure 8.12:** The posterior probability density distribution from the SK atmospheric-only fit. The reactor constraint is not applied. The distribution is given for each two-dimensional permutation of the oscillation parameters of interest. The one-dimensional distribution of each parameter is also given.

### 3100 8.2.2 Atmospheric-Only Sensitivity With Reactor Constraint

3101 The results in subsection 8.2.1 discuss the atmospheric sensitivity when the reactor  
 3102 constraint is not applied. The correlations illustrated in Figure 8.12 indicate that  
 3103 the marginalisation effects could contribute to differing sensitivities when the  
 3104 external reactor constraint is applied. Using the technique discussed in subsec-  
 3105 tion 4.1.1, the posterior distribution of the fit in subsection 8.2.1 can be reweighted  
 3106 to include the reactor constraint of  $\sin^2(\theta_{13}) = (2.18 \pm 0.08) \times 10^{-2}$  [76].

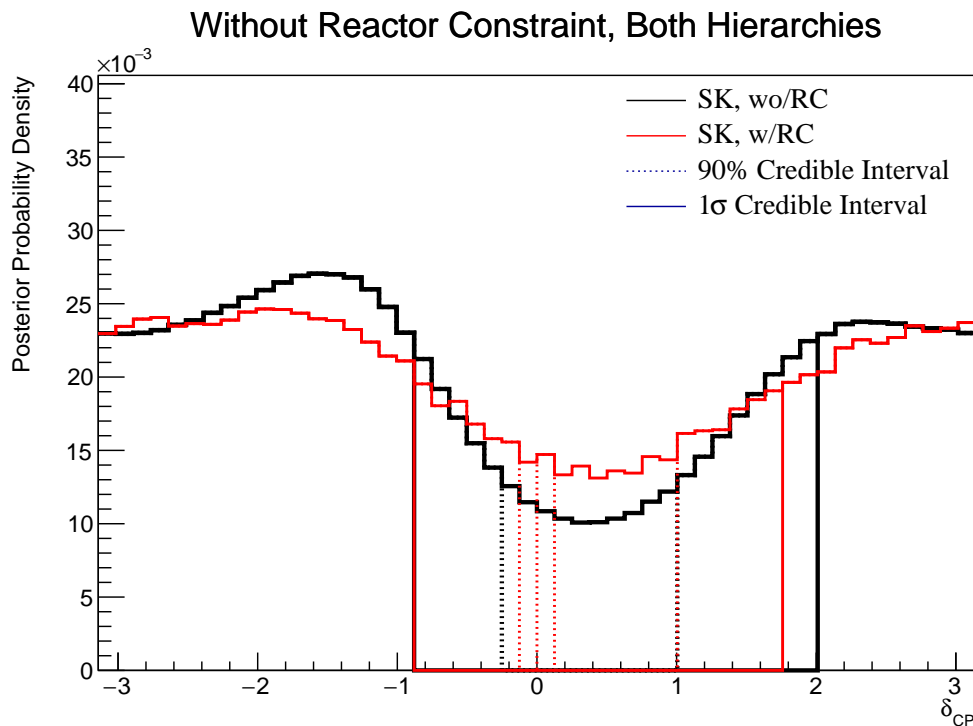


**Figure 8.13:** The one-dimensional posterior probability density distribution in  $\delta_{CP}$  compared between the SK atmospheric-only fit (Black) and the SK atmospheric fit with the reactor constraint applied (Red). The distributions are marginalised over both hierarchies.

3107 Figure 8.13 illustrates the sensitivity to  $\delta_{CP}$  of the atmospheric fit with reactor  
 3108 constraint applied. The distribution is less peaked than the previous results.  
 3109 This is due to the expected marginalisation effect previously discussed. The  
 3110 width of the  $1\sigma$  credible interval is increased when the reactor constraint is  
 3111 applied, indicating less sensitivity to  $\delta_{CP}$  in the region of  $\sin^2(\theta_{13})$  preferred  
 3112 by the reactor constraint.

### Without Reactor Constraint, Both Hierarchies

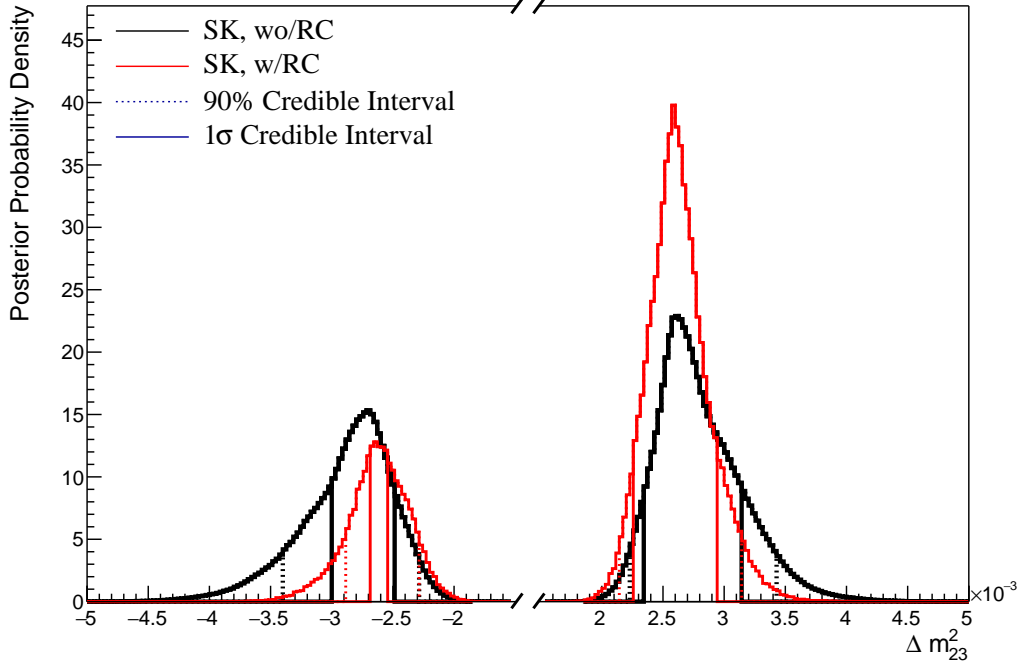


**Figure 8.14:** The one-dimensional posterior probability density distribution in  $\Delta m_{32}^2$  compared between the SK atmospheric-only fit (Black) and the SK atmospheric fit with the reactor constraint applied (Red). The distributions are marginalised over both hierarchies.

3113     The reactor constraint increases the sensitivity of the atmospheric samples to  
 3114      $\Delta m_{32}^2$  as illustrated in Figure 8.14. The  $1\sigma$  credible interval in  $\Delta m_{32}^2$  is determined  
 3115     to be  $[-2.70, -2.55] \times 10^{-3}\text{eV}^2$  and  $[2.25, 2.95] \times 10^{-3}\text{eV}^2$ . The width of the IH  
 3116     credible interval is reduced by  $\sim 70\%$  when the reactor constraint is applied. Due  
 3117     to the marginalisation effects observed in Figure 8.12, the favoured region of  $\Delta m_{32}^2$   
 3118     moves closer to zero for both hierarchies. A clear explanation of this behaviour  
 3119     is illustrated in Figure 8.15 which illustrates the posterior distribution in the  
 3120      $\Delta m_{32}^2 - \sin^2(\theta_{13})$  parameters, marginalised over both hierarchies. The correlation  
 3121     between  $\Delta m_{32}^2$  and  $\sin^2(\theta_{13})$  is such that lower values of  $\sin^2(\theta_{13})$  tend towards  
 3122     lower values of  $|\Delta m_{32}^2|$ . This moves the posterior distribution towards the known  
 3123     oscillation parameter  $\Delta m_{32}^2 = 2.509 \times 10^{-3}\text{eV}^2$ .

3124     Table 8.4 presents the fraction of steps in each hierarchy and octant model  
 3125     for the fit after the reactor constraint has been applied. The reactor constraint  
 3126     significantly increases the NH preference, increasing the Bayes factor from

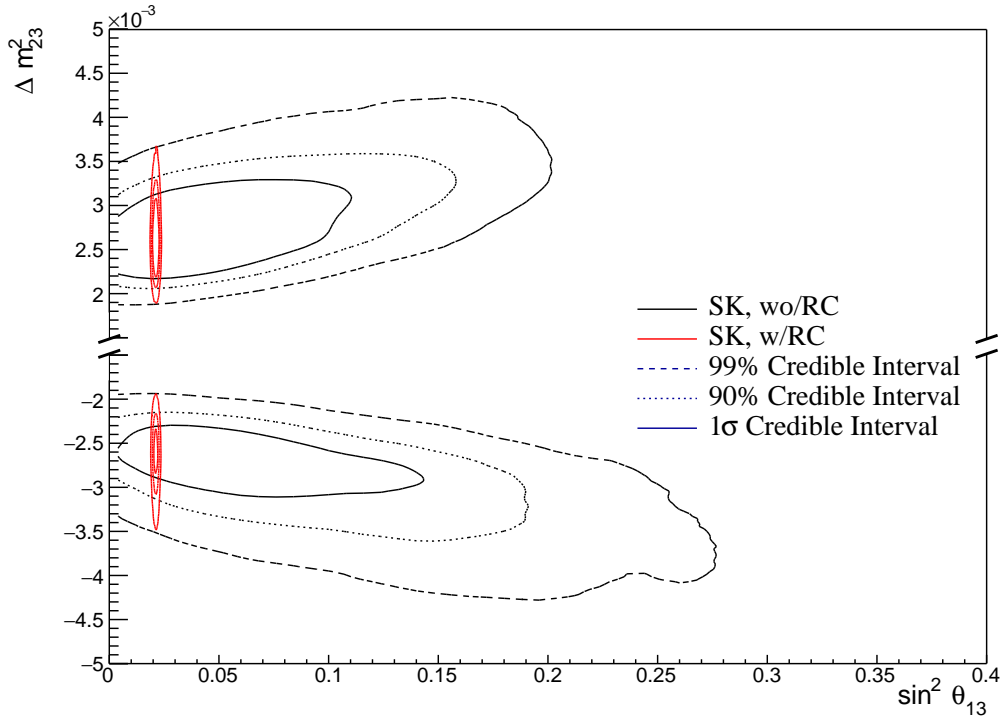


**Figure 8.15:** The two-dimensional posterior probability density distribution in  $\Delta m_{32}^2$  –  $\sin^2(\theta_{13})$  compared between the SK atmospheric-only fit (Black) and the SK atmospheric fit with the reactor constraint (Red). The distributions are marginalised over both hierarchies.

	LO ( $\sin^2 \theta_{23} < 0.5$ )	UO ( $\sin^2 \theta_{23} > 0.5$ )	Sum
NH ( $\Delta m_{32}^2 > 0$ )	0.21	0.53	0.74
IH ( $\Delta m_{32}^2 < 0$ )	0.08	0.18	0.26
Sum	0.29	0.71	1.00

**Table 8.4:** The distribution of steps in an SK atmospheric with reactor constraint fit, presented as the fraction of steps in the upper (UO) and lower (LO) octants and the normal (NH) and inverted (IH) hierarchies. The Bayes factors are calculated as  $B(\text{NH}/\text{IH}) = 2.86$  and  $B(\text{UO}/\text{LO}) = 2.39$ .

<sup>3127</sup>  $B(\text{NH}/\text{IH}) = 1.37$  to  $B(\text{NH}/\text{IH}) = 2.86$  when the reactor constraint is applied.

<sup>3128</sup> This is still defined as a weak preference for NH hypothesis according to Jeffrey's

<sup>3129</sup> scale (see Table 4.1), however, it is a stronger preference than when the constraint

<sup>3130</sup> is not applied. The preference for the correct octant model is slightly increased

<sup>3131</sup> by the application of the reactor constraint which is consistent with expectation.

<sup>3132</sup> However, the conclusion that would be made does not significantly change.

### 3133    8.2.3 Application of Near Detector Constraints for Atmospheric 3134    Samples

3135    The choice of applying the near detector constraints to the low-energy atmo-  
3136    spheric samples was introduced in subsection 6.4.3. This subsection illustrates  
3137    the effect of that choice on the sensitivities of the atmospheric samples to the  
3138    oscillation parameters. This Asimov data was generated assuming the ‘AsimovA’  
3139    oscillation parameter set defined in Table 2.2 and the post-BANFF systematic  
3140    parameter tune.

3141    The change in sensitivity on  $\delta_{CP}$  is given in Figure 8.16. The reactor constraint  
3142    is not applied in either of the fits within this comparison. The shape of the  
3143    posterior is similar although less peaked at the Asimov point ( $\delta_{CP} = -1.601$ )  
3144    and more symmetric between the regions of  $\delta_{CP} = -1.601$  and  $\delta_{CP} \sim 2.5$ . The  
3145    width of the  $1\sigma$  credible intervals are approximately the same (identical to within  
3146    a bin width) and the same conclusion holds for the higher credible intervals. The  
3147    change in sensitivity to other oscillation parameters has been studied and no  
3148    significant discrepancies were found. As expected, the sensitivities are statistics  
3149    dominated and the exact choice of systematic model and constraint does not  
3150    significantly affect the physics conclusions one would make from this analysis.

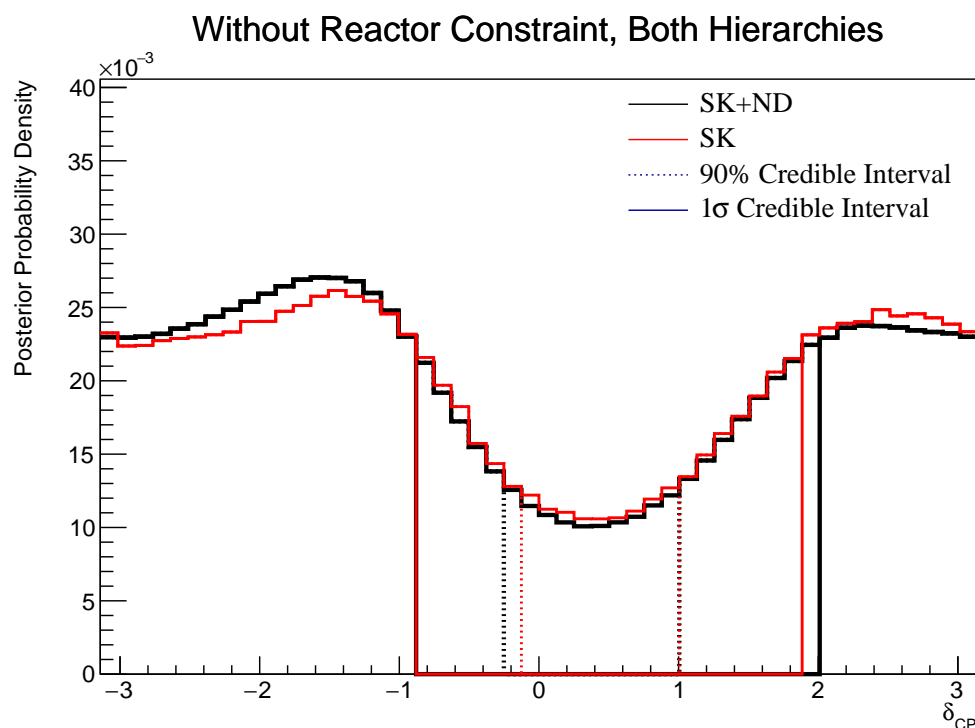


**Figure 8.16:** The one-dimensional posterior probability density distribution in  $\delta_{CP}$  compared between the SK atmospheric-only fit where the near detector constraint is (Black) and is not (Red) applied. The distributions are marginalised over both hierarchies.

### 3151 8.2.4 Atmospheric and Beam Sensitivity without Reactor Con- 3152 straint

3153 This section presents the sensitivities of the simultaneous beam and atmospheric  
 3154 analysis where the reactor constraint is not applied. Similar to the previous  
 3155 studies, the Asimov data is built assuming the post-BANFF cross-section tune  
 3156 and Asimov A oscillation parameters defined in Table 2.2. This fit uses all 18 near  
 3157 detector beam samples, 5 far detector beam samples, and 18 atmospheric samples.  
 3158 The sensitivity to  $\delta_{CP}$ , marginalised over both hierarchies, is given in Figure 8.17.

Without Reactor Constraint, Both Hierarchies

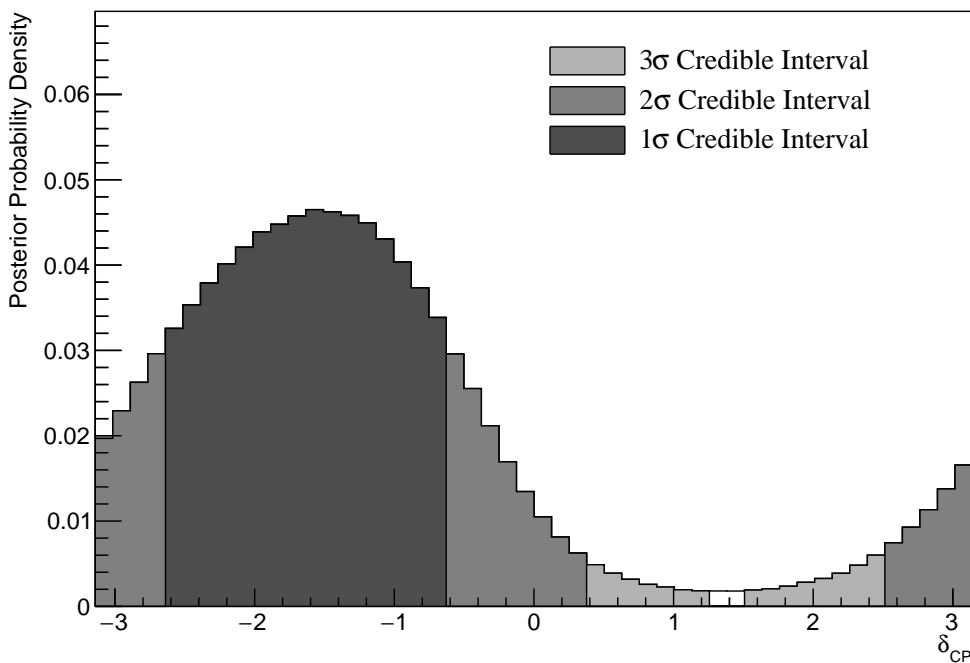


**Figure 8.17:** The one-dimensional posterior probability density distribution in  $\delta_{CP}$ , marginalised over both hierarchies, from the joint beam and atmospheric fit. The reactor constraint is not applied.

3159 The credible intervals and highest posterior distribution for each oscillation  
 3160 parameter is given in Table 8.5. The highest posterior probability density is  
 3161  $\delta_{CP} = -1.58$  and is compatible with the known Asimov A value of  $\delta_{CP} = -1.601$ .  
 3162 The CP-conserving values of  $\delta_{CP} = 0, \pi, -\pi$  are disfavoured at  $1\sigma$  credible  
 3163 interval. There is also a region around  $\delta_{CP} = 1.4$  which is disfavoured at more  
 3164 than  $3\sigma$ . Whilst these conclusions can only be made at this particular Asimov

point, it does show that if the true value of  $\delta_{CP}$  was CP-violating, this joint analysis would be able to disfavour CP conserving values at over  $1\sigma$  without any external constraints. The highest posterior probability density does move further away from the Asimov point when only steps in the NH region are considered. This is due to the correlations between the value of  $\delta_{CP}$  and the mass hierarchy, as will be later discussed.

Parameter	Interval	HPD
$\delta_{CP}$ , (BH)	[−2.64, −0.63]	-1.57
$\delta_{CP}$ , (NH)	[−2.76, −0.63]	-1.45
$\delta_{CP}$ , (IH)	[−2.39, −0.88]	-1.57
$\Delta m_{32}^2$ (BH) [ $\times 10^{-3}\text{eV}^2$ ]	[2.46, 2.58]	2.49
$\Delta m_{32}^2$ (NH) [ $\times 10^{-3}\text{eV}^2$ ]	[2.48, 2.56]	2.51
$\Delta m_{32}^2$ (IH) [ $\times 10^{-3}\text{eV}^2$ ]	[−2.60, −2.52]	-2.55
$\sin^2(\theta_{23})$ (BH)	[0.48, 0.55]	0.509
$\sin^2(\theta_{23})$ (NH)	[0.48, 0.55]	0.509
$\sin^2(\theta_{23})$ (IH)	[0.48, 0.55]	0.521

**Table 8.5:** The position of the highest posterior probability density (HPD) and width of the  $1\sigma$  credible interval for the joint beam and atmospheric fit. The reactor constraint is not applied. The values are presented by which hierarchy hypothesis is assumed: marginalised over both hierarchies (BH), normal hierarchy only (NH), and inverted hierarchy only (IH).

The sensitivity to  $\Delta m_{32}^2$  is illustrated in Figure 8.18, marginalised over both hierarchies. Notably, the  $1\sigma$  credible interval is entirely contained within the normal hierarchy region, as illustrated in Table 8.5. This illustrates reasonable sensitivity to the mass hierarchy model. This is also reflected in the  $1\sigma$  credible intervals being approximately the same when they are made considering both hierarchies and when considering only the NH. The known oscillation parameter is  $\Delta m_{32}^2 = 2.509 \times 10^{-3}\text{eV}^2$ . The normal hierarchy distribution favours this value with the highest posterior probability density of  $\Delta m_{32}^2 = 2.51 \times 10^{-3}\text{eV}^2$ .

The fraction of steps in each of the mass hierarchy regions and octants of  $\sin^2(\theta_{23})$  is given in Table 8.6. The Bayes factors are determined to be  $B(\text{NH}/\text{IH}) =$

3181 3.67 and  $B(\text{UO}/\text{LO}) = 1.74$ . Jeffrey's scale (presented in Table 4.1) states that  
 3182 this value of the hierarchy Bayes factor illustrates substantial evidence for the  
 3183 normal hierarchy hypothesis. This corresponds to the correct hypothesis given  
 3184 the known oscillation parameters. It is a stronger statement than the atmospheric-  
 3185 only analysis can provide. It is important to note that this is a substantial  
 3186 preference that requires no external constraints required. The Bayes factor for  
 3187 octant determination represents a weak preference for the upper octant but does  
 3188 select the correct octant model.

	LO ( $\sin^2 \theta_{23} < 0.5$ )	UO ( $\sin^2 \theta_{23} > 0.5$ )	Sum
NH ( $\Delta m_{32}^2 > 0$ )	0.29	0.50	0.79
IH ( $\Delta m_{32}^2 < 0$ )	0.08	0.13	0.21
Sum	0.37	0.63	1.00

**Table 8.6:** The distribution of steps in a joint beam and atmospheric fit, presented as the fraction of steps in the upper (UO) and lower (LO) octants and the normal (NH) and inverted (IH) hierarchies. The reactor constraint is not applied. The Bayes factors are calculated as  $B(\text{NH}/\text{IH}) = 3.67$  and  $B(\text{UO}/\text{LO}) = 1.74$ .

3189 The sensitivity to  $\sin^2(\theta_{23})$  is presented in Figure 8.19. There is a clear  
 3190 preference for the upper octant but the peak of the distribution is relatively  
 3191 flat. It peaks at  $\sin^2(\theta_{23}) = 0.509$  which is in the region of the known value of  
 3192  $\sin^2(\theta_{23}) = 0.528$ . The difference in the highest posterior distribution and the  
 3193 width of the credible interval is relatively unchanged when considering different  
 3194 hierarchy models showing no strong correlation between  $\sin^2(\theta_{23})$  and  $|\Delta m_{32}^2|$ .  
 3195 The sensitivity presented as a function of the appearance parameters ( $\sin^2(\theta_{13}) -$   
 3196  $\delta_{CP}$ ) is given in Figure 8.20. As expected, the contours follow that given in  
 3197 Figure 8.2, where the  $2\sigma$  credible intervals have a closed contour excluding the  
 3198 region around  $\delta_{CP} \sim 1.2$ . The width of the  $3\sigma$  credible interval is also clearly  
 3199 dependent upon the value of  $\delta_{CP}$ . Close to the Asimov point,  $\delta_{CP} = -1.601$ , the  
 3200 width of the  $3\sigma$  credible interval approximately spans  $\sin^2(\theta_{13}) = [0.013, 0.04]$ .  
 3201 This is reduced to a region of  $\sin^2(\theta_{13}) = [0.023, 0.042]$  at the most disfavoured  
 3202 value of  $\delta_{CP}$ . This follows the behaviour shown in the likelihood scans. The  $1\sigma$

### Without Reactor Constraint, Both Hierarchies

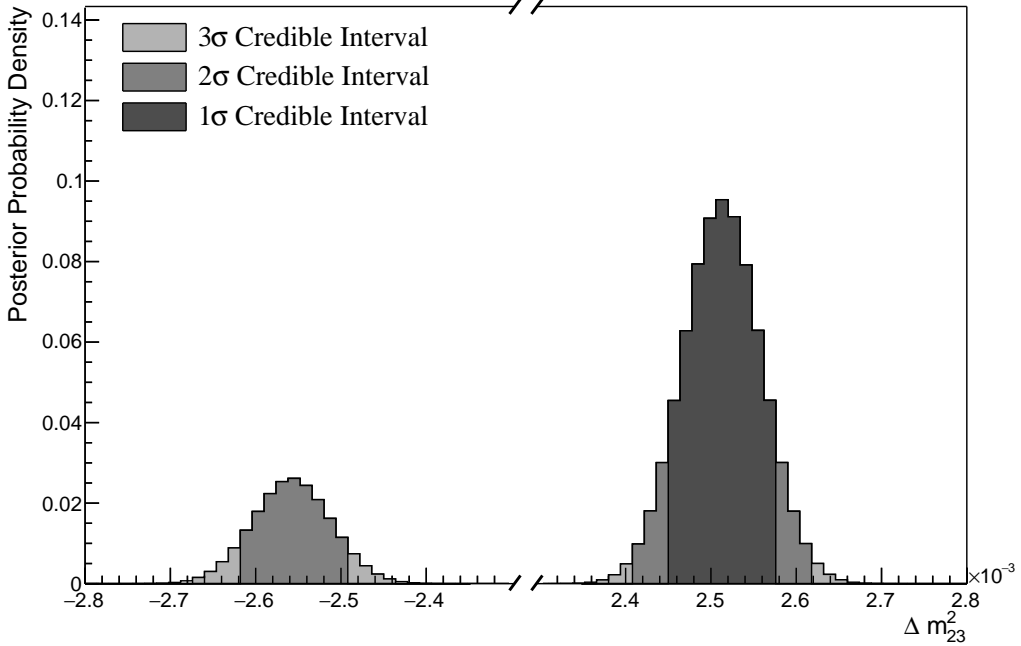


**Figure 8.18:** The one-dimensional posterior probability density distribution in  $\Delta m_{32}^2$ , marginalised over both hierarchies, from the joint beam and atmospheric fit. The reactor constraint is not applied.

credible interval is consistent with both the known oscillation parameter and the reactor constraint ( $\sin^2(\theta_{13}) = (2.18 \pm 0.08) \times 10^{-2}$ ). Application of the reactor constraint would be expected to decrease the width of the 1 $\sigma$  credible intervals of  $\delta_{CP}$  due to the triangular shape of the posterior probability.

The sensitivity in terms of the ‘disappearance’ parameters marginalised over both hierarchies is given in Figure 8.21. The area contained within the IH credible intervals is significantly smaller than those in the NH region. This is reflected in the IH credible intervals being tighter in the  $\sin^2(\theta_{23})$  dimension. No significant correlation is observed between the value of  $\sin^2(\theta_{23})$  and  $|\Delta m_{32}^2|$ .

The two-dimensional posterior distribution for each permutation of the oscillation parameters of interest is given in Figure 8.22. The most notable observation is that the  $\sin^2(\theta_{13})$  and  $\sin^2(\theta_{23})$  are anti-correlated. If the value of  $\sin^2(\theta_{13})$  was known to be closer to the known oscillation parameter value, the preferred value of  $\sin^2(\theta_{23})$  would increase furthering the preference for the UO. That

### Without Reactor Constraint, Both Hierarchies

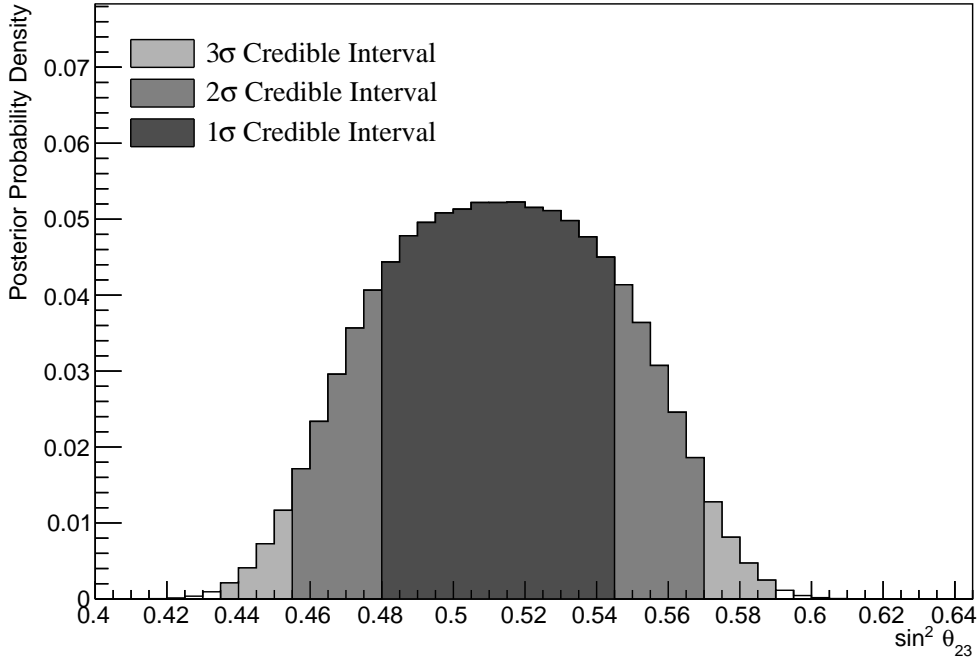


**Figure 8.19:** The one-dimensional posterior probability density distribution in  $\sin^2(\theta_{23})$ , marginalised over both hierarchies, from the joint beam-atmospheric fit. The reactor constraint is not applied.

would move the highest posterior probability closer in line with the Asimov value. This also means that the preference for the UO would be increased if the reactor constraint was to be applied.

Furthermore, the  $\delta_{CP}$  and  $|\Delta m_{32}^2|$  oscillation parameters are anti-correlated, such that higher values of  $|\Delta m_{32}^2|$  prefer lower values of  $\delta_{CP}$ . Whilst this is an interesting result on its own, the width of the  $\Delta m_{32}^2$  contours also depend on  $\sin^2(\theta_{13})$ . This introduces another correlation effect that could modify the sensitivity to  $\delta_{CP}$  once the reactor constraint is applied.

The correlation between  $\sin^2(\theta_{13})$  and  $\Delta m_{32}^2$  can be seen in Figure 8.23. A much larger fraction of the posterior distribution is contained in the NH for lower values of  $\sin^2(\theta_{13})$ . Consequently, the application of the reactor constraint would be expected to significantly increase the preference for NH.

### Without Reactor Constraint, Both Hierarchies

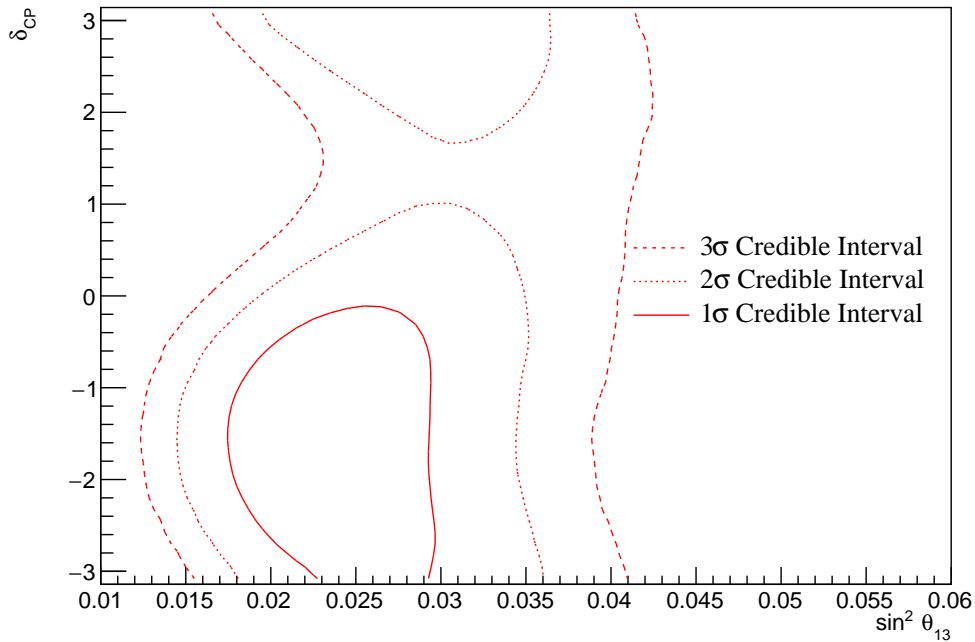


**Figure 8.20:** The two-dimensional posterior probability density distribution in  $\delta_{CP}$  –  $\sin^2(\theta_{13})$ , marginalised over both hierarchies, from the joint beam and atmospheric fit. The reactor constraint is not applied.

### Without Reactor Constraint, Both Hierarchies

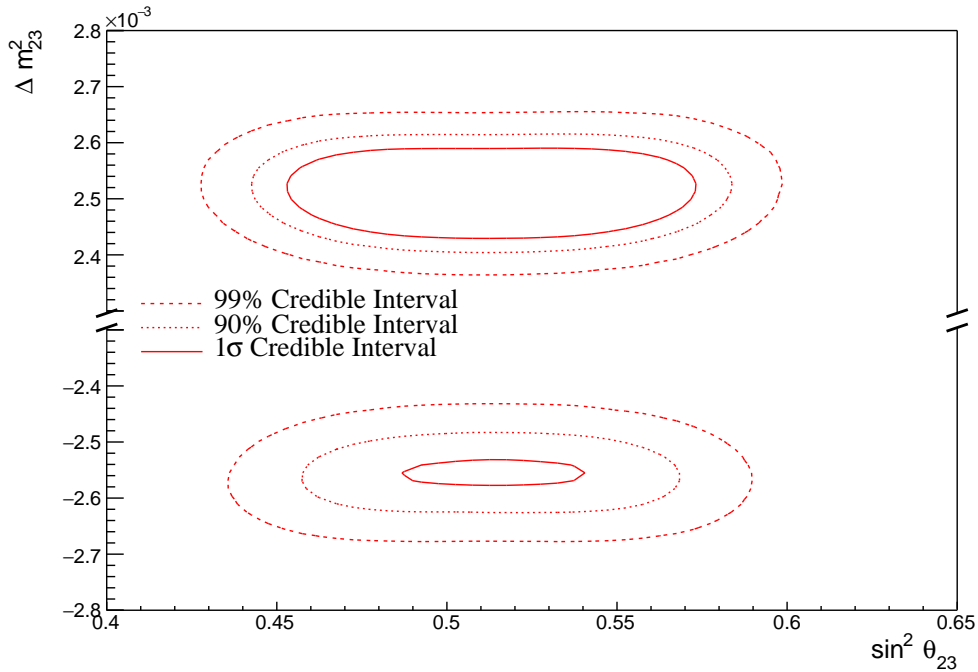


**Figure 8.21:** The two-dimensional posterior probability density distribution in  $\Delta m_{32}^2$  –  $\sin^2(\theta_{23})$ , marginalised over both hierarchies, from the joint beam and atmospheric fit. The reactor constraint is not applied.

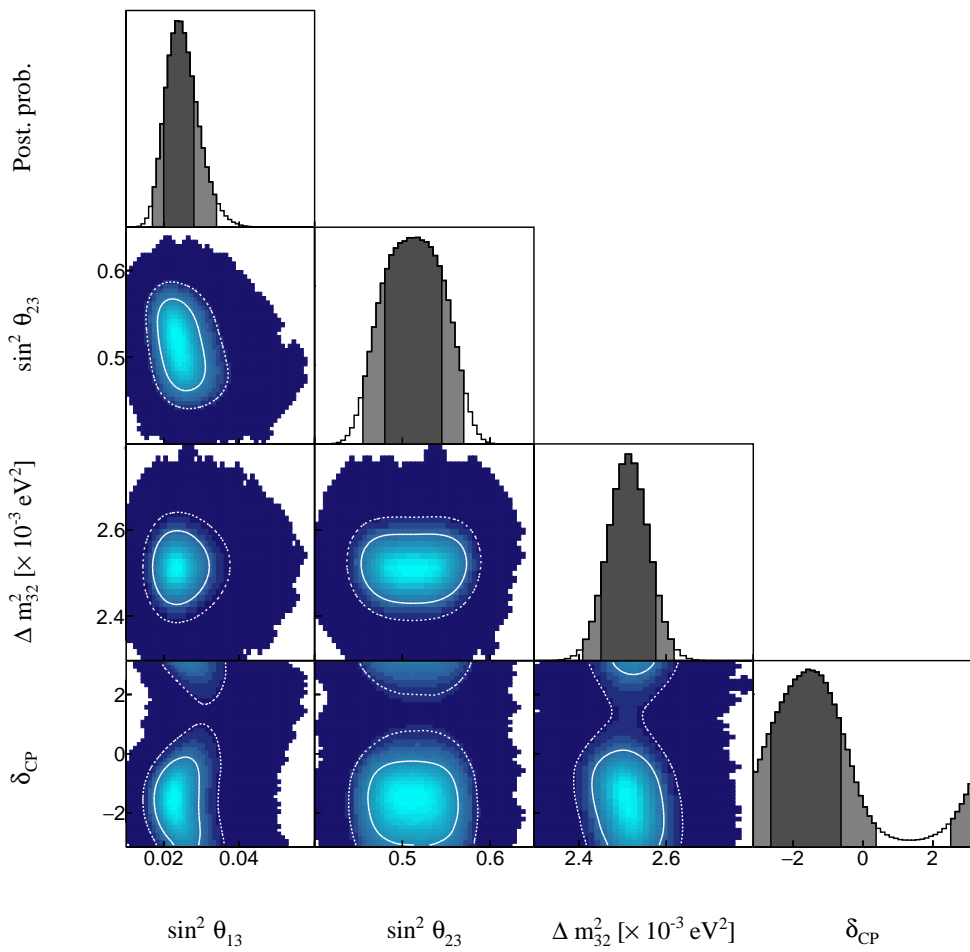


**Figure 8.22:** The posterior probability density distribution from the joint beam and atmospheric fit. The reactor constraint is not applied. The distribution is given for each two-dimensional permutation of the oscillation parameters of interest. The one-dimensional distribution of each parameter is also given.

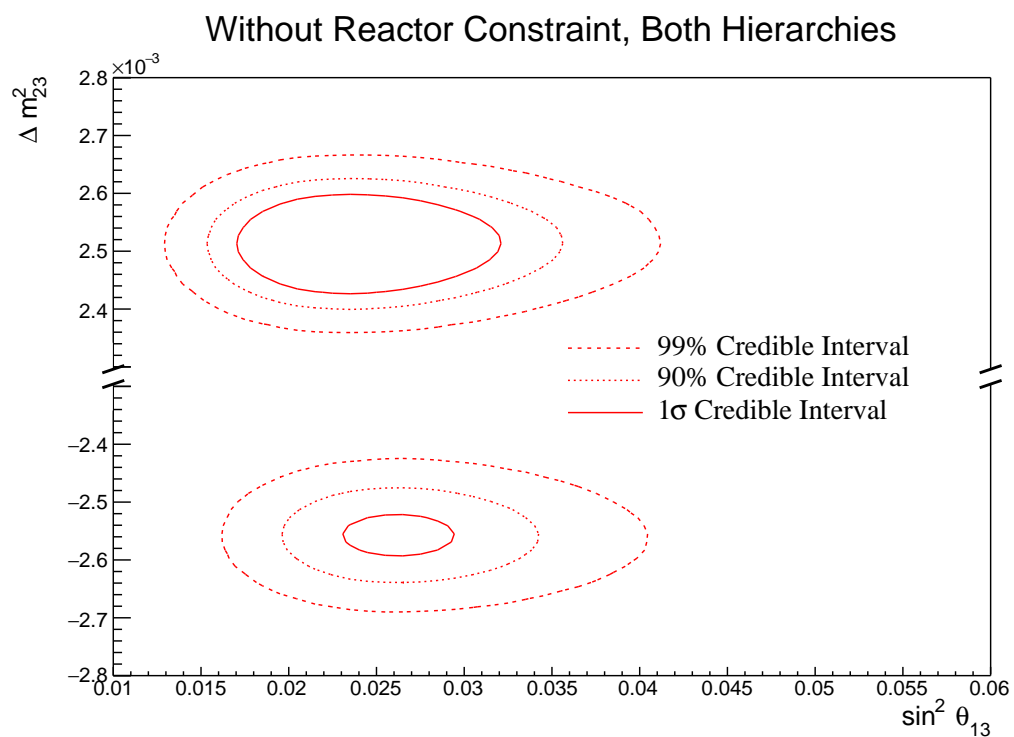


**Figure 8.23:** The two-dimensional posterior probability density distribution in  $\Delta m_{32}^2 - \sin^2(\theta_{13})$ , marginalised over both hierarchies, from the joint beam and atmospheric fit. The reactor constraint is not applied.

### 3229 8.2.5 Atmospheric and Beam Sensitivity with Reactor Constraint

3230 This section presents the sensitivities of the joint beam and atmospheric fit when  
 3231 the reactor constraint is applied to  $\sin^2(\theta_{13})$ . As with the previous studies, the  
 3232 Asimov data is made using the AsimovA oscillation parameter set defined in  
 3233 Table 2.2 and the post-BANFF systematic parameter tune.

With Reactor Constraint, Both Hierarchies

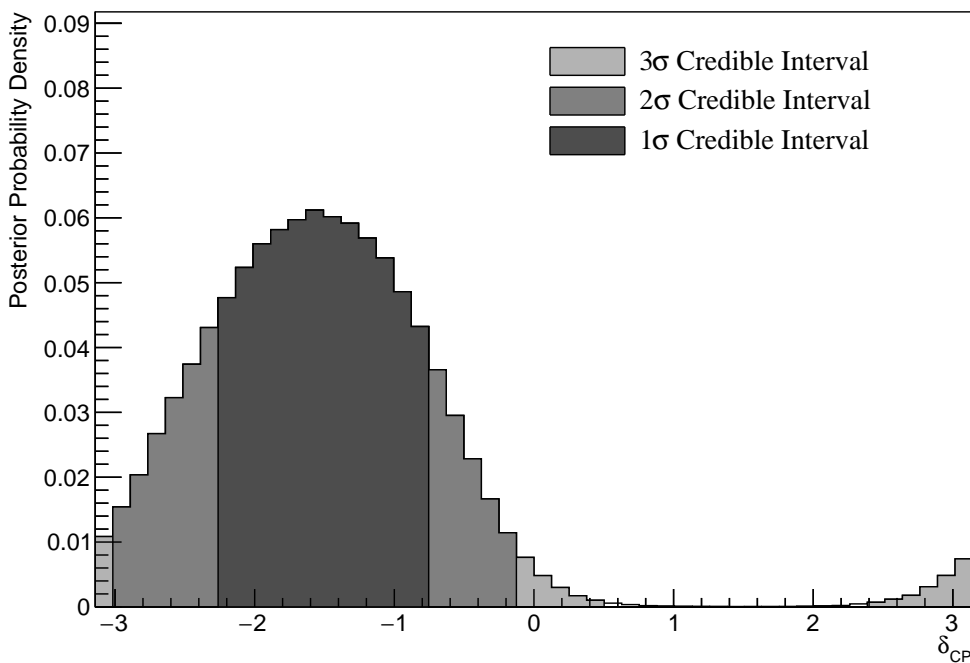


**Figure 8.24:** The one-dimensional posterior probability density distribution in  $\delta_{CP}$ , marginalised over both hierarchies, from the joint beam and atmospheric fit where the reactor constraint is applied.

3234 Figure 8.24 illustrates the sensitivity to  $\delta_{CP}$ , marginalised over both hierarchies.  
 3235 The CP-conserving values of  $\delta_{CP} = -\pi, 0, \pi$  are disfavoured at  $2\sigma$ . Furthermore,  
 3236 the  $3\sigma$  credible interval excludes the region of  $\delta_{CP} = [0.50, 2.39]$ . Thus clearly  
 3237 disfavouring the region of  $\delta_{CP} = \pi/2$  at more than  $3\sigma$  for this particular set  
 3238 of known oscillation parameters. The width of the  $1\sigma$  credible intervals and  
 3239 the position of the highest posterior probability density is given in Table 8.7.  
 3240 The highest posterior probability density in  $\delta_{CP}$  is calculated as  $\delta_{CP} = -1.57$   
 3241 showing no significant biases in the determination of the known oscillation

parameters. The posterior distribution is more peaked around the known oscillation parameter value of  $\delta_{CP} = -1.601$ , as compared to the sensitivities when the reactor constraint is not applied (subsection 8.2.4). This follows from the correlations shown in Figure 8.20, where a lower value of  $\sin^2(\theta_{13})$  results in tighter constraints on  $\delta_{CP}$ .

The effect of applying the reactor constraint for  $\delta_{CP}$  in the joint beam-atmospheric fit is presented in Figure 8.25. The posterior distribution from the two fits are marginalised over both hierarchies. Clearly, the reactor constraint improves the ability of the fit to select the known oscillation parameter as the shape of the distribution is much more peaked. This is also evidenced by the tightening of the  $1\sigma$  and 90% credible intervals. Additionally, the disfavoured region of  $1 < \delta_{CP} < 2$  is wider when the reactor constraint is applied.

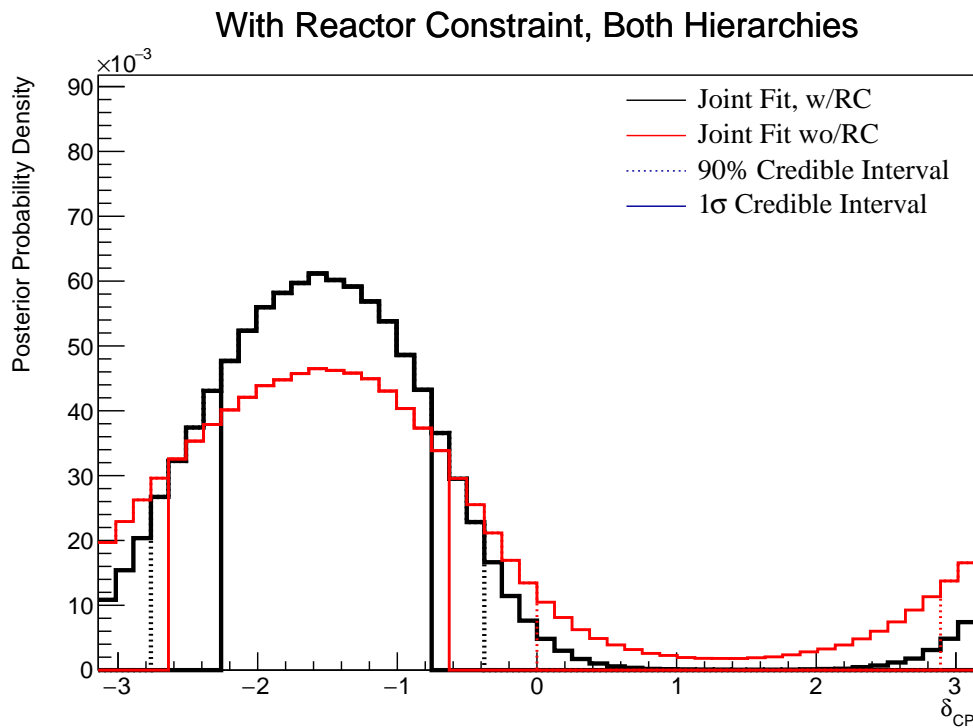


**Figure 8.25:** The one-dimensional posterior probability density distribution in  $\delta_{CP}$  compared between the joint beam-atmospheric fit (Red) and the joint beam and atmospheric fit with the reactor constraint (Black). The distributions are marginalised over both hierarchies.

The sensitivity to  $\sin^2(\theta_{23})$ , marginalised over both hierarchies, is given in Figure 8.26. The highest posterior probability density is located at  $\sin^2(\theta_{23}) = 0.527$

Parameter	Interval	HPD
$\delta_{CP}$ , (BH)	[-2.26, -0.75]	-1.57
$\delta_{CP}$ , (NH)	[-2.26, -0.75]	-1.57
$\delta_{CP}$ , (IH)	[-2.13, -1.00]	-1.57
$\Delta m_{32}^2$ (BH) [ $\times 10^{-3}\text{eV}^2$ ]	[2.46, 2.52]	2.49
$\Delta m_{32}^2$ (NH) [ $\times 10^{-3}\text{eV}^2$ ]	[2.48, 2.56]	2.51
$\Delta m_{32}^2$ (IH) [ $\times 10^{-3}\text{eV}^2$ ]	[-2.60, -2.52]	-2.55
$\sin^2(\theta_{23})$ (BH)	[0.49, 0.55]	0.527
$\sin^2(\theta_{23})$ (NH)	[0.49, 0.55]	0.527
$\sin^2(\theta_{23})$ (IH)	[0.50, 0.56]	0.539

**Table 8.7:** The position of the highest posterior probability density (HPD) and width of the  $1\sigma$  credible interval for the joint beam and atmospheric fit where the reactor constraint is applied. The values are presented by which hierarchy hypothesis is assumed: marginalised over both hierarchies (BH), normal hierarchy only (NH), and inverted hierarchy only (IH).

which agrees with the known value of  $\sin^2(\theta_{23}) = 0.528$ . The distribution clearly favours the UO with almost the entirety of the  $1\sigma$  credible interval contained in the region. Figure 8.27 highlights the sensitivity of the joint fit both with and without the reactor constraint. The fit where the reactor constraint is applied selects the known value much better ( $\sin^2(\theta_{23}) = 0.528$ ). Furthermore, the reactor constraint increases the UO preference which is evidenced by the distribution moving further away from the octant boundary. This indicates that there are marginalisation effects between the two mixing parameters. This follows from the correlation illustrated between  $\sin^2(\theta_{23}) - \sin^2(\theta_{13})$  in Figure 8.22. The posterior distribution of the fit with reactor constraint is more peaked compared to the flatter distribution when the reactor constraint is not applied.

The fraction of steps contained within the two hierarchy and two octant models is given in Table 8.8. The reactor constraint significantly reduces the fraction of steps that are contained within the IH-LO region from 0.08 to 0.02, whilst significantly increasing the fraction of steps within the NH-UO region from 0.53 to 0.64. The application of the reactor constraint increases the Bayes factor

### With Reactor Constraint, Both Hierarchies

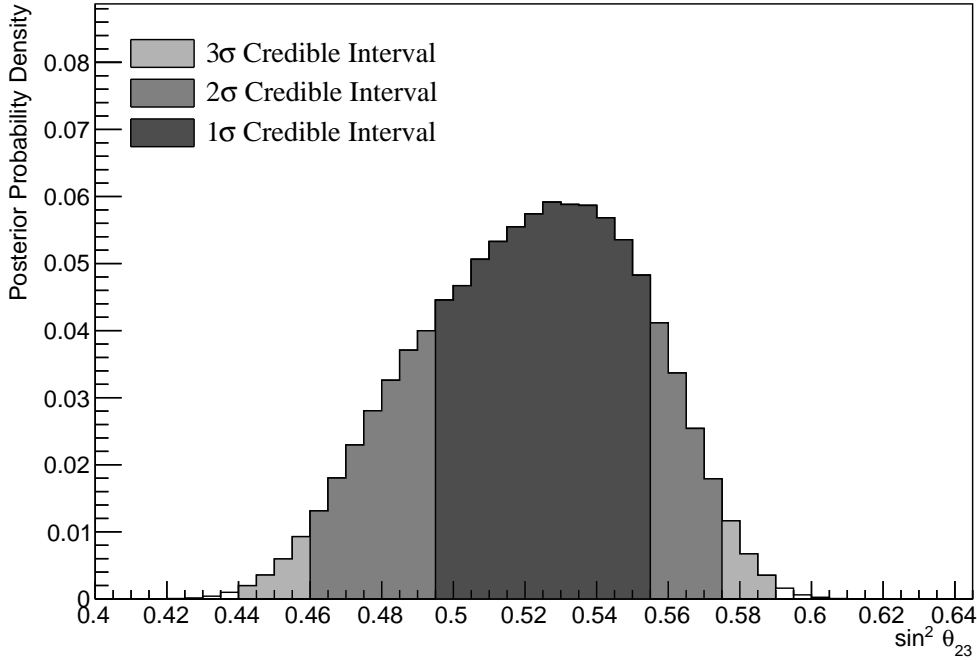


**Figure 8.26:** The one-dimensional posterior probability density distribution in  $\sin^2(\theta_{23})$ , marginalised over both hierarchies, from the joint beam and atmospheric fit where the reactor constraint is applied.

from  $B(\text{NH}/\text{IH}) = 3.67$  to  $B(\text{NH}/\text{IH}) = 7.29$ . There is a very clear preference for the NH, with the Jeffreys scale stating a substantial preference for both fits (see subsection 4.3.3). The Bayes factor for UO preference is calculated as  $B(\text{UO}/\text{LO}) = 2.86$ . Whilst still a weak preference, this is certainly a stronger statement than the sensitivity when the reactor constraint is not applied.

	LO ( $\sin^2 \theta_{23} < 0.5$ )	UO ( $\sin^2 \theta_{23} > 0.5$ )	Sum
NH ( $\Delta m_{32}^2 > 0$ )	0.24	0.64	0.88
IH ( $\Delta m_{32}^2 < 0$ )	0.02	0.10	0.12
Sum	0.26	0.74	1.00

**Table 8.8:** The distribution of steps in a joint beam and atmospheric with the reactor constraint fit applied, presented as the fraction of steps in the upper (UO) and lower (LO) octants and the normal (NH) and inverted (IH) hierarchies. The Bayes factors are calculated as  $B(\text{NH}/\text{IH}) = 7.29$  and  $B(\text{UO}/\text{LO}) = 2.86$ .

The sensitivity to  $\Delta m_{32}^2$ , with the reactor constraint applied, is presented in

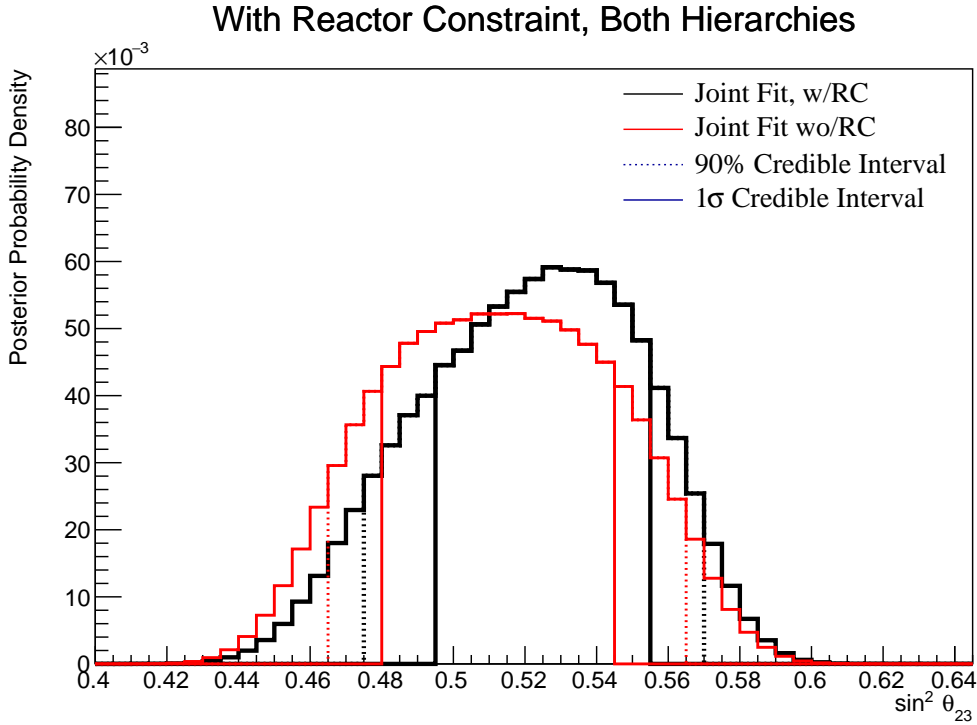


**Figure 8.27:** The one-dimensional posterior probability density distribution in  $\sin^2(\theta_{23})$  compared between the joint beam-atmospheric fit (Red) and the joint beam and atmospheric fit with the reactor constraint (Black). The distributions are marginalised over both hierarchies.

3278 Figure 8.28. The posterior distribution is marginalised over both hierarchies. As  
 3279 expected, the  $1\sigma$  credible interval is entirely contained within the NH region. The  
 3280 position of the highest posterior probability density is given as  $2.49 \times 10^{-3} \text{ eV}^2$ ,  
 3281 illustrating no significant bias between the fit results and the known oscillation  
 3282 parameters. The application of the reactor constraint does move significantly the  
 3283 position of the credible intervals but does reduce their width.

3284 The sensitivity to the appearance parameters ( $\sin^2(\theta_{13}) - \delta_{CP}$ ) is given in  
 3285 Figure 8.29. The distribution is mostly uncorrelated between the two parameters  
 3286 and is centered at the known oscillation parameters. The  $1\sigma$  credible interval  
 3287 excludes  $\delta_{CP} = 0$  and  $\delta_{CP} = (-)\pi$ . Furthermore, the  $3\sigma$  credible intervals  
 3288 exclude the region of  $\delta_{CP} = \pi/2$ .

3289 The sensitivity to the disappearance parameters ( $\sin^2(\theta_{23}) - \Delta m_{32}^2$ ) is illus-  
 3290 trated in Figure 8.30. As expected from the one-dimensional distribution, the  $1\sigma$   
 3291 credible interval is entirely contained within the NH region. Both the NH and

### With Reactor Constraint, Both Hierarchies

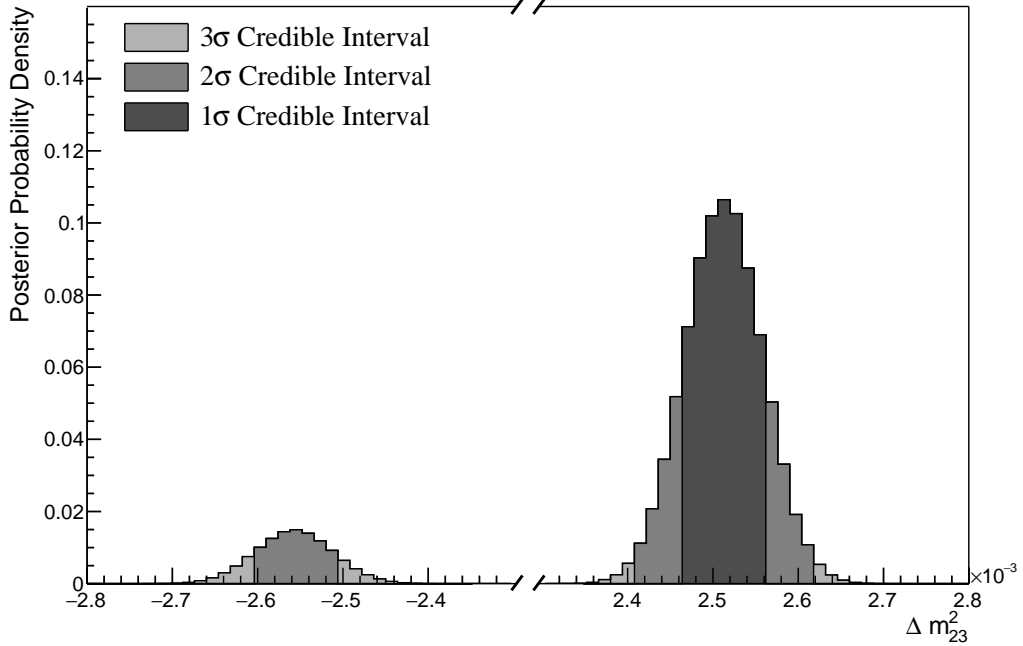


**Figure 8.28:** The one-dimensional posterior probability density distribution in  $\Delta m_{32}^2$ , marginalised over both hierarchies, from the joint beam and atmospheric fit where the reactor constraint is applied.

3292 IH regions favour the UO, with a visually similar preference in both hierarchies.  
 3293 The width of the  $\Delta m_{32}^2$  1 $\sigma$  credible interval does not significantly depend upon  
 3294 the value or octant of  $\sin^2(\theta_{23})$ . This shows that there are no strong correlations  
 3295 between these two parameters.

3296 Figure 8.31 illustrates the posterior distribution for each permutation of  
 3297 two oscillation parameters of interest. The application of the reactor constraint  
 3298 significantly reduces the correlations previously seen in Figure 8.22. There is  
 3299 still a small correlation between  $\delta_{CP}$  and  $\Delta m_{32}^2$ . The application of the reactor  
 3300 constraint has not significantly affected this correlation. The width of the 1 $\sigma$   
 3301 credible interval in  $\Delta m_{32}^2$  is wider for a value of  $\delta_{CP} = 0$  as compared to a value  
 3302 of  $\delta_{CP} = \pi$ . Similarly, the width of the 1 $\sigma$  credible interval in  $\delta_{CP}$  is smaller  
 3303 for lower values of  $\sin^2(\theta_{23})$ .

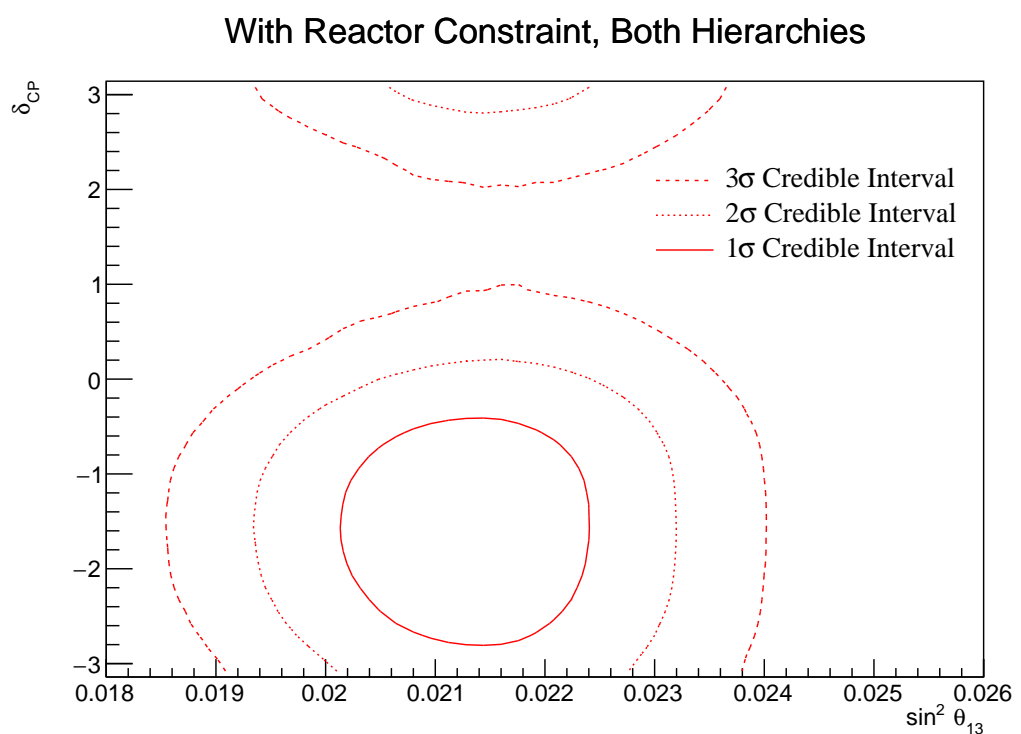


**Figure 8.29:** The two-dimensional posterior probability density distribution in  $\delta_{CP} - \sin^2(\theta_{13})$ , marginalised over both hierarchies, from the joint beam and atmospheric fit where the reactor constraint is applied.

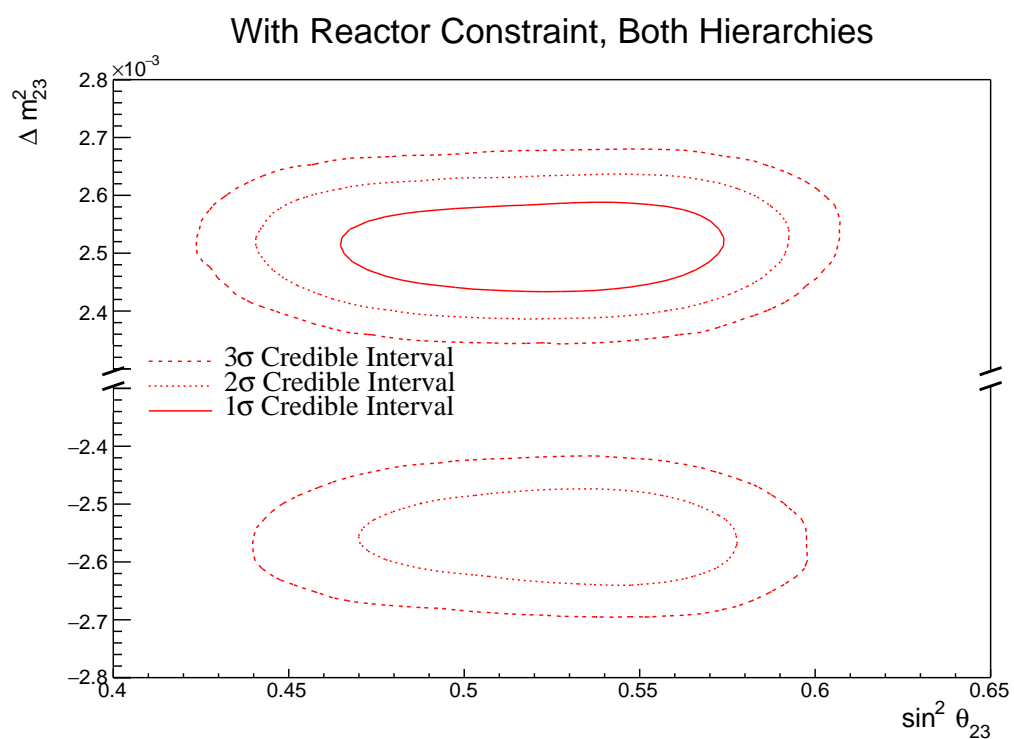


**Figure 8.30:** The two-dimensional posterior probability density distribution in  $\Delta m_{32}^2 - \sin^2(\theta_{23})$ , marginalised over both hierarchies, from the joint beam and atmospheric fit where the reactor constraint is applied.

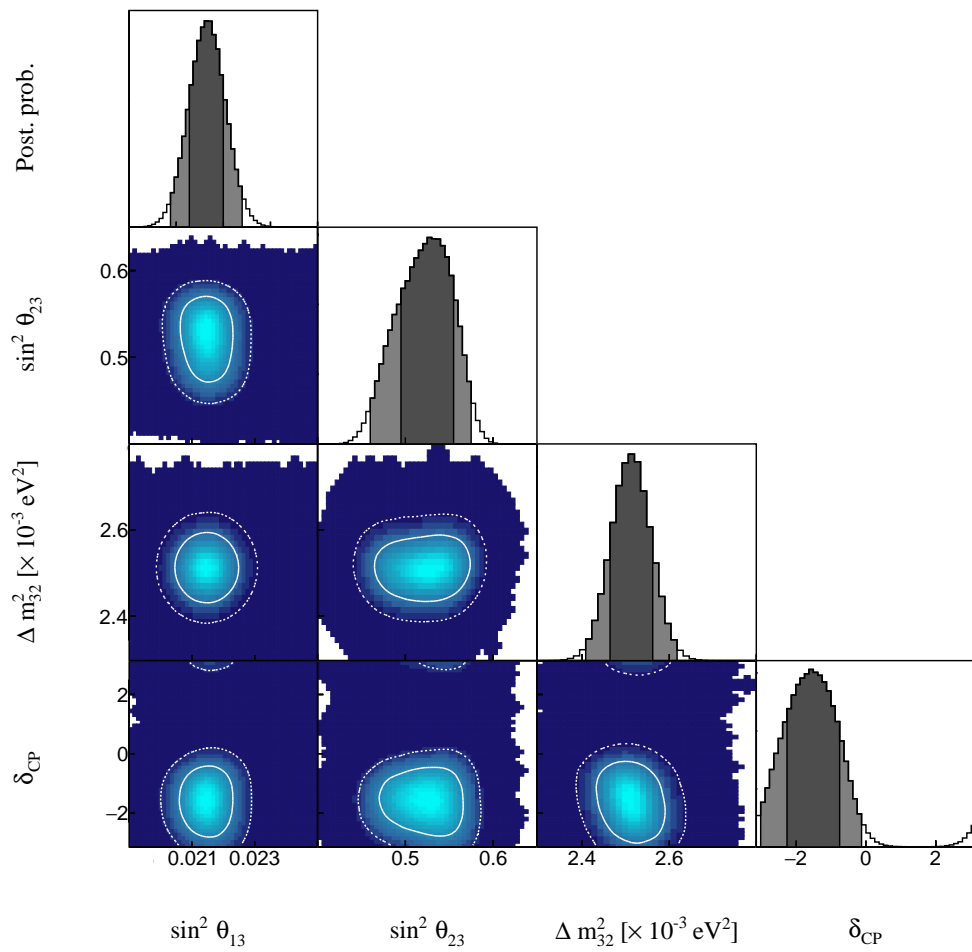


**Figure 8.31:** The posterior probability density distribution from the joint beam and atmospheric fit where the reactor constraint is applied. The distribution is given for each two-dimensional permutation of the oscillation parameters of interest. The one-dimensional distribution of each parameter is also given.

### 3304 8.2.6 Comparison to Latest T2K Sensitivities without Reactor 3305 Constraint

3306 The benefits of the joint beam and atmospheric analysis can be determined by  
 3307 comparing the sensitivities to the beam-only analysis. This section presents those  
 3308 comparisons for sensitivities built using the Asimov A oscillation parameters  
 3309 defined in Table 2.2 and the post-BANFF systematic tune. The reactor constraint  
 3310 is not applied within either of the fits used in these comparisons.

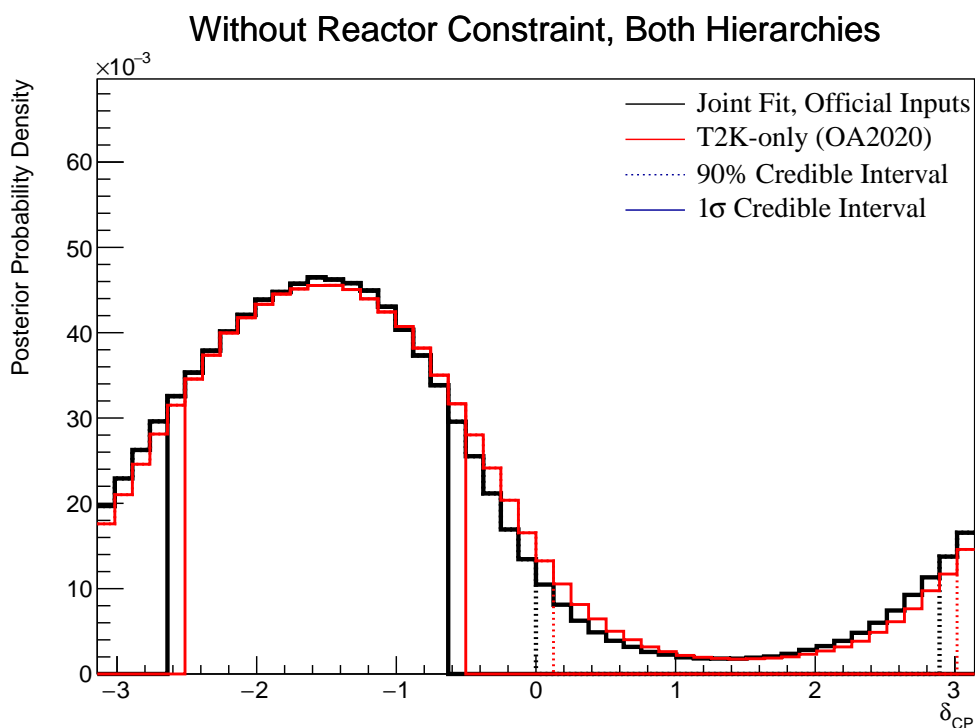


**Figure 8.32:** The one-dimensional posterior probability density distribution in  $\delta_{CP}$  compared between the joint beam-atmospheric fit (Black) and the latest T2K sensitivities (Red) [186]. The reactor constraint is not applied in either fit. The distributions are marginalised over both hierarchies.

3311 The sensitivity, marginalised over both hierarchies, to  $\delta_{CP}$  from the joint  
 3312 beam-atmospheric and beam-only fits is presented in Figure 8.32. As expected  
 3313 from the likelihood scans (Figure 8.4), the sensitivity to  $\delta_{CP}$  is not significantly  
 3314 increased. This is because the known oscillation parameter value ( $\delta_{CP} = -1.601$ )  
 3315 lies at the position where the beam samples dominate the sensitivity compared  
 3316 to the SK samples.

The sensitivity to  $\Delta m_{32}^2$  of the joint beam-atmospheric fit is illustrated in Figure 8.33, where the posterior distribution has been marginalised over both hierarchies. The  $1\sigma$  credible interval of the joint beam and atmospheric fit is entirely contained within the NH region. This shows the significant increase in the ability of the fit to determine the correct mass hierarchy, as compared to the beam-only analysis. This is further evidenced by the fact that the 90% credible intervals from the joint fit are also tighter in the IH region as compared to the beam-only analysis. The Bayes factor for mass hierarchy determination for the beam-only and joint beam and atmospheric are  $B(\text{NH}/\text{IH}) = 1.91$  and  $B(\text{NH}/\text{IH}) = 3.67$ , respectively. According to Jeffrey's scale (Table 4.1), the beam-only analysis represents a weak preference for the NH hypothesis whereas the joint fit returns a substantial preference for the NH hypothesis. To summarise, the joint beam-atmospheric fit has a substantial preference for the correct hierarchy without the requirement of external constraints.

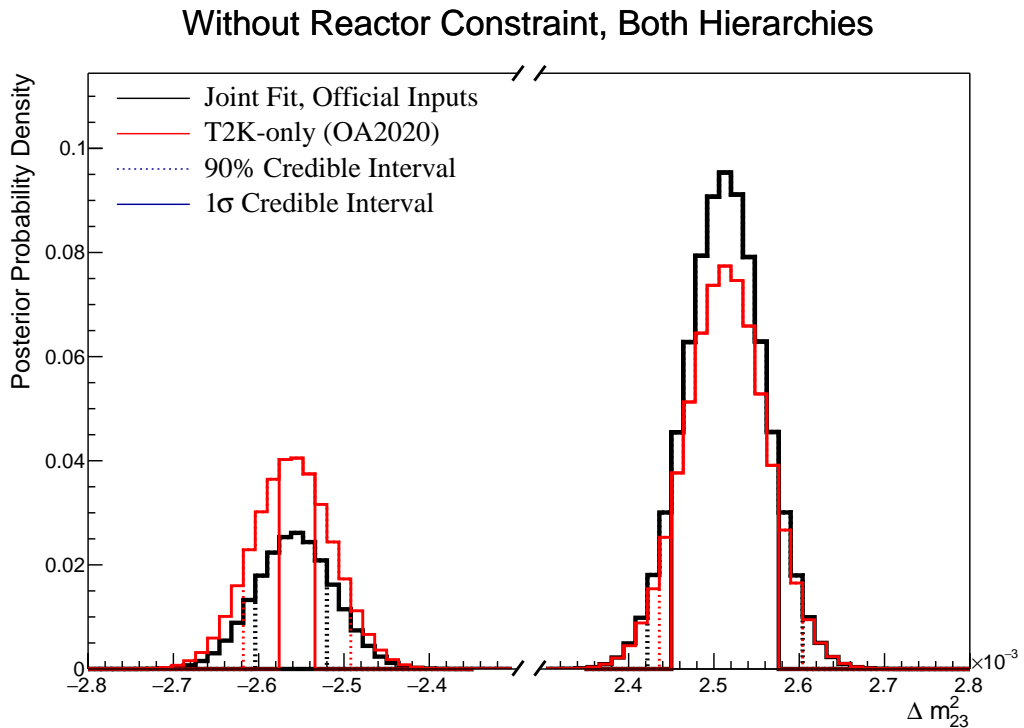


**Figure 8.33:** The one-dimensional posterior probability density distribution in  $\Delta m_{32}^2$  compared between the joint beam-atmospheric fit (Black) and the latest T2K sensitivities (Red) [186]. The reactor constraint is not applied in either fit. The distributions are marginalised over both hierarchies.

3331 The sensitivity to  $\sin^2(\theta_{23})$ , marginalised over both hierarchies, for both the  
 3332 beam-only and joint beam and atmospheric analysis are presented in Figure 8.34.  
 3333 The peak of the posterior distribution from the joint analysis is more aligned  
 3334 with the known value of  $\sin^2(\theta_{23}) = 0.528$  as compared to the beam-only  
 3335 analysis. This indicates that the marginalisation effects from other oscillation  
 3336 parameters ( $\sin^2(\theta_{13}) - \sin^2(\theta_{23})$ ) presented in Figure 8.22) are less prevalent in  
 3337 the projection of this parameter. The Bayes factors for the beam-only and joint  
 3338 beam-atmospheric fit are  $B(\text{UO}/\text{LO}) = 1.56$  and  $B(\text{UO}/\text{LO}) = 1.74$ , respectively.  
 3339 Therefore, the joint beam-atmospheric fit does prefer the UO more strongly than  
 3340 the beam-only analysis, albeit slightly.

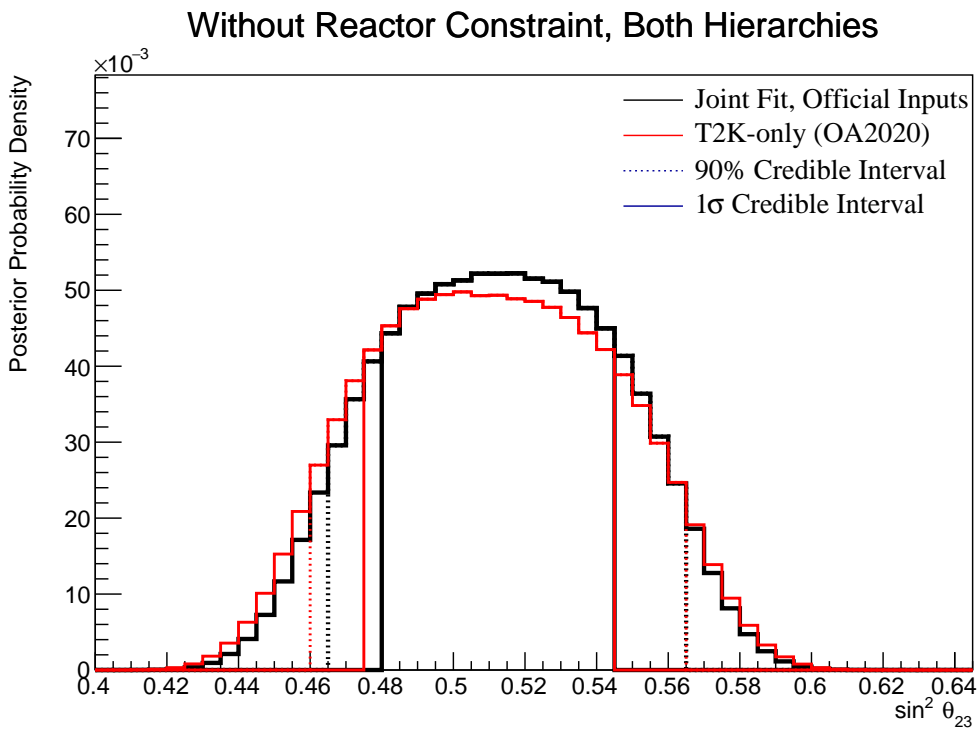


**Figure 8.34:** The one-dimensional posterior probability density distribution in  $\sin^2(\theta_{23})$  compared between the joint beam-atmospheric fit (Black) and the latest T2K sensitivities (Red) [186]. The reactor constraint is not applied in either fit. The distributions are marginalised over both hierarchies.

3341 Whilst the beam-only and joint beam-atmospheric fits have similar sensitivity  
 3342 to  $\delta_{CP}$  and  $\sin^2(\theta_{23})$  when projected in one-dimension, the benefit of the joint  
 3343 analysis becomes more obvious when the sensitivities are presented in two-

3344 dimensions. The sensitivity of the two fits to the appearance parameters ( $\delta_{CP} -$   
3345  $\sin^2(\theta_{13})$ ) are illustrated in Figure 8.35.

3346 The width of the 99% joint fit credible interval in  $\sin^2(\theta_{13})$  is squeezed in the  
3347 region of  $\delta_{CP} \sim 0$  compared to the beam-only analysis. This is the same behaviour  
3348 that is seen in the appearance likelihood scans presented in Figure 8.2. The  $1\sigma$   
3349 and 90% also exhibit slightly tighter constraints on  $\delta_{CP}$ . This is most prevalent  
3350 in the region of  $\delta_{CP} \sim 0$  and  $\sin^2(\theta_{13}) \sim 0.03$ . Whilst the atmospheric samples  
3351 do not have significant sensitivity to  $\sin^2(\theta_{13})$  (as shown in Figure 8.1), they  
3352 aid in breaking the degeneracy between the oscillation parameters allowing  
3353 for tighter constraints.

3354 The sensitivity to the disappearance parameters  $\sin^2(\theta_{23}) - \Delta m_{32}^2$ , marginalised  
3355 over both hierarchies, is presented in Figure 8.36 for both the beam-only and  
3356 joint beam-atmospheric fits. Whilst the one-dimensional sensitivity comparisons  
3357 considered so far show the improvements of the joint fit, the two-dimensional  
3358 projection really shows the benefit of adding the atmospheric samples to the  
3359 beam samples. The area contained within the IH credible intervals is drastically  
3360 reduced in the joint fit. This follows from the better determination of the mass  
3361 hierarchy seen in the Bayes factor comparisons. The  $1\sigma$  joint fit credible interval  
3362 in the IH region more strongly favours the UO as compared to the beam-only fit.  
3363 Even in the NH region, the width of the credible intervals in  $\sin^2(\theta_{23})$  decrease,  
3364 albeit to a smaller extent.

3365 The change in sensitivity to  $\delta_{CP} - \Delta m_{32}^2$  is illustrated in Figure 8.37. As  
3366 expected, the contours presented within the IH region are much smaller in  
3367 the joint fit due to the increased sensitivity to mass hierarchy determination.  
3368 This culminates in a region around  $\delta_{CP} \sim \pi/2$  which is excluded at  $3\sigma$ . This  
3369 behaviour is not present within the beam-only analysis. Consistent with the  
3370 previous observations, the area contained within the IH credible intervals is  
3371 significantly reduced in comparison to the beam-only analysis.

3372 The sensitivity to  $\Delta m_{32}^2$  and  $\sin^2(\theta_{23})$ , as a function of  $\sin^2(\theta_{13})$ , is presented  
3373 in Figure 8.38 and Figure 8.39, respectively. These sensitivities are marginalised

### Without Reactor Constraint, Both Hierarchies

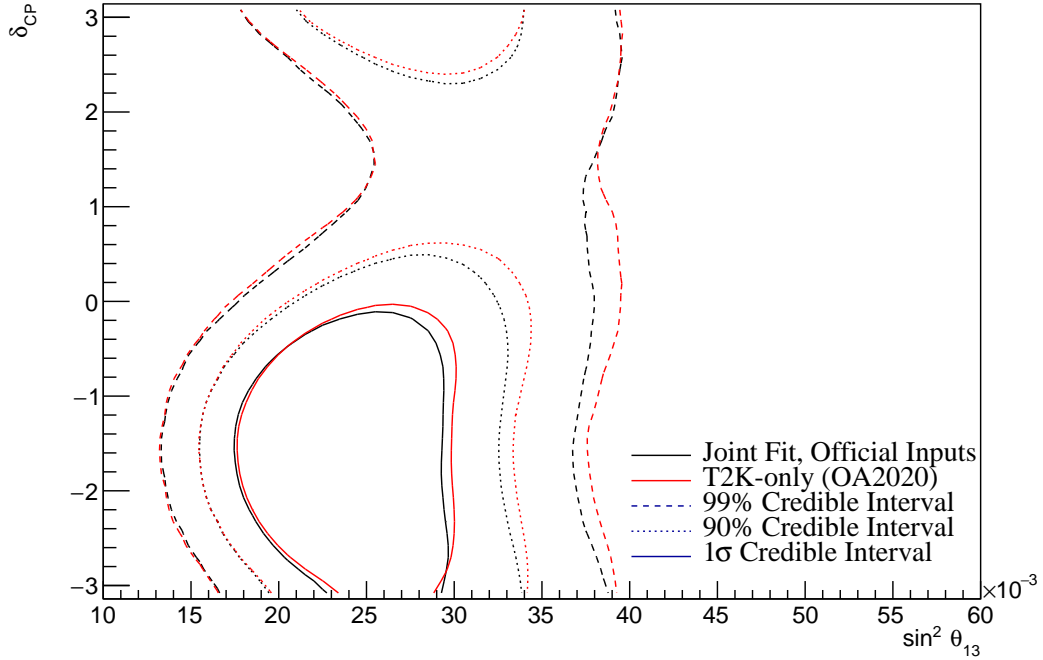


**Figure 8.35:** The two-dimensional posterior probability density distribution in  $\delta_{CP}$  –  $\sin^2(\theta_{13})$  compared between the joint beam-atmospheric fit (Black) and the latest T2K sensitivities (Red) [186]. The reactor constraint is not applied in either fit. The distributions are marginalised over both hierarchies.

over both hierarchies. As expected from the previous observations, the  $\Delta m_{32}^2$  contours within IH region of the joint fit are much smaller than the beam-only analysis. Notably, the joint fit IH  $1\sigma$  credible intervals exclude the region around the reactor constraint. This is not a bias from the fit as the known value for  $\Delta m_{32}^2$  is in the NH region. This does suggest that the application of the reactor constraint would further increase the preference for NH in the joint fit as compared to its effect on the beam-only analysis.

The beam-only and joint beam-atmospheric fits have a slightly different contour shape between the  $\sin^2(\theta_{13})$  and  $\sin^2(\theta_{23})$  parameters, as illustrated by Figure 8.39. The joint analysis disfavours the wrong octant hypothesis more strongly in the region of high  $\sin^2(\theta_{13})$ . This suggests that the application of the reactor constraint will favour the UO more strongly in the joint analysis compared to the beam-only analysis.

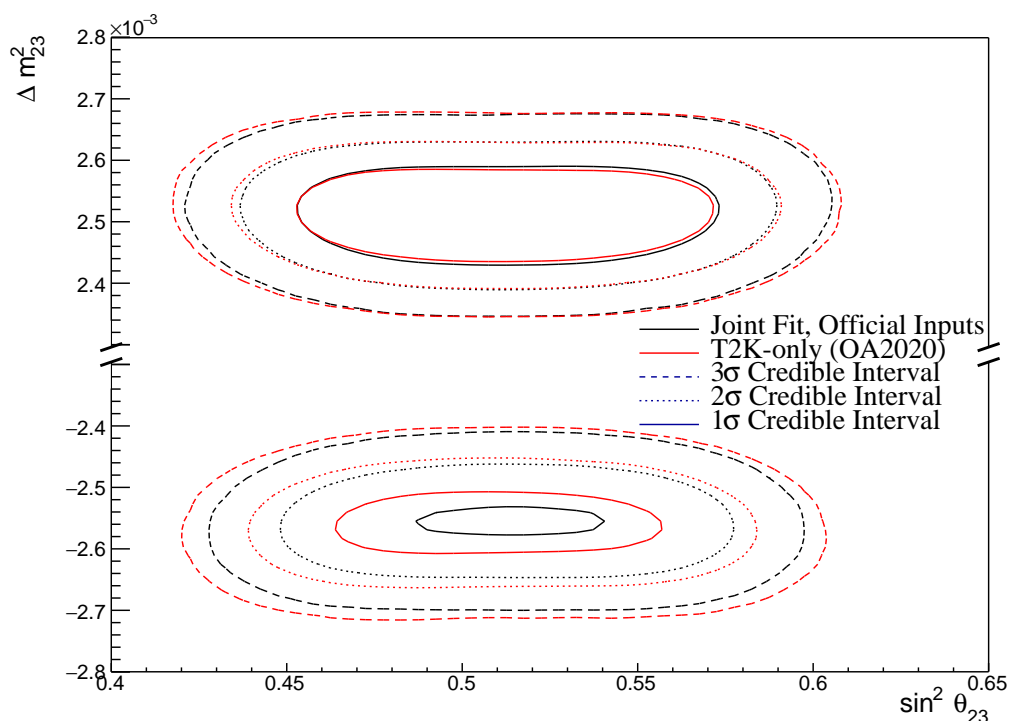


**Figure 8.36:** The two-dimensional posterior probability density distribution in  $\Delta m^2_{32} - \sin^2(\theta_{23})$  compared between the joint beam-atmospheric fit (Black) and the latest T2K sensitivities (Red) [186]. The reactor constraint is not applied in either fit. The distributions are marginalised over both hierarchies.

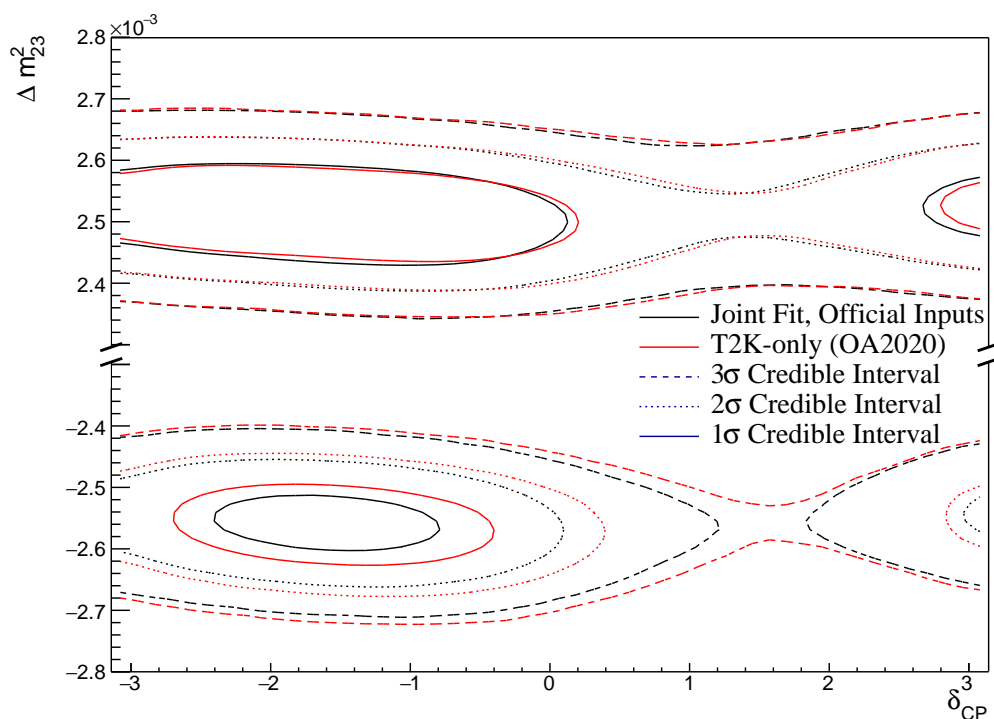


**Figure 8.37:** The two-dimensional posterior probability density distribution in  $\Delta m_{32}^2 - \Delta_{CP}$  compared between the joint beam-atmospheric fit (Black) and the latest T2K sensitivities (Red) [186]. The reactor constraint is not applied in either fit. The distributions are marginalised over both hierarchies.

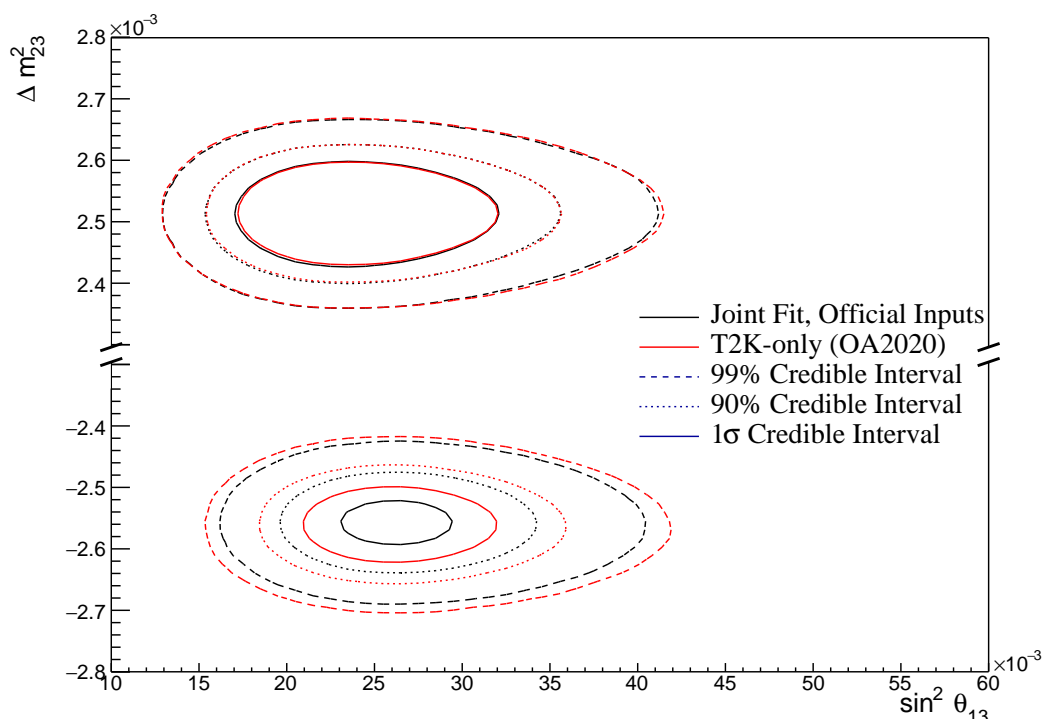


**Figure 8.38:** The two-dimensional posterior probability density distribution in  $\Delta m_{32}^2$  –  $\sin^2(\theta_{23})$  compared between the joint beam-atmospheric fit (Black) and the latest T2K sensitivities (Red) [186]. The reactor constraint is not applied in either fit. The distributions are marginalised over both hierarchies.

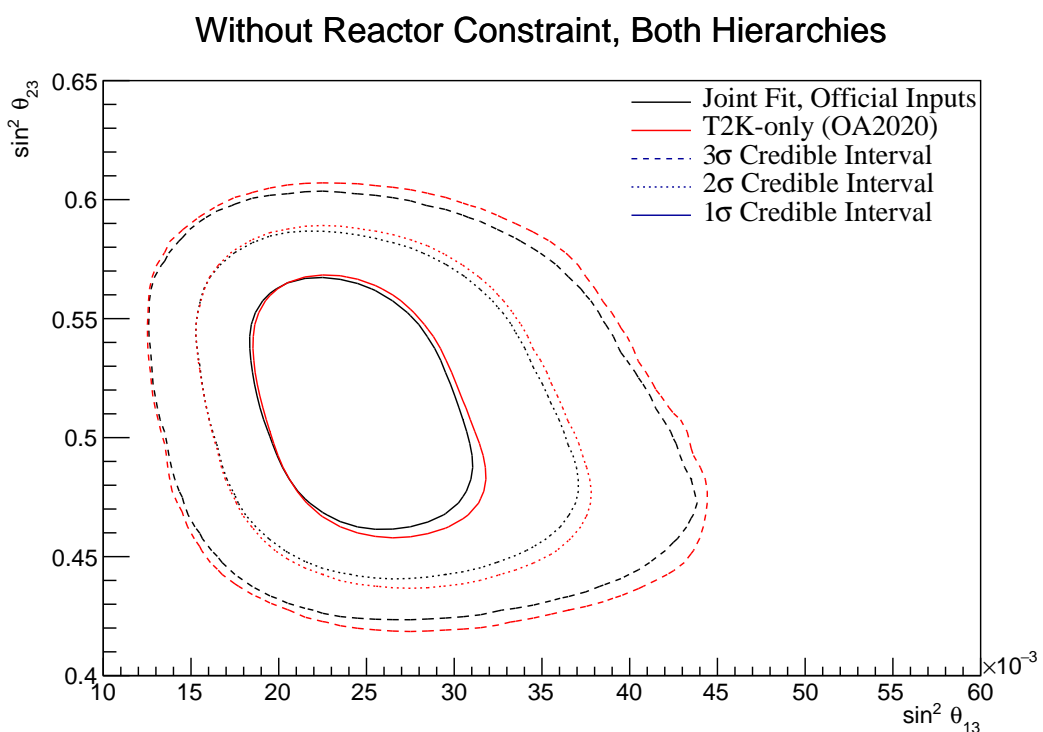


**Figure 8.39:** The two-dimensional posterior probability density distribution in  $\sin^2(\theta_{23})$  –  $\sin^2(\theta_{13})$  compared between the joint beam-atmospheric fit (Black) and the latest T2K sensitivities (Red) [186]. The reactor constraint is not applied in either fit. The distributions are marginalised over both hierarchies.

### 3387 8.2.7 Comparison to Latest T2K Sensitivities with Reactor Con- 3388 straint

3389 The comparison between the beam-only and joint beam-atmospheric fits are  
 3390 compared in subsection 8.2.6. Those comparisons were made with the reactor  
 3391 constraint not applied to either of the fits. This section illustrates the com-  
 3392 parison when the reactor constraint is applied. As shown in Figure 8.38, the  
 3393 application of the reactor constraint is expected to significantly increase the  
 3394 joint fit's preference for the NH hypothesis, as compared to the beam-only  
 3395 analysis. Figure 8.40 illustrates the sensitivities of the two fits to the disappearance  
 3396 parameters ( $\sin^2(\theta_{23}) - \Delta m_{32}^2$ ) marginalised over both hierarchies and with the  
 3397 reactor constraint applied. This plot clearly illustrates the benefit of the joint  
 3398 beam and atmospheric analysis. The  $1\sigma$  credible interval in the IH region is  
 3399 entirely removed in the joint analysis, illustrating the improved NH preference.

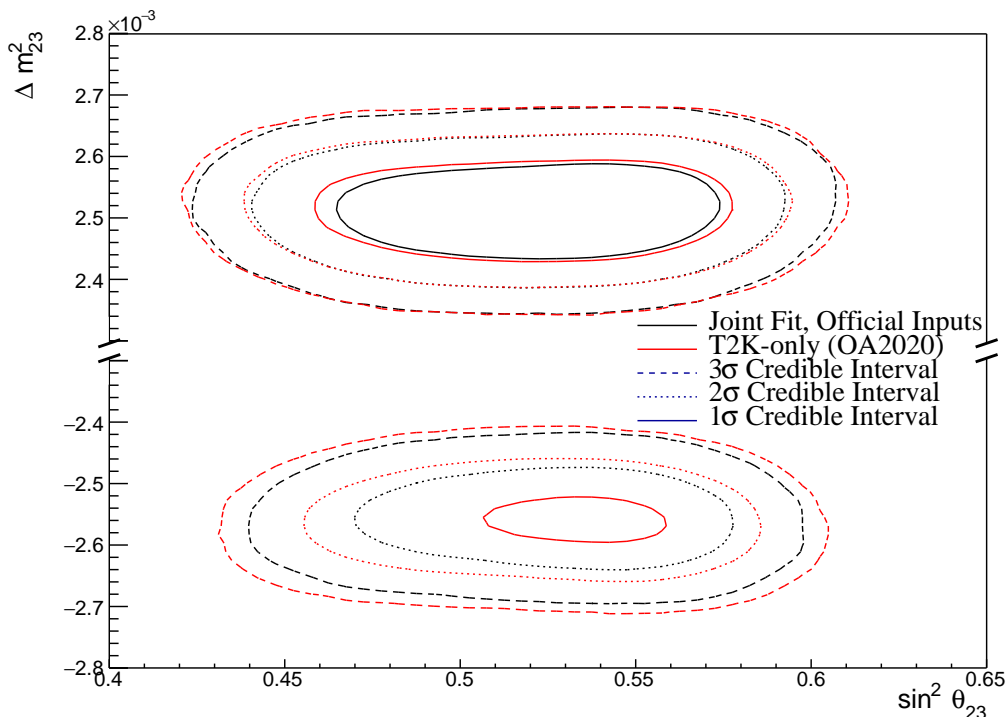


**Figure 8.40:** The two-dimensional posterior probability density distribution in  $\Delta m_{32}^2 - \sin^2(\theta_{23})$  compared between the joint beam-atmospheric fit (Black) and the latest T2K sensitivities (Red) [186]. The reactor constraint is applied in both fits. The distributions are marginalised over both hierarchies.

3400 The credible intervals of the joint fit are also tighter in the  $\sin^2(\theta_{23})$  dimension  
3401 than the beam-only analysis in both mass hierarchy regions. This shows that  
3402 beyond the ability of the joint fit to prefer the NH more strongly than the beam-  
3403 only analysis, the precision to which it can measure  $\sin^2(\theta_{23})$  is also improved.  
3404 The Bayes factor for NH preference is calculated as  $B(\text{NH}/\text{IH}) = 7.29$  and  
3405  $B(\text{NH}/\text{IH}) = 3.41$  for the joint beam-atmospheric and beam-only analysis,  
3406 respectively. Whilst both present a significant preference for the NH hypothesis  
3407 (Table 4.1), the joint fit's preference is much stronger. A similar conclusion can be  
3408 made regarding the Bayes factors for UO preference which are  $B(\text{UO}/\text{LO}) = 2.86$   
3409 and  $B(\text{UO}/\text{LO}) = 2.67$  for the joint beam-atmospheric and beam-only analysis,  
3410 respectively. Both of these represent a mild preference for the UO but there is  
3411 a stronger preference observed in the joint analysis.

3412 The sensitivity of the beam-only and joint beam-atmospheric analyses, to the  
3413 appearance parameters ( $\delta_{CP} - \sin^2(\theta_{13})$ ), are compared in Figure 8.41. These  
3414 results are marginalised over both hierarchies and include the reactor constraint  
3415 on  $\sin^2(\theta_{13})$ . For this particular set of known oscillation parameters (AsimovA  
3416 defined in Table 2.2), the beam-only analysis dominates the sensitivity. The  
3417 joint fit does slightly increase the sensitivity to  $\delta_{CP}$  but it does not change any  
3418 conclusions that would be made.

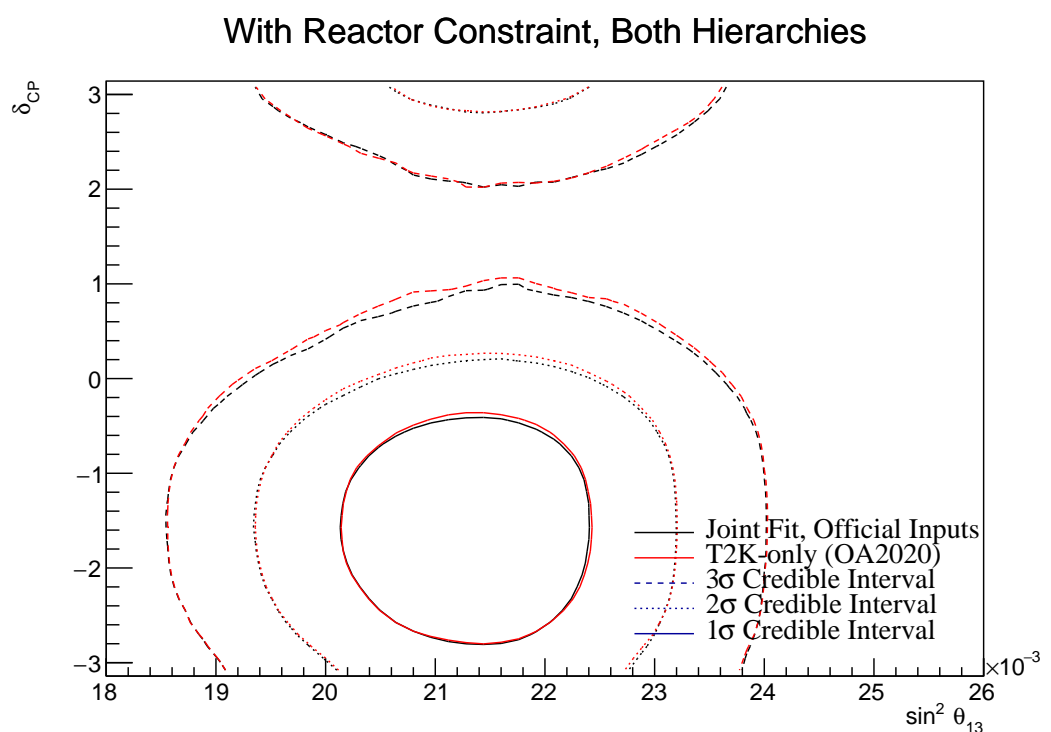


**Figure 8.41:** The two-dimensional posterior probability density distribution in  $\delta_{CP}$  –  $\sin^2(\theta_{13})$  compared between the joint beam-atmospheric fit (Black) and the latest T2K sensitivities (Red) [186]. The reactor constraint is applied in both fits. The distributions are marginalised over both hierarchies.

### 3419 8.2.8 Effect of Asimov Parameter Set

3420 Figure 8.4 and Figure 8.5 show that the choice of the parameter set at which the  
 3421 Asimov data is made can affect the conclusion. ‘AsimovA’ oscillation parameters  
 3422 are defined at a region of  $\delta_{CP}$  which is dominated by the T2K experiment. This  
 3423 explains why the addition of the atmospheric samples does not significantly in-  
 3424 crease the sensitivity to  $\delta_{CP}$ , as illustrated in subsection 8.2.6 and subsection 8.2.7.  
 3425 This section presents the sensitivities when ‘AsimovB’ oscillation parameters,  
 3426 as defined in Table 2.2, are assumed (alongside the post-BANFF tune) when  
 3427 building the Asimov data.

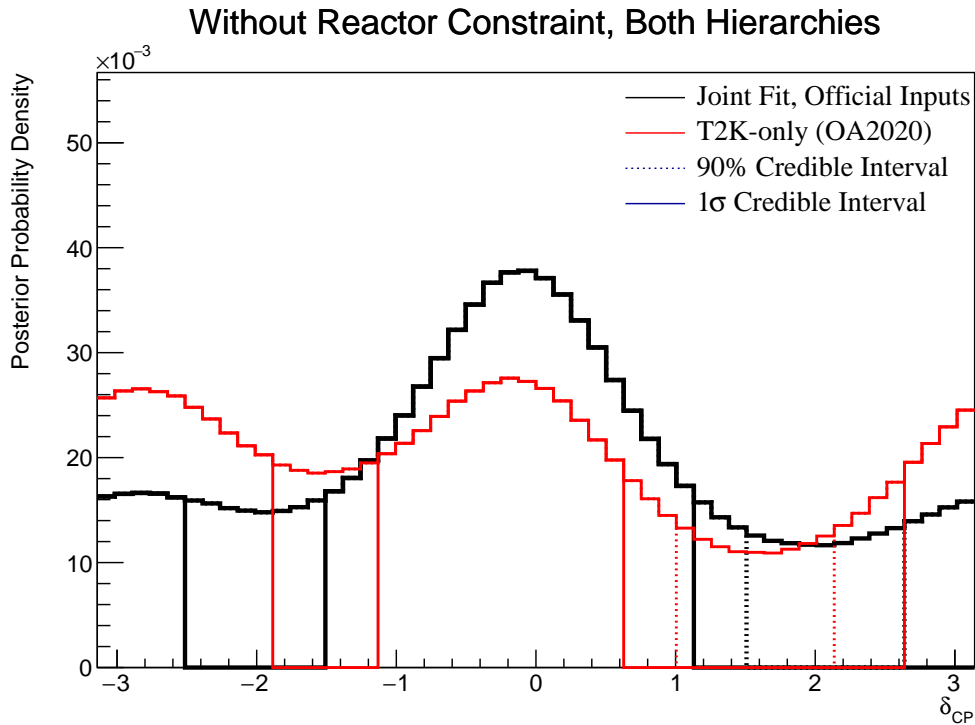


**Figure 8.42:** The one-dimensional posterior probability density distribution in  $\delta_{CP}$  compared between the joint beam-atmospheric fit (Black) and the latest T2K sensitivities (Red) [186]. The reactor constraint is not applied in either fit. The distributions are marginalised over both hierarchies.

3428 The sensitivity to  $\delta_{CP}$  for the joint beam and atmospheric fit is presented  
 3429 in Figure 8.42. The results are compared to those from the beam-only analysis  
 3430 in [186]. The reactor constraint is not applied in either of the fits. The known  
 3431 oscillation parameter value is  $\delta_{CP} = 0$ . The shape of the posterior distribution

from the joint analysis is more peaked at  $\delta_{CP} = 0$  as compared to the beam-only analysis which has approximately the same posterior probability density at  $\delta_{CP} = 0$  and  $\delta_{CP} = \pi$ . This shows the ability of the joint analysis to better determine the correct phase of  $\delta_{CP}$  if the true value was CP-conserving. The  $1\sigma$  credible intervals and the position of the highest posterior probability density are given in Table 8.9.

Parameter	Interval	HPD
$\delta_{CP}$ , (BH)	$[-\pi, -2.51], [-1.51, 1.31]$	-0.06
$\delta_{CP}$ , (NH)	$[-1.13, 1.63]$	0.06
$\delta_{CP}$ , (IH)	$[-3.02, -1.88], [-1.76, 0.13]$	-0.44
$\Delta m_{32}^2$ (BH) [ $\times 10^{-3}$ eV $^2$ ]	$[-2.60, -2.49], [2.46, 2.59]$	2.51
$\Delta m_{32}^2$ (NH) [ $\times 10^{-3}$ eV $^2$ ]	$[2.47, 2.56]$	2.52
$\Delta m_{32}^2$ (IH) [ $\times 10^{-3}$ eV $^2$ ]	$[-2.61, -2.52]$	-2.57
$\sin^2(\theta_{23})$ (BH)	$[0.43, 0.48], [0.55, 0.59]$	0.45
$\sin^2(\theta_{23})$ (NH)	$[0.43, 0.49], [0.55, 0.58]$	0.45
$\sin^2(\theta_{23})$ (IH)	$[0.44, 0.48], [0.54, 0.59]$	0.57

**Table 8.9:** The position of the highest posterior probability density (HPD) and width of the  $1\sigma$  credible interval for the SK atmospheric-only fit. The reactor constraint is not applied. The values are presented by which hierarchy hypothesis is assumed: marginalised over both hierarchies (BH), normal hierarchy only (NH) and inverted hierarchy only (IH).

Naively, if just the  $1\sigma$  credible interval were considered without observing the shape of the distribution, it would appear that the joint analysis would have a worse sensitivity to  $\delta_{CP}$  due to the larger interval around  $\delta_{CP}$ . The  $1\sigma$  credible interval for the beam-only analysis is given as the range  $\delta_{CP} = [-\pi, -1.88], [-1.13, 0.63]$  and  $[2.64, \pi]$  which contains 56% of all values of  $\delta_{CP}$ . The joint beam and atmospheric analysis contains 52% of all  $\delta_{CP}$  values within the  $1\sigma$  credible interval. Therefore, if the area within the  $1\sigma$  credible interval were to be compared between the two fits, the joint analysis would be shown to have better precision.

This contradiction stems from the methodology in which the credible interval is calculated. The technique used in this analysis (documented in subsection 4.3.2)

3448 fills the credible interval by selecting bins in order of magnitude until 68% of the  
3449 posterior density is contained. If instead, the credible interval was calculated  
3450 by expanding around the highest posterior probability, the benefits of the joint  
3451 fit would be more obvious. In the case where the shape of the posterior was  
3452 Gaussian, these two techniques would be equivalent.

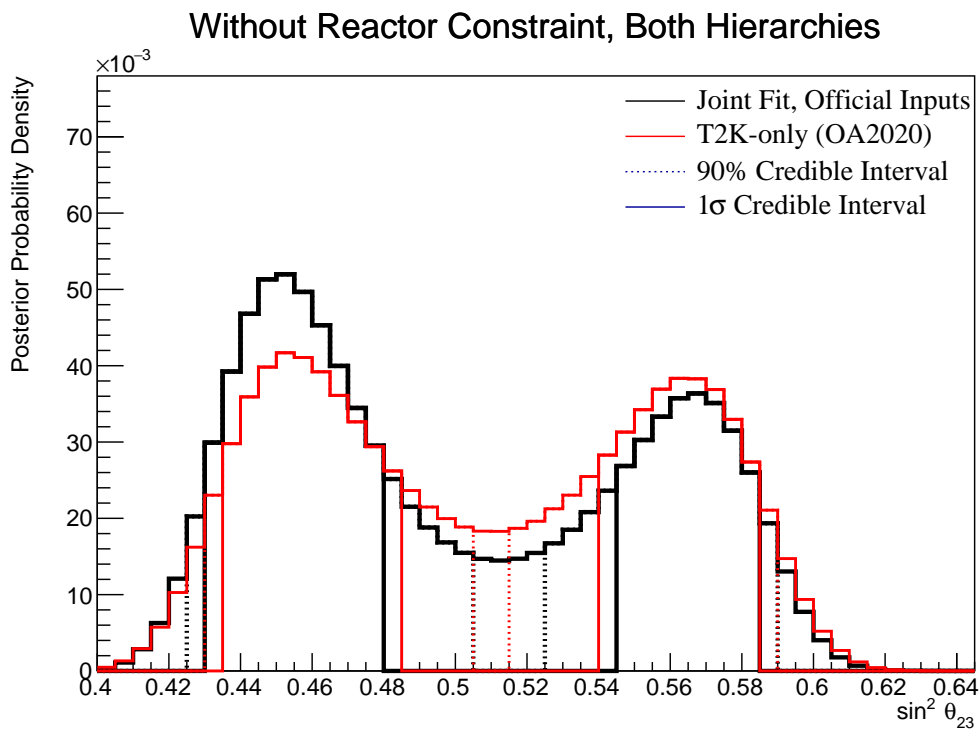


**Figure 8.43:** The one-dimensional posterior probability density distribution in  $\sin^2(\theta_{23})$  compared between the joint beam-atmospheric fit (Black) and the latest T2K sensitivities (Red) [186]. The reactor constraint is not applied in either fit. The distributions are marginalised over both hierarchies.

3453 The sensitivity of the joint beam and atmospheric fit to  $\sin^2(\theta_{23})$  is presented  
3454 in Figure 8.43. The sensitivity is compared to that of the beam-only analysis  
3455 in [186]. The reactor constraint is not applied in either of the fits being com-  
3456 pared. The Asimov parameter value is  $\sin^2(\theta_{23}) = 0.45$  and the sensitivities are  
3457 marginalised over both hierarchies. Clearly, the joint beam and atmospheric  
3458 fit has a much larger probability density in the region surrounding the known  
3459 oscillation parameters. This shows the better octant determination of the joint  
3460 analysis compared to the beam-only fit. The ratio of the posterior density at

the peak of the lower octant to the peak of the upper octant from the joint fit is 1.43 compared to 1.09 from the beam-only analysis. This shows further support for the joint analysis in correctly selecting the lower octant, which is the correct hypothesis given the known oscillation parameters.

	LO ( $\sin^2 \theta_{23} < 0.5$ )	UO ( $\sin^2 \theta_{23} > 0.5$ )	Sum
NH ( $\Delta m_{32}^2 > 0$ )	0.35	0.24	0.59
IH ( $\Delta m_{32}^2 < 0$ )	0.19	0.22	0.41
Sum	0.54	0.46	1.00

**Table 8.10:** The distribution of steps in a joint beam and atmospheric fit, presented as the fraction of steps in the upper (UO) and lower (LO) octants and the normal (NH) and inverted (IH) hierarchies. The reactor constraint is not applied. The Bayes factors are calculated as  $B(\text{NH}/\text{IH}) = 1.43$  and  $B(\text{LO}/\text{UO}) = 1.19$ .

The distribution of steps, split by hierarchy and octant hypothesis, is presented in Table 8.10. The Bayes factor for hierarchy and octant determination are  $B(\text{NH}/\text{IH}) = 1.43$  and  $B(\text{LO}/\text{UO}) = 1.19$ , respectively. The octant Bayes factor is now presented as LO/UO as the known oscillation parameter is contained within the lower octant. These values compare to  $B(\text{NH}/\text{IH}) = 1.08$  and  $B(\text{LO}/\text{UO}) = 0.91$  from the beam-only analysis. This shows additional evidence of the joint analysis's preference for selecting the correct octant and hierarchy hypothesis. Comparisons to the AsimovA Bayes factors presented in Table 8.6 show how the preference for the correct octant and hierarchy depend on the true value of  $\delta_{CP}$  and  $\sin^2(\theta_{23})$ .

The sensitivity of the beam-only and joint beam-atmospheric analysis to  $\Delta m_{32}^2$  is given in Figure 8.44. Both of the results are marginalised over both hierarchies and the reactor constraint is not applied in either analysis. The joint analysis has a stronger preference for the correct hierarchy (NH) which is shown by the higher Bayes factor ( $B(\text{NH}/\text{IH}) = 1.43$ ) compared to the beam-only analysis ( $B(\text{NH}/\text{IH}) = 1.08$ ).

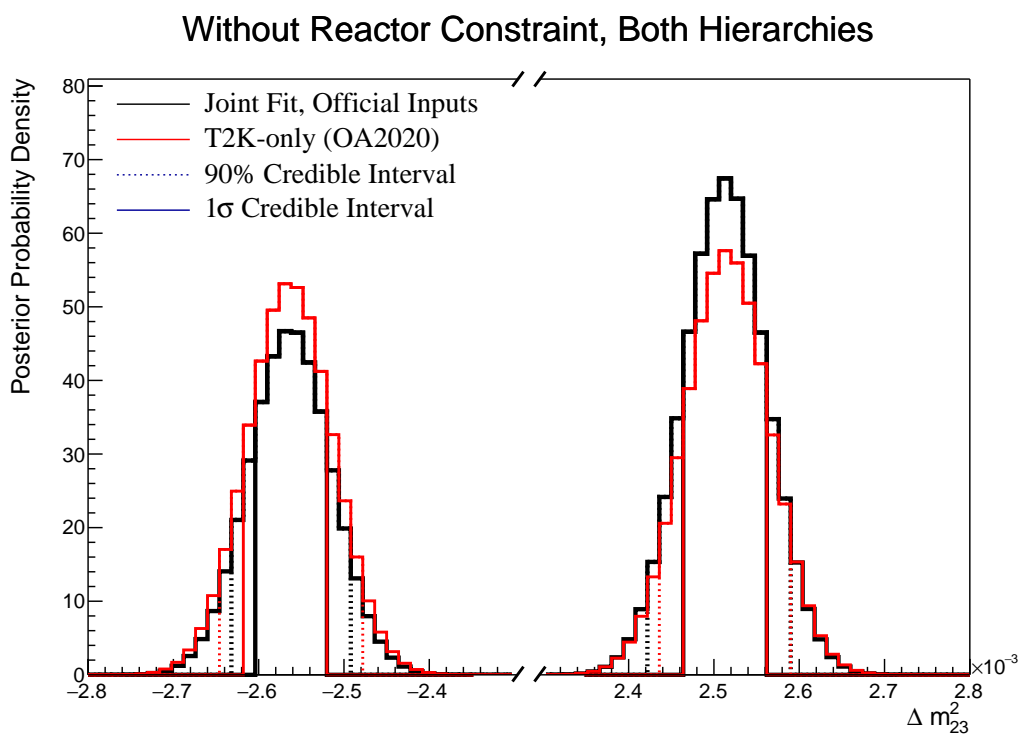


**Figure 8.44:** The one-dimensional posterior probability density distribution in  $\Delta m_{32}^2$  compared between the joint beam-atmospheric fit (Black) and the latest T2K sensitivities (Red) [186]. The reactor constraint is not applied in either fit. The distributions are marginalised over both hierarchies.

# 9

3481

3482

## Conclusions and Outlook

# Appendices

# A

3484

3485

## Atmospheric Sample Spectra

3486 This appendix documents the interaction mode breakdown of all the atmospheric  
3487 samples used within the analysis. The generated tune of the model parameters  
3488 and the Asimov A oscillation parameter set (defined in Table 2.2) are assumed.  
3489 The livetime of SK-IV is taken to be 3244.4 days.

### 3490 A.1 Binning

3491 The lepton momentum and cosine zenith binning edges for the atmospheric  
3492 samples used within this analysis are defined in Table A.1.

### 3493 A.2 Fully Contained Sub-GeV Samples

3494 The interaction mode breakdown of the fully contained Sub-GeV samples are  
3495 shown in Figure A.1 and Figure A.2, for the samples with enriched CC0 $\pi$  and  
3496 CC1 $\pi^\pm$  respectively.

3497 The CC0 $\pi$  sample are dominated by CCQE events ( $\sim 70\%$ ) with smaller  
3498 contributions of 2p2h ( $\sim 12\%$ ) and CC1 $\pi$  ( $\sim 10\%$ ) components. The energy peaks  
3499 around 300 MeV, which is slightly below that of the T2K samples but still has  
3500 significant contribution upto 1 GeV which overlaps the T2K sample energy range.

Sample	$\cos(\theta_Z)$ Bins	Momentum Bin Edges ( $\log_{10}(P)$ MeV)
SubGeV-elike-0dcy	10	2.0, 2.4, 2.6, 2.8, 3.0, 3.2
SubGeV-elike-1dcy	1	2.0, 2.4, 2.6, 2.8, 3.0, 3.2
SubGeV-mulike-0dcy	10	2.0, 2.4, 2.6, 2.8, 3.0, 3.2
SubGeV-mulike-1dcy	10	2.0, 2.4, 2.6, 2.8, 3.0, 3.2
SubGeV-mulike-2dcy	1	2.0, 2.4, 2.6, 2.8, 3.0, 3.2
SubGeV-pi0like	1	2.0, 2.2, 2.4, 2.6, 2.8, 3.2
MultiGeV-elike-nue	10	3.0, 3.4, 3.7, 4.0, 5.0
MultiGeV-elike-nuebar	10	3.0, 3.4, 3.7, 4.0, 5.0
MultiGeV-mulike	10	3.0, 3.4, 5.0
MultiRing-elike-nue	10	3.0, 3.4, 3.7, 5.0
MultiRing-elike-nuebar	10	3.0, 3.4, 3.7, 5.0
MultiRing-mulike	10	2.0, 3.124, 3.4, 3.7, 5.0
MultiRing-Other1	10	3.0, 3.4, 3.7, 4.0, 5.0
PC-Stop	10	2.0, 3.4, 5.0
PC-Through	10	2.0, 3.124, 3.4, 3.7, 5.0
Upmu-Stop	10	3.2, 3.4, 3.7, 8.0
Upmu-Through-Showering	10	2.0, 8.0
Upmu-Through-NonShowering	10	2.0, 8.0

**Table A.1:** The reconstructed cosine zenith and lepton momentum binning assigned to the atmospheric samples. The “ $\cos(\theta_Z)$  Bins” column illustrates the number of bins uniformly distributed over the  $-1.0 \leq \cos(\theta_Z) \leq 1.0$  region for fully and partially contained samples and  $-1.0 \leq \cos(\theta_Z) \leq 0.0$  region for up- $\mu$  samples.

3501      The one-ring CC1 $\pi$  samples, where the pion is tagged via its decay electron,  
 3502      are dominated by CC1 $\pi$  events ( $\sim 75\%$ ) with a small contribution of CCM $\pi$   
 3503      ( $\sim 10\%$ ). The two-ring pion sample is mostly dominated by the NC1 $\pi^0$  via  
 3504      resonances, and has several equally-sized contributions from CCQE, NC1 $\pi^\pm$  via  
 3505      resonances, and NC coherent pion production, where the  $\pi^0$  likely comes from  
 3506      nucleon and  $\pi^\pm$  final state interactions in the nucleus.

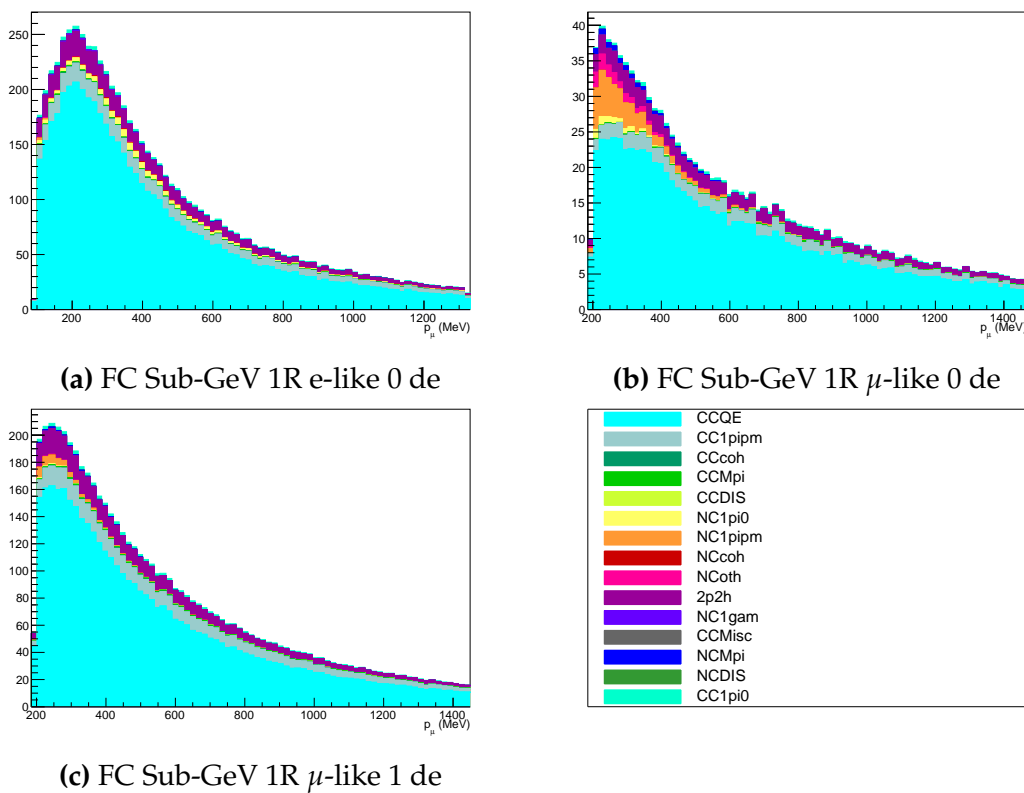


**Figure A.1:** Breakdown by interaction mode of the FC Sub-GeV atmospheric samples targeting CC $0\pi$  events.

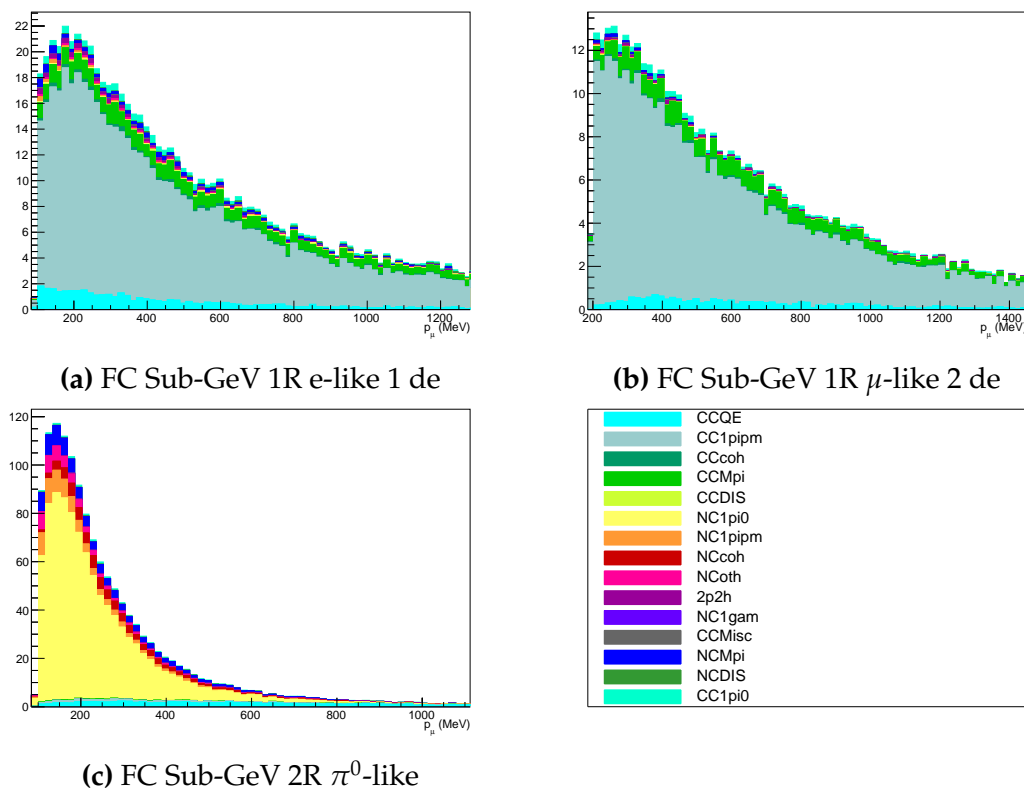


**Figure A.2:** Breakdown by interaction mode of the FC Sub-GeV atmospheric samples targeting single pion events.

### 3507 A.3 Fully Contained Multi-GeV Samples

3508 The interaction mode breakdown of fully contained multi-GeV samples is high-  
 3509 lighted in Figure A.3. Due to the event selection applied in SK which targets  $\pi^+$   
 3510 and  $\pi^-$  separation, the  $\nu_e$  sample mainly consists of events with pions (single pion  
 3511 production or multi-pion/DIS interactions). The pion separation is explained in  
 3512 Section section 6.1. This reasoning also explains the significant CCQE contribution  
 3513 of the  $\bar{\nu}_e$  sample. The muon-like sample is dominated by CCQE interactions with  
 3514  $\sim 10 - 15\%$  2p2h and CC1 $\pi$  contribution of events.

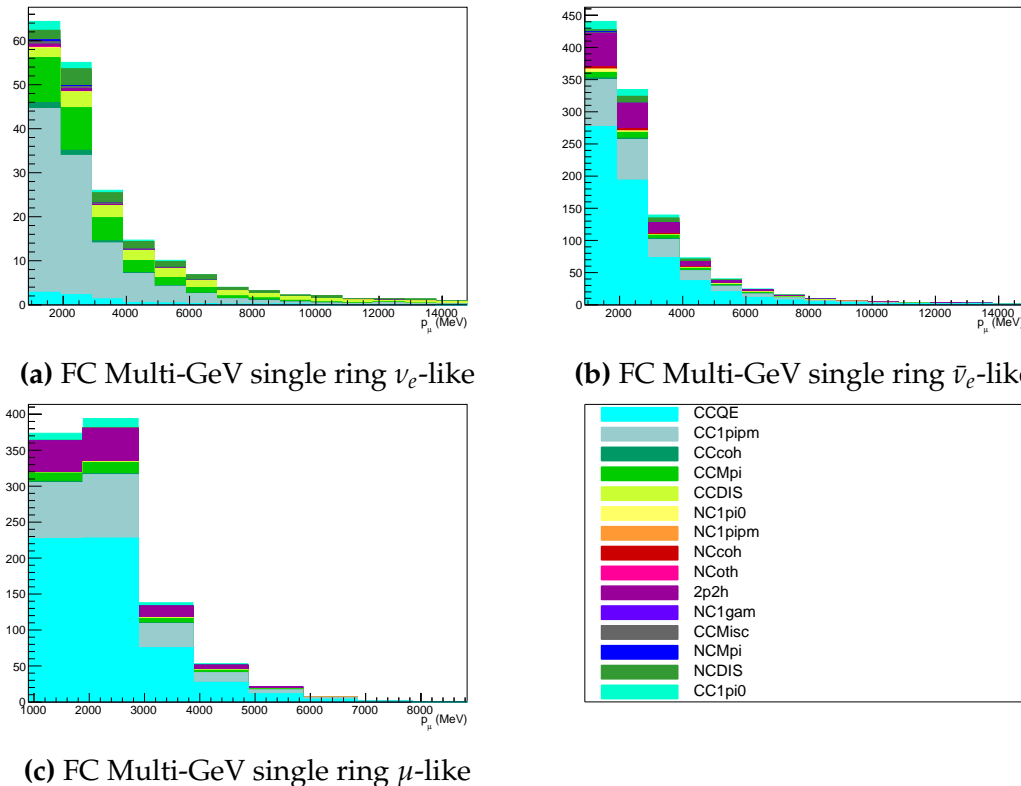


**Figure A.3:** Breakdown by interaction mode of the FC Multi-GeV single ring atmospheric samples.

## 3515 A.4 Fully Contained Multi-Ring Samples

3516 The interaction mode breakdown of fully contained multi-ring events is shown  
 3517 in Figure A.4. These samples see more interaction modes contributing in general,  
 3518 and there is a much larger contribution from multi-pion and DIS interaction  
 3519 modes, compared to the other samples.

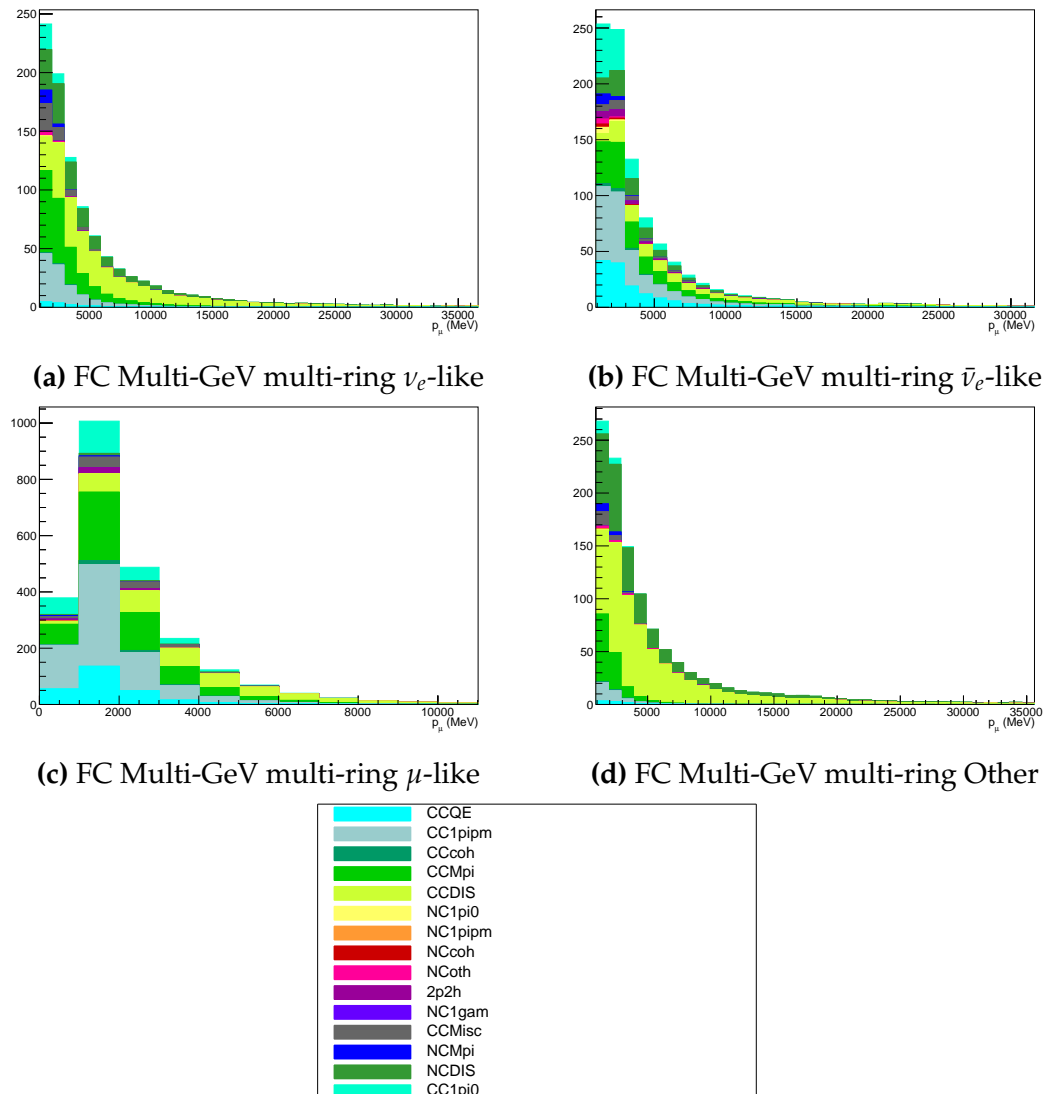


**Figure A.4:** Breakdown by interaction mode of the FC Multi-GeV multi-ring atmospheric samples.

## 3520 A.5 Partially Contained Samples

3521 The breakdown for partially contained samples is highlighted in Figure A.5.  
 3522 As with the multi-ring samples, there is no dominating interaction mode. The  
 3523 neutrino energies of events in this sample extend into the tens of GeV and become  
 3524 dominated by DIS interaction modes in the high energy limit.

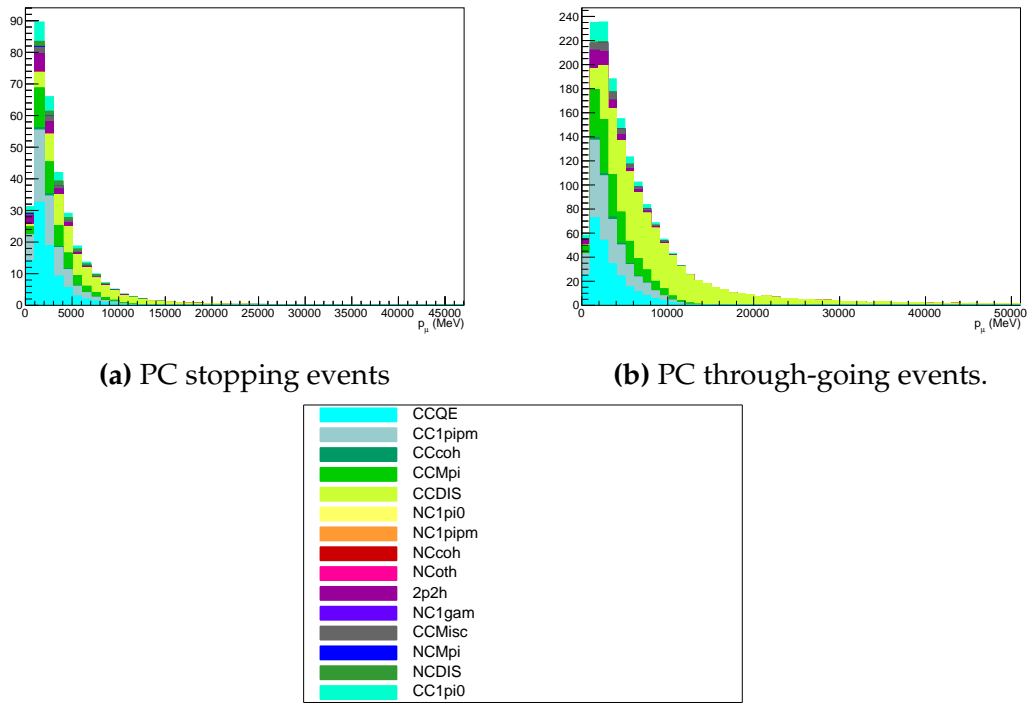


**Figure A.5:** Breakdown by interaction mode of the PC atmospheric samples.

## 3525 A.6 Upward-Going Muon Samples

3526 The breakdown for upward-going muons is illustrated in Figure A.6. These  
 3527 samples are significantly dominated by DIS interactions with energies extending  
 3528 up into the hundreds of GeV.

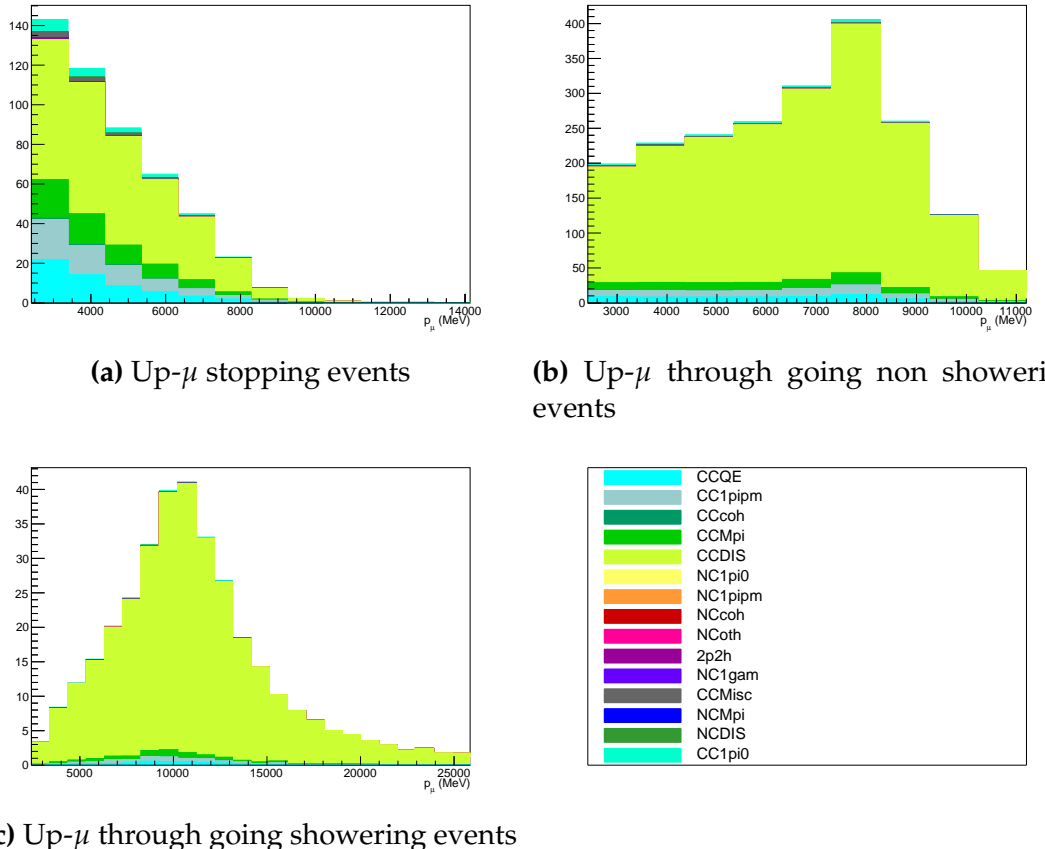


**Figure A.6:** Breakdown by interaction mode of the atmospheric upward going muon samples.

# Bibliography

- [1] J Chadwick. "Intensitätsverteilung im magnetischen Spectrum der  $\beta$ -Strahlen von radium B + C". In: *Verhandl. Dtsc. Phys. Ges.* 16 (1914), p. 383. URL: <http://cds.cern.ch/record/262756>.
- [2] C D Ellis and W A Wooster. "The average energy of disintegration of radium E". en. In: *Proc. R. Soc. Lond. A Math. Phys. Sci.* 117.776 (Dec. 1927), pp. 109–123.
- [3] W. Pauli. "Dear radioactive ladies and gentlemen". In: *Phys. Today* 31N9 (1978), p. 27.
- [4] E. Fermi. "An attempt of a theory of beta radiation. 1." In: *Z. Phys.* 88 (1934), pp. 161–177.
- [5] F. Reines and C. L. Cowan. "Detection of the Free Neutrino". In: *Phys. Rev.* 92 (3 1953), pp. 830–831. URL: <https://link.aps.org/doi/10.1103/PhysRev.92.830>.
- [6] C. L. Cowan et al. "Detection of the Free Neutrino: a Confirmation". In: *Science* 124.3212 (1956), pp. 103–104. eprint: <http://science.sciencemag.org/content/124/3212/103.full.pdf>. URL: <http://science.sciencemag.org/content/124/3212/103>.
- [7] G. Danby et al. "Observation of High-Energy Neutrino Reactions and the Existence of Two Kinds of Neutrinos". In: *Phys. Rev. Lett.* 9 (1 1962), pp. 36–44. URL: <https://link.aps.org/doi/10.1103/PhysRevLett.9.36>.
- [8] K. Kodama et al. "Observation of tau neutrino interactions". In: *Physics Letters B* 504.3 (2001), pp. 218 –224. URL: <http://www.sciencedirect.com/science/article/pii/S0370269301003070>.
- [9] A. Aguilar-Arevalo et al. "Evidence for neutrino oscillations from the observation of anti-neutrino(electron) appearance in a anti-neutrino(muon) beam". In: *Phys. Rev.* D64 (2001), p. 112007. arXiv: [hep-ex/0104049](https://arxiv.org/abs/hep-ex/0104049) [hep-ex].
- [10] A. A. Aguilar-Arevalo et al. "Improved Search for  $\bar{\nu}_\mu \rightarrow \bar{\nu}_e$  Oscillations in the MiniBooNE Experiment". In: *Phys. Rev. Lett.* 110 (16 2013), p. 161801. URL: <https://link.aps.org/doi/10.1103/PhysRevLett.110.161801>.
- [11] Planck Collaboration et al. "Planck 2018 results. VI. Cosmological parameters". In: *aap* 641 (Sept. 2020).
- [12] J. A. Bagger et al. "Precision electroweak measurements on the Z resonance". In: *Physics Reports* 427.5 (2006), pp. 257 –454. URL: <http://www.sciencedirect.com/science/article/pii/S0370157305005119>.
- [13] B. Pontecorvo. "Neutrino Experiments and the Problem of Conservation of Leptonic Charge". In: *Sov. Phys. JETP* 26 (1968). [Zh. Eksp. Teor. Fiz. 53, 1717(1967)], pp. 984–988.

- 3566 [14] B. Pontecorvo. "Inverse beta processes and nonconservation of lepton charge". In:  
3567 *Sov. Phys. JETP* 7 (1958). [Zh. Eksp. Teor. Fiz.34,247(1957)], pp. 172–173.
- 3568 [15] Makoto Kobayashi and Toshihide Maskawa. "CP-Violation in the  
3569 Renormalizable Theory of Weak Interaction". In: *Progress of Theoretical Physics*  
3570 49.2 (1973), pp. 652–657. URL: <http://dx.doi.org/10.1143/PTP.49.652>.
- 3571 [16] Nicola Cabibbo. "Unitary Symmetry and Leptonic Decays". In: *Phys. Rev. Lett.* 10  
3572 (12 1963), pp. 531–533. URL:  
3573 <https://link.aps.org/doi/10.1103/PhysRevLett.10.531>.
- 3574 [17] A Maio and. "Search for Majorana neutrinos with the SNO+ detector at  
3575 SNOLAB". In: *Journal of Physics: Conference Series* 587 (2015), p. 012030. URL:  
3576 <https://doi.org/10.1088/1742-6596/587/1/012030>.
- 3577 [18] A Yu Smirnov. "The MSW effect and solar neutrinos". In: (2003).
- 3578 [19] S.P. Mikheyev and A.Y. Smirnov. "Resonance enhancement of oscillations in  
3579 matter and solar neutrino spectroscopy". In: *Soviet Journal of Nuclear Physics* 42 (6  
3580 1985), pp. 913–917.
- 3581 [20] L. Wolfenstein. "Neutrino oscillations in matter". In: *Phys. Rev. D* 17 (9 1978),  
3582 pp. 2369–2374. URL: <https://link.aps.org/doi/10.1103/PhysRevD.17.2369>.
- 3583 [21] Vernon D. Barger et al. "Matter Effects on Three-Neutrino Oscillations". In: *Phys.*  
3584 *Rev. D* 22 (1980), p. 2718.
- 3585 [22] Y. Ashie et al. "Evidence for an Oscillatory Signature in Atmospheric Neutrino  
3586 Oscillations". In: *Phys. Rev. Lett.* 93 (10 2004), p. 101801. URL:  
3587 <https://link.aps.org/doi/10.1103/PhysRevLett.93.101801>.
- 3588 [23] Q. R. Ahmad et al. "Direct Evidence for Neutrino Flavor Transformation from  
3589 Neutral-Current Interactions in the Sudbury Neutrino Observatory". In: *Phys.*  
3590 *Rev. Lett.* 89 (1 2002), p. 011301. URL:  
3591 <https://link.aps.org/doi/10.1103/PhysRevLett.89.011301>.
- 3592 [24] 2015 Nobel prize in Physics as listed by Nobelprize.org.  
3593 [https://www.nobelprize.org/nobel\\_prizes/physics/laureates/2015/](https://www.nobelprize.org/nobel_prizes/physics/laureates/2015/).  
3594 Accessed: 22-06-2022.
- 3595 [25] J. A. Formaggio and G. P. Zeller. "From eV to EeV: Neutrino Cross Sections  
3596 Across Energy Scales". In: *Rev. Mod. Phys.* 84 (2012), pp. 1307–1341. arXiv:  
3597 1305.7513 [hep-ex].
- 3598 [26] A Oralbaev, M Skorokhvatov, and O Titov. "The inverse beta decay: a study of  
3599 cross section". In: *Journal of Physics: Conference Series* 675.1 (2016), p. 012003. URL:  
3600 <https://doi.org/10.1088/1742-6596/675/1/012003>.
- 3601 [27] A Bellerive. "Review of solar neutrino experiments". en. In: *Int. J. Mod. Phys. A*  
3602 19.08 (Mar. 2004), pp. 1167–1179.
- 3603 [28] Raymond Davis, Don S. Harmer, and Kenneth C. Hoffman. "Search for  
3604 Neutrinos from the Sun". In: *Phys. Rev. Lett.* 20 (21 1968), pp. 1205–1209. URL:  
3605 <https://link.aps.org/doi/10.1103/PhysRevLett.20.1205>.
- 3606 [29] Núria Vinyoles et al. "A new generation of standard solar models". In: *Astrophys.*  
3607 *J.* 835.2 (Jan. 2017), p. 202.

- 3608 [30] V Gribov and B Pontecorvo. "Neutrino astronomy and lepton charge". en. In: *Phys. Lett. B* 28.7 (Jan. 1969), pp. 493–496.
- 3609 [31] K. S. Hirata et al. "Observation of  ${}^8\text{B}$  solar neutrinos in the Kamiokande-II detector". In: *Phys. Rev. Lett.* 63 (1 1989), pp. 16–19. URL: <https://link.aps.org/doi/10.1103/PhysRevLett.63.16>.
- 3610 [32] W Hampel et al. "GALLEX solar neutrino observations: results for GALLEX IV". en. In: *Phys. Lett. B* 447.1-2 (Feb. 1999), pp. 127–133.
- 3611 [33] J. N. Abdurashitov et al. "Measurement of the solar neutrino capture rate with gallium metal". In: *Phys. Rev. C* 60 (5 1999), p. 055801. URL: <https://link.aps.org/doi/10.1103/PhysRevC.60.055801>.
- 3612 [34] Q R Ahmad et al. "Direct evidence for neutrino flavor transformation from neutral-current interactions in the Sudbury neutrino observatory". en. In: *Phys. Rev. Lett.* 89.1 (June 2002).
- 3613 [35] Borexino Collaboration. "Comprehensive measurement of pp-chain solar neutrinos". en. In: *Nature* 562.7728 (Oct. 2018), pp. 505–510.
- 3614 [36] B Aharmim et al. "A search for neutrinos from the SolarhepReaction and the diffuse supernova neutrino background with the Sudbury neutrino observatory". en. In: *Astrophys. J.* 653.2 (Dec. 2006), pp. 1545–1551.
- 3615 [37] M Agostini et al. "Experimental evidence of neutrinos produced in the CNO fusion cycle in the Sun". In: (2020).
- 3616 [38] G Danby et al. "Observation of high-energy neutrino reactions and the existence of two kinds of neutrinos". In: *Phys. Rev. Lett.* 9.1 (July 1962), pp. 36–44.
- 3617 [39] K. Abe et al. "T2K neutrino flux prediction". In: *Physical Review D* 87.1 (2013). URL: <https://doi.org/10.1103%2Fphysrevd.87.012001>.
- 3618 [40] D. G. Michael et al. "Observation of Muon Neutrino Disappearance with the MINOS Detectors in the NuMI Neutrino Beam". In: *Phys. Rev. Lett.* 97 (19 2006), p. 191801. URL: <https://link.aps.org/doi/10.1103/PhysRevLett.97.191801>.
- 3619 [41] G. Danby et al. "Observation of High-Energy Neutrino Reactions and the Existence of Two Kinds of Neutrinos". In: *Phys. Rev. Lett.* 9 (1 1962), pp. 36–44. URL: <https://link.aps.org/doi/10.1103/PhysRevLett.9.36>.
- 3620 [42] M. A. Acero et al. "First measurement of neutrino oscillation parameters using neutrinos and antineutrinos by NOvA". In: *Phys. Rev. Lett.* 123 (15 2019), p. 151803. URL: <https://link.aps.org/doi/10.1103/PhysRevLett.123.151803>.
- 3621 [43] K. Abe et al. "The T2K experiment". In: *Nuclear Instruments and Methods in Physics Research Section A: Accelerators, Spectrometers, Detectors and Associated Equipment* 659.1 (2011), pp. 106 –135. eprint: <http://www.sciencedirect.com/science/article/pii/S0168900211011910>.
- 3622 [44] B Abi et al. "Long-baseline neutrino oscillation physics potential of the DUNE experiment". en. In: *Eur. Phys. J. C Part. Fields* 80.10 (Oct. 2020).
- 3623 [45] Hyper-Kamiokande Proto-Collaboration et al. "Physics potential of a long-baseline neutrino oscillation experiment using a J-PARC neutrino beam and Hyper-Kamiokande". In: *Prog. Theor. Exp. Phys.* 2015.5 (May 2015), pp. 53C02–0.

- 3652 [46] Carlos Blanco, Dan Hooper, and Pedro Machado. "Constraining sterile neutrino  
3653 interpretations of the LSND and MiniBooNE anomalies with coherent neutrino  
3654 scattering experiments". In: *Physical Review D* 101.7 (2020). URL:  
3655 <https://doi.org/10.1103%2Fphysrevd.101.075051>.
- 3656 [47] MicroBooNE Collaboration et al. *Search for an Excess of Electron Neutrino*  
3657 *Interactions in MicroBooNE Using Multiple Final State Topologies*. 2021. URL:  
3658 <https://arxiv.org/abs/2110.14054>.
- 3659 [48] B. Armbruster et al. "Upper limits for neutrino oscillations  $\bar{\nu}_\mu \rightarrow \bar{\nu}_e$  from muon  
3660 decay at rest". In: *Phys. Rev. D* 65 (11 2002), p. 112001. URL:  
3661 <https://link.aps.org/doi/10.1103/PhysRevD.65.112001>.
- 3662 [49] T K Gaisser and M Honda. "Flux of Atmospheric Neutrinos". In: (2002).
- 3663 [50] G. D. Barr et al. "Three-dimensional calculation of atmospheric neutrinos". In:  
3664 *Physical Review D* 70.2 (2004). URL:  
3665 <https://doi.org/10.1103/physrevd.70.023006>.
- 3666 [51] M. Honda et al. "Calculation of atmospheric neutrino flux using the interaction  
3667 model calibrated with atmospheric muon data". In: *Physical Review D* 75.4 (2007).  
3668 URL: <https://doi.org/10.1103/physrevd.75.043006>.
- 3669 [52] M. Honda et al. "New calculation of the atmospheric neutrino flux in a  
3670 three-dimensional scheme". In: *Phys. Rev. D* 70 (4 2004), p. 043008. URL:  
3671 <https://link.aps.org/doi/10.1103/PhysRevD.70.043008>.
- 3672 [53] M. Honda et al. "Improvement of low energy atmospheric neutrino flux  
3673 calculation using the JAM nuclear interaction model". In: *Phys. Rev. D* 83 (12  
3674 2011), p. 123001. URL:  
3675 <https://link.aps.org/doi/10.1103/PhysRevD.83.123001>.
- 3676 [54] A. Fasso et al. "FLUKA: status and prospects for hadronic applications". In:  
3677 (2001).
- 3678 [55] Y. Ashie et al. "Measurement of atmospheric neutrino oscillation parameters by  
3679 Super-Kamiokande I". In: *Physical Review D* 71.11 (2005). URL:  
3680 <https://doi.org/10.1103/physrevd.71.112005>.
- 3681 [56] F Reines et al. "Evidence for high-energy cosmic-ray neutrino interactions". In:  
3682 *Phys. Rev. Lett.* 15.9 (Aug. 1965), pp. 429–433.
- 3683 [57] D. Casper et al. "Measurement of atmospheric neutrino composition with the  
3684 IMB-3 detector". In: *Phys. Rev. Lett.* 66 (20 1991), pp. 2561–2564. URL:  
3685 <https://link.aps.org/doi/10.1103/PhysRevLett.66.2561>.
- 3686 [58] K S Hirata et al. "Observation of a small atmospheric  $\nu_\mu/\nu_e$  ratio in Kamiokande".  
3687 en. In: *Phys. Lett. B* 280.1-2 (Apr. 1992), pp. 146–152.
- 3688 [59] Z. Li et al. "Measurement of the tau neutrino cross section in atmospheric  
3689 neutrino oscillations with Super-Kamiokande". In: *Physical Review D* 98.5 (2018).  
3690 URL: <https://doi.org/10.1103/physrevd.98.052006>.
- 3691 [60] Kamiokande Collaboration et al. "Atmospheric neutrino oscillation analysis with  
3692 external constraints in Super-Kamiokande I-IV". In: (2017).
- 3693 [61] T2K Collaboration. "Constraint on the matter-antimatter symmetry-violating  
3694 phase in neutrino oscillations". en. In: *Nature* 580.7803 (Apr. 2020), pp. 339–344.

- 3695 [62] M A Acero et al. "First measurement of neutrino oscillation parameters using  
3696 neutrinos and antineutrinos by NOvA". en. In: *Phys. Rev. Lett.* 123.15 (Oct. 2019),  
3697 p. 151803.
- 3698 [63] M G Aartsen et al. "Measurement of atmospheric neutrino oscillations at 6–56  
3699 GeV with IceCube DeepCore". In: *Phys. Rev. Lett.* 120.7 (Feb. 2018).
- 3700 [64] P Adamson et al. "Combined analysis of  $\nu\mu$  Disappearance  
3701 and  $\nu\mu \rightarrow \nu e$  Appearance in MINOS using accelerator and atmospheric neutrinos".  
3702 In: *Phys. Rev. Lett.* 112.19 (May 2014).
- 3703 [65] M. Sajjad Athar et al. "Status and perspectives of neutrino physics". In: *Progress*  
3704 *in Particle and Nuclear Physics* 124 (2022), p. 103947. URL:  
3705 <https://doi.org/10.1016/Fj.pnpp.2022.103947>.
- 3706 [66] Soo-Bong Kim, Thierry Lasserre, and Yifang Wang. "Reactor Neutrinos". In: *Adv.*  
3707 *High Energy Phys.* 2013 (2013), pp. 1–34.
- 3708 [67] Mohammad Sajjad Athar et al. "Status and perspectives of neutrino physics". In: *Prog. Part. Nucl. Phys.* 124 (2022), p. 103947. arXiv: 2111.07586 [hep-ph].
- 3710 [68] K Abe et al. "First gadolinium loading to Super-Kamiokande". en. In: *Nucl.*  
3711 *Instrum. Methods Phys. Res. A* 1027.166248 (Mar. 2022), p. 166248.
- 3712 [69] F. P. An et al. "Observation of Electron-Antineutrino Disappearance at Daya Bay".  
3713 In: *Phys. Rev. Lett.* 108 (17 2012), p. 171803. URL:  
3714 <https://link.aps.org/doi/10.1103/PhysRevLett.108.171803>.
- 3715 [70] J. K. Ahn et al. "Observation of Reactor Electron Antineutrinos Disappearance in  
3716 the RENO Experiment". In: *Phys. Rev. Lett.* 108 (19 2012), p. 191802. URL:  
3717 <https://link.aps.org/doi/10.1103/PhysRevLett.108.191802>.
- 3718 [71] Y. Abe et al. "Indication of Reactor  $\bar{\nu}_e$  Disappearance in the Double Chooz  
3719 Experiment". In: *Phys. Rev. Lett.* 108 (13 2012), p. 131801. URL:  
3720 <https://link.aps.org/doi/10.1103/PhysRevLett.108.131801>.
- 3721 [72] JUNO Collaboration et al. *TAO Conceptual Design Report: A Precision Measurement*  
3722 *of the Reactor Antineutrino Spectrum with Sub-percent Energy Resolution*. 2020. arXiv:  
3723 2005.08745 [physics.ins-det].
- 3724 [73] M P Decowski. "KamLAND's precision neutrino oscillation measurements". en.  
3725 In: *Nucl. Phys. B*. 908 (July 2016), pp. 52–61.
- 3726 [74] A. Gando et al. "Constraints on  $\theta_{13}$  from a three-flavor oscillation analysis of  
3727 reactor antineutrinos at KamLAND". In: *Phys. Rev. D* 83 (5 2011), p. 052002. URL:  
3728 <https://link.aps.org/doi/10.1103/PhysRevD.83.052002>.
- 3729 [75] Patrick Dunne. *Latest Neutrino oscillation results from T2K*. 2020.
- 3730 [76] Particle Data Group et al. "Review of particle physics". en. In: *Prog. Theor. Exp.*  
3731 *Phys.* 2020.8 (Aug. 2020).
- 3732 [77] R. L. Workman and Others. "Review of Particle Physics". In: *PTEP* 2022 (2022),  
3733 p. 083C01.
- 3734 [78] K. Abe et al. "Precise Measurement of the Neutrino Mixing Parameter  $\theta_{23}$  from  
3735 Muon Neutrino Disappearance in an Off-Axis Beam". In: *Phys. Rev. Lett.* 112 (18  
3736 2014), p. 181801. URL:  
3737 <https://link.aps.org/doi/10.1103/PhysRevLett.112.181801>.

- 3738 [79] Roger Wendell. "Three Flavor Oscillation Analysis of Atmospheric Neutrinos in  
3739 Super-Kamiokande". PhD thesis. University of North Carolina, 2008.
- 3740 [80] Adam M Dziewonski and Don L Anderson. "Preliminary reference Earth model".  
3741 en. In: *Phys. Earth Planet. Inter.* 25.4 (June 1981), pp. 297–356.
- 3742 [81] Y Fukuda et al. "Evidence for oscillation of atmospheric neutrinos". In: *Phys. Rev.*  
3743 *Lett.* 81.8 (Aug. 1998), pp. 1562–1567.
- 3744 [82] K. Abe et al. "Calibration of the Super-Kamiokande detector". In: *Nuclear*  
3745 *Instruments and Methods in Physics Research Section A: Accelerators, Spectrometers,*  
3746 *Detectors and Associated Equipment* 737 (2014), pp. 253–272. URL:  
3747 <https://doi.org/10.1016/j.nima.2013.11.081>.
- 3748 [83] Linyan Wan. "Atmospheric Neutrino\_Super-K". In: (2022). URL:  
3749 <https://zenodo.org/record/6694761>.
- 3750 [84] Miao Jiang. "Study of the neutrino mass hierarchy with the atmospheric neutrino  
3751 data collected in Super-Kamiokande IV". PhD thesis. Kyoto University, 2019.
- 3752 [85] S Fukuda et al. "The super-kamiokande detector". en. In: *Nucl. Instrum. Methods*  
3753 *Phys. Res. A* 501.2-3 (Apr. 2003), pp. 418–462.
- 3754 [86] S. Fukuda et al. "The Super-Kamiokande detector". In: *Nuclear Instruments and*  
3755 *Methods in Physics Research Section A: Accelerators, Spectrometers, Detectors and*  
3756 *Associated Equipment* 501.2 (2003), pp. 418 –462. eprint:  
3757 <http://www.sciencedirect.com/science/article/pii/S016890020300425X>.
- 3758 [87] Y Itow et al. "The JHF-Kamioka neutrino project". In: (2001).
- 3759 [88] M Jiang et al. "Atmospheric neutrino oscillation analysis with improved event  
3760 reconstruction in Super-Kamiokande IV". en. In: *Prog. Theor. Exp. Phys.* 2019.5  
3761 (May 2019).
- 3762 [89] H. Kume et al. "20 inch diameter photomultiplier". In: *Nuclear Instruments and*  
3763 *Methods in Physics Research* 205.3 (1983), pp. 443–449. URL:  
3764 <https://www.sciencedirect.com/science/article/pii/0167508783900078>.
- 3765 [90] A. Suzuki et al. "Improvement of 20 in. diameter photomultiplier tubes". In:  
3766 *Nuclear Instruments and Methods in Physics Research Section A: Accelerators,*  
3767 *Spectrometers, Detectors and Associated Equipment* 329.1-2 (May 1993), pp. 299–313.  
3768 URL: [https://doi.org/10.1016/0168-9002\(93\)90949-i](https://doi.org/10.1016/0168-9002(93)90949-i).
- 3769 [91] Y Nakano et al. "Measurement of the radon concentration in purified water in  
3770 the Super-Kamiokande IV detector". en. In: *Nucl. Instrum. Methods Phys. Res. A*  
3771 977.164297 (Oct. 2020), p. 164297.
- 3772 [92] Hamamatsu. *Hamamatsu Photonics Photomultiplier Tubes Handbook*. URL:  
3773 [https://www.hamamatsu.com/content/dam/hamamatsu-photonics/sites/documents/99\SALES\LIBRARY/etd/PMT\\\_handbook\\_v4E.pdf](https://www.hamamatsu.com/content/dam/hamamatsu-photonics/sites/documents/99\SALES\LIBRARY/etd/PMT\_handbook_v4E.pdf).
- 3775 [93] K Abe et al. "First gadolinium loading to Super-Kamiokande". en. In: *Nucl.*  
3776 *Instrum. Methods Phys. Res. A* 1027.166248 (Mar. 2022), p. 166248.
- 3777 [94] John F. Beacom and Mark R. Vagins. "Antineutrino Spectroscopy with Large  
3778 Water Čerenkov Detectors". In: *Phys. Rev. Lett.* 93 (17 2004), p. 171101. URL:  
3779 <https://link.aps.org/doi/10.1103/PhysRevLett.93.171101>.

- 3780 [95] Ll Marti et al. "Evaluation of gadolinium's action on water Cherenkov detector  
3781 systems with EGADS". en. In: *Nucl. Instrum. Methods Phys. Res. A* 959.163549  
3782 (Apr. 2020), p. 163549.
- 3783 [96] Ll Marti et al. "Evaluation of gadolinium's action on water Cherenkov detector  
3784 systems with EGADS". In: (2019).
- 3785 [97] Mark Vagins. *Solar/DSNB Neutrino\_SK-Gd*. 2022.
- 3786 [98] John Focht. PhD thesis. Massachusetts Institute of Technology, 2004.
- 3787 [99] T. Tanimori et al. "Design and performance of semi-custom analog IC including  
3788 two TACs and two current integrators for 'Super-Kamiokande'". In: *IEEE*  
3789 *Transactions on Nuclear Science* 36.1 (1989), pp. 497–501.
- 3790 [100] J. Hosaka et al. "Solar neutrino measurements in Super-Kamiokande-I". In: *Phys.*  
3791 *Rev. D* 73 (11 2006), p. 112001. URL:  
3792 <https://link.aps.org/doi/10.1103/PhysRevD.73.112001>.
- 3793 [101] H Nishino et al. "High-speed charge-to-time converter ASIC for the  
3794 Super-Kamiokande detector". en. In: *Nucl. Instrum. Methods Phys. Res. A* 610.3  
3795 (Nov. 2009), pp. 710–717.
- 3796 [102] S. Yamada et al. "Commissioning of the New Electronics and Online System for  
3797 the Super-Kamiokande Experiment". In: *IEEE Transactions on Nuclear Science* 57.2  
3798 (2010), pp. 428–432.
- 3799 [103] Satoru Yamada et al. "New online system without hardware trigger for the  
3800 Super-Kamiokande experiment". In: *2007 IEEE Nuclear Science Symposium  
3801 Conference Record*. Honolulu, HI, USA: IEEE, Oct. 2007.
- 3802 [104] Giada Carminati. "The new wide-band solar neutrino trigger for  
3803 super-kamiokande". In: *Phys. Procedia* 61 (2015), pp. 666–672.
- 3804 [105] P A Čerenkov. "Visible radiation produced by electrons moving in a medium  
3805 with velocities exceeding that of light". In: *Phys. Rev.* 52.4 (Aug. 1937),  
3806 pp. 378–379.
- 3807 [106] I Frank and Ig Tamm. "Coherent visible radiation of fast electrons passing  
3808 through matter". In: *Selected Papers*. Berlin, Heidelberg: Springer Berlin  
3809 Heidelberg, 1991, pp. 29–35.
- 3810 [107] The T2K Collaboration. "Letter of Intent: Neutrino Oscillation Experiment at  
3811 JHF". In: *KEK Proposal* (2001). eprint:  
3812 <http://neutrino.kek.jp/jhfnu/loi/loi.v2.030528.pdf>.
- 3813 [108] Y Itow et al. "The JHF-Kamioka neutrino project". In: (June 2001). arXiv:  
3814 [hep-ex/0106019](https://arxiv.org/abs/hep-ex/0106019) [hep-ex].
- 3815 [109] The K2K Collaboration and S H Ahn. "Detection of Accelerator-Produced  
3816 Neutrinos at a Distance of 250 km". In: (Feb. 2001). arXiv: [hep-ex/0103001](https://arxiv.org/abs/hep-ex/0103001)  
3817 [hep-ex].
- 3818 [110] The T2K Collaboration. "Tokai-to-Kamioka (T2K) Long Baseline Neutrino  
3819 Oscillation Experiment Proposal". In: *KEK Proposal* (2006). eprint: {{<http://j-parc.jp/researcher/Hadron/en/pac\0606/pdf/p11-Nishikawa.pdf>} }.
- 3821 [111] Christophe Bronner. *Accelerator Neutrino I\_Recent results from T2K*. 2022.

- 3822 [112] K. Abe et al. "Observation of Electron Neutrino Appearance in a Muon Neutrino  
3823 Beam". In: *Phys. Rev. Lett.* 112 (6 2014), p. 061802. eprint:  
3824 <https://link.aps.org/doi/10.1103/PhysRevLett.112.061802>.
- 3825 [113] T. Fukuda et al. "Proposal for precise measurement of neutrino-water  
3826 cross-section in NINJA physics run". Proposal for J-PARC and KEK. 2017.
- 3827 [114] T. Ovsianikova et al. "New experiment WAGASCI to measure cross sections of  
3828 neutrino interactions in water and hydrocarbon using J-PARC beam". In: *Physics*  
3829 of Particles and Nuclei 48.6 (2017), pp. 1014–1017. eprint:  
3830 <https://doi.org/10.1134/S1063779617060478>.
- 3831 [115] M. Antonova et al. "Baby MIND: a magnetized segmented neutrino detector for  
3832 the WAGASCI experiment". In: *Journal of Instrumentation* 12.07 (2017), p. C07028.  
3833 eprint: <http://stacks.iop.org/1748-0221/12/i=07/a=C07028>.
- 3834 [116] K. Abe et al. "First measurement of the charged current  $\bar{\nu}_\mu$  double differential  
3835 cross section on a water target without pions in the final state". In: *Phys. Rev. D*  
3836 102 (1 2020), p. 012007. URL:  
3837 <https://link.aps.org/doi/10.1103/PhysRevD.102.012007>.
- 3838 [117] K Abe et al. "Measurements of  $\bar{\nu}_\mu$  and  $\bar{\nu}_\mu + \nu_\mu$  charged-current cross-sections  
3839 without detected pions or protons on water and hydrocarbon at a mean  
3840 anti-neutrino energy of 0.86 GeV". In: *Progress of Theoretical and Experimental*  
3841 *Physics* 2021.4 (Mar. 2021). URL: <https://doi.org/10.1093/ptep/ptab014>.
- 3842 [118] K. Matsuoka et al. "Design and performance of the muon monitor for the T2K  
3843 neutrino oscillation experiment". In: *Nuclear Instruments and Methods in Physics*  
3844 *Research Section A: Accelerators, Spectrometers, Detectors and Associated Equipment*  
3845 624.3 (2010), pp. 591 –600. eprint:  
3846 <http://www.sciencedirect.com/science/article/pii/S016890021002098X>.
- 3847 [119] K Abe et al. "Improved constraints on neutrino mixing from the T2K experiment  
3848 with  $3.13 \times 10^{21}$  protons on target". en. In: *Phys. Rev. D*. 103.11 (June 2021).
- 3849 [120] Tomislav Vladisavljevic. *Predicting the T2K neutrino flux and measuring oscillation*  
3850 *parameters*. 1st ed. Springer theses. Cham, Switzerland: Springer Nature, Sept.  
3851 2020.
- 3852 [121] D Beavis, A Carroll, and I Chiang. "Long baseline neutrino oscillation  
3853 experiment at the AGS. Physics design report". In: (Apr. 1995).
- 3854 [122] P.-A. Amaudruz et al. "The T2K fine-grained detectors". In: *Nuclear Instruments*  
3855 *and Methods in Physics Research Section A: Accelerators, Spectrometers, Detectors and*  
3856 *Associated Equipment* 696 (Dec. 2012), pp. 1–31. URL:  
3857 <https://doi.org/10.1016/j.nima.2012.08.020>.
- 3858 [123] N. Abgrall et al. "Time projection chambers for the T2K near detectors". In:  
3859 *Nuclear Instruments and Methods in Physics Research Section A: Accelerators,*  
3860 *Spectrometers, Detectors and Associated Equipment* 637.1 (May 2011), pp. 25–46. URL:  
3861 <https://doi.org/10.1016/j.nima.2011.02.036>.
- 3862 [124] S. Assylbekov et al. "The T2K ND280 off-axis pi-zero detector". In: *Nuclear*  
3863 *Instruments and Methods in Physics Research Section A: Accelerators, Spectrometers,*  
3864 *Detectors and Associated Equipment* 686 (Sept. 2012), pp. 48–63. URL:  
3865 <https://doi.org/10.1016/j.nima.2012.05.028>.

- 3866 [125] D Allan et al. "The electromagnetic calorimeter for the T2K near detector  
3867 ND280". In: *Journal of Instrumentation* 8.10 (2013), P10019–P10019. URL:  
3868 <https://doi.org/10.1088%2F1748-0221%2F8%2F10%2Fp10019>.
- 3869 [126] *UA1 magnet sets off for a second new life*. 2022. URL: <https://cerncourier.com/a/ua1-magnet-sets-off-for-a-second-new-life/>.
- 3871 [127] F. Vannucci. "The NOMAD Experiment at CERN". In: *Advances in High Energy  
3872 Physics* 2014 (2014), pp. 1–20. URL: <https://doi.org/10.1155/2014/129694>.
- 3873 [128] S. Aoki et al. "The T2K Side Muon Range Detector (SMRD)". In: *Nuclear  
3874 Instruments and Methods in Physics Research Section A: Accelerators, Spectrometers,  
3875 Detectors and Associated Equipment* 698 (Jan. 2013), pp. 135–146. URL:  
3876 <https://doi.org/10.1016/j.nima.2012.10.001>.
- 3877 [129] K. Suzuki et al. "Measurement of the muon beam direction and muon flux for the  
3878 T2K neutrino experiment". In: *Progress of Theoretical and Experimental Physics*  
3879 2015.5 (2015), pp. 53C01–0. URL: <https://doi.org/10.1093%2Fptep%2Fptv054>.
- 3880 [130] S. Brooks et al. *Handbook of Markov Chain Monte Carlo*. CRC Press, 2011.
- 3881 [131] W. R. Gilks, S. Richardson, and D. J. Spiegelhalter. *Markov Chain Monte Carlo in  
3882 Practice*. Chapman & Hall/CRC Interdisciplinary Statistics, 1995.
- 3883 [132] Clarence Wret. "Minimising systematic uncertainties in the T2K experiment using  
3884 near-detector and external data". PhD thesis. Imperial College London, 2018.
- 3885 [133] Kirsty Elizabeth Duffy. "Measurement of the Neutrino Oscillation Parameters  
3886  $\sin^2 \theta_{23}$ ,  $\Delta m_{32}^2$ ,  $\sin^2 \theta_{13}$ , and  $\delta_{CP}$  in Neutrino and Antineutrino Oscillation at T2K".  
3887 PhD thesis. Oriel College, University of Oxford, 2016.
- 3888 [134] C. Bojeckho and A. Kabooth. "Muon neutrino disappearance simultaneous fit of  
3889 ND280 and SK with Run 1+2+3 data using Markov Chain Monte Carlo Analysis".  
3890 In: *T2K Technical Note* 140 (2013).
- 3891 [135] Thomas Bayes Rev. "An essay toward solving a problem in the doctrine of  
3892 chances". In: *Phil. Trans. Roy. Soc. Lond.* 53 (1764), pp. 370–418.
- 3893 [136] Artur Sztuc. "Standard and Non-Standard Neutrino-Antineutrino Oscillation  
3894 Analyses and Event Reconstruction Studies using Markov Chain Monte Carlo  
3895 Methods at T2K". PhD thesis. Imperial College London, 2021.
- 3896 [137] N. Metropolis et al. "Equation of State Calculations by Fast Computing  
3897 Machines". In: *Journal of Chemical Physics* 21.6 (1970).
- 3898 [138] W. K. Hastings. "Monte Carlo Sampling Methods Using Markov Chains and  
3899 Their Applications". In: *Biometrika* 57.1 (1970).
- 3900 [139] Joanna Dunkley et al. "Fast and reliable Markov chain Monte Carlo technique for  
3901 cosmological parameter estimation". en. In: *Mon. Not. R. Astron. Soc.* 356.3 (Jan.  
3902 2005), pp. 925–936.
- 3903 [140] Harold Jeffreys. *The Theory of Probability*. Oxford Classic Texts in the Physical  
3904 Sciences. 1939.
- 3905 [141] Robert E Kass and Adrian E Raftery. "Bayes factors". en. In: *J. Am. Stat. Assoc.*  
3906 90.430 (June 1995), pp. 773–795.

- 3907 [142] T.T. Böhlen et al. "The FLUKA Code: Developments and Challenges for High  
3908 Energy and Medical Applications". In: *Nuclear Data Sheets* 120 (2014), pp. 211  
3909 –214. eprint:  
3910 <http://www.sciencedirect.com/science/article/pii/S0090375214005018>.
- 3911 [143] René Brun et al. *GEANT: Detector Description and Simulation Tool; Oct 1994*. CERN  
3912 Program Library. Long Writeup W5013. Geneva: CERN, 1993. eprint:  
3913 <http://cds.cern.ch/record/1082634>.
- 3914 [144] K. Abe et al. "T2K neutrino flux prediction". In: *Phys. Rev. D* 87 (1 2013),  
3915 p. 012001. URL: <https://link.aps.org/doi/10.1103/PhysRevD.87.012001>.
- 3916 [145] C. Zeitnitz and T.A. Gabriel. "The GEANT-CALOR interface and benchmark  
3917 calculations of ZEUS test calorimeters". In: *Nuclear Instruments and Methods in  
3918 Physics Research Section A: Accelerators, Spectrometers, Detectors and Associated  
3919 Equipment* 349.1 (1994), pp. 106 –111. eprint:  
3920 <http://www.sciencedirect.com/science/article/pii/0168900294906130>.
- 3921 [146] A. Fiorentini et al. "Flux Prediction and Uncertainty Updates with NA61 2009  
3922 Thin Target Data and Negative Focussing Mode Predictions". In: *T2K Technical  
3923 Note* 217 (2017).
- 3924 [147] N. Abgrall et al. "Measurements of cross sections and charged pion spectra in  
3925 proton-carbon interactions at 31 GeV/ $c$ ". In: *Physical Review C* 84.3 (2011). URL: <https://doi.org/10.1103/physrevc.84.034604>.
- 3926 [148] N. Abgrall et al. "Measurement of production properties of positively charged  
3927 kaons in proton-carbon interactions at 31 GeV/ $c$ ". In: *Physical Review C* 85.3 (2012). URL: <https://doi.org/10.1103/physrevc.85.035210>.
- 3928 [149] N. Abgrall et al. "Pion emission from the T2K replica target: Method, results and  
3929 application". In: *Nuclear Instruments and Methods in Physics Research Section A:  
3930 Accelerators, Spectrometers, Detectors and Associated Equipment* 701 (2013), pp. 99  
3931 –114. eprint:  
3932 <http://www.sciencedirect.com/science/article/pii/S016890021201234X>.
- 3933 [150] M. Apollonio et al. "Forward production of charged pions with incident protons  
3934 on nuclear targets at the CERN Proton Synchrotron". In: *Phys. Rev. C* 80 (3 2009),  
3935 p. 035208. eprint: <https://link.aps.org/doi/10.1103/PhysRevC.80.035208>.
- 3936 [151] B. Blau et al. "The superconducting magnet of AMS-02". In: *Nuclear Physics B -  
3937 Proceedings Supplements* 113.1-3 (Dec. 2002), pp. 125–132. URL:  
3938 [https://doi.org/10.1016/s0920-5632\(02\)01831-5](https://doi.org/10.1016/s0920-5632(02)01831-5).
- 3939 [152] S. Haino et al. "Measurements of primary and atmospheric cosmic-ray spectra  
3940 with the BESS-TeV spectrometer". In: *Physics Letters B* 594.1-2 (July 2004),  
3941 pp. 35–46. URL: <https://doi.org/10.1016/j.physletb.2004.05.019>.
- 3942 [153] NASA. *U.S. Standard Atmosphere, 1976*. 1976.

- 3949 [154] S. Roesler, R. Engel, and J. Ranft. "The Monte Carlo Event Generator  
3950 DPMJET-III". In: *Advanced Monte Carlo for Radiation Physics, Particle Transport*  
3951 *Simulation and Applications*. Springer Berlin Heidelberg, 2001, pp. 1033–1038. URL:  
3952 <https://doi.org/10.1007/978-3-642-18211-2\166>.
- 3953 [155] Koji Niita et al. "PHITS—a particle and heavy ion transport code system". In:  
3954 *Radiation Measurements* 41.9-10 (Oct. 2006), pp. 1080–1090. URL:  
3955 <https://doi.org/10.1016/j.radmeas.2006.07.013>.
- 3956 [156] T Sanuki et al. "Measurements of atmospheric muon spectra at mountain  
3957 altitude". In: *Physics Letters B* 541.3-4 (2002), pp. 234–242. URL:  
3958 <https://doi.org/10.1016%2Fs0370-2693%2802%2902265-7>.
- 3959 [157] P. Achard et al. "Measurement of the atmospheric muon spectrum from 20 to  
3960 3000 GeV". In: *Physics Letters B* 598.1-2 (2004), pp. 15–32. URL:  
3961 <https://doi.org/10.1016%2Fj.physletb.2004.08.003>.
- 3962 [158] Kazufumi Sato. *Atmospheric Neutrino\_Reviews on neutrino fluxes (low E atm nu)*.  
3963 2022.
- 3964 [159] Yoshinari Hayato and Luke Pickering. "The NEUT neutrino interaction  
3965 simulation program library". In: *The European Physical Journal Special Topics* 230.24  
3966 (Oct. 2021), pp. 4469–4481. URL:  
3967 <https://doi.org/10.1140/epjs/s11734-021-00287-7>.
- 3968 [160] Yoshinari Hayato. "A Neutrino Interaction Simulation Program Library NEUT".  
3969 In: *Acta Physica Polonica B* 40.9 (2009).
- 3970 [161] C.H. Llewellyn Smith. "Neutrino reactions at accelerator energies". In: *Physics*  
3971 *Reports* 3.5 (1972), pp. 261 –379. eprint:  
3972 <http://www.sciencedirect.com/science/article/pii/0370157372900105>.
- 3973 [162] Omar Benhar, Adelchi Fabrocini, and Stefano Fantoni. "The nucleon spectral  
3974 function in infinite nuclear matter". In: *Nuclear Physics A* 497 (June 1989),  
3975 pp. 423–430. URL: [https://doi.org/10.1016/0375-9474\(89\)90484-3](https://doi.org/10.1016/0375-9474(89)90484-3).
- 3976 [163] R. Bradford et al. "A New Parameterization of the Nucleon Elastic Form Factors".  
3977 In: *Nuclear Physics B - Proceedings Supplements* 159 (2006). Proceedings of the 4th  
3978 International Workshop on Neutrino-Nucleus Interactions in the Few-GeV  
3979 Region, pp. 127 –132. eprint:  
3980 <http://www.sciencedirect.com/science/article/pii/S0920563206005184>.
- 3981 [164] A. A. Aguilar-Arevalo et al. "First measurement of the muon neutrino charged  
3982 current quasielastic double differential cross section". In: *Physical Review D* 81.9  
3983 (2010). URL: <https://doi.org/10.1103%2Fphysrevd.81.092005>.
- 3984 [165] R. Gran et al. "Neutrino-nucleus quasi-elastic and 2p2h interactions up to 10  
3985 GeV". In: *Phys. Rev. D* 88 (11 2013), p. 113007. eprint:  
3986 <https://link.aps.org/doi/10.1103/PhysRevD.88.113007>.
- 3987 [166] Ch. Berger and L. M. Sehgal. "Lepton mass effects in single pion production by  
3988 neutrinos". In: *Phys. Rev. D* 76 (11 2007), p. 113004. URL:  
3989 <https://link.aps.org/doi/10.1103/PhysRevD.76.113004>.
- 3990 [167] Ch. Berger and L. M. Sehgal. "Partially conserved axial vector current and  
3991 coherent pion production by low energy neutrinos". In: *Phys. Rev. D* 79 (5 2009),  
3992 p. 053003. eprint: <https://link.aps.org/doi/10.1103/PhysRevD.79.053003>.

- 3993 [168] Torbjörn Sjöstrand. "High-energy-physics event generation with PYTHIA 5.7 and  
3994 JETSET 7.4". In: *Computer Physics Communications* 82.1 (Aug. 1994), pp. 74–89.  
3995 URL: [https://doi.org/10.1016/0010-4655\(94\)90132-5](https://doi.org/10.1016/0010-4655(94)90132-5).
- 3996 [169] Christophe Bronner and Mark Hartz. "Tuning of the Charged Hadrons  
3997 Multiplicities for Deep Inelastic Interactions in NEUT". In: *Proceedings of the 10th*  
3998 *International Workshop on Neutrino-Nucleus Interactions in Few-GeV Region*  
3999 (*NuInt15*). Journal of the Physical Society of Japan, Dec. 2016. URL:  
4000 <https://doi.org/10.7566/jpsc.12.010041>.
- 4001 [170] M. Glück, E. Reya, and A. Vogt. "Dynamical parton distributions revisited". In:  
4002 *The European Physical Journal C* 5.3 (1998), pp. 461–470. URL:  
4003 <https://doi.org/10.1007%2Fs100529800978>.
- 4004 [171] Arie Bodek and Un-ki Yang. *Axial and Vector Structure Functions for Electron- and*  
4005 *Neutrino- Nucleon Scattering Cross Sections at all  $Q^2$  using Effective Leading order*  
4006 *Parton Distribution Functions*. 2010. URL: <https://arxiv.org/abs/1011.6592>.
- 4007 [172] Arie Bodek and Un-Ki Yang. "Update to the Bodek-Yang Unified Model for  
4008 Electron- and Neutrino- Nucleon Scattering Cross Sections". In: (2010). URL:  
4009 <https://arxiv.org/abs/1012.0261>.
- 4010 [173] Sowjanya Gollapinni. "Neutrino Cross section Future". In: (2016). URL:  
4011 <https://arxiv.org/abs/1602.05299>.
- 4012 [174] E. S. Pinzon Guerra et al. "Using world  $\pi^\pm$ -nucleus scattering data to constrain  
4013 an intranuclear cascade model". In: *Phys. Rev. D* 99 (5 2019), p. 052007. URL:  
4014 <https://link.aps.org/doi/10.1103/PhysRevD.99.052007>.
- 4015 [175] S. Agostinelli et al. "GEANT4: A Simulation toolkit". In: *Nucl. Instrum. Meth.*  
4016 A506 (2003), pp. 250–303.
- 4017 [176] R. Brun et al. "GEANT3". In: (Sept. 1987).
- 4018 [177] et al. A. Himmel. "Super-Kamiokande events and data quality studies for T2K  
4019 Runs 5 and 6". In: *T2K Technical Note* 219 (2015).
- 4020 [178] et al. S. Berkman. "fiTQun: A New Reconstruction Algorithm for Super-K". In:  
4021 *T2K Technical Note* 146 (2013).
- 4022 [179] R.B. Patterson et al. "The extended-track event reconstruction for MiniBooNE".  
4023 In: *Nuclear Instruments and Methods in Physics Research Section A: Accelerators,*  
4024 *Spectrometers, Detectors and Associated Equipment* 608.1 (2009), pp. 206–224. URL:  
4025 <https://doi.org/10.1016%2Fj.nima.2009.06.064>.
- 4026 [180] M. Shiozawa. "Reconstruction algorithms in the Super-Kamiokande large water  
4027 Cherenkov detector". In: *Nuclear Instruments and Methods in Physics Research*  
4028 *Section A: Accelerators, Spectrometers, Detectors and Associated Equipment* 433.1-2  
4029 (Aug. 1999), pp. 240–246. URL:  
4030 [https://doi.org/10.1016/s0168-9002\(99\)00359-9](https://doi.org/10.1016/s0168-9002(99)00359-9).

- 4031 [181] K. Abe et al. "Search for <mml:math  
4032 xmlns:mml="http://www.w3.org/1998/Math/MathML"  
4033 display="inline"><mml:mi>C</mml:mi><mml:mi>P</mml:mi></mml:math>  
4034 Violation in Neutrino and Antineutrino Oscillations by the T2K Experiment with  
4035 <mml:math xmlns:mml="http://www.w3.org/1998/Math/MathML"  
4036 display="inline"><mml:mn>2.2</mml:mn><mml:mo>x</mml:mo><mml:msup><mml:mn  
4037 Protons on Target". In: *Physical Review Letters* 121.17 (Oct. 2018). URL:  
4038 <https://doi.org/10.1103/physrevlett.121.171802>.
- 4039 [182] K. Abe et al. "Measurements of neutrino oscillation in appearance and  
4040 disappearance channels by the T2K experiment with<mml:math  
4041 xmlns:mml="http://www.w3.org/1998/Math/MathML"  
4042 display="inline"><mml:mn>6.6</mml:mn><mml:mo>x</mml:mo><mml:mn>1</mml:mn  
4043 on target". In: *Physical Review D* 91.7 (Apr. 2015). URL:  
4044 <https://doi.org/10.1103/physrevd.91.072010>.
- 4045 [183] F and James. "MINUIT: Function Minimization and Error Analysis Reference  
4046 Manual". In: (1998). CERN Program Library Long Writeups. URL:  
4047 <https://cds.cern.ch/record/2296388>.
- 4048 [184] Xiaoyue Li and Michael Wilking. "FiTQun Event Selection Optimization". In:  
4049 *T2K Technical Note* 319 (2017).
- 4050 [185] Shimpei Tobayama. "An Analysis of the Oscillation of Atmospheric Neutrinos".  
4051 PhD thesis. British Columbia U., 2016.
- 4052 [186] et al. D. Barrow. "Super-Kamiokande Data Quality, MC, and Systematics in Run  
4053 10". In: *T2K Technical Note* 399 (2020).
- 4054 [187] A. Maghrabi, A. Aldosari, and M. Almutairi. "Correlation analyses between solar  
4055 activity parameters and cosmic ray muons between 2002 and 2012 at high cutoff  
4056 rigidity". In: *Advances in Space Research* 68.7 (Oct. 2021), pp. 2941–2952. URL:  
4057 <https://doi.org/10.1016/j.asr.2021.05.016>.
- 4058 [188] K. Abe et al. "Atmospheric neutrino oscillation analysis with external constraints  
4059 in Super-Kamiokande I-IV". In: *Phys. Rev. D* 97 (7 2018), p. 072001. eprint:  
4060 <https://link.aps.org/doi/10.1103/PhysRevD.97.072001>.
- 4061 [189] J. Beringer et al. "Review of Particle Physics". In: *Phys. Rev. D* 86 (1 2012),  
4062 p. 010001. URL: <https://link.aps.org/doi/10.1103/PhysRevD.86.010001>.
- 4063 [190] S. Nakayama K. Iyogi and Y. Obayashi. "T2K data acquisition and FC event  
4064 selection at Super-Kamiokande". In: *T2K Technical Note* 027 (2011).
- 4065 [191] LeeKaPik. "Study of the neutrino mass hierarchy with the atmospheric neutrino  
4066 data observed in Super-Kamiokande". PhD thesis. Tokyo University, 2012.
- 4067 [192] R. Wendell et al. "Atmospheric neutrino oscillation analysis with subleading  
4068 effects in Super-Kamiokande I, II, and III". In: *Phys. Rev. D* 81 (9 2010), p. 092004.  
4069 URL: <https://link.aps.org/doi/10.1103/PhysRevD.81.092004>.
- 4070 [193] J. Hosaka et al. "Three flavor neutrino oscillation analysis of atmospheric  
4071 neutrinos in Super-Kamiokande". In: *Phys. Rev. D* 74 (3 2006), p. 032002. URL:  
4072 <https://link.aps.org/doi/10.1103/PhysRevD.74.032002>.

- 4073 [194] Laura Munteanu et al. "Constraining the Flux and Cross Section Models with  
 4074 Data from ND280 using FGD1 and FGD2 for the 2020 Oscillation Analysis". In:  
 4075 *T2K Technical Note 395* (2020).
- 4076 [195] P. Bartet et al. " $\nu_\mu$  CC event selections in the ND280 tracker using Run 2+3+4  
 4077 data". In: *T2K Technical Note 212* (2015).
- 4078 [196] Will Parker. "Constraining Systematic Uncertainties at T2K using Near Detector  
 4079 Data". PhD thesis. Royal Holloway University of London, 2020.
- 4080 [197] V. Berardi et al. " $\bar{\nu}_\mu$  event selection in the ND280 tracker using Run 5c and Run 6  
 4081 anti-neutrino beam data". In: *T2K Technical Note 246* (2015).
- 4082 [198] Brian Kirby Jiae Kim and Michael Wilking. "Michel Electron Tagging in FGD1".  
 4083 In: *T2K Technical Note 104* (2012).
- 4084 [199] James Missert. "TN-318: Fit to Super-K Atmospheric Neutrino Data for  
 4085 Optimization of the fiTQun Fiducial Volume Cuts and Estimation of Detector  
 4086 Uncertainties". In: *T2K Technical Note 318* (2017).
- 4087 [200] et al. J. Chakrani. "NIWG model and uncertainties for 2021 oscillation analysis".  
 4088 In: *T2K Technical Note 414* (2022).
- 4089 [201] Morgan Wascko. "T2K Status, Results, and Plans". *Neutrino 2018*. 2018.
- 4090 [202] et al. Tomislav Vladisavljevic. "Flux Prediction and Uncertainty with  
 4091 NA61/SHINE 2009 Replica-Target Data (TN354 version 3.3)". In: *T2K Technical*  
 4092 *Note 354* (2020).
- 4093 [203] G Ambrosini et al. "K/ $\pi$  production ratios from 450 GeV/c protons on  
 4094 beryllium". en. In: *Phys. Lett. B* 420.1-2 (Feb. 1998), pp. 225–232.
- 4095 [204] et al. Edward Atkin. "NIWG model and uncertainties for 2019-2020 oscillation  
 4096 analysis". In: *T2K Technical Note 344* (2019).
- 4097 [205] et al. D. Barrow. "Flux and interaction models for the initial T2K-SK atmospheric  
 4098 joint fit studies". In: *T2K Technical Note 422* (2022).
- 4099 [206] et al. D. Barrow. "SK atmospheric T2K beam joint fit technical note, MaCh3  
 4100 details". In: *T2K Technical Note 426* (2022).
- 4101 [207] A. A. Aguilar-Arevalo et al. "Measurement of  $\nu_\mu$  and  $\bar{\nu}_\mu$  induced neutral current  
 4102 single  $\pi^0$  production cross sections on mineral oil at  $E_\nu \sim \mathcal{O}(1 \text{ GeV})$ ". In: *Phys.*  
 4103 *Rev. D* 81 (1 2010), p. 013005. eprint:  
 4104 <https://link.aps.org/doi/10.1103/PhysRevD.81.013005>.
- 4105 [208] Patrick de Perio and James Imber. "Super-K Systematic Uncertainties for RUN1-4  
 4106 Joint  $\nu_e$  and  $\nu_\mu$  Analyses". In: *T2K Technical Note 186* (2014).
- 4107 [209] Patrick de Perio and James Imber. "Update of SK  $\nu_e$  systematic error for 2012a  
 4108 oscillation analysis". In: *T2K Technical Note 107* (2012).
- 4109 [210] Cris Vilela Daniel Barrow. *T2K-SK Detector Matrix Uncertainties - MaCh3*  
 4110 *Integration*. <https://git.t2k.org/t2k-sk/t2ksk-detcovmat/-/tree/feature/MaCh3Integration>. Accessed: 22-06-2022.
- 4112 [211] Roger Barlow and Christine Beeston. "Fitting using finite Monte Carlo samples".  
 4113 en. In: *Comput. Phys. Commun.* 77.2 (Oct. 1993), pp. 219–228.

- 4114 [212] J S Conway. *Incorporating nuisance parameters in likelihoods for multisource spectra*.  
4115 2011.
- 4116 [213] et al. D. Barrow. "Oscillation probability calculation for the T2K+SK atmospheric  
4117 joint fit". In: *T2K Technical Note 425* (2022).
- 4118 [214] R G Calland, A C Kaboro, and D Payne. "Accelerated event-by-event neutrino  
4119 oscillation reweighting with matter effects on a GPU". In: 9.04 (Apr. 2014),  
4120 P04016–P04016. URL: <https://doi.org/10.1088/1748-0221/9/04/p04016>.
- 4121 [215] R. Wendell. <http://www.phy.duke.edu/raw22/public/Prob3++/>.
- 4122 [216] Felix Kallenborn et al. "Massively parallel computation of atmospheric neutrino  
4123 oscillations on CUDA-enabled accelerators". In: *Computer Physics Communications*  
4124 234 (2019), pp. 235–244. URL: <https://www.sciencedirect.com/science/article/pii/S0010465518302790>.
- 4125 [217] Liban Warsame. *MaCh3 Analysis Progress*. URL: <https://indico.fnal.gov/event/50217/contributions/241232/attachments/155318/202209/MaCh3ProgressforDUNELBL\underscoreMay17%20%282%29.pdf>.
- 4126 [218] Simon Bourret, João A B Coelho, and Véronique Van Elewyck and. "Neutrino  
4127 oscillation tomography of the Earth with KM3NeT-ORCA". In: *Journal of Physics: Conference Series* 888 (2017), p. 012114. URL:  
4128 <https://doi.org/10.1088%2F1742-6596%2F888%2F1%2F012114>.
- 4129 [219] C. Rott, A. Taketa, and D. Bose. "Spectrometry of the Earth using Neutrino  
4130 Oscillations". In: *Scientific Reports* 5.1 (Oct. 2015). URL:  
4131 <https://doi.org/10.1038/srep15225>.
- 4132 [220] Kaoru Hagiwara, Naotoshi Okamura, and Ken ichi Senda. "The earth matter  
4133 effects in neutrino oscillation experiments from Tokai to Kamioka and Korea". In:  
4134 *Journal of High Energy Physics* 2011.9 (Sept. 2011). URL:  
4135 [https://doi.org/10.1007/jhep09\(2011\)082](https://doi.org/10.1007/jhep09(2011)082).
- 4136 [221] Dave Typinski. *Earth Gravity*.  
4137 <http://www.typnet.net/Essays/EarthGravGraphics/EarthGrav.pdf>.  
4138 Accessed: 24-06-2022.
- 4139 [222] D. Barrow. *T2K Beam + SK Atmospheric Joint Fit*. 2022.